Rydberg-Stark deceleration and trapping of helium atoms above electrical transmission-lines

Patrick Lancuba

Supervisor: Dr. Stephen D. Hogan

Co-supervisor: Prof. Peter Barker

Department of Physics and Astronomy

University College London

March 2016

A THESIS SUBMITTED TO UNIVERSITY COLLEGE LONDON FOR THE DEGREE OF

Doctor of Philosophy

Declaration

I, Patrick Lancuba confirm that the work presented in this thesis is my own. Where information has been derived from other sources, I confirm that this has been indicated in the thesis.

Date: . . . . . Signature: . . . . . .

Abstract

The experimental realisation of a set of surface-based devices for controlling the positions and velocities of Rydberg atoms initially travelling in pulsed supersonic beams is described. The unique aspect of these devices is that they are based on the geometry of two-dimensional electrical transmission-lines and are therefore suited to integration with chip-based microwave circuits to realise a complete Rydberg laboratory on a chip. Such a chip-based laboratory could be exploited in hybrid approaches to quantum information processing, and for studies of collisions and decay processes of highly excited atoms and molecules. The devices operate through the generation of inhomogeneous electric fields and take advantage of the large electric dipole moments associated with high Rydberg states to exert forces on the atoms. In the experiments, helium atoms in Rydberg-Stark states with principal quantum numbers ranging from 48 to 52 and electric dipole moments of $\sim$ 10000 D are employed.

The devices developed include electrostatic guides which permitted control over the transverse motion of beams of atoms. These were used to transport samples, initially travelling at $\sim$ 1950 m/s and deflect them away from their initial axis of propagation. The guided atoms were detected by pulsed electric field ionisation. To control the longitudinal motion of the samples, the transmission-lines were modified to permit the generation of sets of continuously moving electric traps. The resulting *transmission-line decelerators* were then employed to guide, accelerate and decelerate atoms trapped in three-dimensions. Accelerations up to -2.3 x 10^7 m/s^2 were applied to decelerate samples from 2000 m/s to zero-velocity in the laboratory-fixed frame of reference, leading to the removal of $\sim$80 meV of kinetic energy, the largest achieved in any Stark decelerator to date. The decelerated atoms were trapped in stationary electric traps and detected *in-situ*. The phase-space acceptances of the decelerators were calculated to characterise the effects of acceleration and deceleration on the trapped atoms. The results of the calculations were employed in the interpretation of the experimental data, and to identify effects of collisions and blackbody transitions.

Acknowledgments

My doctoral work has been an extraordinary experience. During this time, I was surrounded by a positive environment and people. In agreement with Epictetus, this has been of great importance to call forth my best. To these people I would now like to express my gratitude.

I would like to thank my supervisor, Dr. Stephen Hogan, for giving me the opportunity to carry out academic research in such a fascinating area of physics and physical chemistry. As I was the first PhD student of his newly established research group at University College London, I was in the rare position to work on the design and construction of a new experimental laboratory. This allowed me to develop a variety of projects, starting from their imaginative conception, to the experimental realisation. I am grateful for his support throughout these three years, as it allowed me to learn how to carry out research in an investigative, scientifically critical and cooperative way, and the results are a source of pride and excitement.

I would like to express my deep gratitude to Prof. Frédéric Merkt, of the ETH Zürich, for his support in helping me to pursue and realise my academic interests. His trust in me and in my abilities provided the foundation for me to persevere and to excel. This became the starting point with which I realised, as first mentioned by Aristotle, that quality is indeed not an act, but it is a habit.

As this work required strong self-motivation and commitment, I reinstate the importance of moral support, without which all of this would have not been possible. For this reason, I would like to sincerely thank my family, particularly my mother Daniela and my sister Manuela, for their unconditional support throughout my studies. I would like to express my deepest appreciation and love to my partner, Caroline, as she always has been on my side, and her support never wavered. I would like to thank my friends and colleagues for their brilliant insights and words of encouragement.

My PhD work allowed me not only to learn new skills and knowledge, but also to grow as a person. It has given me an excellent foundation on which to build my future career.

Contents

List of Figures

List of Tables

Publications

1. P. Lancuba and S. D. Hogan, *Guiding Rydberg atoms above surface-based transmission lines*, Phys. Rev. A, **88**, 043427 (2013).

2. P. Lancuba and S. D. Hogan, *Transmission-line decelerators for atoms in high Rydberg states*, Phys. Rev. A, **90**, 053410 (2014).

3. P. Lancuba and S. D. Hogan, *Electrostatic trapping and in situ detection of Rydberg atoms above electrical transmission lines*, J. Phys. B: At. Mol. Opt. Phys., accepted for publication (2016).

Chapter 1

Application of Rydberg states

Rydberg states are excited electronic states of atoms or molecules with high principal quantum number n. Samples of atoms and molecules in these states are of importance in a range of areas of research at the interface between physics and physical chemistry. In particular translationally cold samples of atoms and molecules in high Rydberg states are ideally suited for (a) precision spectroscopy measurements, (b) studies of interactions between Rydberg atoms and molecules and surfaces, (c) hybrid approaches to quantum information processing, and (d) experiments with positronium and antihydrogen. The chip-based devices for guiding, transporting and trapping atoms and molecules in high Rydberg states that are described in this thesis are relevant in each of these areas.

The controlled manipulation of atoms and molecules by using substrate mounted microstructures was first investigated in the early 1990's [1]. These devices, which were the result of miniaturisation and integration of matter-wave optics, allowed strong confinement, well-established production procedures and the knowledge of the exact location of the atom relative to other structures on the surface to the precision of the fabrication process.

A variety of atom optical devices have been realised on such atom-chips. The first experiments were focussed on the manipulation and trapping of neutral atoms and led to the development of tightly confining traps and guides [2, 3, 4], beam splitters [5] and mirrors [6].

Following this, chip-based devices allowing confinement of ions have been developed. Compared to chips for trapping neutral atoms, ion traps with similar dimensions offer higher confinement forces and better control on single atoms [7]. These are of interest for the development of miniature-mass spectrometer arrays [8], compact atomic clocks [9], and large-scale quantum infor-

mation processors [10, 11].

Experiments involving trapping molecules on a chip were first carried out by using a microstructured electrode array that was used as a mirror for deflecting state-selected beams of ammonia [12]. This was followed by trapping of CO molecules on a microstructured array of electrodes, which allowed state-selected polar molecules to be conveyed in travelling potential wells [13, 14].

The use of chip-based devices for trapping and manipulating ground-state molecules was extended afterwards to atoms and molecules in high-excited states, as historically described in detail in Chapter 2. Furthermore, this provided the motivational basis to the work presented in this thesis, which is presented in this chapter by starting with the description of the applications of atoms and molecules in Rydberg states. It follows an historical description of methods involving Rydberg-Stark deceleration and trapping in Chapter 2. A theoretical background describing the physical principles that are of importance throughout this work is presented in Chapter 3. The experimental methods used in the experiments discussed in this thesis are presented in Chapter 4. This is followed by the experimental results involving guiding helium atoms in high Rydberg states (Chapter 5) and decelerating and trapping helium Rydberg atoms (Chapter 6). Studies of trajectories and calculations of the phase-space acceptances and time-of-flight distributions of this decelerator are described in Chapter 7. A second generation transmission-line decelerator for trapping and stopping helium Rydberg atoms is presented in Chapter 8. This is followed by final considerations in the concluding Chapter 9.

1.1 Precision spectroscopy

High resolution spectroscopy of Rydberg states is of interest for precision measurements of important physical quantities, including the determination of dissociation and ionisation energies of atoms and molecules [15, 16], and in the determination of effects of nuclear spin in photoionisation [17]. An example of this can be seen in high-resolution millimeter-wave spectroscopic studies of Rydberg states of krypton presented in Figure 1.1. In the spectra in this figure, the dependence of the spectral resolution on the interaction time between the atoms and the millimeter-wave radiation field is displayed [18].

These spectra were recorded for interaction times between the excited krypton atoms and the millimeter-wave radiation of 1 μs, 3 μs and 18 μs. As can be seen, the line-widths decrease pro-

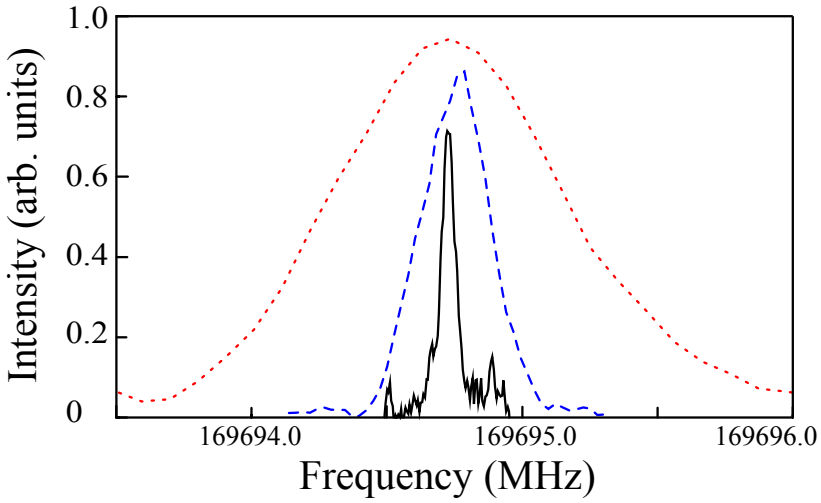

Figure 1.1: Millimeter-wave spectra of the $77d[3/2](J'=1) \rightarrow 93p[3/2](J=1)$ transition in krypton (adapted from Ref. [18]). The measurements were carried out for interaction times between the atoms and the millimeter-wave radiation of 1 μs (red, dotted line), 3 μs (blue, dashed line) and 18 μs (black, continuous line), respectively.

gressively as the interaction times increase, from 350 kHz in the case of an interaction time of 1 μs, to 60 kHz when the interaction times are increased to 18 μs. The experimental resolution is therefore strongly affected by the interaction time between the radiation field and the atomic/molecular sample. This is a consequence of the time-energy uncertainty relation

$$\Delta E \Delta t \geq \hbar, \tag{1.1}$$

which can be written in terms of a frequency uncertainty as

$$\Delta \nu \geq \frac{1}{2\pi \Delta t}. \tag{1.2}$$

In the case in Figure 1.1, the temporal profile of the millimeter-wave pulse is not described by a simple analytical function. Hence, the lower limit associated with Equation 1.2 was not achieved. The measurements displayed in Figure 1.1 highlight the need to produce translationally cold samples to increase interaction times and improve the spectroscopic resolution in experiments of this kind.

Precise spectroscopic measurements of high Rydberg states are also of importance in the determination of the dissociation and ionisation energies of small molecules, for example H_2 [15],

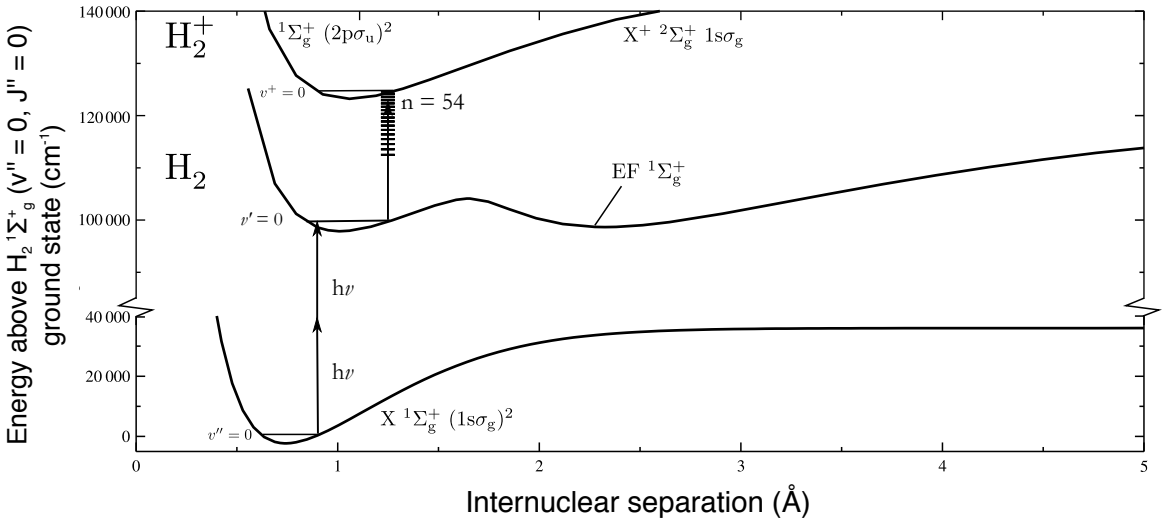

Figure 1.2: Potential energy diagram of the hydrogen molecule, adapted from Ref. [27]. The potential energy surface associated with the $X^1\Sigma_g^+(v'' = 0)$ ground state, the excited state $EF^1\Sigma_g^+(v' = 0)$ and the $X^+\ ^2\Sigma_g^+(v = 0)$ state of the H_2^+ ion are represented, along with the corresponding transitions used in the precise determination of the ionisation energy of the hydrogen molecule.

HD [19], D_2 [20] and He_2 [21]. As direct measurements of either dissociation and ionisation energies require e.g. the determination of the onset of their respective spectral continua [22, 23], or kinetic energies measurements [24], these measurements attained best accuracies of about 1 GHz [25]. Indirect measurement techniques involving high-resolution measurements of spectra of atoms or molecules in high Rydberg states have been developed and because they rely on their sharp spectroscopic transitions, typically higher resolution of ~ 300 MHz have been achieved [19, 16, 15, 20, 21]. Furthermore, such measurements are of importance for better understanding the nature of the chemical bonds and for understanding the density of molecules containing hydrogen bonds of the early universe [26].

In the case of the hydrogen molecule, for example, experiments have been carried out by Liu et al. [15], in which samples of ortho-H_2 in the 54p Rydberg state were prepared and the energy intervals between these states measured, together with intervals between the high Rydberg states to realise precise measurement of the ionisation energy. An energy diagram of the corresponding photoexcitation scheme is presented in Figure 1.2.

In the first step of the photoexcitation process, molecules were excited from the $X^1\Sigma_g^+(v = 0)$ level to the $EF^1\Sigma_g^+(v = 0)$ level in a non-resonant-enhanced two-photon excitation process using

pulsed uv laser radiation at a wavelength of 202 nm. In the second step, the hydrogen molecules in the $EF^1\Sigma_g^+(v=0)$ state were excited to the $54p_1(S=0), F=0-2$ Rydberg state using a second uv laser operating at a wavelength of 397 nm. High resolution millimeter-wave spectroscopy was then performed to precisely determine the energy intervals between the high Rydberg states and the ionisation limit. Measurements of the ionisation and dissociation energies of HD and D_2, determined using a similar experimental approach, have also been reported by Sprecher et al. The measurements of the ionisation and dissociation energies of the hydrogen molecule and its isotopomers are limited by the interaction time of the molecules between the laser and the millimeter-wave radiation [19].

1.2 Interactions of Rydberg atoms and molecules with surfaces

Studies of interactions between Rydberg atoms and molecules and surfaces are important in many areas of physics and physical chemistry. At atom-surface distances of ~ 1 mm, Rydberg states can be exploited to sensitively probe stray surface electric fields [28, 29, 30]. These fields, which can arise from patch potentials or adsorbates can lead to decoherence in hybrid quantum systems, and can be detrimental to measurements of antimatter gravity using charged potentials, e.g. antiproton or electron/positron [31, 32].

At shorter range, dipole-image-dipole interactions between an atom or molecule in a Rydberg state and its electrical image in a metallic surface become important and must be considered in a complete treatment of atom-surface interactions [33, 34].

When the atoms are closer to the surface, at distances < 100 nm, charge-transfer reactions can occur in which a Rydberg atom or molecule is ionised as the Rydberg electron is transferred into the conduction band of the surface [35, 36]. In this context, Rydberg states are ideal systems with which to obtain a clear understanding of this fundamental process.

Studies of charge-transfer (ionisation) of xenon atoms in Rydberg states close to surfaces have been reported by Hill et al [37]. In these experiments, the atoms in states with principal quantum numbers in the range from $n = 13-20$ were directed at near grazing incidence toward Au(111) surfaces. The dependence of the rate of ionisation on the distance from the surface was studied. This ionisation distance was found to be dependent on the classical radius of the Rydberg electron orbit, i.e. on $\sim n^2$. Later, Lloyd et al. [38] studied interactions between hydrogen molecules, excited to Rydberg states with values of n in the range from $n = 17-22$, with aluminium and gold surfaces.

By detecting the ions produced when the Rydberg electrons tunnelled into the metal surface, it was found that the rotational degrees of freedom of the molecules played a significant role in the tunnel ionisation process. The results obtained highlighted that the chemical nature of the surface is determinant in surface-ionisation effects, as the ionisation of hydrogen Rydberg atoms and hydrogen Rydberg molecules displayed analogous behaviour.

Following this, Sashikesh at al. investigated the interaction of hydrogen molecules with doped silicon surfaces, with particular attention on the effect of ionisation for p-doped, and n-doped silicon [39]. This work highlighted ion detectability dependence on the dopant density and on the value of n. Higher-n Rydberg states show stronger surface-ionisation effects than lower-n Rydberg states. This difference became smaller as the dopant concentration in silicon was increased. A p-doped Si surface has large regions of positive charge that repel the H_2^+ ions and n-type doped Si surfaces have large regions of negative charge that attract the ions. Therefore, as the dopant concentration increases, the surface of silicon becomes increasingly more neutral and the ionisation rates become similar to that of gold (Au).

Most recently, and of particular relevance to the work discussed in this thesis, Gibbard et al. studied charge transfer of hydrogen Rydberg atoms with principal quantum numbers in the range from $n = 25 - 34$ as they approach Copper Cu(100) surfaces [40]. The electronic structure of Cu(100) is such that it possess a band gap at the energy of these Rydberg states and thus ionisation was observed only through the creation of image dipoles at the surface of the metal. Resonances in the surface ionisation cross-sections were observed, revealing the importance of the material identity on the charge transfer ionisation process. Studies of the effects of collision energies on the surface ionisation process revealed a propensity to more efficient ionisation for more slowly moving atoms, as can be seen in Figure 1.3.

The figure shows a velocity dependence on the ionisation of Rydberg atoms on the surface. As the velocity of the incident hydrogen atoms increases, a smaller mean distance of ionisation and a higher field is required to extract the ion. Furthermore, the profiles shift to higher fields as n decreases, since greater fields are required to prevent the ions being pulled closer to the surface by its own image charge.

The efficient preparation of velocity-tunable, decelerated beams using the methods described in this thesis for use in more detailed studies of these collisions and ionisation processes is therefore of

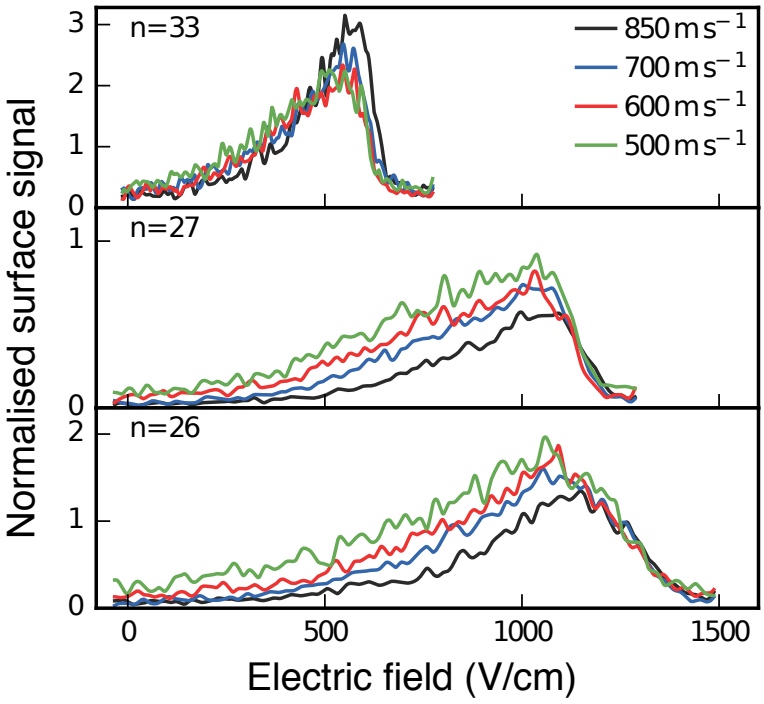

Figure 1.3: Velocity dependence of hydrogen Rydberg atoms on ionisation at surfaces. The profiles have been recorded for values of n from $n = 26$, 27 and 33 for selected collisional velocities. Adapted from Ref. [40].

interest.

1.3 Hybrid approaches to quantum information processing

Atoms in high Rydberg states are of interest in quantum information processing because (a) they can be strongly coupled to microwave resonators in cavity quantum electrodynamics (QED) architectures [41], and (b) the strong dipolar interactions between Rydberg atoms can be exploited for the preparation of many-body entangled states [42, 43]. Rydberg states have played important roles in the history and development of microwave cavity QED [44]. Most recently, this had led to proposals to exploit them in hybrid cavity QED. This has extended from an analysis by Rabl et al. [45] of the use of ground state polar molecules as long-coherence-time quantum memories, when coupled via microwave transmission-line resonators to solid-state qubits in superconducting microwave circuits. The advantages of using Rydberg atoms in those experiments rather than ground state molecules,

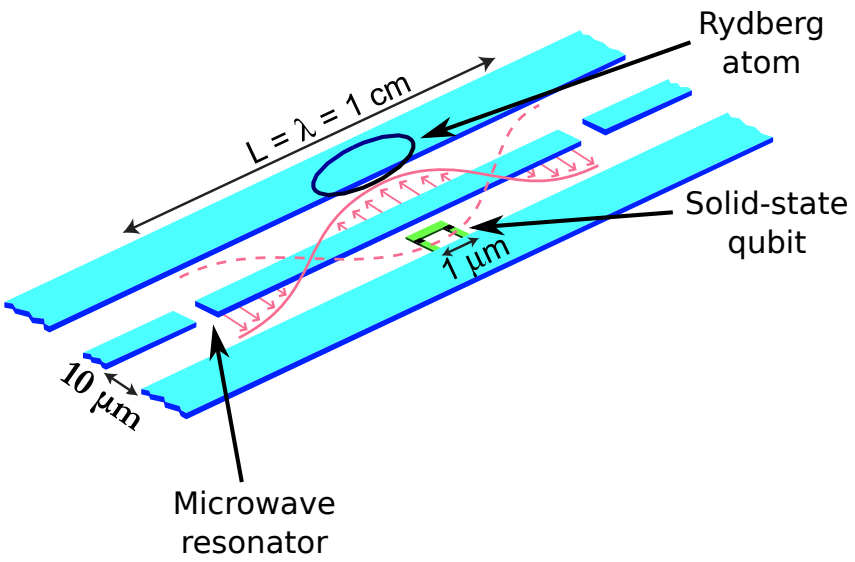

Figure 1.4: Schematic representation of a hybrid circuit QED architecture, adapted from Ref. [46]. An ensemble of Rydberg atoms (cigar-shaped oval) are coupled via a co-planar microwave resonator to a solid-state qubit.

result from their extreme sensitivity to microwave radiation.

Because the frequencies of transitions between Rydberg states that differ in n by 1 scale with n^{-3}, and lie below 50 GHz for $n > 53$, and the transition dipole moments for these transitions, $\langle n+1, \ell+1|\mu|n, \ell\rangle$ scale with n^2 and exceed 10000 Debye for $n > 52$, vacuum Rabi frequencies for atom-resonator couplings in the order of 10 MHz appear to be achievable. This indicates that fast state preparation and manipulation can be foreseen. This, combined with coherence times larger than 1 ms would permit fast transfer of quantum information from superconducting qubits to Rydberg quantum-memories in hybrid architectures for quantum information processing, a schematic representation of which is displayed in Figure 1.4.

Inspired by these ideas, Hogan et al. [47] investigated the coupling of atoms in high Rydberg states to microwave fields propagating in solid-state coplanar waveguides, as depicted in Figure 1.5.

In these experiments, helium atoms in states for which $n = 30 - 35$ were prepared and travelled across the waveguide, where a microwave pulse at a frequency in the range between 25 and 38 GHz, allowed transitions between Rydberg states to be driven, and the interaction of the atoms

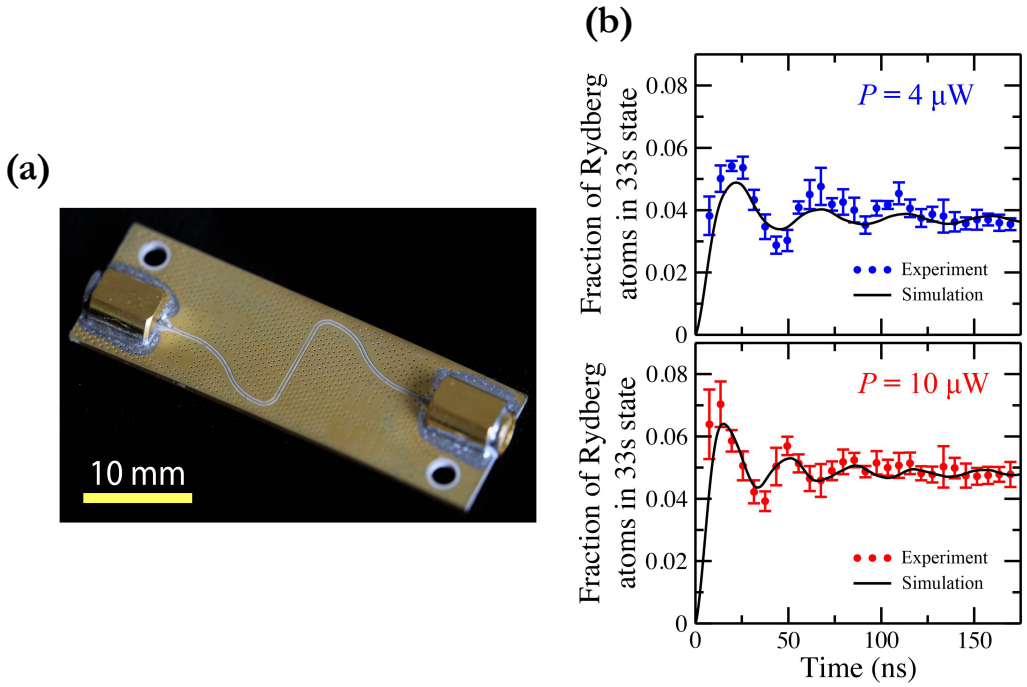

Figure 1.5: (a) A photograph of the microwave waveguide used in the experiments of Hogan et al. (from Ref. [28]). The Rydberg atoms travelled above the circuit and then a pulse of microwaves was applied to induce transitions from selected np-states to ns-states. (b) The fraction of atoms in the ns-state as a function of the microwave pulse duration for selected powers at the microwave source (4 μW and 10 μW, respectively). The solid black lines are the results of numerical simulations. From Ref. [47].

with the wave guide to be characterised. The coupling that resulted between the microwaves in the wave-guide and the atoms allowed transitions between the np-states and the ns-states to be driven, which betrayed the presence of inhomogeneous electric fields. This work was of importance in the development of hybrid approaches to cavity QED, as electric field inhomogeneities emanating from surfaces can affect the lifetime and coherence times of the Rydberg states.

The electrical transmission-line guides, decelerators and traps for Rydberg atoms and molecules described in this thesis are ideally suited for integration with microwave circuits of this kind and therefore of importance in these developments in hybrid quantum information processing.

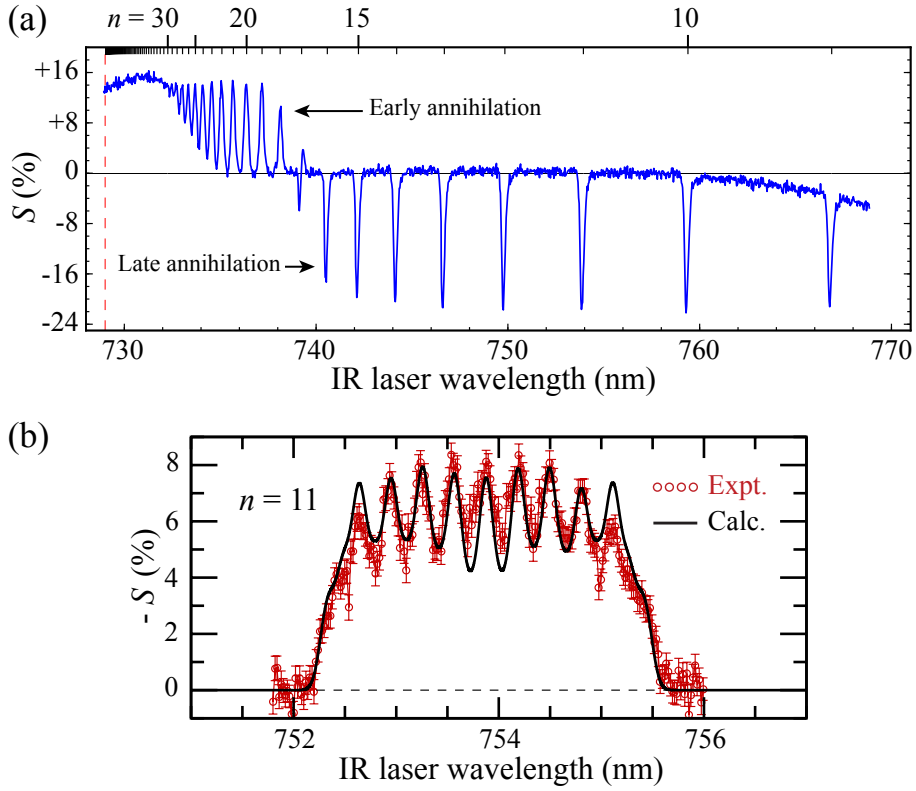

Figure 1.6: (a) Field-free spectrum of Rydberg states of positronium. (b) Measured (points) and calculated (lines) Rydberg-Stark spectra of $n = 11$ Ps atoms in an electric field of 1.9 kV/cm. From Ref. [52].

1.4 Positronium and antihydrogen

Opportunities to control the translational motion and trap cold atoms in high Rydberg states is of particular interest in experiments with atomic antimatter systems, for example positronium and antihydrogen. This interest arises from the necessity of exciting positronium to Rydberg states to avoid self-annihilation [48] and the fact that antihydrogen atoms are produced in high Rydberg states by antiproton-positron recombination [49]. Experiments with both of these species are particularly directed toward identifying the underlying regimes for the matter-antimatter asymmetry in our observable universe [50]. These include spectroscopic studies of energy intervals [51], and measurements of the acceleration of particles composed of antimatter in the gravitational field of the Earth [48].

As can be seen in Figure 1.6, recent experiments with positronium have demonstrated the possibility to selectively excite Rydberg-Stark states with electric dipole moments of ~ 840 D [52].

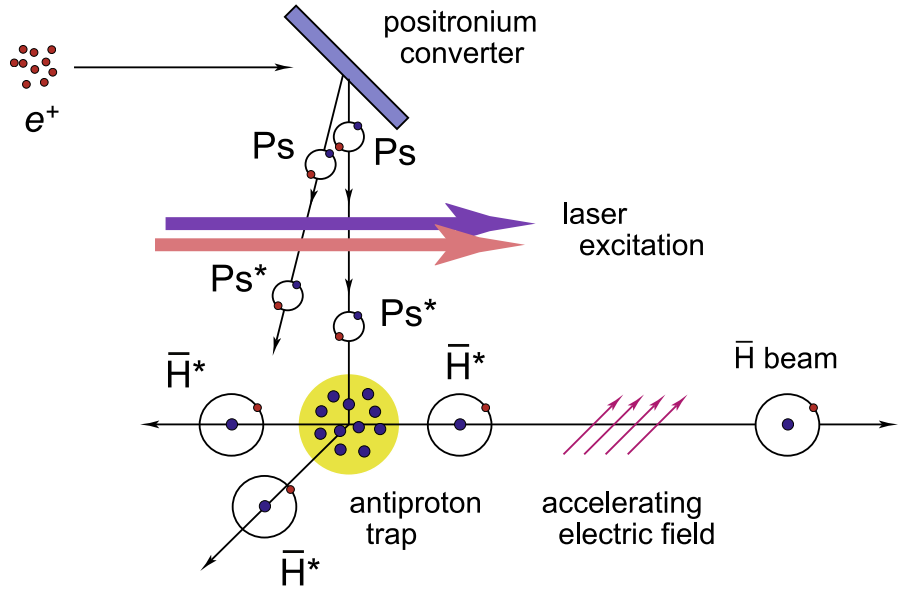

Figure 1.7: Schematic diagram of the synthesis of antihydrogen, and implementation of a Rydberg-Stark accelerator in the AEGIS experiment [53].

Positronium atoms in these states are therefore well suited for use in the kind of deceleration and traps described in this thesis (see Chapters 6-8). By implementing Rydberg atom optics element of this kind, beams of positronium atoms could be transported for precision spectroscopy or free-fall gravitational measurements [48].

In experiments with antihydrogen, it is possible to exploit the techniques of Rydberg-Stark deceleration described here to prepare velocity controlled beams. Indeed, the AEGIS antihydrogen experiment currently under construction at CERN [53] will incorporate a Rydberg-Stark accelerator (see Figure 1.7) for this purpose. In this experiment Rydberg antihydrogen atoms will be prepared in selected high Rydberg states by charge-exchange with Rydberg positronium. These anti-atoms will then be accelerated out of the production region using these Rydberg-Stark accelerators to prepare cold, velocity-controlled beams for spectroscopic studies and gravity measurements.

Chapter 2

Rydberg-Stark deceleration

The use of inhomogeneous fields to manipulate atoms was first demonstrated using magnetic fields and beams of silver atoms in the classic experiments of Gerlach and Stern in the 1920s [54]. This was followed by work on the manipulation of polar molecules using inhomogeneous electric fields by Gordon et al. [55]. The suggestion to use inhomogeneous electric fields to control the translational motion of atoms and molecules in high excited Rydberg states which exhibit very large electric dipole moments was first made by Wing [56] and Breeden and Metcalf [57] around 1980. The central idea behind these proposals is that in an electric field a neutral atom or molecule in a high Rydberg state with a large electric dipole moment experiences an energy shift that is approximately linearly dependent on the field strength. This Stark shift, W, is proportional to the scalar product of the electric dipole moment of the atom, $\vec{\mu}$, and the electric field vector $\vec{F}$, such that [58]

$$W = -\vec{\mu} \cdot \vec{F} \tag{2.1}$$

In the presence of a spatially inhomogeneous electric field this Stark effect leads to a force, $\vec{f}$,

$$\begin{aligned} \vec{f} &= -\nabla W \\ &= \nabla(\vec{\mu} \cdot \vec{F}). \end{aligned} \tag{2.2}$$

The direction in which this force is exerted therefore depends on the relative orientation of the electric dipole moment of the atom or molecule and the electric field vector. If an atom is prepared in a state with a positive Stark energy shift, i.e. $\vec{\mu}$ is aligned in the opposite direction to $\vec{F}$, as it travels

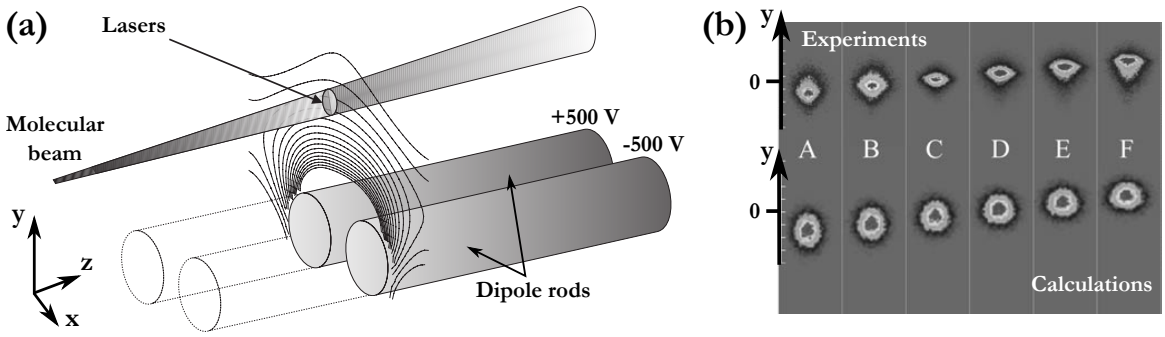

Figure 2.1: (a) Schematic representation of the experimental apparatus used by Townsend et al. to deflect beams of krypton atoms. The images in (b) were recorded using a position sensitive MCP detector. Atoms in states with electric dipole moments oriented parallel (antiparallel) to $\vec{F}$ were deflected down (up) by the fields. Adapted from Ref. [59].

from a weak electric field to a strong electric field, i.e., through a positive electric field gradient, it will increase its potential energy and hence it will lose kinetic energy. It will therefore be forced toward regions of weak electric fields. For this reason, states which exhibit positive Stark energy shifts are often known as "low-field-seeking" states. On the other hand, for an atom in a state with a negative Stark energy shift, $\vec{\mu}$ is oriented parallel to $\vec{F}$, and the atom decreases in potential energy as it travels from a weak electric field to a strong electric field. It is therefore attracted toward regions of high electric field strength. Such states are therefore often known as"high-field-seeking" states.

2.1 Early experiments with time-independent fields

Building on these concepts, first experiments to manipulate Rydberg atoms using inhomogeneous electric fields were performed by Townsend et al. [59] in 2001. In this work, krypton atoms in Rydberg-Stark states with values of n ranging from 16 to 19 were transversally deflected. A schematic representation of the apparatus used in these experiments is displayed in Figure 2.1(a).

In these experiments high-field seeking (images A, B and C) and low-field-seeking (images D, E and F) Rydberg-Stark states were selectively prepared using a two-photon excitation scheme. The inhomogeneous electric field above the rods pictured in Figure 2.1(a) caused the atoms to experience forces deflecting them up or down with respect to their propagation axis. Position sensitive detection was performed using a microchannel plate detector (MCP) coupled to a phosphor screen.

As can be seen in the images in Figure 2.1(b), the magnitude of the deflection of the atoms depends on the electric dipole moment of the state prepared and its orientation with respect to the field. The largest deflection is seen for the states with the largest electric dipole moment (A and F). While a reduced deflection is seen for states with small electric dipole moment (C and D). Good agreement was achieved between the results of the experiments and numerical particle trajectory calculations (upper and lower set of images, respectively).

Later, in a proof of principle experiment, fast beams of hydrogen molecules in Rydberg-Stark states with principal quantum number $n \sim 17$ were deflected, and decelerated [60]. These experiments were performed by positioning the rods displayed in Figure 2.1(a) perpendicular to the axis of propagation of the molecular beam, with the beam passing between them. The resulting electric field distribution had a gradient which decreased in magnitude along the propagation axis as the distance from the rods increased. This implied that as the molecules moved towards the rods after excitation they experienced a positive gradient when the electrical potential were pulsed on for a short period of time (~ 1 μs). The distribution of arrival times, for excitation of an extreme low-field-seeking state and an extreme high-field-seeking state of the $n = 17$ manifold, at a MCP detector located down stream in the apparatus can be seen in Figure 2.2.

In these experiments, the changes in the flight-time of the molecules corresponded to a change in kinetic energy during acceleration/deceleration of ± 1.6 meV ($\equiv \pm 13$ cm^{-1}). This maximal change in kinetic energy that could be achieved in these experiments was limited by the presence of avoided crossings in the Stark map for the low-M_J states used in the experiments. At such avoided crossings the low- and high-field-seeking Stark states prepared at the time of photoexcitation lose their electric dipole moments and can therefore no longer be efficiently accelerated or decelerated. This limitation can however be overcome by exploiting time-dependent fields in the experiments.

2.2 Experiments with time-dependent fields

The first experiments in which atoms were decelerated using time-dependent electric fields were performed by Vliegen and Merkt using beams of argon Rydberg atoms in states with principal quantum number $n \sim 25$ [62, 63]. A schematic representation of the apparatus used with these experiments is displayed in Figure 2.3.

To compare the use of time-independent electric fields to the use of time-dependent fields,

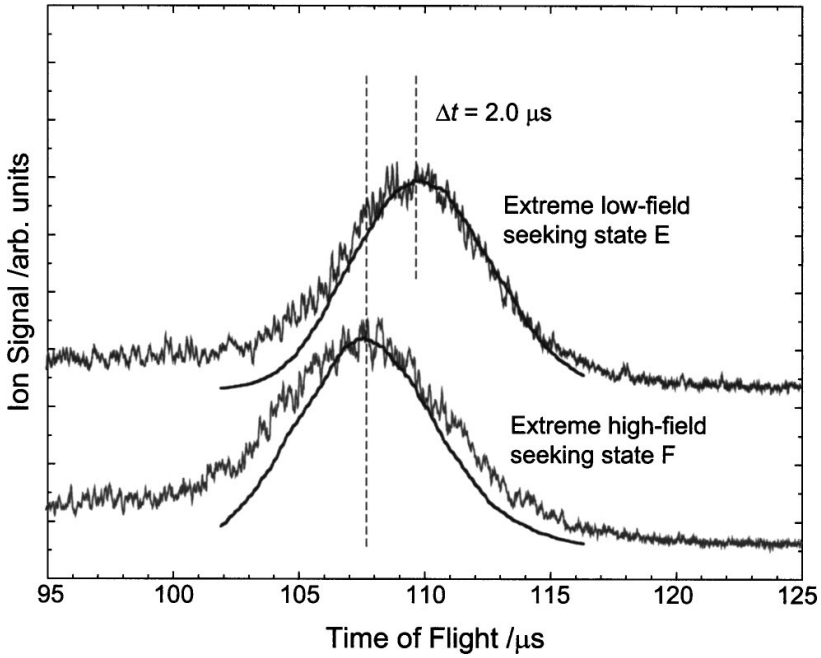

Figure 2.2: Time-of-flight distributions of hydrogen molecules in low-, and high-field-seeking Rydberg-Stark states following deceleration and acceleration in a time-independent electric field (from Ref. [61]).

these experiments were performed in two ways, as represented in Figure 2.3(a) and (b), respectively. Preparation of the Rydberg states was carried out by photoexcitation using a tunable, narrow-bandwidth vacuum ultraviolet (vuv) laser to excite argon atoms from their ground state to Rydberg states for which $n = 15 - 30$. This occurred at the cross marked between electrodes 1 and 2 in Figure 2.3, with the atomic beam propagating in the z-dimension.

In the time-independent field configuration, after excitation the atoms travelled out of the high-field region between electrodes 1 and 2, in which they were excited, and toward the zero-field point between electrodes 3 and 4 [Figure 2.3(a)]. In this negative electric field gradient, atoms in low-field-seeking states will accelerate, while those in high-field-seeking states will decelerate. The result of experiments in which the flight-times of the atoms in selected Stark states were measured as they travelled out of the electrode setup and toward a MCP detector positioned downstream on the z-axis of the apparatus are displayed in Figure 2.4.

In this figure, the time-of-flight distributions for atoms excited to states with zero electric dipole moment are indicated by the black, continuous curve. In the time-independent field configuration,

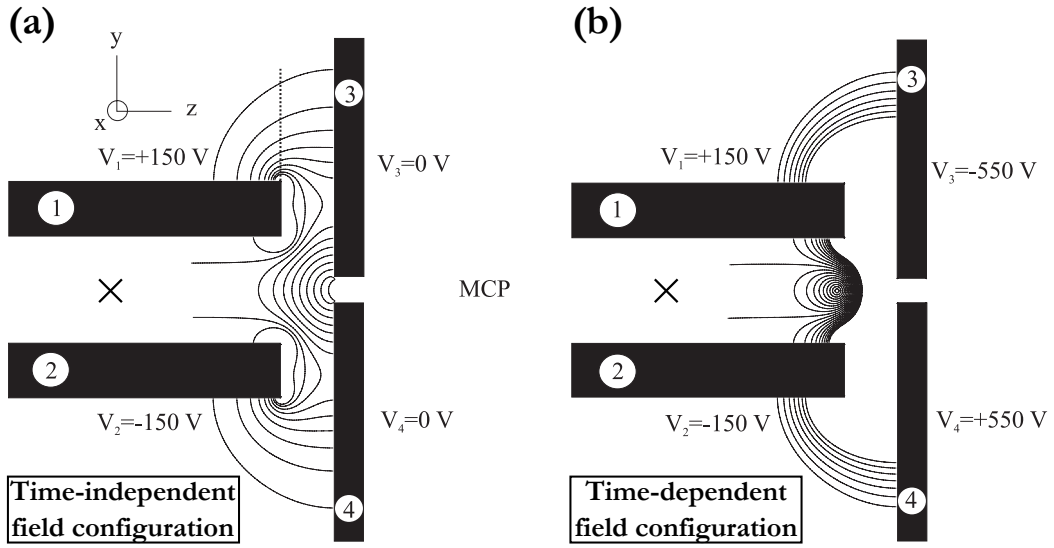

Figure 2.3: Schematic representation of the experimental setup used to accelerate and decelerate argon Rydberg atoms using time-independent, and time-dependent electric fields (adapted from Ref. [63]).

atoms in low-field-seeking Stark states (dashed, red curve) were accelerated, arriving slightly earlier (approx. -3 μs) at the MCP that the unperturbed atoms, while those in high-field-seeking states (red, dotted curve) arrived later (approx. $+3$ μs).

Acceleration/deceleration using time-dependent fields to circumvent limitations imposed by avoided crossings in the Stark map was achieved by switching the potentials on electrodes 3 and 4 to $\pm$550 V immediately after photoexcitation. The resulting large positive electric field gradient experienced by the atoms was maintained while keeping the fields below those for which non-hydrogenic effects limit the deceleration efficiency by allowing these potentials to decay exponentially with a time constant of 2.2 μs. As a result, atoms in low-field-seeking states were decelerated [dotted, blue curve in Figure 2.4], while those in high-field-seeking states were accelerated [dashed, blue curve in Figure 2.4]. In these time-dependent fields, significantly greater changes in kinetic energy ($\pm$7.4 meV $\equiv$ $\pm$60 cm^{-1}) of the Rydberg atoms were achieved compared to the time-independent-field case (4.0 meV $\equiv$ 32 cm^{-1}).

These experiments opened up a range of opportunities for manipulation of the translational motion and deceleration of atoms and molecules in high Rydberg states. Vliegen at al. [64] prepared hydrogen atoms in states with $n = 27$ and decelerated, stopped and reversed their direction of travel

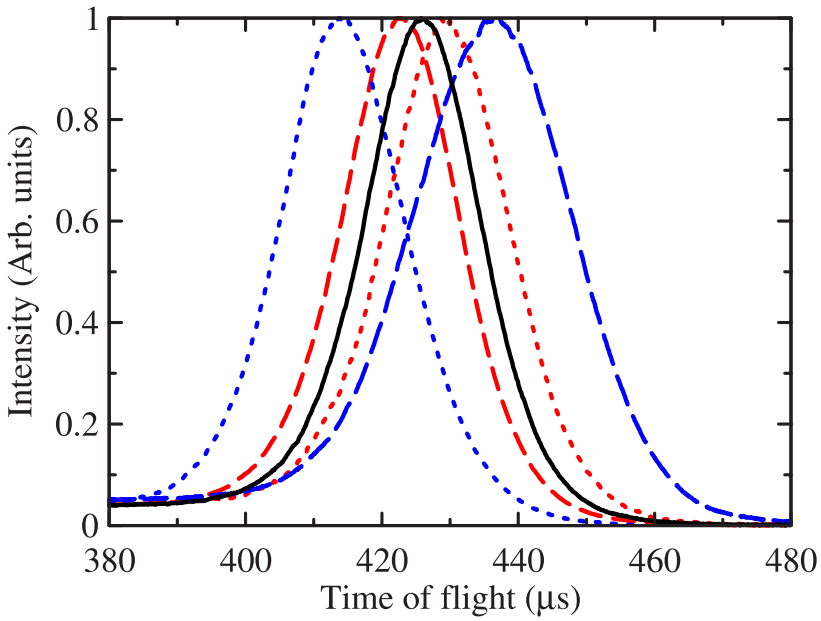

Figure 2.4: Time-of-flight distributions of argon Rydberg atoms ($n = 19$) recorded following acceleration/deceleration in time-independent and time-dependent electric fields. The black, solid line represent the time-of-flight distribution for atoms in Stark states with zero electric dipole moment, while the dotted (dashed) curves correspond to high-field-seeking states (low-field-seeking states). The two red distributions which peak closer to the $k = 0$ time-of-flight were recorded in time-independent fields, while the two blue distributions at the extremes of the figure were recorded using time-dependent-fields. Adapted from Ref. [63].

using Rydberg atom mirrors. Later, the possibility to transversally focus beams of Rydberg atoms was also demonstrated [65].

2.3 Electrostatic trapping

The complete deceleration and retroreflection of beams of hydrogen atoms in low-field-seeking Rydberg-Stark states, demonstrated by Vliegen and Merkt [64], suggested that electrostatic trapping could be achieved if, at the turning point in the trajectory of the atoms, the potentials applied to the decelerator electrodes were switched to generate a quadrupole electric field distribution with a minimum at the position of the atoms. Experimentally this was achieved by using time-dependent exponentially decaying potentials applied for deceleration on a continually moving electric field gradient. The time constraint associated with the exponential decay of these potentials was selected so

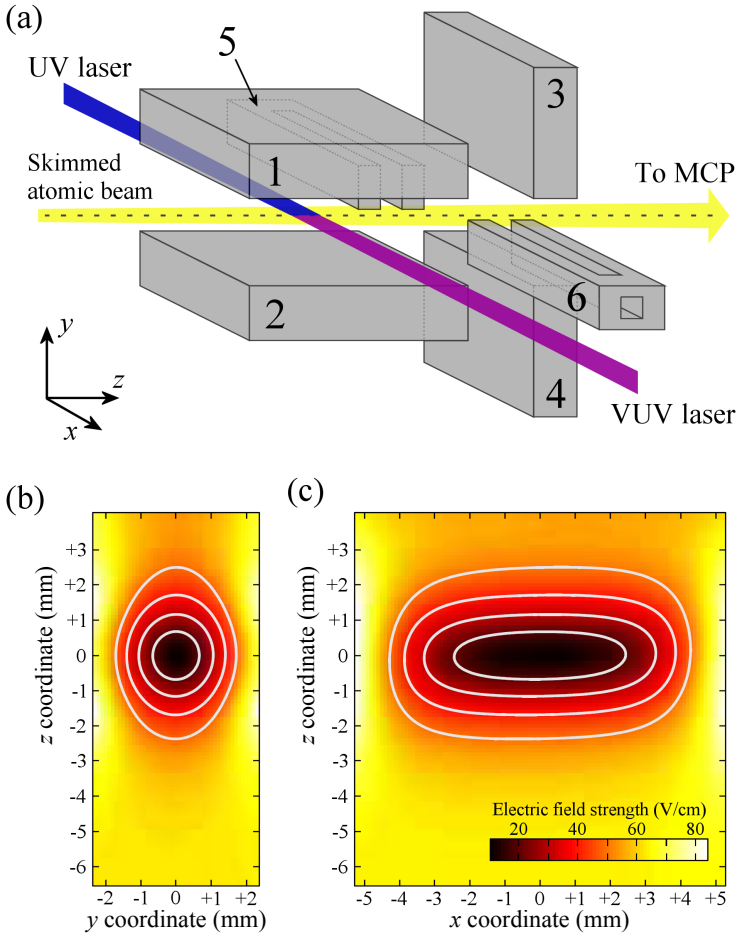

Figure 2.5: Schematic representation of the electrode configuration used by Hogan and Merkt for Rydberg-Stark deceleration and 3D electrostatic trapping. Panels (b) and (c) show the electric field distributions in the *yz* and *xz* planes at the centre of the trap with $V_1 = V_4 = \pm 20$ V, $V_2 = V_3 = \pm -20$ V and $V_5 = -V_6 = \pm 55$ V. The electric field lines increase by 10 V/cm starting from 20 V/cm. From [67].

that at the end of the decay process a quadrupole electric field minimum was generated [66, 67]. The design of the electrostatic trap in these experiments is showed in Figure 2.5(a), and included a pair of end-cap electrodes to close-off the quadrupole in the third dimension and permit the generation of a non-zero electric field minimum.

This three-dimensional electrostatic trap was first used to trap hydrogen Rydberg atoms [67] and later hydrogen Rydberg molecules [68, 69, 70]. The trapped atoms were confined for times on the order of 100 μs. However, a rapid decay of particles from the trap observed at early trapping

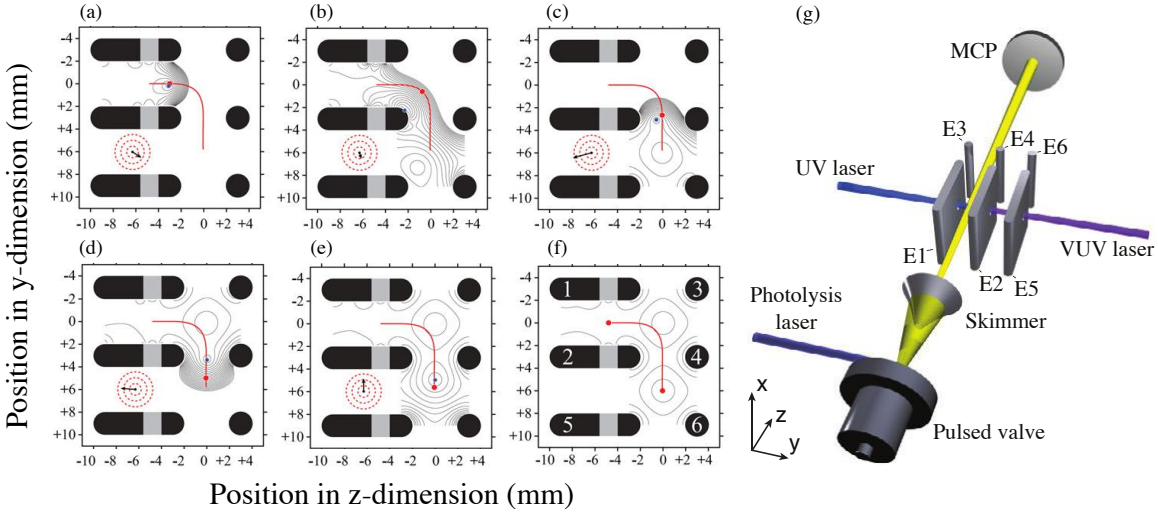

Figure 2.6: (a-f) Schematic representation of the electrode arrangement and electric field distributions, indicated in increments of 20 V/cm, used to decelerate and trap atoms in low-field-seeking Rydberg-Stark states off-axis. A vector indicating the instantaneous acceleration of the electric-field minimum is displayed in the lower-left-hand half of each panel. (g) A schematic representation of the Rydberg-Stark decelerator and off-axis electrostatic trap. Adapted from Ref. [71].

times in these experiments suggested that in these trap geometries, in which the decelerated atoms were trapped on the axis of the atomic or molecular beams within which they were photoexcited to Rydberg states, collisions with the trailing components of the beams played a role in the subsequent decay of the samples from the trap. To study and minimise the effects of these collisions on the trapped atoms this trap design was further developed to permit off-axis trapping [69].

The general design and principle of operation of this off-axis trap can be seen in Figure 2.6 where electric field distributions in the yz-plane at the centre of the trap electrodes are displayed. In the panels (a-f) of this figure, the metallic electrodes are indicated by the dark shaded regions. In this plane the upper and lower end-cap electrodes between electrodes 1,2,3 and 4 and between electrodes 2,3,5 and 6 are not visible. The atomic or molecular beams propagated in the positive z-dimension at $y = 0$. The electric field distributions in the panels correspond to selected times during deceleration, off-axis transport and trapping. The red lines represent the path of a typical hydrogen Rydberg atom in a low-field seeking state toward the off-axis trap.

The decay of hydrogen atoms from this off-axis trap was seen to be slower than in the on-axis trap at early trapping times. This indicated that the effects of the collisions with the trailing

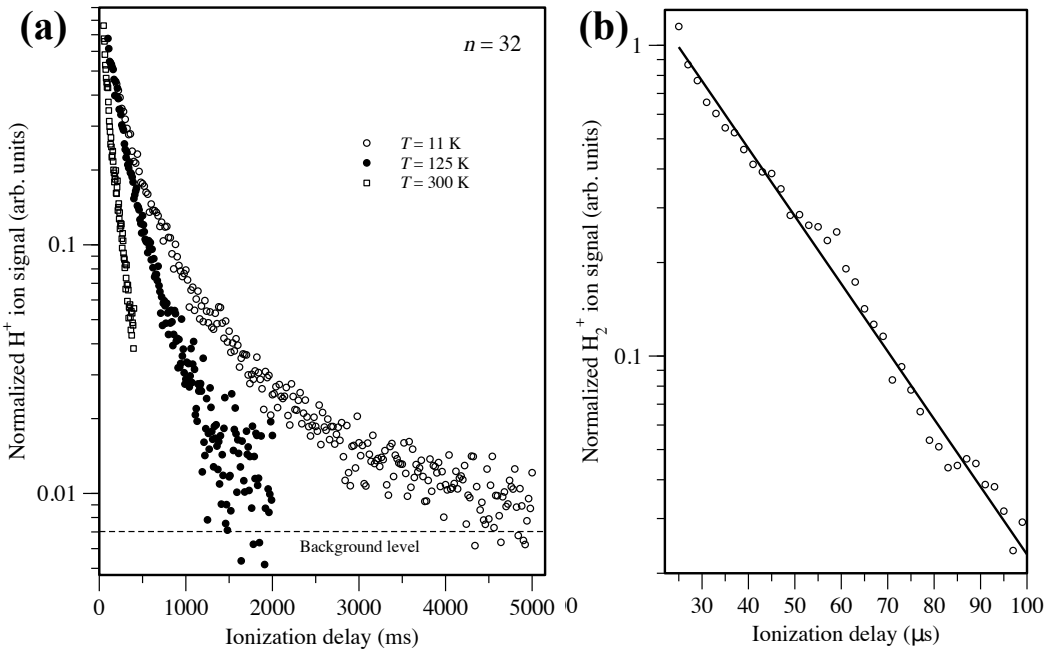

Figure 2.7: Measurements of the decay of (a) trapped hydrogen atoms in an off-axis electrostatic trap for blackbody temperatures of 300 K, 125 K and 11 K, (b) hydrogen molecules trapped in a 300 K environment in an on-axis electrostatic trap. From Ref. [71].

components of the atomic beams at these early trapping times were successfully minimised in this off-axis trap geometry. In this case the decay of the trapped atoms was dominated by fluorescence to the ground state. However, transitions driven by blackbody radiation also played an important role as can be seen in Figure 2.7(a).

In this figure, the signal associated with the number of atoms confined in the off-axis trap when operated at three different temperatures (11K, 125K and 300K) is displayed. Rydberg-Stark states with $n = 32$ were initially prepared before photoexcitation in each case. As the blackbody temperature increased, the decay of the trapped atoms became faster. This can be understood by correlating the effects of the blackbody radiation on the trapped atoms at each temperature. Particularly by comparing the wave number between adjacent Rydberg states at $n = 32$ ($\equiv 7$ cm^{-1}) and the wavenumber below the ionisation limit for this state ($\equiv 109$ cm^{-1}), with the corresponding number of blackbody photons per mode at each temperature (see Table 2.1).

Of these two decay processes driven by blackbody radiation, the transition strength and number of photons available at each temperature to drive n-changing transitions mean that this process dominates blackbody photoionisation. However, blackbody transitions between Rydberg-Stark states

T (K)	$\bar{n}$ ($\nu = 210$ GHz)	$\bar{n}$ ($\nu = 3270$ GHz)
300	29.3	1.5
125	11.9	0.4
11	0.7	0

Table 2.1: Blackbody photon occupation numbers for selected temperatures at frequencies of $\nu = 210$ GHz and $\nu = 3270$ GHz.

with different values of n, tend to be strongest between states with similar electric dipole moments, i.e. transitions are most likely to occur from one low-field-seeking state with one value of n and another low-field-seeking state with a a different value of n. This is because of the larger overlap between the wavefunctions of such states. As a result, blackbody n-changing transitions do not lead to significant direct trap loss, but rather a redistribution of population among a range of Rydberg states with different values of n over time. Blackbody photoionisation does, however, lead to an immediate loss of atoms from the trap. In the data displayed in Figure 2.7(a) it is therefore the changes in the contributions from blackbody photoionisation that lead to the observed reduction in the trap decay rate with temperature at times earlier than ~ 1 ms. At later times, the apparent reduction on the rate of decay of atoms from the trap is a result of higher n-states, populated following multiple single-photon blackbody transitions, remaining at these times. These states spontaneously decay more slowly than the $n = 32$ states initially populated, leading to the signal observed.

To ensure that the dynamics of the sample of atoms during the deceleration and trap loading process did not directly contribute to the trap decay, off-axis trapping experiments were also performed with deuterium atoms [71]. In this work, identical trap decay curves were recorded to those for hydrogen atoms. These experiments also highlighted the role of the quadratic Stark effect in the deceleration process in strong electric fields.

The Rydberg-Stark decelerators and traps described above have also been employed to prepare cold, trapped samples of hydrogen molecules [see Figure 2.7(b)]. These molecules were prepared in long-lived high-ℓ states by resonance-enhanced three-photon excitation. When trapped in on-axis traps [Figure 2.7(b)], they were observed to decay more rapidly from the trap than hydrogen atoms trapped in states with similar values of n. This is because collisions with the trailing components of the molecular beam can transfer population to very short-lived dissociative states not present in atoms. This process leads to immediate loss from the trap. However, when trapped in

off-axis traps, at low blackbody temperatures long atom-like trapping times exceeding 1 ms have been observed [72].

2.4 Chip-based decelerators and traps

The decelerators and electrostatic traps for Rydberg atoms and molecules that have been developed most recently have been designed around two-dimensional arrays of surface-based electrodes [47]. Because of their surface-based design, these devices can readily be extended to include larger numbers of electrodes without affecting their operation. They are therefore very scalable, modular and have the additional advantage that they present the possibility for integration with microwave electronic circuits [47] for applications in cold chemistry [36] and quantum information processing [43].

The strong electric field gradients and the possibility to engineer complicated electric field structures on a chip are ideal for the precise manipulation and confinement of neutral atoms [1, 2, 3, 4], ions [7] and neutral molecules [12]. The use of a microstructured array of electrodes to generate locally, periodic electric field minima was implemented by Meek et al. to develop a Stark decelerator able to load, trap and decelerate to zero-velocity supersonic beams of metastable $^3\Pi$ CO molecules [13, 14, 73, 74]. A schematic representation of the experimental apparatus is displayed in Figure 2.8(b).

The schematic diagram in Figure 2.8(a) shows three different level of magnification of the chip employed. The device operated on the superposition of electric fields generated by ~ 1500 equidistant electrodes that composed the chip. These had a width of 10 μm and they were spaced one from another by 40 μm, for a total number of 1254 electrodes. To each of these electrodes, different potentials were applied and therefore each electrode generated an electric field, which depended on the sign and magnitude of the potential applied. When two dipolar fields with different distances and opposite field directions are superimposed, a minimum in the electric field strength is created at the point where the long-range dipoles that dominate far from the surface of the electrodes are canceled by the short-range dipole that dominate close to that same surface. This way, a trap for CO molecules in low-field-seeking Stark states was generated. To implement these dipoles with opposite field directions, to each adjacent electrode this sign was alternated from positive to negative. Furthermore, these potentials were modulated with a sinusoidal function such that for the n^{th}

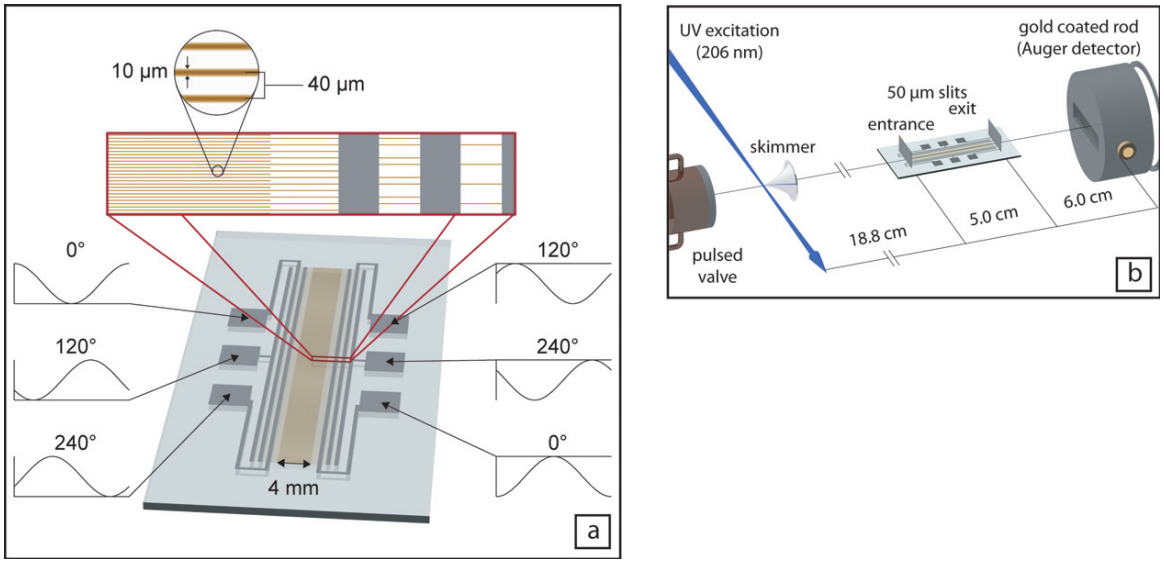

Figure 2.8: (a) Schematic representation of the chip decelerator and magnification of the electrodes that compose it. The waveforms that are applied to the pads are schematically shown. (b) Scheme of the experimental setup used for loading and decelerating CO metastable polar molecules. From Ref. [74].

electrode, and when n was odd, the resulting potentials were,

$$V = -V_0\ (1+\cos(\omega\, t_a+\phi_n)), \tag{2.3}$$

where $V_0 = 60$ V, ω was the angular frequency chosen so that $\omega(t_b - t_a) = \omega(t_c - t_b) = \pi/6$ and $(\omega\, t_a+\phi_n)$ was equal to $2\pi/3$, $4\pi/3$ and 0 for electrodes 1, 3, and 5, respectively. For the even numbered electrodes, the potentials applied were,

$$V = +V_0\ (1+\cos(\omega\, t_a+\phi_n)), \tag{2.4}$$

where $(\omega\, t_a+\phi_n)$ was equal to 0, $2\pi/3$, $4\pi/3$ for electrodes 2, 4, and 6, respectively.

The calculated electric field strengths for a series of applied potentials are displayed in Figure 2.9. The different potentials applied according to Equations 2.3 and 2.4 generated trap minima which travelled along the electrodes as the potentials were varied sinusoidally. Furthermore, because these potentials were repeating themselves every six electrodes, a series of identical, consecutive traps were generated at every 240 μm and at a height above the substrate of 25 μm $\pm$5 μm. The po-

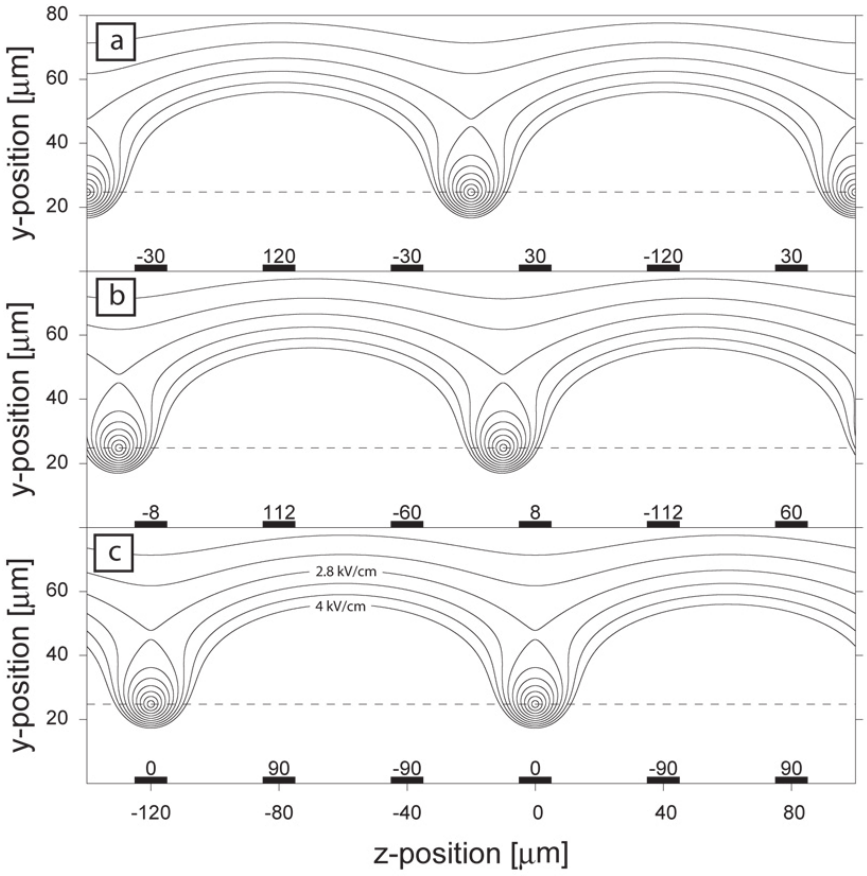

Figure 2.9: (a-c) Calculated electric field distributions for selected potentials, which are displayed above each electrode as indicated. These correspond to three different times in the sinusoidal cycle. The contour lines are displayed one from another at intervals of 400 V/cm. From Ref. [74].

tential wells thus generated were 15-35 mK deep. The speed at which the trap moves about the array of electrodes can be related to the angular frequency, ω, by using the geometrical characteristics of the chip, so that $v_{\mathrm{tr}} = 120\,\mu\mathrm{m} \cdot \omega/(2\pi)$.

As the beam of CO metastable molecules, initially travelling at a speed of 360 m/s, entered the experimental region, the potentials of the electrodes were switched on to load the CO molecules in these trap minima. This way, CO molecules were guided and decelerated. The experimental results are displayed in Figure 2.10. In these experiments, as the CO molecules were loaded in the traps, the angular frequency of the electrodes was varied to adjust their translational velocity. The time-of-flight distributions displayed in Figure 2.10 show CO molecules guided at constant speed by varying the waveforms with a frequency of 3 MHz. To decelerate the molecules, this initial frequency was

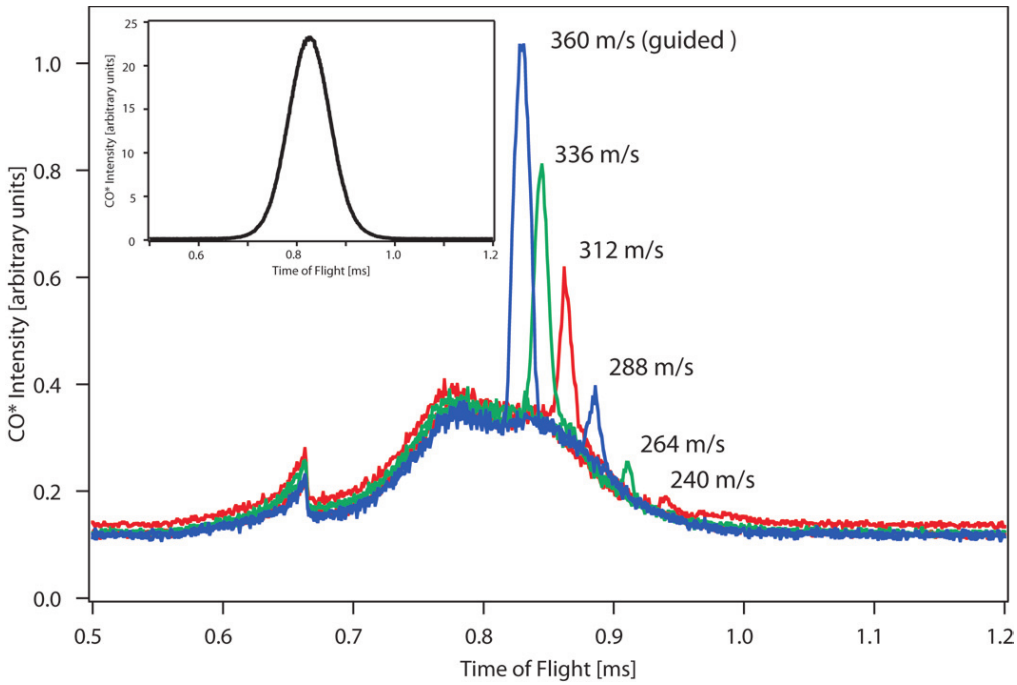

Figure 2.10: Measured time-of-flight distributions of metastable CO molecules for selected accelerations. The molecules had an initial velocity of 360 m/s and were brought to final velocities indicated adjacent to the main peaks. The inset figure represents the time-of-flight distribution when the potentials applied to the electrodes were set to zero. From Ref. [74].

linearly reduced in time and molecules decelerated to final velocities as low as 240 m/s were produced. Eventually Meek et al. brought CO molecules to a standstill [74].

The successful loading and trapping process in this Stark decelerator depended on the initial location of the bunch of CO molecules. Those that were not initially located in a potential well were deflected away from the surface of the device and lost. Furthermore, because the speed of the traps was related to the frequency applied to the waveforms, molecules that were initially in the potential wells but that had a significant velocity difference relative to the traps escaped from the potentials wells and were lost.

As an array of about 250 electric field traps is loaded on a chip, a small number of the CO molecules will successfully be loaded in a trap. As estimated number of $\sim$ 10 CO molecules were loaded in each trap [14]. This number was smaller by an order to magnitude when accelerations were applied to bring the molecules to a standstill, as the trap depth in the moving frame of reference was reduced as a function of the magnitude of the deceleration applied.

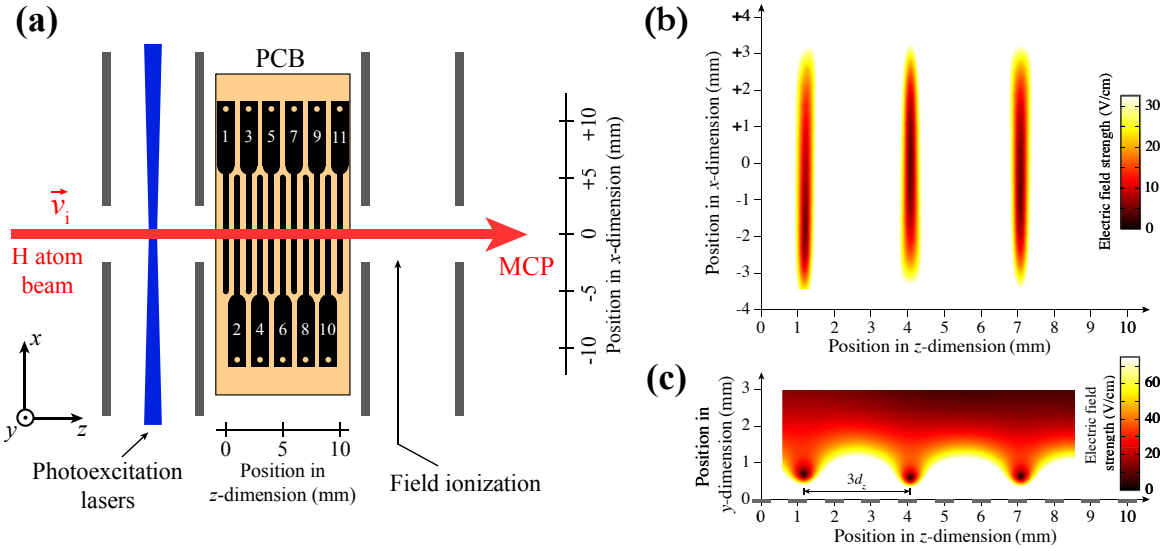

Figure 2.11: (a) Surface electrode Rydberg-Stark decelerator. Typical electric field distribution in (b) the *xz*-plane and (c) the *yz*-plane employed for acceleration, deceleration and trapping are displayed. The series of electric field minima, traps, are separated by 3 mm [28]. The positions of the decelerator electrodes are indicated on the horizontal axis in panel (c). Adapted from Ref. [47].

Following this work on deceleration of neutral molecules, the first experimental demonstration of a chip-based decelerator for Rydberg atoms [47, 28] exploited a device, the design and operation of which was inspired by these chip-based Stark decelerators developed for ground state polar molecules [13]. However, this decelerator had the important advantage over these previously described chip-based decelerators that all of the excited atoms ($\sim 10^5$) were loaded into one single travelling trap with dimensions on the order of 1 mm in the propagation dimension, rather than being distributed over many traps, as in the device used by Meek et al. [13, 14, 73, 74] for ground state molecules.

The experimental setup used in these chip-based Rydberg-Stark deceleration experiments is displayed schematically in Figure 2.11(a). In these experiments, a beam of hydrogen atoms was photoexcited to Rydberg-Stark states with $n = 23 - 70$ before reaching the decelerator. This beam then entered the region where the chip-based Rydberg-Stark decelerator was located. Beyond the decelerator the excited atoms were detected by pulsed electric field ionisation. A typical electric field distribution generated above the surface electrodes for guiding, accelerating and decelerating is displayed in Figure 2.11(b). The atoms in low-field-seeking Rydberg-Stark states were trapped about

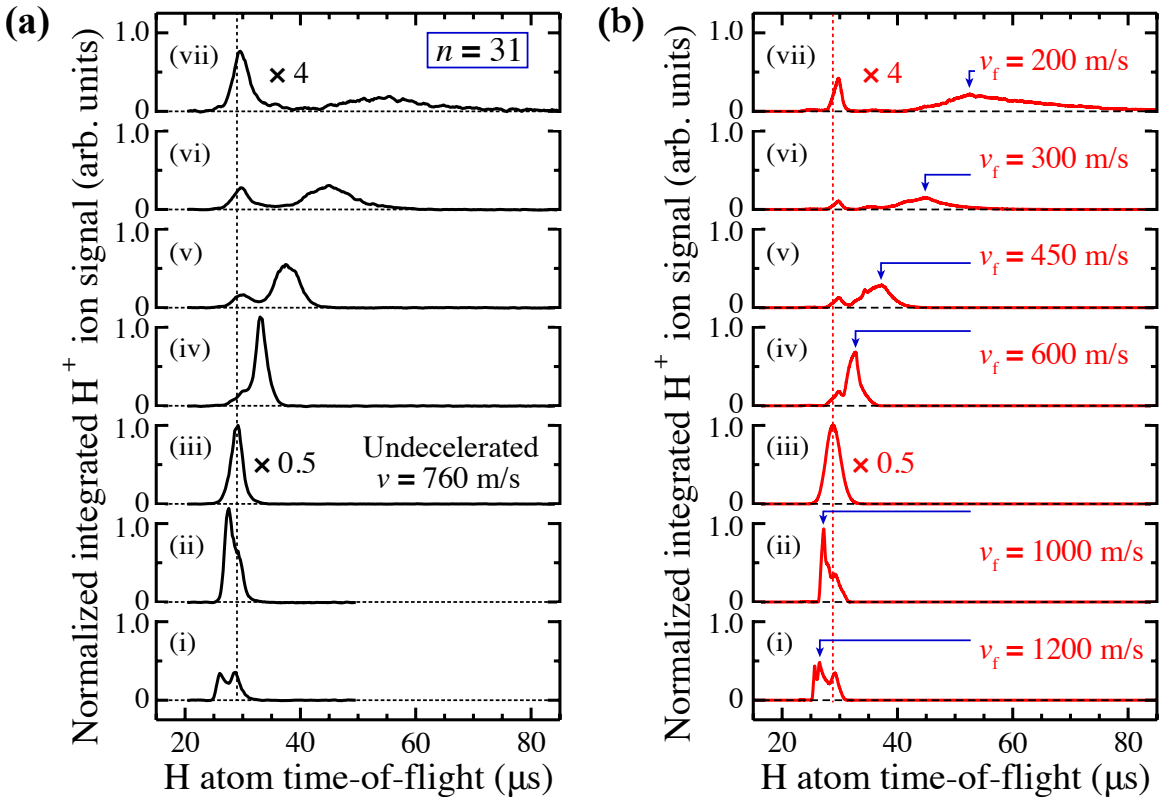

Figure 2.12: (a) Experimental and (b) simulated hydrogen atom time-of-flight distributions demonstrating acceleration and deceleration at $n = 31$ from $v_i = 760$ m/s to $v_f = 1200$, 1000, 600, 450, 300 and 200 m/s. From Ref. [75].

a single electric field minimum. The generation of these electric field minima in this device was achieved by the application of a set of 6 electric potentials to the individually addressable electrodes printed on the electrical circuit board. This set of potentials were then applied in a repeated fashion on every 7^{th} electrode. These potentials led to the generation of the electric field distributions that are displayed in Figure 2.11(b). However, if these potentials are set to oscillate sinusoidally in time the electric field minima will move continuously above the surface. The speed at which the minima move is therefore directly proportional to the angular frequency at which the potentials oscillate. If a frequency chirp is applied to the potentials, acceleration and deceleration is possible.

The results of a set of measurements of hydrogen atom time-of-flight from the photoexcitation position to the detection region are displayed in Figure 2.12(a). The results highlighted structures in the time-of-flight signals. While guiding at constant speed, the time-of-flight recorded peaked at $\sim$ 29 μs. As acceleration (deceleration) were applied, the peak of the time-of-flight shifted to

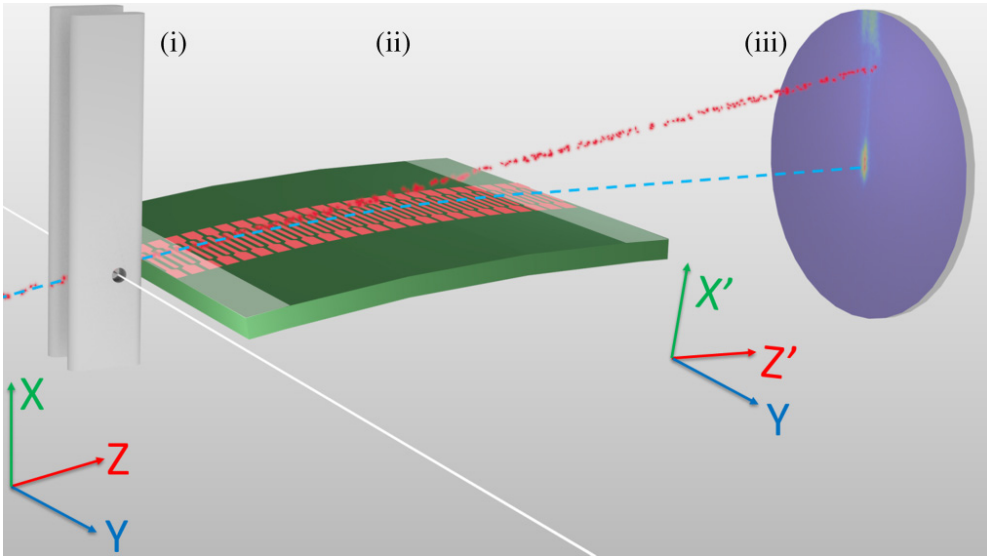

Figure 2.13: Schematic representation of a surface-electrode device used to trap and deflect hydrogen molecules away from their initial axis of propagation at an angle of 10° (from Ref. [77]).

earlier (later) times. However, a persistence of the peak at $\sim$ 29 μs can be observed in all traces. This corresponded to atoms which traversed the chip in metastable trajectories and arrived at the detection location without being accelerated or decelerated. Furthermore, in all the distributions it can be observed that for higher accelerations/decelerations, the H^+ ion signal was progressively reduced. The reduced detection efficiency of the more slowly moving samples is a consequence of the geometry of the detection region, in which the bunch of decelerated atoms expanded in the longitudinal and transverse dimensions in the time between the switch-off of the decelerator and detection. Transverse expansion after deceleration resulted in particle loss and led to a reduction of the overall signal. This signal reduction is consistent with the numerical particle trajectory calculations produced for comparison with the experimental data, which results are displayed in Figure 2.12(b).

Although the first experiments with these chip-based decelerators and traps were performed using hydrogen atoms, further devices have been developed to decelerate and trap helium atoms in singlet Rydberg states [76].

By introducing a curvature in the plane of the electrode surface off-axis transport of hydrogen molecules in Rydberg states has also been demonstrated (see Figure 2.13) [77]. In these experiments the transport of trapped samples away from the initial axis of propagation of the molecular beam was identified by detection on a MCP detector with phosphor screen for imaging. This device

was developed for use in studies of collisions between samples in two separate pulsed supersonic beams, one containing Rydberg atoms or molecules, and the other containing ground state samples. The chip-based decelerator/deflector will permit fine control over the relative speed of the collision partners which will co-propagate after the two beams are merged.

These chip-based decelerators, and the possibility to develop a Rydberg laboratory-on-a-chip with which comprehensive control over the quantum-states, motion and interactions of samples of Rydberg atoms can be achieved has provided the general motivation for the work described in this thesis.

Chapter 3

Theoretical background

For all of the experiments described in this thesis a precise knowledge of the effects of electric fields on high Rydberg states of atoms is essential. These effects are described here, first for the case of the hydrogen atom and then for the helium atom as required for the experiments. The rates of radiative decay by spontaneous emission, and by transitions driven by blackbody radiation, are also discussed.

3.1 Rydberg states of the hydrogen atom

The simplest Rydberg series are those associated with the hydrogen atom, which can be described by the Schrödinger equation, neglecting the electron and nuclear spins [78],

$$\hat{H}_0\Psi = (-\frac{\hbar^2}{2\mu}\nabla_{\mathrm{e}}^2 + V)\Psi = E\Psi, \tag{3.1}$$

where $\hat{H}_0$ is the field-free Hamilton operator, Ψ the Rydberg electron wavefunction, $\hbar = h/2\pi$ with the Planck constant h, V the potential experienced by the Rydberg electron, E the energy of the eigenstate and $\mu = \frac{m_{\mathrm{p}}m_{\mathrm{e}}}{m_{\mathrm{p}}+m_{\mathrm{e}}}$ the reduced mass of the electron-proton system.
Equation 3.1 is separable in spherical coordinates (r,θ,ϕ) and in parabolic coordinates (ξ,η,φ) [58]. These are related to the Cartesian coordinates by the transformations,

$$\begin{aligned} \xi &= r+z \\ \eta &= r-z \\ \varphi &= \arctan\left(\frac{y}{x}\right) \end{aligned} \tag{3.2}$$

where $r = \sqrt{x^2+y^2+z^2}$. The set of spherical coordinates is most appropriate for dealing with the pure Coulomb problem in the absence of external electric fields where

$$V = -\frac{e^2}{4\pi\varepsilon_0 r} \tag{3.3}$$

with e, the charge of the electron, and ε_0 the permittivity of vacuum. On the other hand, parabolic coordinates are better suited when homogenous electric fields perturb the symmetry of the pure Coulomb potential [58].

The solution of Equation 3.1 in spherical coordinates leads to the set of bound eigenstates, the wavefunctions of which can be expressed as a product of radial $R_{n\ell}(r)$ and angular $Y_{\ell m}(\theta,\phi)$ functions, such that [78]

$$\Psi_{n\ell m}(r,\theta,\phi) = R_{n\ell}(r)\cdot Y_{\ell m}(\theta,\phi) \tag{3.4}$$

where $Y_{\ell m}(\theta,\phi)$ are the normalized spherical harmonic functions. The radial wavefunctions $R_{n\ell}(r)$ can be expressed analytically as [78]

$$R_{n\ell}(r) = N_{n\ell}\left(\frac{2Zr}{na}\right)^{\ell}\cdot\exp\left(-\frac{Zr}{na}\right)\cdot L_{n-\ell-1}^{2\ell+1}\left(\frac{2Zr}{na}\right) \tag{3.5}$$

where Z is the charge of ion core, $a = (m_e/\mu_H)a_0$ with the Bohr radius $a_0 = 4\pi\varepsilon_0\hbar^2/(m_e e^2)$, $L_{n-\ell-1}^{2\ell+1}$ are the associated Laguerre polynomials, and $N_{n\ell}$ is a normalization factor [28]. The normalisation factor is dependent upon n and takes the values

$$N_{n\ell} = \left(\frac{2Z}{na}\right)^{3/2}\sqrt{\frac{(n-\ell-1)!}{2n(n+\ell)!}}. \tag{3.6}$$

The states are therefore characterised by the principal quantum number $n = 1, 2, 3, \ldots$, the angular momentum quantum number ℓ ($0 \leq \ell \leq n-1$) and the azimuthal quantum number m ($-\ell \leq m \leq \ell$). Each set, $n\ell m$, of quantum numbers refers to a different wave function (atomic orbital) [79].
However, for the hydrogen atom the energies associated with the eigenstates of Equation 3.4 depends only on the principal quantum number n ad are given by the Rydberg formula [80, 81, 58]

$$E_{n\ell m} = E_{\text{ion}} - \frac{hc \cdot R_{\text{H}}}{n^2} \tag{3.7}$$

where E_{ion} is the ground state ionisation energy and $R_{\text{H}} = \frac{R_\infty}{m_e}\mu_{\text{H}}$ is the Rydberg constant for the hydrogen atom.

In atomic hydrogen, the energy of each eigenstate depends only on n and the bound states have an electronic degeneracy equal to n^2. As the principal quantum number increases, the binding energy of the Rydberg electron to the ion core decreases with n^{-2}, while the energy difference between adjacent eigenstates scales with n^{-3}. The radiative lifetime scales as n^3[82].

3.2 Rydberg states of non-hydrogenic atoms

For non-hydrogenic atoms the Coulomb potential is perturbed because the ion core is no longer spherically symmetric. This can be accounted for in Equation 3.7 by replacing the principal quantum number n with an effective principal quantum number $n^* = n - \delta_\ell$, where δ_ℓ is the quantum defect that depends on the value of ℓ [82]. The new eigenenergies therefore become

$$E_{n\ell m} = E_{\text{ion}} - \frac{hc \cdot R_M}{(n-\delta_\ell)^2}, \tag{3.8}$$

where R_M is now the Rydberg constant for the particular atom or molecule of interest with mass M. A diagram indicating the differences in the energies of the Rydberg states of hydrogenic and non-hydrogenic atoms is presented in Figure 3.1 [28].

As can be seen in this figure, the effect of the non-hydrogenic ion core is greater for states in which the Rydberg electron approaches more closely the ion, i.e. states with low values of ℓ. For

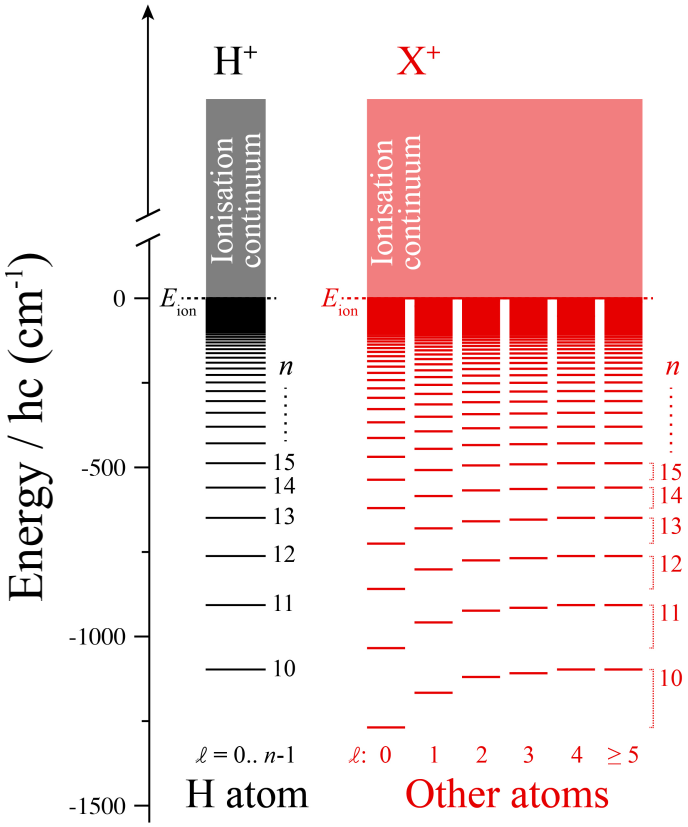

Figure 3.1: Schematic diagram of Rydberg states of hydrogen (H) and non-hydrogenic (X) atoms (adapted from Ref. [28]).

high-ℓ states (typically for $\ell \geq 4$), in which the centrifugal barrier ensures that the Rydberg electron and ion core do not significantly overlap, $\delta_\ell \simeq 0$.

3.3 Rydberg states lifetimes

Rydberg states of atoms have finite lifetimes, decaying by spontaneous emission to energetically lower-lying states. The fluorescence lifetime of Rydberg states are equal to the sum of the decay rates from the initially populated $|n\ell m\rangle$ state to all lower-lying $|n'\ell'm'\rangle$ states accessible via the selection rules for electric dipole transitions.

From considerations of the role of spontaneous emission from an ensemble of $N_{n\ell m}$ two-level atoms initially populated in the excited state $|n,\ell,m\rangle$ which can decay to the lower-lying $|n',\ell',m'\rangle$ state [83],

$$\frac{\mathrm{d}N_{n'\ell'm'}}{\mathrm{d}t} = -\frac{\mathrm{d}N_{n\ell m}}{\mathrm{d}t} = A_{n'\ell'm',n\ell m}N_{n\ell m}, \tag{3.9}$$

where $A_{n'\ell'm',n\ell m}$ is the Einstein A-coefficient for spontaneous emission. From Equation 3.9 it can be concluded that $A_{n'\ell'm',n\ell m}$ is the spontaneous emission rate of the excited state, which can be expressed as [83],

$$A_{n'\ell'm',n\ell m} = \frac{2\omega^3_{n'\ell'm',n\ell m}}{3\varepsilon_0 hc^3}\,|D_{n'\ell'm',n\ell m}|^2, \tag{3.10}$$

where $\omega = 2\pi\nu_{n'\ell'm',n\ell m}$ is the angular frequency corresponding to the energy difference between the states $|n'\ell'm'\rangle$ and $|n\ell m\rangle$, and $D_{n'\ell'm',n\ell m}$ is the transition dipole moment. Since the rate of spontaneous emission is independent from the emission direction in free-space, the Einstein's A-coefficient therefore does not depend on m. Equation 3.10 can thus be rewritten as [58],

$$A_{n'\ell',n\ell} = \frac{2e^2\omega^3_{n'\ell',n\ell}}{3\varepsilon_0 hc^3}\,\frac{\ell_{\max}}{2\ell+1}\,|\langle n'\ell'|r|n\ell\rangle|^2, \tag{3.11}$$

where $\ell_{\max}$ is $\max(\ell',\ell)$, and $\langle n'\ell'|r|n\ell\rangle$ is a radial integral. The radial integral determines whether a transition between the state $n'\ell'$ and the state $n\ell$ can occur based on the parity of the initial and final state wavefunctions, and it contributes to the overall strength of the transition.

In a multilevel system for which there are many pathways via which the excited state can spontaneously decay, the total spontaneous emission rate $\Gamma_{n,\ell,m}$ is equal to the sum of the rates of decay associated with each of these pathways, i.e.

$$\Gamma_{n,\ell} = \sum_{n',\ell'} A_{n'\ell',n\ell}. \tag{3.12}$$

The radiative, or fluorescence, lifetime of the excited state is then

$$\tau_{n'\ell'} = \Gamma^{-1}_{n'\ell'}. \tag{3.13}$$

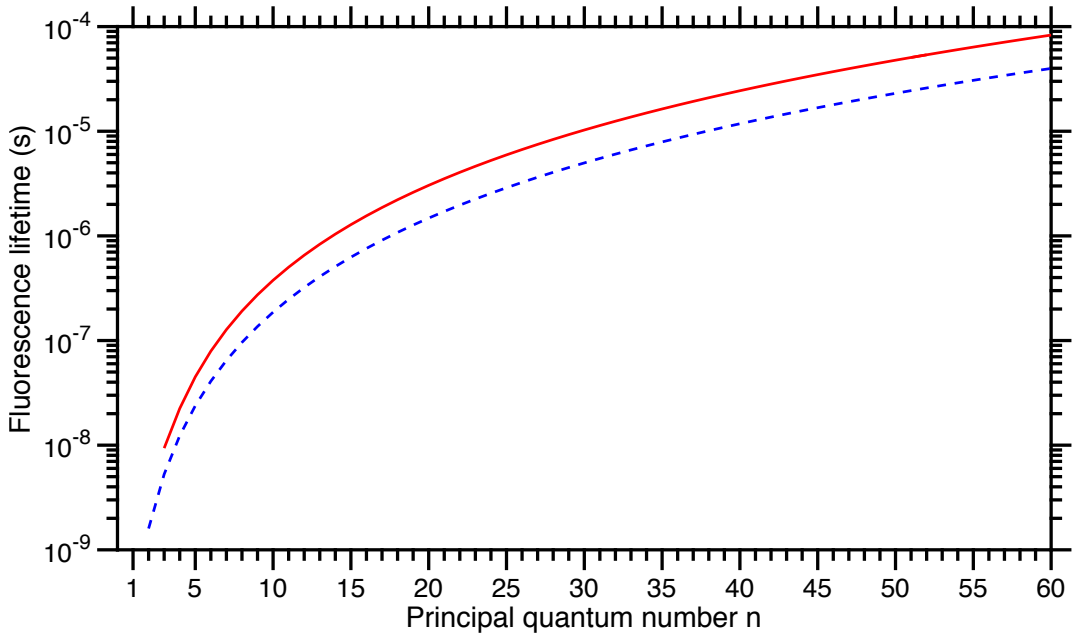

Figure 3.2: Calculated fluorescence lifetimes of excited np Rydberg states of hydrogen (blue, dashed curve), and triplet np Rydberg states of helium (red, continuous curve).

Using this approach, the radiative lifetimes of the np Rydberg states of hydrogen and, the triplet np Rydberg states of helium have been calculated. These are displayed in Figure 3.2.

Because the Einstein's A-coefficient depends on ω^3, the decay to the state with the lowest allowed principal quantum number n will dominate the fluorescence process. Hence, the spontaneous decay of high Rydberg states is typically dominated by fluorescence to the ground state. The effect of this is that as decelerated or trapped ensembles of atoms decay, they result in cold samples of ground state atoms.

3.4 Rydberg atoms in homogeneous electric fields

In the presence of a homogeneous electric field, $\vec{F}$, the angular momentum degeneracy of the Rydberg states is removed. Under these conditions, the Hamiltonian can be rewritten [58, 28] as,

$$H = -\frac{\hbar^2}{2m_e}\nabla_e^2 - \frac{e^2}{4\pi\varepsilon_0 r} + eF_z z \tag{3.14}$$

for an electric field $\vec{F} = (0,0,F_z)$.

In this situation the Stark problem can be solved analytically in parabolic coordinates [84, 85]. For each value of n, the ℓ-mixing caused by the electric field results in a manifold of Stark states. To first order these states exhibit linear energy shifts as the electric field strength is increased. The resulting energy levels can be expressed in terms of the parabolic quantum numbers n_1 and n_2, as

$$E_{n,n_1,n_2,m} = -\frac{hc \cdot R_{\mathrm{H}}}{n^2} + \frac{3}{2}(n_1 - n_2)nF_z ea_0. \tag{3.15}$$

The quantum numbers n_1 and n_2 fullfil the relation,

$$n = n_1 + n_2 + |m| + 1. \tag{3.16}$$

The index $k = n_1 - n_2$ is often used to label the Stark states with the result that Equation 3.15 can be expressed as,

$$E_{n,n_1,n_2,m} = -\frac{hc \cdot R_H}{n^2} + \frac{3}{2}nkF_z ea_0 \tag{3.17}$$

where the index k takes values from $-(n-1-|m_\ell|)$ to $+(n-1-|m_\ell|)$ in intervals of two. Comparison of Equation 3.17 with Equation 2.3 indicates that the electric dipole moment $\vec{\mu}_{\mathrm{elec}}$ of each Rydberg-Stark state is therefore,

$$\vec{\mu}_{\mathrm{elec}} = -\frac{3}{2}nkea_0. \tag{3.18}$$

In strong electric fields higher order corrections to the energy of each Rydberg-Stark state must also be considered. Analytic expressions for these higher-order terms can be determined [86] with, for example the second order correction

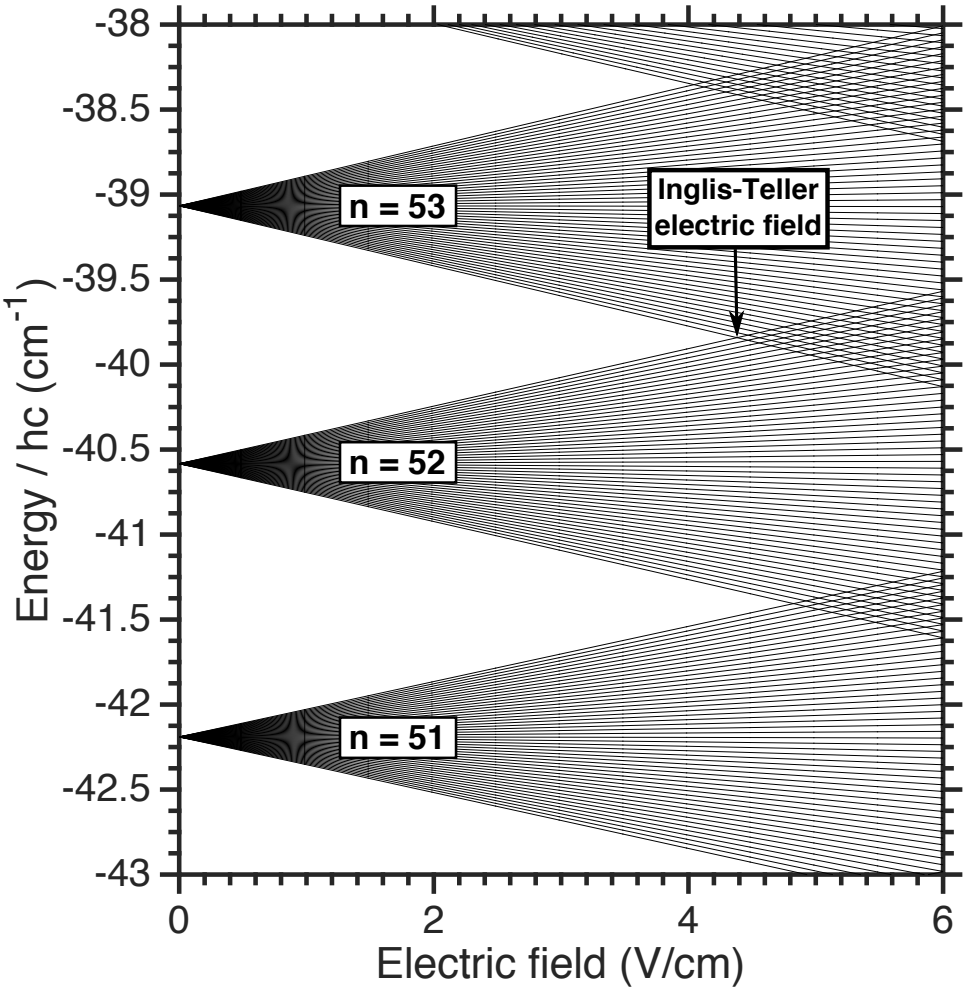

Figure 3.3: Stark map of the hydrogen atom calculated for Rydberg states with $n = 51$, 52, 53 and $|m| = 0$.

$$E^{(2)}_{n,k,m} = -\frac{F_z^2}{16} n^4 [17n^2 - 3k^2 - 9m^2 + 19] \cdot \frac{\mathrm{e}^2 \mathrm{a}_0^2}{2hc \cdot R_\mathrm{H}}, \tag{3.19}$$

A Stark map for the hydrogen atom including these corrections to second order is displayed in Figure 3.3. In this Stark map, the lowest electric field in which states associated with consecutive values of n cross each other is known as the Inglis-Teller field, F_IT. Considering the first-order Stark shift and the energy difference between consecutive field-free Rydberg states it is found that $F_\mathrm{IT} \propto n^{-5}$ and can be expressed completely as

	$\|2,0\rangle$	$\|2,1\rangle$	$\|3,0\rangle$	$\|3,1\rangle$	$\|3,2\rangle$
$\langle 2,0\|$	$-\frac{hc\cdot R_M}{(2-\delta_s)^2}$	0	0	0	0
$\langle 2,1\|$	0	$-\frac{hc\cdot R_M}{(2-\delta_p)^2}$	0	0	0
$\langle 3,0\|$	0	0	$-\frac{hc\cdot R_M}{(3-\delta_s)^2}$	0	0
$\langle 3,1\|$	0	0	0	$-\frac{hc\cdot R_M}{(3-\delta_p)^2}$	0
$\langle 3,2\|$	0	0	0	0	$-\frac{hc\cdot R_M}{(3-\delta_d)^2}$

Table 3.1: Example of a field-free Hamiltonian matrix for basis states $|n,\ell,m\rangle$ of a non-hydrogenic atom for which $|m| = 0$.

$$F_{\mathrm{IT}} = \frac{2hc\cdot R_M}{3ea_0\cdot n^5} \tag{3.20}$$

The above expression for the energies of Rydberg-Stark states in an electric field are valid for hydrogenic systems, i.e. one electron atoms or ions in which the core can be considered to be spherically symmetric, and for high-ℓ Rydberg states of other systems in which the Rydberg electron does not penetrate the ion core. In atoms other than hydrogen, and in molecules, the ion core does not display such a symmetry. Therefore, because the Hamiltonian is not separable, exact solutions to Equation 3.14 do not exist for low-ℓ states. However, perturbation theory can still be applied to the field-free eigenstates [87, 58]. For such calculations, measured or calculated values of the quantum defects of the low-ℓ states can be employed to determine the unperturbed energy of each level. An example of such a field-free Hamiltonian matrix for states with $n = 2$ and $n = 3$ is given in Table 3.1.

All of the experiments described in this thesis were carried out using triplet Rydberg states of helium close to $n = 52$. The quantum defects for those states with values of $\ell \leq 5$ are given in Table 3.2 [88].

ℓ	δ_ℓ
0	0.296671
1	0.068353
2	0.002889
3	0.000447
4	0.000127
5	0.000049

Table 3.2: Quantum defects for triplet Rydberg states of helium with $\ell = 0-5$ [88, 89].

The contribution of the external electric field, F_z, in this basis is to couple pairs of states through the introduction of off-diagonal matrix elements. The electric field component in the Hamiltonian of Equation 3.14 can be expressed as [28],

$$\begin{aligned}\psi^* H_F \psi &= e\langle n'\ell'm'|F_z z|n\ell m\rangle \\ &= eF_z\langle \ell'm'|\cos\theta|\ell m\rangle\langle n'\ell'|r|n\ell\rangle \\ &= eF_z\sqrt{\frac{4\pi}{3}}\,\langle \ell'm'|Y_{10}|\ell m\rangle\langle n'\ell'|r|n\ell\rangle\end{aligned} \tag{3.21}$$

where Y_{10} is a spherical harmonic function for $\ell = 1$ and $|m| = 0$. The angular integral, $\langle \ell'm'|Y_{10}|\ell m\rangle$, is therefore zero unless $\ell' - \ell = \pm 1$ and $m' - m = 0$. By using the properties of spherical harmonics, the angular matrix elements can be determined to be [28],

$$\langle \ell - 1, m|\cos\theta|\ell, m\rangle = \sqrt{\left(\frac{\ell^2 - m^2}{(2\ell+1)(2\ell-1)}\right)} \tag{3.22}$$

and

$$\langle \ell + 1, m|\cos\theta|\ell, m\rangle = \sqrt{\left(\frac{(\ell+1)^2 - m^2}{(2\ell+3)(2\ell+1)}\right)}. \tag{3.23}$$

The radial integrals $\langle n'\ell'|r|n\ell\rangle$ on the other hand must be evaluated numerically. For non-hydrogenic Rydberg states this is achieved using the Numerov method [28], which is based on the consideration that far from the ion core, the potential experienced by the Rydberg electron will be purely Coulombic.

Using this approach the complete Hamiltonian matrix for a non-hydrogenic Rydberg atom in the presence of a time-independent electric field can be calculated. By way of example, such a matrix, containing basis states with $n = 2$ and $n = 3$, and with $m = 0$, is presented in Table 3.3.

The energies of the eigenstates in the presence of the electric field can then be determined by calculating the eigenvalues of this matrix. The coefficients of the eigenvectors can then be employed to determine the contribution of each basis state to the resulting Stark states, and hence the transition strength for photoexcitation, and fluorescence rates.

	$\|2,0\rangle$	$\|2,1\rangle$	$\|3,0\rangle$	$\|3,1\rangle$	$\|3,2\rangle$
$\langle 2,0\|$	$-\frac{hc\cdot R_M}{(2-\delta_s)^2}$	$e\langle 20\|z\|21\rangle F_z$	0	$e\langle 20\|z\|31\rangle F_z$	0
$\langle 2,1\|$	$e\langle 21\|z\|20\rangle F_z$	$-\frac{hc\cdot R_M}{(2-\delta_p)^2}$	$e\langle 21\|z\|30\rangle F_z$	0	$e\langle 21\|z\|32\rangle F_z$
$\langle 3,0\|$	0	$e\langle 30\|z\|21\rangle F_z$	$-\frac{hc\cdot R_M}{(3-\delta_s)^2}$	$e\langle 30\|z\|31\rangle F_z$	0
$\langle 3,1\|$	$e\langle 31\|z\|20\rangle F_z$	0	$e\langle 31\|z\|30\rangle F_z$	$-\frac{hc\cdot R_M}{(3-\delta_p)^2}$	$e\langle 31\|z\|32\rangle F_z$
$\langle 3,2\|$	0	$e\langle 32\|z\|21\rangle F_z$	0	$e\langle 32\|z\|31\rangle F_z$	$-\frac{hc\cdot R_M}{(3-\delta_d)^2}$

Table 3.3: Example of a complete Hamiltonian matrix including non-zero off-diagonal elements arising from the contributions from an external electric field, F_z, in an $|n,\ell,m\rangle$ basis with $|m| = 0$.

The result of such calculations for triplet Rydberg states of helium with values of n close to 52 can be seen in Figure 3.4. The calculations were carried out including basis states ranging from $n = 49$ to $n = 55$, and the figures are centered on the state with $n = 52$. Panels (a), (b) and (c) in this figure represent the results of calculations carried out for $|m| = 0, 1$ and 2, respectively. As can be seen, by selecting the value of $|m|$, control can be exerted over the contributions of the s- and p-states in each Stark manifold. When $|m| = 0$ states for which $0 \leq \ell \leq\ n-1$ are present, while for $|m| = 1$ and $|m| = 2$, only states for which $1 \leq \ell \leq\ n-1$, and $2 \leq \ell \leq\ n-1$ are present, respectively.

When $|\vec{F}| = 0$ the energy levels of each state with angular quantum number ℓ are orthogonal, and ℓ-mixing does not occur. However, as can be seen in Figure 3.4, as the electric field strength is increased, it distorts the shape of the atomic orbitals, leading to ℓ-mixing, quadratic energy shifts of the low-ℓ states, and linear energy shifts of the high-ℓ, hydrogenic states. In addition, the low-ℓ, non-hydrogenic states with non-zero quantum defects give rise to avoided crossings at the Inglis-Teller limit. For low values of $|m|$, when the lowest ℓ-states contribute to the Stark map, these avoided crossings are large [Figure 3.4(a)]. In such cases the outer Stark states with the largest electric dipole moments in fields below F_{IT}, lose their electric dipole moments. However, for higher values of $|m|$ these avoided crossings are significantly reduced [Figure 3.4(b) and (c)] and can be traversed diabatically without the outer Stark states losing their dipole moments.

From the coefficients of the eigenvectors determined in the matrix diagonalization procedure, the spectral intensity of the transitions to each Stark-state can be calculated [90, 61]. The results of such calculations are displayed in Figure 3.5. The spectra displayed correspond to the electric dipole allowed 3p $\rightarrow$ ns and 3p $\rightarrow$ nd transitions in Figure 3.5(a) and (b). The upper part of each figure is a stick spectrum, which represents the square of the s-, or d-coefficients of the eigenvectors for each case. The square of the angular integral associated with the transition from the 3p state have been

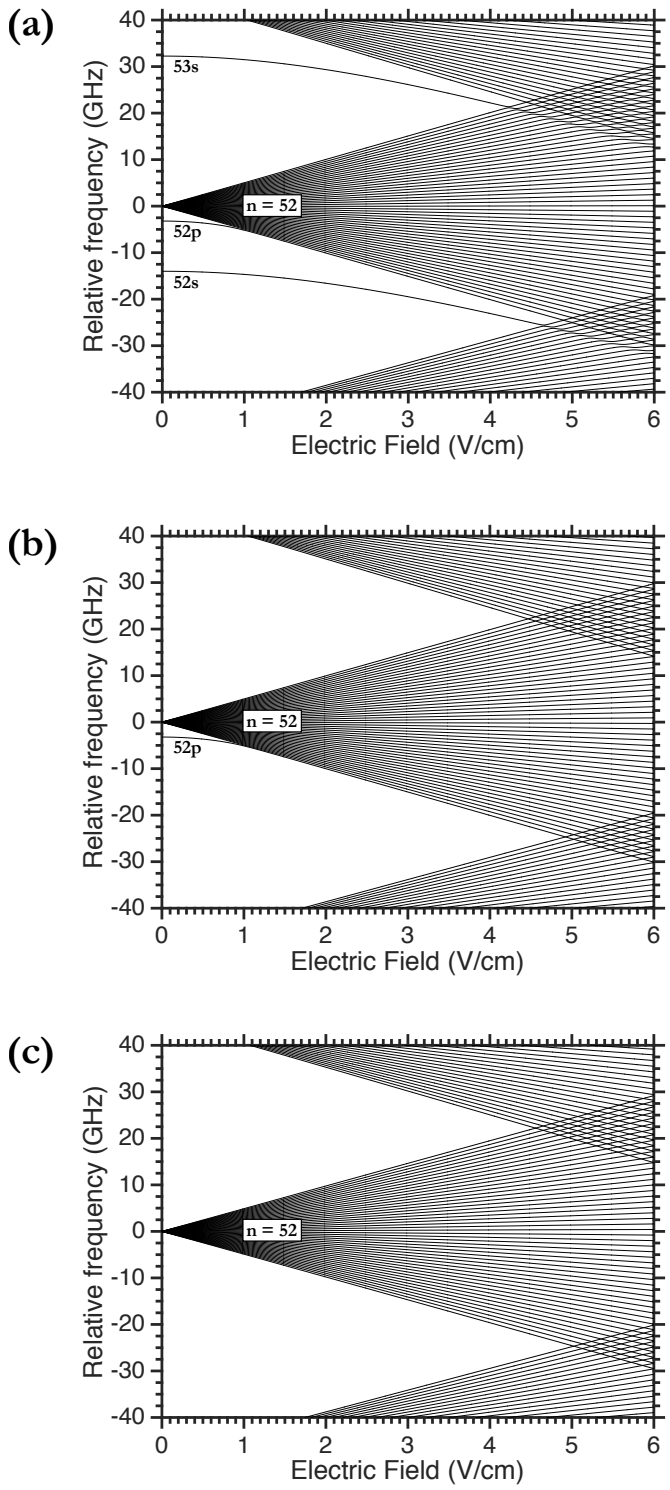

Figure 3.4: Stark maps of triplet Rydberg states of helium in the vicinity of $n = 52$. Stark maps with $|m| = 0, 1$ and 2 have been calculated separately and are shown in (a), (b) and (c), respectively. A basis of states from $n = 49$ to $n = 55$ was included in each calculation.

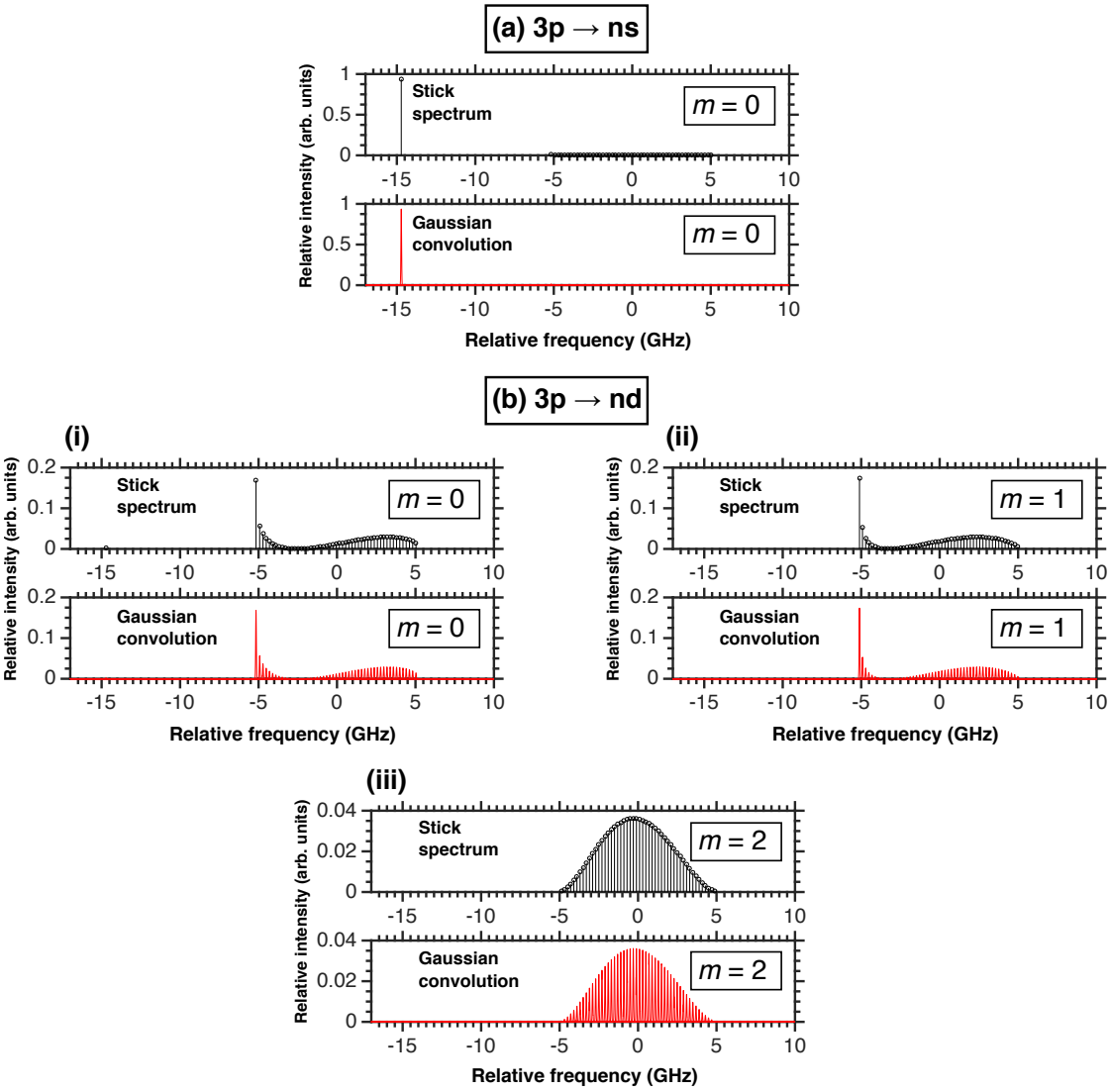

Figure 3.5: Calculated Stark spectra of Rydberg states of helium with $n = 52$ in an electric field $|\vec{F}| = 1$ V/cm. (a) The 3p $\rightarrow$ ns transitions, (b) 3p $\rightarrow$ nd transitions to states for which (i) $|m| = 0$, (ii) $|m| = 1$ and (iii) $|m| = 2$. The upper (lower) panel in each figure in (b) represents a stick spectrum (Gaussian convolution).

calculated using Equations 3.17 and 3.19 to account for the relative intensities of the transitions in (b). Calculations have been carried out for (i) $|m| = 0$, (ii) $|m| = 1$ and (iii) $|m| = 2$. To account for the effects of experimental spectral resolution, these data were convoluted with Gaussian functions with full-width-at-half-maximum (FWHM) of 25 MHz, and the results are displayed in the lower panel of each subfigure of Figure 3.5.

Calculated $|m| = 1$ relative spectra intensity distributions to state with ns and nd character (as

indicated) for a range of electric fields are displayed in Figure 3.6. The changes in the relative intensity of the transitions to each Stark state in these spectra as the electric field strength is increased, arise from the corresponding changes in the s- or d-character of each state. The increased separation between individual Stark states can be clearly seen as the applied field $\vec{F}$ increases in magnitude. The gradual increase in the spectral intensity of the transition to the state that adiabatically evolves to the 52p state in zero electric field arises from the increased d-character it acquires as a result of the ℓ-mixing by the external electric field.

From the linear energy shift of each Stark state in the electric field, the magnitude of the corresponding electric dipole moment can be determined. For the hydrogenic states, in the center of the Stark manifold, these electric dipole moments are approximately equal to those of states with the same values of n and $|m|$ in the hydrogen atom, i.e. $\vec{\mu}_{\rm elec} \simeq \frac{3}{2} nkea_0$. As a result these states are often labelled by the hydrogenic index k.

When the magnitude of the electric field dependent term in the Hamiltonian in Equation 3.14 approaches the Coulomb energy, electric-field ionisation of the Rydberg states can occur. In this situation, the electric field term in the Hamiltonian gives rise to a saddle point in the potential experienced by the Rydberg electron, as can be seen in Figure 3.7. As a result states that lie close to, and above, the saddle point will tunnel ionise. The classical ionisation field associated with this saddle point, calculated including Stark energy shifts is [58],

$$F_{\rm ion} = \frac{2hc\, R_M}{ea_0 9n^4}. \tag{3.24}$$

In considering more carefully effects of tunnel ionisation, this classical ionisation field is approximately equal to the field in which the ionisation rate of the outermost high-field-seeking Stark states at each value of n exceed $\sim 10^8$ s^{-1}. The outermost low-field-seeking states exhibit a similar rate of tunnel ionisation in fields approximately twice as large as those given by Equation 3.24 [58, 86].

The Rydberg states with values of $n > 50$ used in the experiments described here completely ionise in fields exceeding ~ 200 V/cm. This must be taken into account in selecting the most appropriate electric fields to use in guiding, decelerating and trapping experiments. However, it is also exploited for efficient detection of excited Rydberg atoms by pulsed electric field ionisation [58].

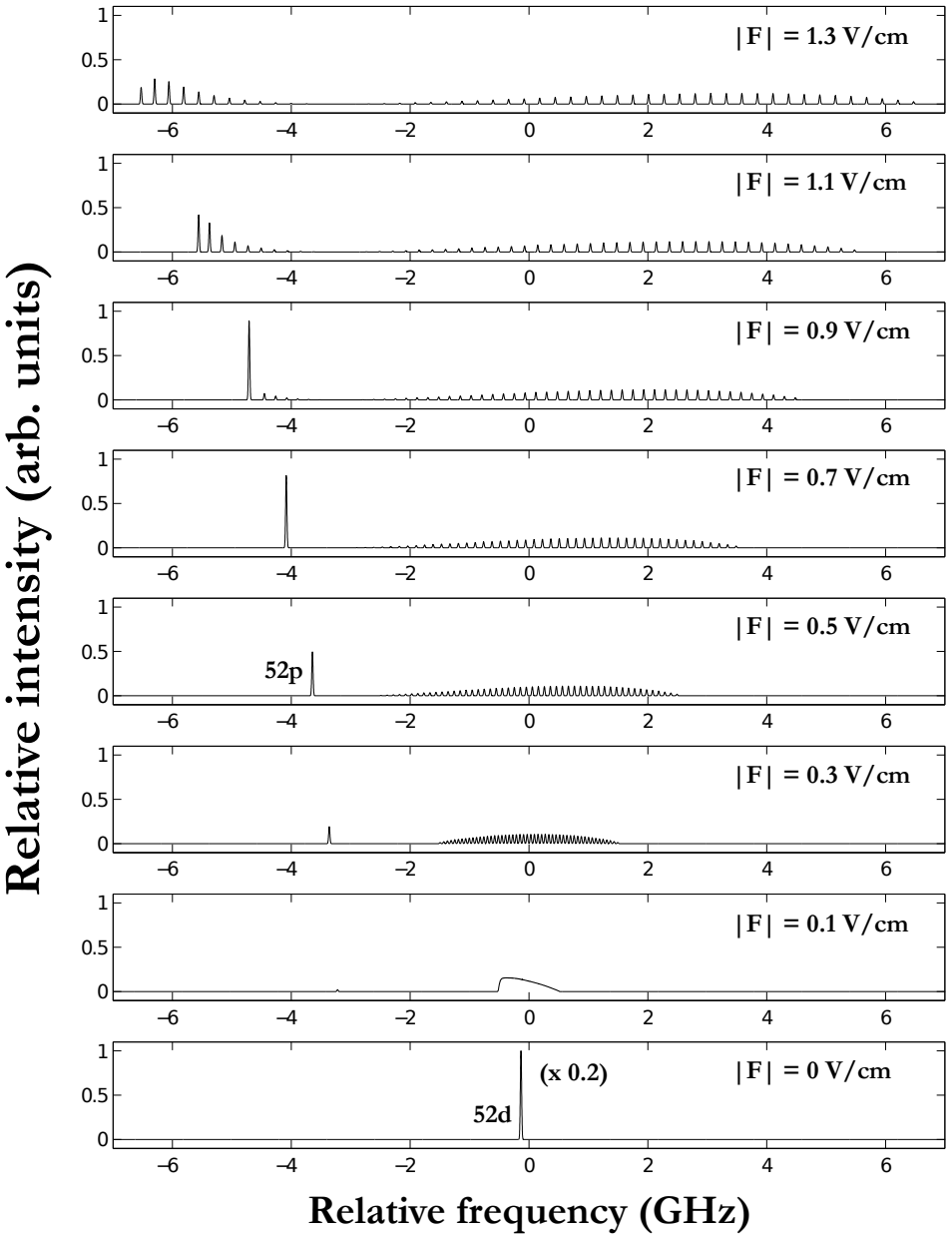

Figure 3.6: Stark spectra of Rydberg Stark states with $n = 52$ excited from the 3p state. Calculations have been carried out by considering contributions from states with $\ell = 2$. Each spectrum is convoluted with a Gaussian function with a FWHM = 25 MHz. The 52d state is indicated in the lowest panel, while the state that evolves adiabatically to the field-free 52p state is indicated in the spectrum for which $F = 0.5$ V/cm.

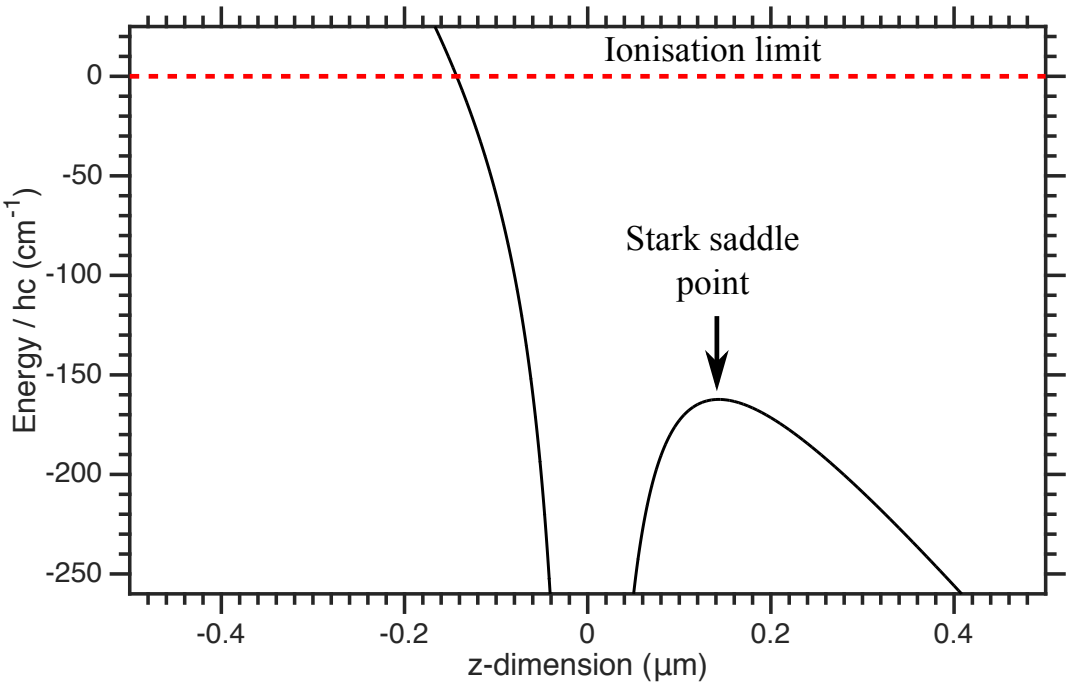

Figure 3.7: Potential energy distribution resulting from the addition of an electric $\vec{F} = (0, 0, -F_z)$ to a pure Coulomb potential.

3.5 Blackbody radiation effects

Since from the Rydberg energy formula in Equation 3.7 the energy, E_n, of each Rydberg state is,

$$E_n \propto \frac{1}{n^2}, \tag{3.25}$$

the energy intervals between states are,

$$\frac{dE_n}{dn} \propto \frac{1}{n^3}. \tag{3.26}$$

Therefore as n increases, the frequencies associated with the energy intervals between Rydberg states which differ in n by $+1$ rapidly decrease, entering the millimeter-wave and microwave regimes for values $n \geq 18$. Therefore transitions between these states can be driven by blackbody radiation. The rate at which these blackbody transitions occur depends on the photon occupation number, $\bar{n}_{\mathrm{p}}$, in the

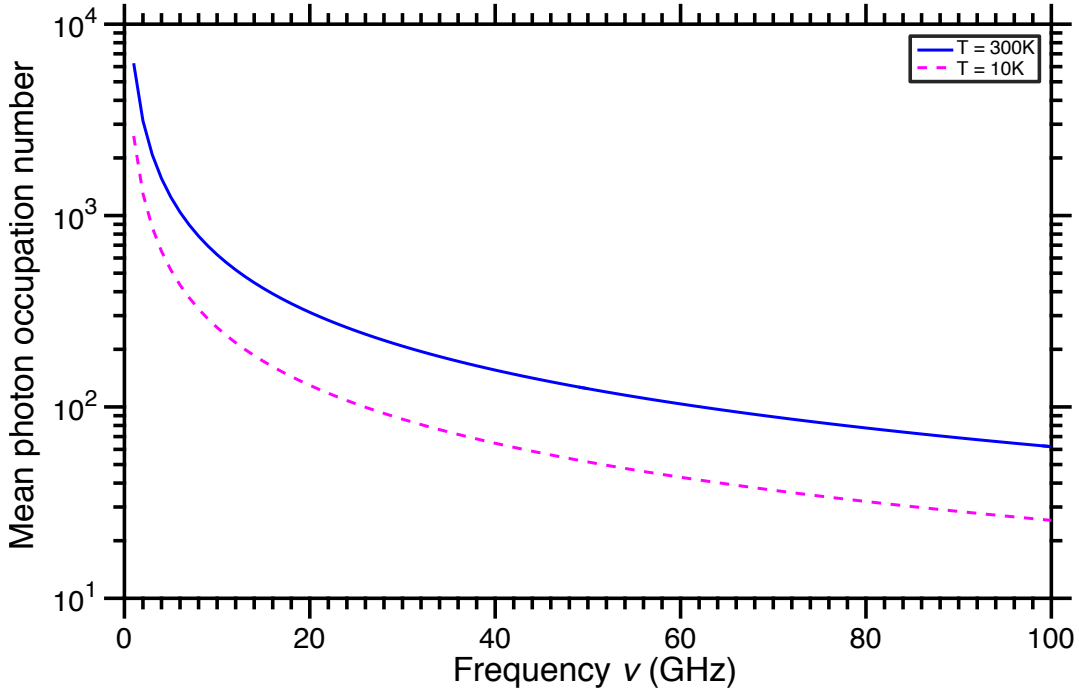

Figure 3.8: Dependence of the mean blackbody photon occupation number per mode on frequency for blackbody temperatures $T = 300$ K, and $T = 10$ K.

blackbody radiation field. The frequency dependence of $\bar{n}_{\rm p}$ is shown in Figure 3.8 and is expressed as [91],

$$\bar{n}_{\rm p} = \frac{1}{e^{h\nu/k_{\rm B}T} - 1}, \tag{3.27}$$

where ν is the frequency of the transition, T is the temperature at which the transition occurs and $k_{\rm B}$ is the Boltzmann constant. In the presence of this thermal radiation field, the transition rate from an initial state $|n,\ell,m\rangle$ to a final state $|n',\ell',m'\rangle$ is given by the product of the mean photon occupation number at the frequency of the transition and the Einstein A coefficient [58],

$$\Gamma_{\rm BB} = \bar{n} A_{n'\ell',n\ell}, \tag{3.28}$$

The corresponding n-changing transitions driven by blackbody radiation become significant for high values of n. For example, at room temperature $\Gamma_{\rm BB} \sim 10^4 - 10^5$ s^{-1}. As discussed in Chapter

2, Section 3, blackbody *n*-changing transitions between Rydberg-Stark states occur predominantly between states with similar electric dipole moments. They therefore do not lead directly to trap loss, but must be taken into account in considering the evolution of the trapped ensembles of atoms.

Chapter 4

Experimental methods

The research reported in Chapters 5-8 of this thesis involved the design, construction and implementation of several sets of experiments. The specific details of the Rydberg atom guides, decelerators and traps used in these experiments are described in the relevant chapters. However, many experimental techniques are common to all the experiments. These common aspects are described in this chapter. They include pulsed supersonic beams, the generation of metastable helium atoms in an electric discharge, the photoexcitation of helium atoms to high Rydberg states, the detection of excited Rydberg atoms by pulsed electric field ionisation, and the general operation of the experiments and data acquisition via a purpose built LabVIEW interface.

A schematic overview of the apparatus used in all experiments described is presented in Figure 4.1. The experiments were performed in a vacuum chamber operated at pressures of $10^{-7} - 10^{-8}$ mbar. In this chamber, pulsed supersonic beams of metastable helium atoms in the 1s2s $^3S_1$ state were generated and subsequently photoexcited to high Rydberg states. Metastable helium was chosen for these experiments because (1) it can be efficiently prepared at high density in pulsed supersonic beams by electric discharge; (2) it possesses strong electronic transitions at frequencies that are appropriate for narrow-bandwidth cw laser excitation; (3) it is light and therefore amenable to efficient manipulation using inhomogeneous electric fields; and (4) in the longer term, in an apparatus cooled to cryogenic temperatures, the effects of condensation on cold surfaces will be minimal [28].

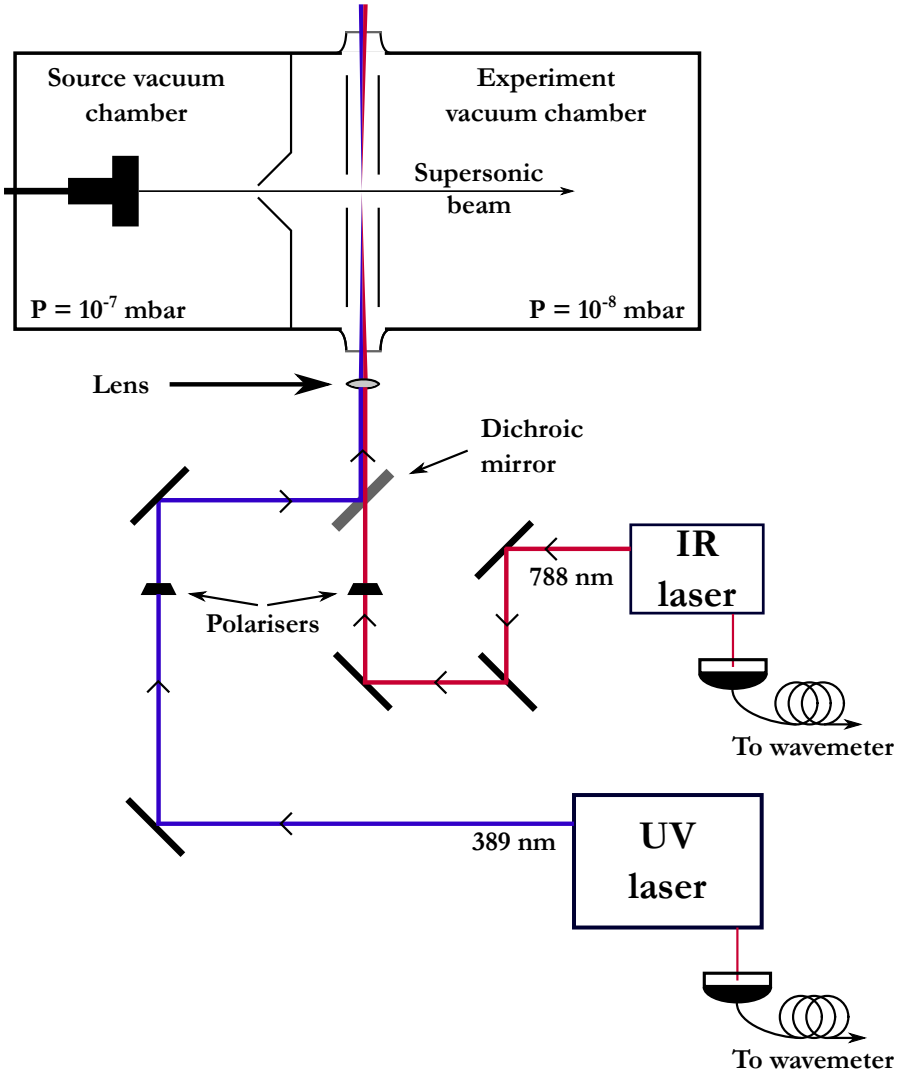

Figure 4.1: Overview of the experimental apparatus (not to scale), including the uv-, and ir- lasers and the vacuum system.

4.1 Pulsed supersonic beams

The central component of the apparatus is the vacuum system in which the experiments were performed. This can be seen in more detail in Figure 4.2.

The experiments operated at a repetition rate of 50 Hz beginning each cycle with the generation of a pulsed supersonic beam of metastable helium. This was achieved at the exit of a pulsed valve located inside the source vacuum chamber. The expansion of a gas from a reservoir into vacuum can occur in two general ways depending upon the relationship between the mean-free-path of the gas atoms in the reservoir, λ_0, and the diameter of the expansion orifice, D [92, 93]. In the limit where

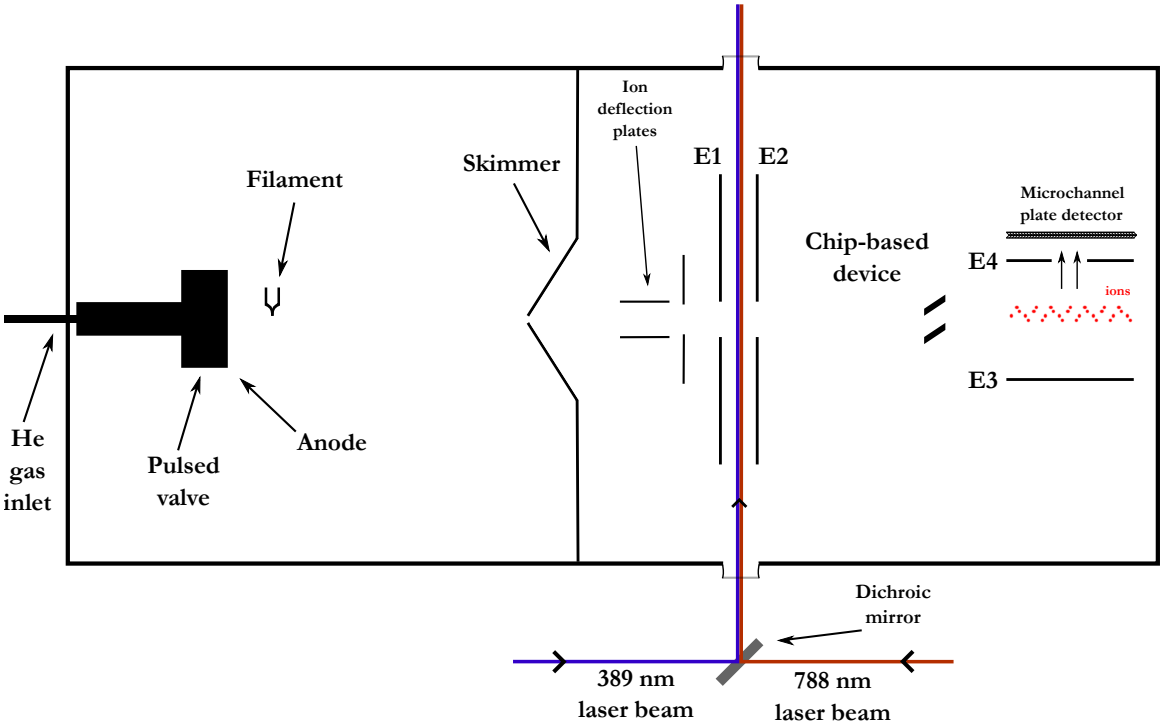

Figure 4.2: Schematic diagram of the vacuum chamber used in the experiments described here (not to scale). A pulsed supersonic beam was generated at the exit of a pulsed valve. This beam was then collimated by a skimmer. Rydberg photo-excitation took place between the metallic plates labelled E1 and E2. Detection by pulsed electric field ionisation took place between plates E3 and E4.

$\lambda_0 \gg D$, the number of collisions experienced by an atom as it exits the reservoir approaches zero and an effusive beam is generated. On the other hand, a supersonic expansion is formed in the limit where $D \gg \lambda_0$. In this case as the particles exit the reservoir they experience many collisions. Since the resulting expansion of the gas can be regarded as adiabatic, the enthalpy is almost completely converted into directed mass flow, leading to high forward velocities, but low velocity spreads (i.e. low translational temperatures in the moving frame of reference) [94]. A schematic view of the generation of a supersonic beam is displayed in Figure 4.3.

Based on the conservation of the system enthalpy and on the first law of thermodynamics [92],

$$H + \frac{1}{2}mv^2 = H_0, \tag{4.1}$$

where H is the molar enthalpy of the gas, H_0 is the total enthalpy of the system, v is the average flow

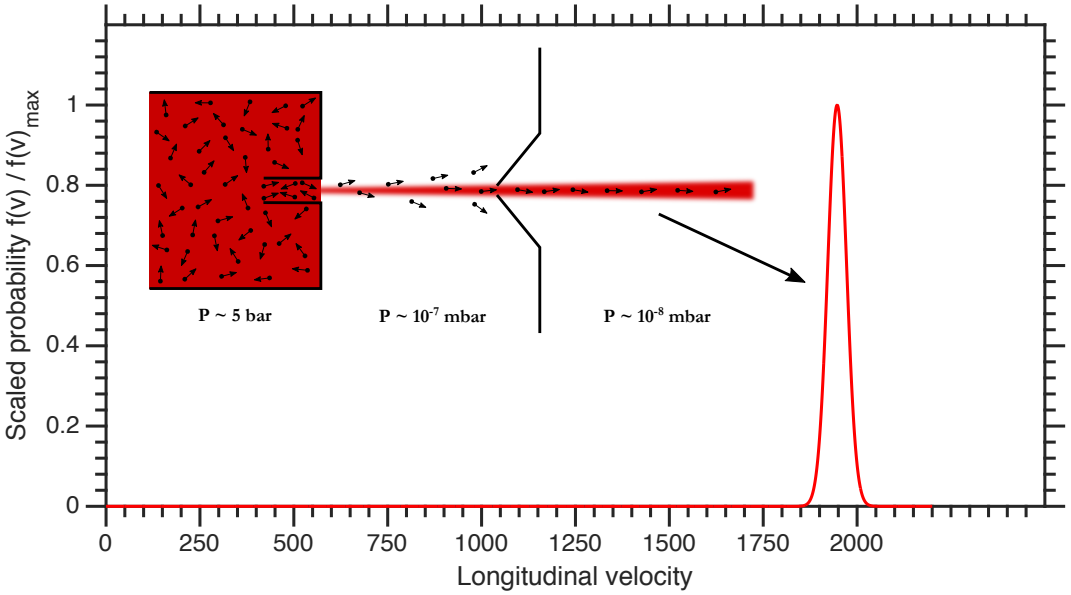

Figure 4.3: Schematic view of the generation of a supersonic beam. The typical velocity distribution of a pulsed supersonic beam of helium atoms expanding from a reservoir operated at 365 K is also displayed. After Ref. [94].

velocity, and m the mass of a single atom or molecule. The specific heat, C_{p}, at constant pressure of the gas is defined as,

$$C_{\mathrm{p}} = \frac{\mathrm{d}H}{\mathrm{d}T_0}, \tag{4.2}$$

where T_0 is the temperature of the reservoir. Substituting Equation 4.2 into Equation 4.1 leads to the result that,

$$v_{\mathrm{max}} = \sqrt{\frac{2H(T_0)}{m}} = \sqrt{\frac{2C_{\mathrm{p}} \cdot (T - T_0)}{m}}, \tag{4.3}$$

where $H(T_0)$ is the molar enthalpy of the gas at the temperature of the reservoir, T_0. From these considerations, it is possible to derive the translational temperature $T(L)$ at a distance L from the exit of the valve as [95],

$$T(L) = \frac{T_0}{1+\frac{1}{2}(\gamma-1)M(L)^2}, \tag{4.4}$$

where $M(L)$ is the Mach number, which is defined as the ratio of the velocity, v, of the beam in the laboratory-fixed frame of reference to the local speed of sound in the beam, and $\gamma = C_p/C_V$ is the ratio of the heat capacity at constant pressure to that at constant volume. The dependence of $M(L)$ on the distance from the exit of the valve can be written as [28],

$$M(L) = A\left(\frac{L}{D}-B\right)^{\gamma-1} - C\left(\frac{L}{D}-B\right)^{1-\gamma}, \tag{4.5}$$

where for a monoatomic gas $A = 3.26$, $B = 0.075$, $C = 0.61$ and $\gamma = 5/3$.

The mean longitudinal velocity of a supersonic beam can be expressed as function of the Mach number $M(L)$ as,

$$\overline{v}_z = M(L)\sqrt{\frac{\gamma\, k_{\mathrm{B}} T(L)}{m}}, \tag{4.6}$$

with the velocity distribution [95],

$$f_n(v) = N_n v^n e^{-(v-\overline{v}_z)^2/\xi}, \tag{4.7}$$

where N_n is a normalisation factor and $\xi = \sqrt{2k_{\mathrm{B}}T(L)/m}$.

In the experiments described here, pulsed supersonic beams of helium were generated using a pulsed valve operated at a temperature of $T_0 = 365$ K and with an exit aperture, $D = 0.5$ mm. The longitudinal velocity distribution of such a beam at a distance of $L = 40$ mm from the valve opening is displayed in Figure 4.3.

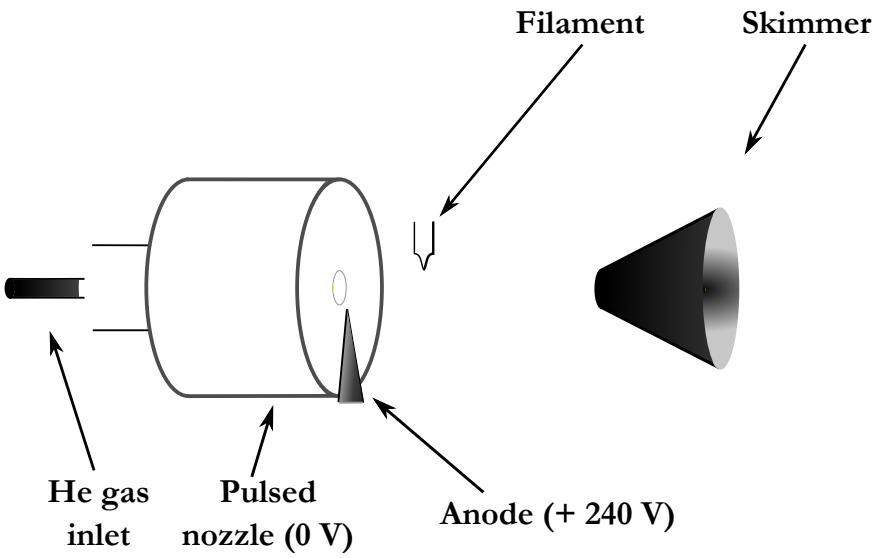

Figure 4.4: Schematic diagram of the discharge source used for the generation of beams of metastable helium atoms (not to scale).

4.2 Generation of a beam of metastable helium atoms

To generate pulsed supersonic beams of metastable helium atoms in the 1s2s $^3S_1$ state, an electric discharge was struck at the exit of the valve. A schematic diagram of the components used to generate this discharge is displayed in Figure 4.4. The approach used is identical to that of Halfmann et al. [96]. The electric discharge was initiated directly at the exit of the valve by applying a potential of +240V to a sharp metal tip located approximately 1 mm downstream from the baseplate, and $\sim 0.25 - 0.5$ mm off axis. This metal tip acted as an anode, while the grounded baseplate of the valve acted as the cathode. Ignition of the discharge required charged particles with sufficient kinetic energy. This can be achieved by generating a very large electric field across the gas sample with potentials on the order of 10 kV cm^{-1}. However, this approach tends to heat the atomic beam and results in low shot-to-shot stability of the discharge. To ignite the discharge at a lower electric field, it can be seeded with electrons as done in the experiments presented in this thesis. This was achieved by placing a heated tungsten filament in front of the valve [96], approximately 15 mm downstream from the exit, and a $1 - 3$ mm off axis. Under the experimental conditions described here, a time-averaged current in the discharge of 1 mA was obtained by applying a current of 2.6A to heat the filament. The recombination of the plasma generated by the discharge leads to populating of the metastable 1s2s $^3S_1$ level.

This metastable state in helium is very long lived, with a lifetime of ∼8000 seconds [97, 98, 99]. It therefore acted as the effective ground state for all experiments performed. The metastable 2^1S_0 state was also produced in the discharge source, but the combination of its short, $\sim$ 20 ms [100], lifetime, the reduction in the number density by optical pumping to the ground state by the light emitted by the filament and discharge, and the shorter lifetime of the singlet Rydberg states than the triplet Rydberg states makes it less suited to the experiments described.

After exiting the discharge region, the supersonic beam of metastable helium atoms travelled toward a conical skimmer of 2 mm diameter, where a fraction of the atoms passed through to the photoexcitation region of the apparatus. The skimmer sampled the central part of the atomic beam and permitted the creation of a well-defined, cylindrical beam with a homogeneous phase-space density (see Figure 4.4). To deflect any ions that may travel along with the beam of metastable atoms, a pair of deflection electrodes were placed immediately after the skimmer as depicted in Figure 4.2.

The vacuum chamber used in the experiments was operated at pressures in the range of $10^{-7} - 10^{-8}$ mbar. These pressures ($< 10^{-6}$ mbar) were necessary to minimise losses of metastable helium atoms or helium Rydberg atoms by Penning ionisation collisions with the background gas. The penning ionisation process which follows the pathway [100, 101],

$$\mathrm{He}^* + \mathrm{X} \rightarrow \mathrm{He} + \mathrm{X}^+ + \mathrm{e}^-, \tag{4.8}$$

plays a particularly significant role for metastable helium atoms because of their large internal energy of $\sim$ 19 eV. This large internal energy makes Penning ionisation of all species of background gas, for example N_2, O_2, H_2O possible [101].

4.3 Laser photoexcitation

After passing through the skimmer and ion-deflection system, the metastable helium atoms entered the photoexcitation region in the apparatus. This was located between two parallel metal plates labelled E1 and E2 in Figure 4.1. Arbitrary electric potentials can be applied to these plates to generate homogeneous electric fields in the region between them to allow selective laser photoexcitation of high Rydberg states.

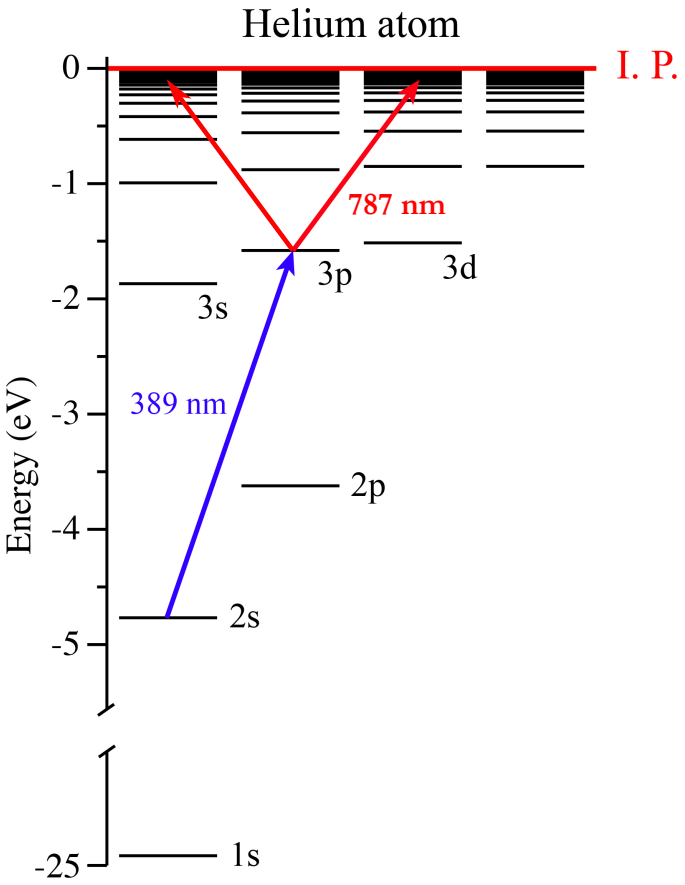

Figure 4.5: Energy levels of atomic helium. The 1s2s $^3S_1 \rightarrow$ 1s3p $^3P_2$ transition required radiation of 388.975 nm while ir radiation at a wavelength of 787.059 nm was employed for the subsequent transition to the high Rydberg states.

Photoexcitation was carried out using the resonance-enhanced two-colour, two-photon excitation scheme,

$$1s2s\ ^3S_1 \xrightarrow{h\nu_1} 1s3p\ ^3P_2 \xrightarrow{h\nu_2} 1s\ ns/1s\ nd, \tag{4.9}$$

depicted in Figure 4.5. This scheme was implemented using two narrow-bandwidth continuous wave (cw) lasers. In this excitation process the first transition, from the 1s2s $^3S_1$ level to the 1s3p $^3P_2$ level, occurred at 25708.58759 cm^{-1} ($\equiv$ 388.975 nm) in the ultraviolet (uv) region of the electromagnetic spectrum. The second transition, from the 1s3p $^3P_2$ level to high Rydberg states lied in the range from 12624.191 cm^{-1} ($\equiv$ 792.130 nm) for finding Rydberg states with values of $n = 30$, to

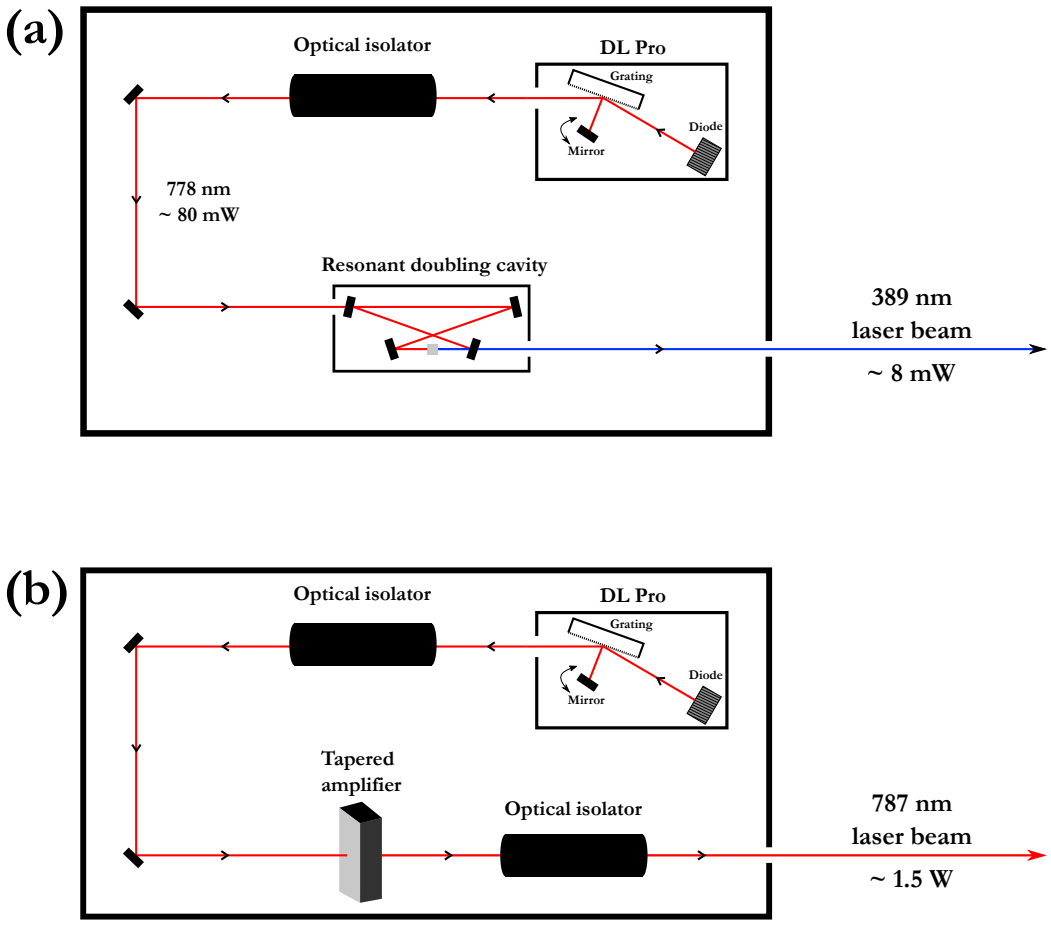

Figure 4.6: Schematic representation of Toptica DL Pro lasers with (a) second harmonic generation, and (b) a tapered amplifier, as used in the experiments described here [102].

12746.104 cm^{-1} ($\equiv$ 784.553 nm) at the ionisation limit of helium. The majority of the experiments described here were performed using Rydberg states for which $n = 52$ or $n = 48$. This therefore required laser excitation at 12705.527 cm^{-1} ($\equiv$ 787.059 nm) or at 12698.479 cm^{-1} ($\equiv$ 787.496 nm) for excitation, respectively.

Narrow-bandwidth laser radiation at these wavenumbers was generated using two diode laser systems supplied by Toptica Photonics AG [102]. Both lasers were DL Pro systems, the output from one of which was frequency doubled to obtain the required uv radiation, while the output from the second was amplified in a tapered amplifier to obtain sufficient power to efficiently drive the second transition in the excitation scheme. Schematic diagrams indicating the layout of the two laser systems are displayed in Figure 4.6. In both systems, the primary radiation source was a tunable diode laser. These are electrically pumped semiconductor lasers in which the gain is generated by

an electrical current flowing through a p-i-n structure. In such a structure, the electrons and holes can recombine, releasing the energy as light. In order to select the appropriate wavelength, a diffraction grating is added such that a cavity is formed. Both lasers employed in the work described here used the Littman-Metcalf cavity configuration [103]. In this configuration, the grating orientation is fixed, and an additional mirror is used to reflect the first order diffracted beam back into the laser diode. The wavelength is tuned by rotating the mirror. The radiation emitted in both of these diode lasers is in the infrared region. After passing through an optical isolator the radiation from the first laser entered a resonant frequency doubling cavity, where a nonlinear crystal was used to double the frequency [see Figure 4.6(a)]. In this frequency doubling process, the input electromagnetic wave generated a second wave at twice the optical frequency (i.e. half the wavelength) in the medium. This process is also called second-harmonic generation. Because this process is dependent on the square of the laser intensity, the crystal was placed within a resonant enhancement cavity. The resulting second harmonic conversion efficiency was $\sim 10\%$ and the second-harmonic beam had a wavelength of 388.975 nm ($\equiv 25708.58759\ \mathrm{cm}^{-1}$) with a power $P_{\mathrm{uv}} = 8$ mW. After passing through the optical isolator, the radiation from the second ir laser entered a tapered amplifier. This permitted up to 1.5 W of IR radiation to be generated at 787 nm, which was necessary to saturate the transitions to the high Rydberg states.

4.4 Pulsed electric field ionisation and MCP detector

After the Rydberg atoms passed through the surface-based electrostatic guides, decelerators or traps in the center of the vacuum chamber, they reached the detection region. This was composed of two elements: a metal electrode labelled E3 in Figure 4.1 and a microchannel plate (MCP) detector. The MCP detector used in the experiments described in this thesis was composed of an array of 10^6 miniature electron multiplier tubes oriented parallel to one another [104]. Their diameters were 10μm, their center-to-center spacing was 12μm, and the ratio of their length to their diameter was 60:1. The channel-ends were electrically connected by a metallic layer. An electric field was applied across each plate to accelerate the electrons generated by electron or ion impact on the front plate as can be seen in Figure 4.7. A potential difference U of +1 kV was applied across each MCP in the pair. In the experiments discussed here, the MCPs used were mounted in pairs rotated by 180° to each other. This configuration is called a “chevron” configuration and allows electron multiplication

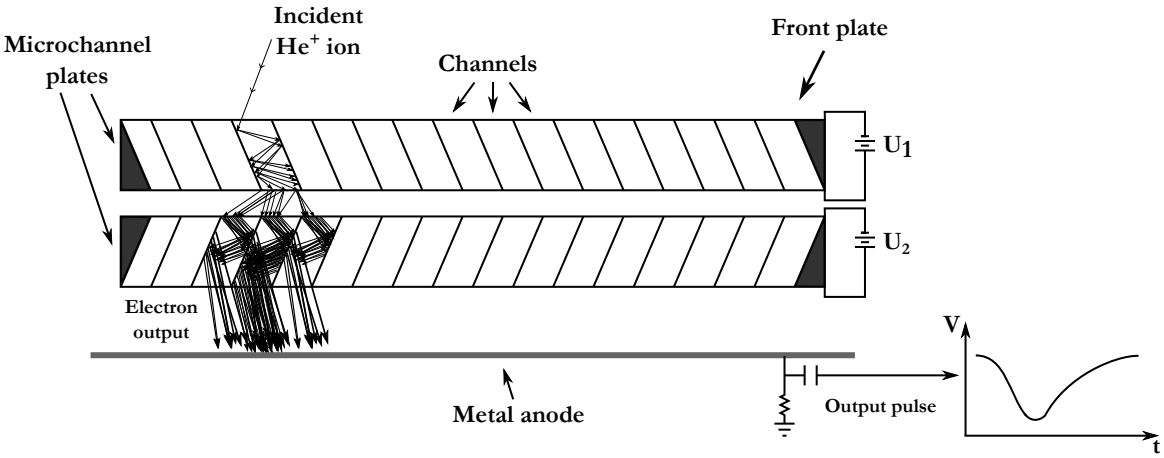

Figure 4.7: Schematic diagram of a MCP detector pair in a "chevron" configuration. A single electron incident on the front plate triggers a cascade process that multiplies the detected signal intensity. The electric current on the metal anode represents the detected signal.

factors as high as 10^8 [105]. Applying appropriate combinations of electrical potentials to the MCP plates and anode permits, vuv photons, electrons, ions or neutral Rydberg atoms to be detected [106].

In all experiments described here He^+ ions incident on the MCP were detected. When the Rydberg atoms entered the region in front of the MCP detector [between E3 and E4 in Figure 4.2], a pulsed potential of ~ 1 kV was rapidly applied to the plate E3 with a rise time of ~ 800 ns. The resulting field of ~ 350 V/cm was sufficient to completely ionise the Rydberg atoms. The same electric field then accelerated the He^+ ions produced by this process through the aperture in E4 which was constantly maintained at 0 V and onto the front panel of the MCP. To maximise the kinetic energy of the incident ions the front plate of the MCP was operated at a potentials of -2.4 kV. In this configuration the potential of the back plate of the MCP was -400 V and the potential on the anode was 0 V.

4.5 LabVIEW control and data acquisition program

The experimental apparatus was controlled, and data acquired, using a purpose-built data acquisition program developed in LabVIEW as part of this thesis work. This application was designed to interface with the laser system, wavelength/frequency calibration unit, pulse delay generators, arbitrary waveform generators, microwave sources and the oscilloscope used for data acquisition. It permitted the integration of electron and ion time-of-flight signals imported from the oscilloscope

and the storage of all data to file for later analysis.

The structure of the LabVIEW application was based on the multiple requirements of the experiments. These included (i) the possibility to adjust the number and sequence of commands sent to the oscilloscope easily and efficiently; (ii) the rapid execution of repeated sets of measurements; (iii) the possibility to read and refresh the waveform readings on the oscilloscope before importing the data; (iv) the ability to select integration windows within each imported waveform; (v) the storage of the data associated with the waveforms and the integration windows for a large number of measurements; (vi) the control of electrical potentials, time delays and microwave frequencies of interest in the measurements, and (vii) the generation of waveforms, subsequently sent to a set of arbitrary waveform generators, for guiding, deceleration and trapping experiments.

The LabVIEW software package operates by executing all commands simultaneously. As a result, the only natural temporal constraints arise because of (i) the relative speed of each process, i.e., faster subroutines will be completed first, and (ii) the availability of input variables, i.e., particular sections of the program will not be executed until the necessary inputs they require are available. For this reason it was necessary to develop a program structure capable of imposing and maintaining a chronological order when sending a series of commands from the computer to the external devices and receiving and recording the experimental data. These considerations and the desire to design a program which could be easily expanded in the future led to the decision to implement a LabVIEW code based on a Queued-State Machine (QSM) architecture. The structure of such architecture is well suited for the development of mid to large-scale programs. A simplified schematic diagram of the architecture employed is displayed in Figure 4.8.

A QSM is composed of three main components: (i) the producer loop, (ii) the consumer loop, and (iii) the queue. The producer loop represents a collection of events which are triggered by external signals from the front panel, graphical interface, of the program. The consumer loop consists of a stacked collection of state-machine architectures, which each perform precisely defined operations. The communication between the producer and the consumer loops is achieved via the queue. This queue imposes and maintains chronological ordering by sending commands from the producer loop to the consumer loop. The action of the queue is therefore to ensure that any individual command cannot bypass any other command, until the previous one is executed. The basic information needed in the queue for the QSM architecture to operate is the enumerated element (an "*enum*"). For each

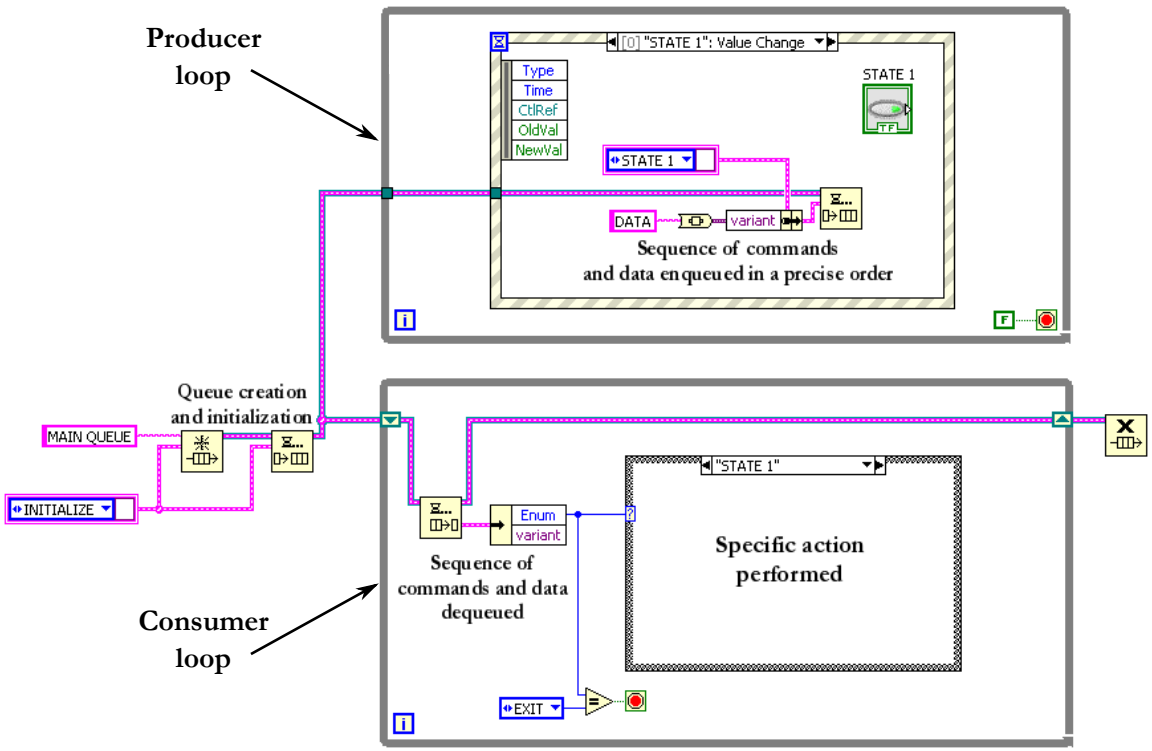

Figure 4.8: LabVIEW block diagram of a simplified Queued-State-Machine architecture. The top section of the diagram is the producer loop, while the bottom section is the consumer loop. The connection between the two loops is achieved via a queue.

possible operation in the consumer loop, an enum is required to uniquely label it. The entire collection of enums form a set, which is available to both the producer and the consumer loops. When an external signal is sent to the producer loop, a particular event case is selected, one or more commands are generated and "*enqueued*", to be transmitted to the consumer loop. Here, commands are extracted from the queue, "*dequeued*" one by one, and for each the execution of a case is triggered. The particular case executed depends on the values of the enums selected. In addition, the queue can be composed of elements other than enums. These can be enqueued by injection and enqueueing in the producer loop and be accessed by dequeueing them in the consumer loop. In this way data other than enums can be sent and received, permitting communication between the producer loop and the consumer loop.

There are several advantages of using a QSM architecture in a control and data acquisition program of this kind. These include (i) the control that can be exerted over the speed of operation the separate parts of the program. This is important because the producer loop is typically much faster

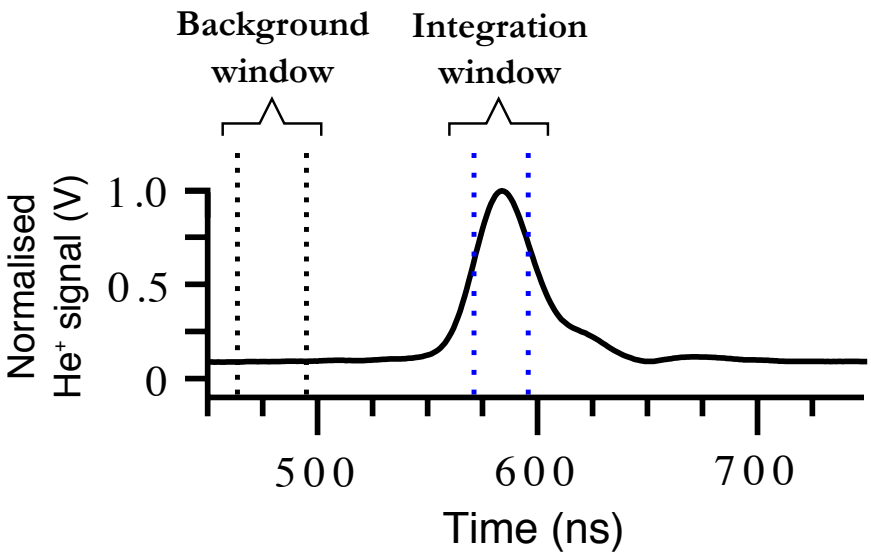

Figure 4.9: Measured He^+ time-of-flight signal to the MCP detector following pulsed electric field ionisation of a sample of Rydberg atoms. The background and signal time windows used in the signal integration procedure implemented in the LabVIEW data acquisition programme are indicated.

than the consumer loop; (ii) the possibility to program the execution of a set of tasks, rather than trigger each command individually. This leads to the efficient implementation of repetitive actions (e.g., reading, writing, saving and refreshing data); and (iii) its modular structure, which makes it possible to add further actions to the producer loop and further executable tasks to the consumer loop, without implementing major modifications to the general structure of the preexisting software.

This LabVIEW application allowed data to be recorded while a wide range of experimental parameters were adjusted over preset ranges and in preselected intervals. In each case, the raw data corresponded to one, or a set of, oscilloscope traces. An example of one of these traces, representing a time-of-flight distribution of He^+ ions after pulsed electric field ionisation of a sample of helium Rydberg atoms is displayed in Figure 4.9. Within the application, this raw data could be directly saved to disk. However, it could also be integrated and used in the measurement of a laser photoexcitation spectrum, microwave spectrum, or neutral helium Rydberg atom time-of-flight distribution. To perform this integration of the signal, two time windows were set within the application. The first represented the time range over which the signal was averaged to determine the background level (see Figure 4.9 “Background window”). After subtracting this background from the recorded oscilloscope trace, the signal within the second time window was integrated (see Figure 4.9 “Integrated window”). The resulting integrated ion signal corresponded to the signal from the Rydberg

atoms for one particular measurement point. In recording a photo-excitation spectrum or time-of-flight measurement, for each frequency or time-flight one such point was recorded. These were accumulated to form the final measured spectrum.

Chapter 5

Guiding Rydberg atoms above electrical transmission-lines

Recent experiments directed toward the implementation of hybrid approaches to quantum information processing have seen gas-phase atoms in highly excited Rydberg states coherently coupled to microwave fields in the vicinity of chip-based coplanar microwave transmission-lines. In these experiments the decoherence and dephasing of the atom-field interaction arose as a result of the large spatial extension ($\sim$ 1 mm) of the Rydberg atom cloud and its motion in stray electric fields close to the chip surfaces.

To increase coherence times and reduce dephasing it is therefore important to develop methods by which to precisely locate the atoms above the surfaces and ultimately also control their longitudinal motion. In this chapter an electrostatic guide for Rydberg atoms and molecules, the design of which is based on that of a coplanar electrical transmission-line, is described. The scientific content of this chapter has been published in

- P. Lancuba and S. D. Hogan, ”Guiding Rydberg atoms above surface-based transmission lines”, Phys. Rev. A, 88, 043427 (2013),

but the text from this article has been adapted here to fit within the context of this thesis.

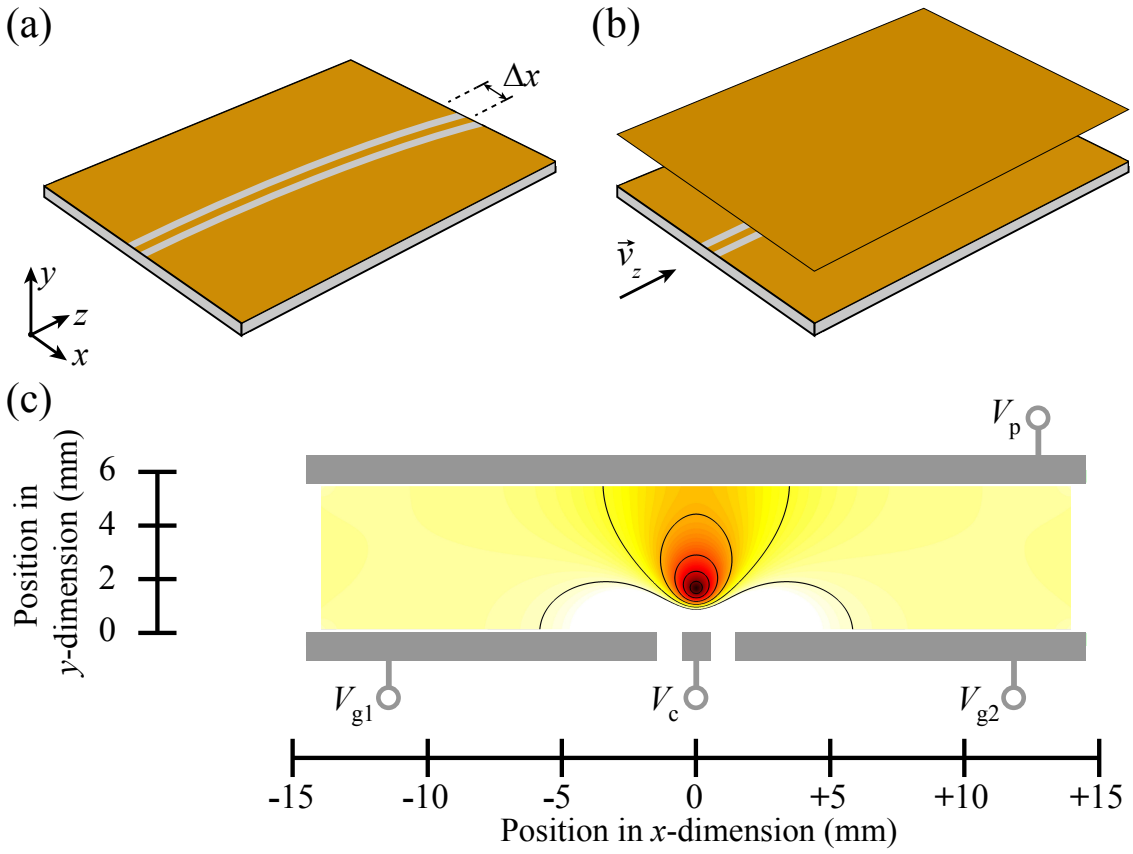

Figure 5.1: (a) Curved surface-based electrical transmission line. (b) Geometry in which a metallic plate is placed above the surface of the transmission line to permit the generation of an electric field distribution appropriate for guiding atoms in high Rydberg states. (c) Electric field distribution in the *xy*-plane in the region between the transmission line and metallic plate depicted in (b). The electric field distribution corresponds to that generated when $V_p = V_c = -10$ V, and $V_{g1} = V_{g2} = 0$ V. Contours of equal electric field strength are displayed in increments of 5 V/cm starting at 5 V/cm.

5.1 Design of the transmission-line guide

The electrical transmission-line guides which have been developed to control the transverse motion of beams of helium Rydberg atoms are composed of a two-dimensional, surface-based electrical transmission-line above which a plane metal electrode is placed parallel to the surface. A schematic diagram of such a surface-based, co-planar electrical transmission line is displayed in Figure 5.1(a).

By positioning a parallel plane metal plate above the surface of the transmission line, Figure 5.1(b), a quadrupole electric field minimum can be generated above the center conductor. This is achieved by applying equal, non-zero, electric potentials to the center conductor, V_c, and this

plane electrode, $V_{\rm p}$, while the outer ground planes of the transmission line, $V_{\rm g1}$ and $V_{\rm g2}$, are set to 0 V. The electric field distribution, in the xy-plane, surrounding a surface-based transmission line with a center conductor of width 1 mm, which is separated from the outer ground planes on either side by a distance of 1 mm, and a parallel plane electrode located 5.6 mm above the surface in the y-dimension, is depicted in Figure 5.1(c). In the calculation of this electric field distribution $V_{\rm p} = V_{\rm c} = -10$ V, and $V_{\rm g1} = V_{\rm g2} = 0$ V. In this figure, contours of equal electric field strength are displayed in increments of 5 V/cm beginning at 5 V/cm. The design of this guide, although not identical, has some similarities to electrostatic guides developed by Xia el al [107] for velocity selection of beams of polar molecules, in which a conducting wire is positioned between a pair of parallel plate electrodes.

The electric field distribution displayed in Figure 5.1(c) is designed to efficiently guide atoms in low-field-seeking Rydberg-Stark states. As they travel along the guide, atoms in these states continually experience forces directed toward the electric field minimum located 1.7 mm above the surface of the transmission line in the y-dimension. Under conditions corresponding to those in Figure 5.1(c) the guide has a depth in the xz-plane of $E/e = 0.36$ meV (or $E/k_{\rm B} = 4$ K, where $k_{\rm B}$ is the Boltzmann constant), for the outermost $n = 52,\ k = 51$ Rydberg-Stark states of helium. For applications associated with coupling Rydberg atoms to microwave circuits, it is important to note that equivalent electric field distributions can be generated by applying the non-zero electric potentials of equal strength to the ground planes while the center conductor and the parallel plane electrode are set to 0 V. In addition, the location of the electric field minimum can be adjusted with respect to the position of the center conductor of the transmission line in the x- and y-dimensions by generating potential differences $|V_{\rm g1} - V_{\rm g2}| < 0$ and $|V_{\rm c} - V_{\rm p}| > 0$, respectively.

5.2 Description of the experimental apparatus

To demonstrate the operation of these transmission-line guides for fast beams of helium Rydberg atoms, an experiment was constructed in which the change in the transverse position of the Rydberg atom at the end of the guide could be detected. A schematic diagram of the apparatus used in the experiments described here is presented in Figure 5.2. Upon entering between the pair of metallic electrodes, labelled E1 and E2 in Figure 5.2, metastable helium atoms in a pulsed supersonic beam with a mean longitudinal speed of $\sim$ 1950 m/s (See Chapter 4) were photoexcited from the $2^3{\rm S}_1$

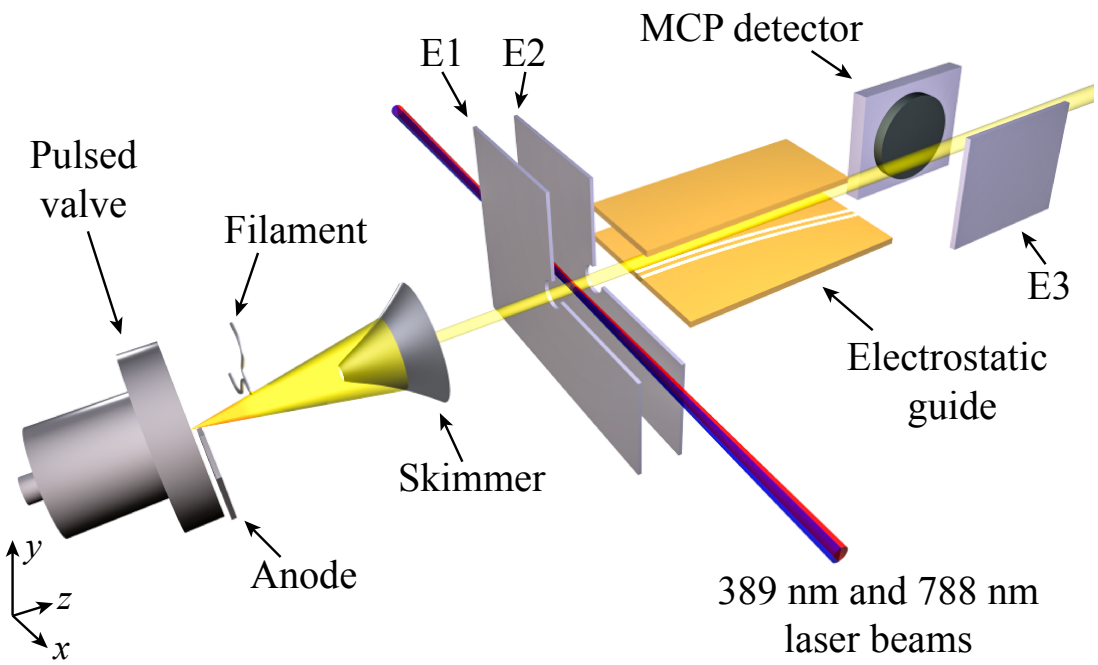

Figure 5.2: Schematic diagram of the experimental apparatus used to demonstrate guiding and deflection of helium Rydberg atoms above a surface-based electrical transmission-line (not to scale). Note that part of the plane metal plate positioned above the transmission line in the y-dimension to form the electrostatic guide has been removed for clarity.

state to Rydberg states with $n = 52$, in a resonant two-photon excitation scheme via the 3p state. In this photoexcitation region, a homogeneous dc electric field of 0.6 V/cm was generated by applying an electric potential of +0.8 V to E1 while E2 was maintained at a potential of 0 V. The magnitude of this electric field was chosen to permit selective excitation of the individual Stark sub-levels at $n = 52$. The relative orientations of the linear polarisation of each laser beam and the local electric field vector at the excitation position are chosen to selectively prepare Rydberg states with azimuthal quantum number $|m| = 1$. In this case the $\ell = 0$ components are absent from the manifold of the Rydberg Stark states leading to predominantly diabatic traversal of all avoided crossings in electric fields beyond the Inglis-Teller limit.

Following photoexcitation, the beams of helium Rydberg atoms travel through a 3 mm diameter aperture in the center of E2, and toward the part of the apparatus containing the surface-based transmission-line guide. In the experiments performed two types of curved transmission lines were used to generate electric field distributions to guide and deflect Rydberg atoms in low-field-seeking states away from their initial axis of propagation and into the positive x-dimension. In each case, the

structures of the guides were 90 mm long in the z-dimension. The curvature of each transmission line was described by a unique quadratic function in the xz-plane with a displacement Δx from the propagation axis of the unguided atomic beam at the end of the guide [see Figure 5.1(a)].

After passing through the electrostatic guide the helium Rydberg atoms entered the part of the apparatus in front of the MCP detector where they were ionised by a pulsed electric field generated by applying a pulsed potential of +800 V to the metal electrode labelled E3 in Figure 5.2. The resulting He^+ ions were then accelerated in the negative x-direction toward the MCP detector. In this configuration, information on the position of the Rydberg atoms in the x-dimension at the time of pulsed electric field ionisation could be obtained from the time of flight of the He^+ ions to the MCP detector. Atoms located close to the MCP detector at the time of ionisation gave rise to an ion signal at early times after the ionising electric field was switched on, while the ion signal corresponding to atoms located further from the MCP arrived at later times.

5.3 Experimental results

The operation of two transmission-line guides, one with displacement $\Delta x = 2.5$ mm, and the other with $\Delta x = 5.0$ mm was studied by observing changes in the time of flight of the He^+ ions to the MCP detector when equal electric potentials, $V_p = V_c$, of increasing magnitude were applied to the center conductor of the transmission-line and the upper metal plate. The He^+ time-of-flight signal recorded following photoexcitation to the $n = 52$, $k = 40$ Rydberg-Stark state, with an electric dipole moment of 7930 D, with the $\Delta x = 2.5$ mm guide switched off, i.e., $V_p = V_c = 0$ V, is displayed in Figure 5.3. The flight-time associated with the peak of the signal displayed in Figure 5.3(a) is denoted τ_1 (dotted black vertical line) and arrives 585 ns after the application of the ionisation pulse.

As the electric potential $V_p = V_c$ is adjusted from -8 V to -32 V the Rydberg atoms are guided and deflected away from their initial axis of propagation and into the positive x-dimension. The He^+ ions corresponding to the guided atoms therefore arrive later at the MCP detector as can be seen in Figure 5.3(b-e). For this $\Delta x = 2.5$ mm guide, the change in the flight time associated with the peak of the He^+ ion signal when the guide was on is $\tau_2 - \tau_1 = 30$ ns. Inserting the second guide for which $\Delta x = 5.0$ mm in the same apparatus under the same experimental conditions results in a further delay in the arrival time of the He^+ ion signal as can be seen in Figure 5.3(f). By increasing Δx by a factor of 2 for this measurement, the shift in the time-of-flight associated with the peak of

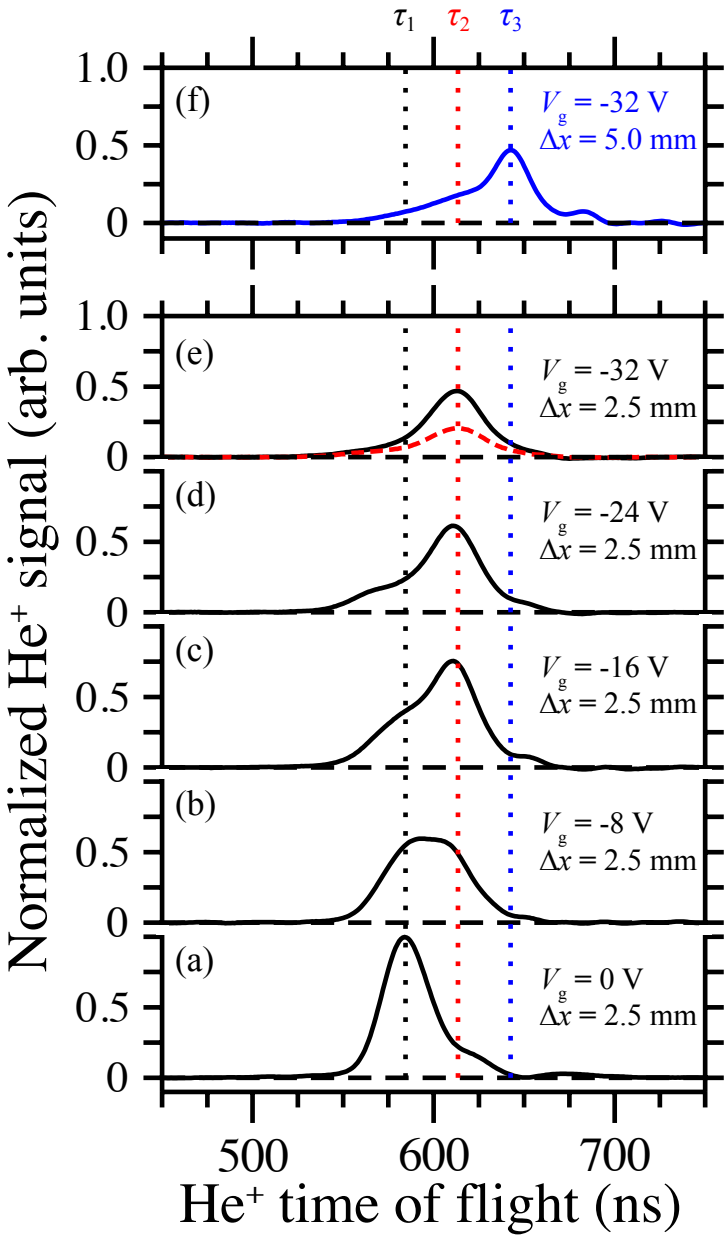

Figure 5.3: Time-of-flight distributions of He^+ ions detected after pulsed electric field ionisation of helium Rydberg atoms initially excited to states with electric dipole moments of 7930 D that were guided using curved transmission line guides with displacements of (a-e) $\Delta x = 2.5$ mm, and (f) $\Delta x = 5.0$ mm. The origin of the horizontal axis represents the time at which the ionisation pulse was applied. The dotted vertical lines indicate the times at which the maxima of the ion signals corresponding to the unguided atoms (τ_1 black), and those guided using the $\Delta x = 2.5$ mm (τ_2 red), and $\Delta x = 5.0$ mm (τ_3 blue) transmission-line guides were detected. The red dashed time-of-flight distribution in (e) was recorded with $V_p = V_c = +32$V.

the He^+ ion signal (dotted red vertical line) for this second guide is also increased by a factor of two from that in Figure 5.3(e), i.e.,$\tau_3 - \tau_1 = 2(\tau_2 - \tau_1) = 60$ ns. The increase in the signal in the wings of this time-of-flight distribution, with respect to that displayed in Figure 5.3(e), indicates a reduction in the acceptance of the guide for the particular states prepared in the experiments, and possible losses arising from the adiabatic traversal of avoided crossings in the Stark map.

For each of the measurements presented in Figure 5.3, negative electrical potentials were applied to the center conductor and upper plate electrodes of the guide. This ensured that the excited Rydberg atoms did not pass through regions of zero electric field strength as they travelled from their position of photoexcitation to the guide. The effect of passing through a zero-field region can however be seen in Figure 5.3(e) where the dashed, red time-of-flight distribution displayed was recorded with $V_p = V_c = +32$V. Under these conditions the atoms pass through a region of zero electric field strength as they travel through electrode E2 on their trajectories toward the guide. The absence of a quantisation axis in this zero-field region leads to a scrambling of the Stark states and a resulting loss of population from the initially prepared low-field-seeking states. The reduction in the intensity of the guided He^+ ion signal by approximately a factor of 0.5 when $V_p = V_c = +32$V, compared to the case when $V_p = V_c = -32$V, highlights the importance of maintaining a non-zero electric field quantisation axis throughout these experiments.

More detailed information on the electric dipole acceptance of the transmission-line guides can be obtained by studying the magnitude of the signal associated with the guided atoms as the frequency of the infrared laser is scanned over the $n = 52$ Rydberg-Stark manifold. The results of such measurements, performed using the $\Delta x = 5.0$ mm guide, can be seen in Figure 5.4.

For reference a photoexcitation spectrum of the $|m| = 1$, hydrogenic Stark states of He, recorded in an electric field of 0.6 V/cm with $V_p = V_c = 0$V is displayed in Figure 5.4(i-c). To record spectra in which only the states with electric dipole moments appropriate for efficient guiding can be identified only the signal associated with guided atoms was detected. This was achieved by setting a time window within the He^+ time-of-flight distribution, between the time τ_3 and τ_3 + 30 ns [see Figure 5.3(f)], within which the ion signal was integrated. The resulting integrated signal was then recorded as the frequency of the infrared laser was scanned. To further improve the separation between the signals from the guided and unguided atoms, two circular metallic slits with diameters of 3 mm were placed after the guide before the detection region. One of these slits was centered on

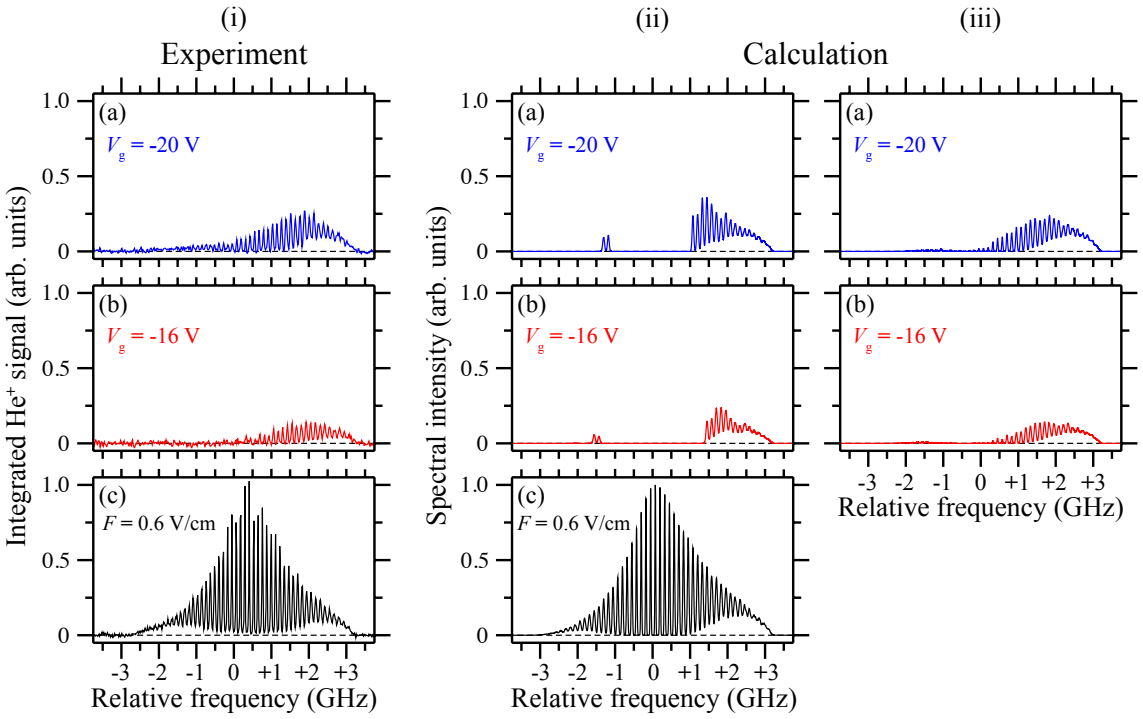

Figure 5.4: (i) Experimentally recorded, and (ii,iii) calculated spectra of the $n = 52$, $|m| = 1$ triplet Rydberg-Stark states of helium. In each case (c) is a photo-excitation spectrum in an electric field of 0.6 V/cm, while (b) and (a) are spectra indicating the states in which atoms are efficiently guided when $V_p = V_c = -16$V and $V_p = V_c = -20$V, respectively. The calculated spectra in (ii-a) and (ii-b) do not account for effects of state changing arising from the interaction of the atoms with the surrounding blackbody radiation field and collisions between the Rydberg atoms in the guide, while those in (iii-a) and (iii-b) incorporate a simple Monte Carlo model that accounts for these effects.

the axis of propagation of the unguided atomic beam while the other, displaced from this axis in the x-dimension, was centered on the end of the $\Delta x = 5.0$ mm guide. The narrow integration window, combined with the spatial separation provided by the circular slits permitted only guided atoms to be detected as can be seen by comparing the signal intensity within this time range in Figure 5.3(a) and Figure 5.3(f). The photoexcitation spectrum recorded under these conditions with $V_p = V_c = -16$V is displayed in Figure 5.4(i-b). As expected, only atoms in the outer low-field-seeking states, with the largest electric dipole moments, on the high energy side of the $n = 52$ Stark manifold appear in this spectrum. When the electric potential applied to the guide was increased to $V_p = V_c = -20$V the electric field gradients of the guide also increased and states closer to the center of the Stark manifold, with smaller electric dipole moments, were also guided as can be seen in Figure 5.4(i-a).

The operation of the electrostatic guide can be further characterised by comparison of the experimental spectra in Figure 5.4(i) with calculated spectra that incorporate the results of numerical simulations of the trajectories of Rydberg atoms through it (particle trajectory simulations of this kind are discussed in detail in Chapter 7). The results of these calculations are presented in Figure 5.4(ii) and Figure 5.4(iii). In each of these calculated spectra, the spectral intensities of the Rydberg-Stark states at photo-excitation [see Figure 5.4(ii-c)] were determined from the $\ell = 2$ components of the eigenvectors associated with each state in the appropriate energy range in Figure 3.4(b) [87]. At the edges of the experimentally recorded spectrum presented in Figure 5.4(i-c) the spectral features associated with transitions to the outer Stark states with the largest electric dipole moments are broadened giving rise to a non-zero spectral intensity between individual features in these spectral regions. This is an effect of electrical noise [108] and inhomogeneities in the photo-excitation volume and can be crudely accounted for by including an electric field gradient of ~ 0.05 V/cm^2 across the ensemble of excited atoms in the calculations [see Figure 5.4(ii-c)]. By convoluting this calculated spectrum with the guiding efficiency for each Rydberg-Stark state, the spectra presented in Figure 5.4(ii-b) and Figure 5.4(ii-c) were calculated for $V_{\rm p} = V_{\rm c} = -16$V and $V_{\rm p} = V_{\rm c} = -20$V, respectively.

The calculated spectra presented in Figure 5.4(ii) exhibit the same general appearance as those recorded experimentally, i.e., the atoms are seen to be most efficiently guided when initially photoexcited to the outermost low-field-seeking Stark states with the largest electric dipole moments. However, there are two notable features of the calculated spectra which differ from the experimental observations. These are: (i) a sharp cut-off in the spectral intensity of the low-field-seeking states on the high-energy side of the Stark manifold for states with electric dipole moments below 4860 D and 3750 D in Figure 5.4(ii-b) and Figure 5.4(ii-a), respectively; and (ii) the presence in each spectrum of two intensity maxima corresponding to atoms guided in high-field-seeking states. As they travel through the guide, atoms in low-field-seeking Stark states follow trajectories on the outside of the guide where the radial electric field gradient is positive. Since this guiding field gradient approaches zero with increasing distance from the electric field minimum, beams of atoms with a narrow longitudinal velocity distributions will only be efficiently guided if their dipole moments are larger than a particular threshold value. In states with dipole moments below this threshold value, which is dependent upon the electric potentials $V_{\rm p}$ and $V_{\rm c}$, the Rydberg atoms will escape from the

guide leading to a cut-off in the acceptance. This effect can be seen in the experimental data and the results of the calculations. However, the sharp cut-off seen in the calculated spectra is not apparent in the experimental data. In addition, the high-field-seeking states that follow quasi-stable trajectories around the inside of the guide, where the radial electric field gradient is negative, and are present in the calculated spectra are also absent in the experimental data.

In the experimental measurements presented in Figure 5.4(i) the flight-time of the Rydberg atoms from the photo-excitation region to the position where they were detected by pulsed electric field ionisation was 85 μs. During this time the atoms interact with each other and undergo transitions driven by the room temperature blackbody radiation field with which they interact. As has been discussed in Chapter 3 and in the literature previously, with regard to experiments involving electrostatically trapped Rydberg atoms and molecules [69], in the presence of an external electric field blackbody transitions between Rydberg-Stark states occur primarily between states with different values of n, but with similar electric dipole moments. As a result these blackbody transitions do not lead to a significant loss of atoms from the guide, but instead a modification of the Stark-state acceptance.

In the experiments described here the metal plates of the surface-based transmission line and parallel plane electrode form a parallel-plate microwave cavity. This cavity strongly modifies the electromagnetic mode structure in the vicinity of the guide and consequently has a significant effect on the blackbody radiation spectrum with which the Rydberg atoms interact as they travel through the guide. This, combined with the strong dependence of the blackbody transition rates on the magnitude of the electric field experienced by the atoms, makes it difficult to construct a complete numerical model to account for the effects of blackbody transitions on the spectra of the guided Rydberg atoms. However, by implementing a simple hydrogenic Monte Carlo model in which the value of k, which determines the electric dipole moment $\mu_{\rm elec} = (3/2)nkea_0$, changes by ± 1 at a predefined rate, the effects of state changing, arising from collisions between the guided atoms and blackbody transitions, on the calculated spectra displayed in Figure 5.4(ii) can be elucidated. The results of incorporating this simple model, with a $|\Delta k| = 1$ transition rate of 10^7 s^{-1}, into the calculation of the spectra of the guided atoms are presented in Figure 5.4(iii-b) and Figure 5.4(iii-a) for $V_{\rm p} = V_{\rm c} = -16$V and $V_{\rm p} = V_{\rm c} = -20$V, respectively. From these calculated spectra it can be seen that the comparatively small changes in electric dipole moment that result from these transitions

give rise to a broadening of the dipole acceptance of the guide. The sharp cut-off in acceptance which is apparent in Figure 5.4(ii-b) and Figure 5.4(ii-a) is no longer observed and the calculated spectra are closer in appearance to those recorded experimentally. In addition, the narrow range of high-field-seeking states which follow quasi-stable trajectories through the guide appear not to be sufficiently stable to result in efficient guiding if the magnitude of their dipole moments changes during their trajectory through the guide.

It is important to note that the k-changing rate included in the calculation of the spectra in Figure 5.4(iii) does not represent the mean 300 K blackbody depopulation rate of the Rydberg-Stark states in the experiments. This is expected to be close to 10^5 s^{-1}. The state changing rate included in the calculations does not distinguish between effects arising from collisions between the Rydberg atoms in the guide, and effects of blackbody transitions, and does not explicitly account for transitions for which $|\Delta k| > 1$ or transitions between states of the same electric dipole moment but different values of n. To disentangle these processes and to minimise the effects of blackbody radiation in future experiments (i) the central part of the experimental apparatus can be cooled to reduce the blackbody photon occupation numbers at the microwave frequencies to which the Rydberg states are most sensitive (see Chapter 3, section 5), and (ii) the electromagnetic mode structure of the space surrounding the guide can be engineered to modify these blackbody photon occupation numbers from their values in free-space [109]. For electrostatically trapped samples of hydrogen Rydberg atoms, it has been shown that at blackbody temperature close to 10 K, the purity of Rydberg-Stark states with values of n close to 30 is maintained for several hundred microseconds [110]. However, by appropriately engineering the electromagnetic mode structure of the environment in which the atoms are located similar conditions may be achievable at higher temperatures.

5.4 Conclusions

In the experiments described in this chapter, fast beams of helium atoms in high Rydberg states were efficiently guided and deflected in the inhomogeneous electrostatic fields surrounding electrical transmission lines. The effects of non-adiabatic transitions which can occur when the excited Rydberg atoms traverse regions of zero electric field strength were identified and highlight the importance of maintaining an electric field quantisation axis throughout the entire path of the Rydberg atoms in these experiments. By comparing experimentally recorded photoexcitation spectra corre-

sponding to the signal from the guided atoms, with calculations that account for the particle trajectories through the guide and a simple model to treat the effects of blackbody radiation, the important role that collisions and blackbody radiation play when these experiments are performed in a room temperature environment has been demonstrated. The simple geometries of these transmission-line guides makes them very scalable, and the possibility of integrating them into chip-based microwave circuits is expected to see them play an important role in the future in surface-based architectures for manipulating Rydberg atoms and molecules.

Chapter 6

Transmission-line decelerators for atoms in high Rydberg states

The electrode geometry employed in the experiments described in Chapter 5 to efficiently control the transverse motion of fast moving beams of helium Rydberg atoms does not permit direct control over the longitudinal motion of the beam of atoms. However, as described in this chapter, by periodically segmenting the center conductor electrode, and applying appropriate electrical potentials to each of the resulting segments, three-dimensional electric traps can be formed within the device. These traps can then be conveyed above the segmented center conductor of the transmission-line and be exploited to transport, accelerate and decelerate Rydberg atoms confined within them. The scientific content of this chapter has been published in

- P. Lancuba and S. D. Hogan, "Transmission-line decelerators for atoms in high Rydberg states", Phys. Rev. A, 90, 053420 (2014),

but the text from this article has been adapted here to fit within the context of this thesis.

6.1 Introduction

The chip-based Rydberg-Stark decelerator described here, and referred to as a *transmission-line decelerator*, relies upon the continuous motion of a periodic array of electric field minima in the void between a two-dimensional (2D) surface-based arrangement of metallic electrodes, and a parallel plane metal plate [see Figure 6.1(a)]. This decelerator differs from previously developed

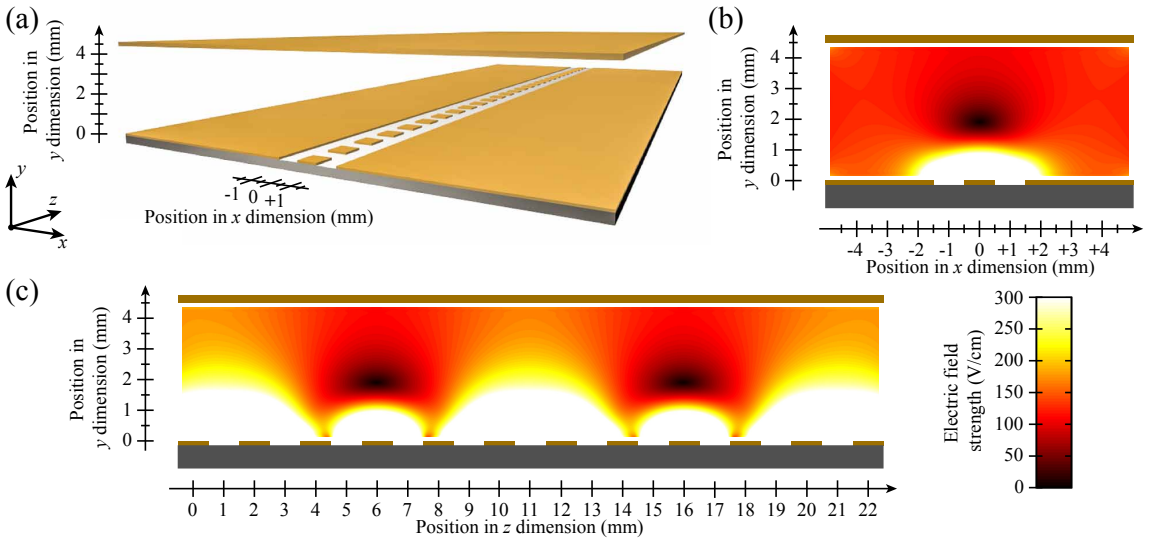

Figure 6.1: (a) Schematic diagram of the transmission-line decelerator. Electric field distributions in (b) the xy-plane, and (c) the zy-plane, for $V_0 = +120$ V, and $V_u = -V_0/2$. The colour scale in the lower right of the figure is common to (b) and (c).

chip-based decelerators for polar ground-state molecules [13, 14, 111] and for Rydberg atoms and molecules [75, 76, 77], and other Stark decelerators that employ continuously moving electric traps [112, 113, 114], in that it is based upon the geometry of the surface-based transmission-line guides described in Chapter 5 [115]. To transform one of these guides into a device suitable for acceleration, or deceleration, of samples traveling in pulsed supersonic beams, the center-conductor has been divided into discrete, individually addressable segments. This geometry permits the generation of three-dimensional electric traps that provide strong confinement of atoms or molecules in all three spatial dimensions throughout the decelerator. This makes the device compatible with the introduction of curvatures in the plane of the 2D electrode array without causing excessive distortion of the fields, and with direct coupling to transmission-line guides [115] and beam-splitters. It also provides a well defined electromagnetic environment in which trapped Rydberg atoms or molecules can be transported and manipulated. This is essential for investigating, and controlling, effects of blackbody radiation.

In the following, the design and operation principles of the transmission-line decelerator are first presented. An overview of the experimental apparatus in which the decelerator was installed to perform the experiments reported here is then provided. Thereafter, the results of experiments in which

beams of helium atoms in Rydberg-Stark states with $n = 52$, and traveling with an initial speeds close to 1950 m/s, were guided at constant speed through the decelerator are presented. Finally, the results of experiments involving the acceleration and deceleration of these atoms to final speeds ranging from 2700 m/s to 1350 m/s are discussed.

6.2 Decelerator design

A schematic diagram of the transmission-line decelerator used in the experiments described in this chapter is displayed in Figure 6.1(a). The design, based upon that of an electrostatic transmission-line guide (Chapter 5 and Ref. [115]), includes a 2D surface-based array of metallic electrodes, and a parallel plane metal plate. The 2D electrode array, located 4.5 mm below the upper plate, is composed of a segmented center-conductor surrounded on either side by two extended ground planes. The insulating gap between the center-conductor and each ground plane is 1 mm wide. The segments of the center-conductor are square, with sides of length 1 mm, and a center-to-center spacing $d_{\mathrm{cc}} = 2$ mm. The electrode array used in the experiments described here was fabricated by chemical etching. Electrical contact was made to the individual decelerator segments via small holes drilled through each to an array of miniature sockets located beneath the substrate. The center conductor of this device contained 45 segments, and the array had a total length of 90 mm in the z-dimension, and a width of 70 mm in the x-dimension.

With equal, non-zero electric potentials applied to one single segment of the center-conductor and the upper plate, while all other electrodes including the ground planes are set to 0 V, a single stationary three-dimensional electric field minimum is generated above this active segment. The resulting electric field distribution is analogous to that generated in two-dimensions in an electrostatic transmission-line guide [115], and forms the basic field distribution around which the decelerator is designed. By applying an appropriate set of potentials to the complete 2D array of decelerator segments and upper plate, a periodic array of similar electric field minima can be generated within the device. The spatial periodicity of this array of electric field minima is dependent upon the number of electric potentials, and therefore decelerator segments, contributing to each. Exploiting larger numbers of segments leads to increasingly harmonic traps with reduced variations in the trap-width with position along the decelerator axis. In the decelerator described here a set of 5 electric potentials are

employed to achieve an appropriate compromise between the total number of unique potentials that must be generated, and any undesirable position dependence of the trap-widths. These 5 potentials are applied to consecutive decelerator segments and repeated periodically along the center conductor. The magnitude of the potential applied to each electrode, labelled with an index $i = 1, 2, \ldots$, can be expressed as

$$V_i = V_0 \cos[-(i-1)\,\phi], \tag{6.1}$$

where V_0 is the amplitude of the potential applied to electrode 1, and $\phi = 2\pi/5$ is the phase-shift from one decelerator segment to the next. With a dc potential, V_u, applied to the upper plate, such that $V_u = -V_0/2$, a set of electric field minima is generated with a spatial periodicity of $5\,d_{cc}$. Electric field distributions calculated using this configuration of potentials, with $V_0 = +120$ V, and a phase shift of $\pi/5$, to position the electric field minima above electrodes $i = 4, 9, \ldots$, are displayed in Figure 6.1(b), and Figure 6.1(c). In these figures, each electric field minimum represents a trap for atoms in low-field-seeking Rydberg-Stark states. Close to each trap minimum the electric field gradient is ~ 650 V/cm^2, and the lowest saddle-point of each trap occurs in the y-dimension at a field strength of ~ 110 V/cm. The maximum usable value of V_0 is set by the onset of electric field ionisation of the trapped Rydberg atoms and is therefore n-dependent. For the Rydberg-Stark states with $n = 52$ used in the experiments reported here, complete diabatic electric field ionisation occurs at ~ 140 V/cm [58]. By operating the decelerator with $V_0 = +120$ V the fields experienced by the atoms as they travel through the decelerator are maintained below this value, limiting particle loss by direct field ionisation.

To convey samples of trapped Rydberg atoms through the decelerator, it is necessary to vary the positions of the electric traps in time. This is achieved by introducing a time-dependence to the potentials in Equation (6.1). To realise a continuous motion of the array of traps in the positive z-dimension, the potential applied to the decelerator electrodes is chosen to oscillate at an angular frequency ω, such that

$$V_i(t) = V_0 \cos[\omega t - (i-1)\,\phi]. \tag{6.2}$$

The speed with which the traps then move, v_{trap}, is directly proportional to ω, and the spatial periodicity of the array, i.e., $v_{trap} = 5 d_{cc}\omega/(2\pi)$.

As the traps move through the decelerator in the positive z-dimension, their proportions change

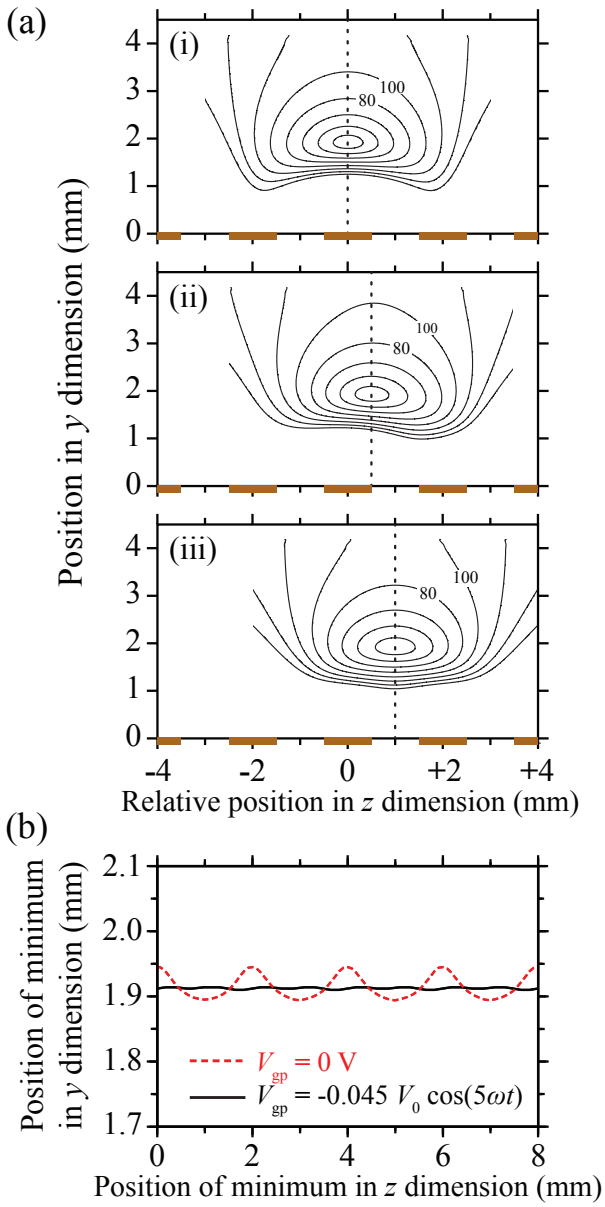

Figure 6.2: (a) Electric field distributions in the zy-plane for traps located (i) above a decelerator segment, (ii) one quarter of the way between two segments, and (iii) half-way between two segments. In each case contours of equal electric field strength are displayed in increments of 20 V/cm, from 20 V/cm to 160 V/cm, and the positions of the decelerator segments are indicated by the thick bars on the horizontal axis. (b) The dependence of the position of the electric field minimum in the y-dimension upon its location along the decelerator axis when a potential $V_{\rm gp} = 0$ V is applied to the ground planes (dashed red curve), and when the potential $V_{\rm gp} = -0.045 V_0 \cos(5\omega t)$ is applied (continuous black curve).

slightly as they travel from locations directly above a decelerator segment to those between two segments. This can be seen in Figure 6.2(a), where electric field distributions in the zy-plane containing an electric field minimum are displayed at instants in time when a trap is located (i) directly above a decelerator segment, (ii) one quarter of the way between two segments, and (iii) half-way between two segments. When the trap is located directly above a decelerator segment it is deeper than when located half-way between two segments. The resulting breathing motion leads to an oscillation in the full-width-at-half-maximum of the traps of $\sim 10\%$, and consequently a small amount of heating of the trapped atoms. However, if cold samples are confined close to a trap minimum heating effects arising from this breathing motion can be minimised.

When a potential $V_{\mathrm{gp}} = 0$ V is applied to the ground planes of the decelerator, with $V_0 = +120$ V, the positions of the trap minima oscillate in the y-dimension as the traps travel through the decelerator. This oscillatory motion has a peak-to-peak amplitude of $\sim 50\,\mu$m as can be seen in Figure 6.2(b). If not compensated, these oscillations give rise to a non-zero center-of-mass motion of the ensemble of trapped atoms in this dimension. This motion of the electric field minimum can be stabilised through the application of a time-dependent potential, V_{gp}, to the ground planes. For the decelerator described here, the optimal ground-plane potential was found to be one that oscillates in-phase with V_1 at a frequency $\omega_{\mathrm{gp}} = 5\,\omega$, and with an amplitude of $-0.045\,V_0$ such that,

$$V_{\mathrm{gp}}(t) = -0.045\,V_0\cos(5\,\omega t). \tag{6.3}$$

The higher oscillation frequency of this potential, with respect to those applied to the segments of the decelerator center-conductor, arises from the requirement that an equal correction to the position of the traps in the y-dimension is applied every time a trap is located above (between etc ...) a decelerator segment. Therefore the period of the oscillation of V_{gp} must equal the time taken for the traps to travel from one segment to the next, a distance d_{cc}. With this potential applied to the ground planes, the oscillation of the position of the trap minima in the y-dimension is reduced to an amplitude of less than $10\,\mu$m as indicated by the continuous black curve in Figure 6.2(b).

When operated at a constant frequency the transmission-line decelerator can be used to convey trapped atoms at constant speed. To accelerate or decelerate the samples, it is necessary to change the frequency of the oscillating electric potentials in time, introducing a frequency chirp. For a selected initial speed, $v_{\mathrm{trap}}(0)$, and an acceleration, a_{trap}, the required time-dependent oscillation

frequency can be expressed as

$$\omega(t) = \omega(0) + \frac{\pi a_{\rm trap}}{5\,d_{\rm cc}}\,t, \tag{6.4}$$

where $\omega(0) = 2\pi v_{\rm trap}(0)/(5\,d_{\rm cc})$ is the initial angular frequency.

The introduction of a frequency chirp to accelerate, or decelerate, trapped samples leads to a reduction in the effective depth of the traps. This has been discussed previously in the literature in the context of chip-based decelerators for polar ground-state molecules [14], with the consequences most clearly seen in the moving frame-of-reference associated with an individual electric field minimum. In Figure 6.3(a-i), and Figure 6.3(a-ii), the electric field distributions associated with a single trap of the decelerator are displayed in the *zy*- and *xy*-planes containing the electric field minimum. These electric field distributions have been calculated for the case when the trap is located one quarter of the way between two decelerator segments, a position that is close to the most probable location of the traps as they travel through the decelerator, with $V_0 = +120$ V.

For a helium atom in a low-field-seeking Rydberg-Stark state with an electric dipole moment of 6939 D, i.e., the $|n,k\rangle = |52,35\rangle$ state used in the experiments reported here, the corresponding potential energy distributions are displayed in terms of a temperature, i.e., $E/k_{\rm B}$, in Figure 6.3(b-i), and Figure 6.3(b-ii). For atoms in the $|52,35\rangle$ state the traps have a depth of $E/k_{\rm B} \simeq 18$ K ($\simeq 1.55$ meV) when stationary or when moving at constant speed.

In the moving frame of reference associated with an electric field minimum in the decelerator, the effect of the acceleration, $\vec{a}_{\rm trap}$, of the traps can be accounted for through the introduction of a pseudo-potential

$$V_{\rm pseudo} = m\,\vec{a}_{\rm trap}\cdot\vec{s}, \tag{6.5}$$

where m is the mass of an individual atom, and $\vec{s}$ is the displacement from the electric field minimum. In the experiments described here a curved decelerator was employed to reduce effects of collisions of the accelerated, or decelerated, atoms with the surrounding components of the pulsed supersonic beam [69]. The curvature was introduced in the plane of the 2D electrode array. The radius of curvature of ~ 0.81 m that was selected resulted in the exit of the decelerator being displaced by 5 mm in the negative x-dimension with respect to the entrance. In this curved device, acceleration of the trapped particles therefore takes place in two directions. These are: (i) the acceleration tangential to the curvature of the decelerator, $a_{\rm t}$, that is exploited to modify the longitudinal motion

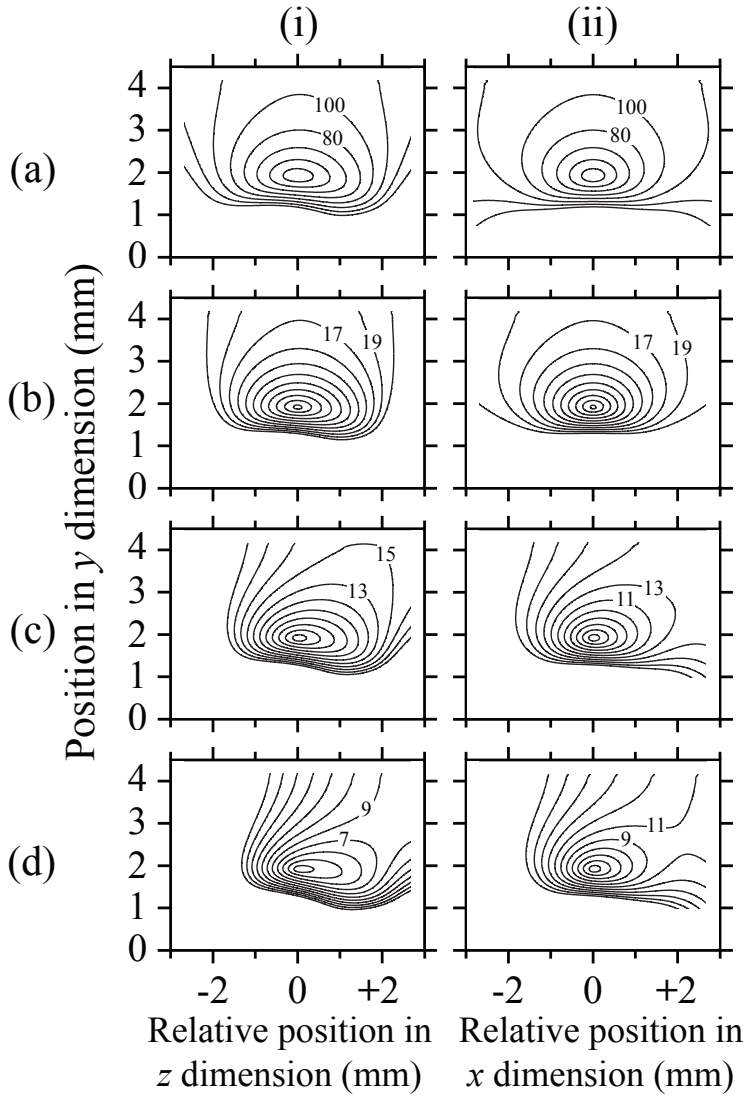

Figure 6.3: (a) Electric field distributions in (i) the *zy*-plane, and (ii) the *xy*-plane, containing an electric field minimum located one quarter of the way between two decelerator segments. Contours of equal electric field strength are displayed in increments of 20 V/cm beginning at 20 V/cm. (b-d) Potential energy distributions in (i) the *zy*-plane, and (ii) the *xy*-plane, experienced by a helium atom in the $|n,k\rangle = |52,35\rangle$ Rydberg-Stark state. In (c-i) and (d-i), a pseudo potential is included to account for tangential accelerations of -0.5×10^7 m/s^2 and -1.15×10^7 m/s^2, respectively. In (c-ii) and (d-ii), the effects of centripetal accelerations of -0.47×10^7 m/s^2 and -0.71×10^7 m/s^2 are included. In the curved decelerator described here, these centripetal accelerations correspond to tangential velocities of 1950 m/s and 2400 m/s, respectively. In (b-d) contour lines of equal potential energy are displayed in terms of a temperature, i.e., E/k_{B}, in increments of 2 K beginning at 1 K.

of the atoms, and (ii) the centripetal acceleration, a_c, associated with the curvature of the decelerator. The effects of these two accelerations can be investigated by studying the shape of the moving traps in the *zy*- and *xy*-planes, respectively.

For a small section of the decelerator, as considered in Figure 6.3, the tangential acceleration acts along the decelerator axis, i.e., in the *z*-dimension. The effect of this acceleration can therefore be accounted for by adding the pseudo potential $V^{t}_{pseudo} = m\,a_t\,\Delta z$ to the potential energy distribution in Figure 6.3(b-i). For helium atoms in the $|n,k\rangle = |52,35\rangle$ Rydberg-Stark state, accelerations on the order of 10^6 m/s^2 begin to noticeably distort the unperturbed potential. The effect of tangential accelerations of $a_t = -0.5\times10^7$ m/s^2, and $a_t = -1.15\times10^7$ m/s^2 can be seen in Figure 6.3(c-i), and Figure 6.3(d-i), respectively. In Figure 6.3(c-i) the negative tangential acceleration (deceleration) leads to a reduction in the effective depth of the trap in the forward direction which becomes more pronounced as the magnitude of the acceleration is increased. When the traps are decelerated with $a_t = -1.15\times10^7$ m/s the saddle point of the trap in the forward direction is further reduced, from $\sim$ 18 K when stationary, to $\sim$ 8 K. For an acceleration of $a_t = -2.2\times10^7$ m/s^2 the trap opens completely in the forward direction, setting the limit on the tangential acceleration at which the decelerator can be operated for atoms in this Rydberg-Stark state.

The centripetal acceleration in a similar length of a curved decelerator acts in the direction perpendicular to the decelerator axis, i.e., in the *x*-dimension in Figure 6.3. In this case the effect of the acceleration can be accounted for by adding the pseudo potential $V^{c}_{pseudo} = m\,a_c\,\Delta x$, to the potential energy distribution in Figure 6.3(b-ii). For a radius of curvature of 0.81 m, centripetal accelerations on the order of 10^6 m/s^2 occur for tangential velocities exceeding 1000 m/s. The effects of centripetal accelerations of $a_c = -0.47\times10^7$ m/s^2, and $a_c = -0.71\times10^7$ m/s^2, which correspond to tangential velocities of 1950 m/s and 2400 m/s, respectively, are displayed in Figure 6.3(c-ii), and Figure 6.3(d-ii). In the experiments reported here the initial longitudinal speed of the beams of He Rydberg atoms was 1950 m/s. Therefore even when the traps of the decelerator are moving at this constant initial speed the centripetal acceleration already plays an important role in setting the effective trap depth of $\sim$ 14 K. For the conditions under which the potential energy distributions in Figure 6.3 were calculated, the maximal tangential velocity at which the decelerator can be operated before the traps open completely in the *x*-dimension is 4360 m/s. This tangential velocity corresponds to a centripetal acceleration of $a_c = -2.35\times10^7$ m/s^2. An overview of the variation of

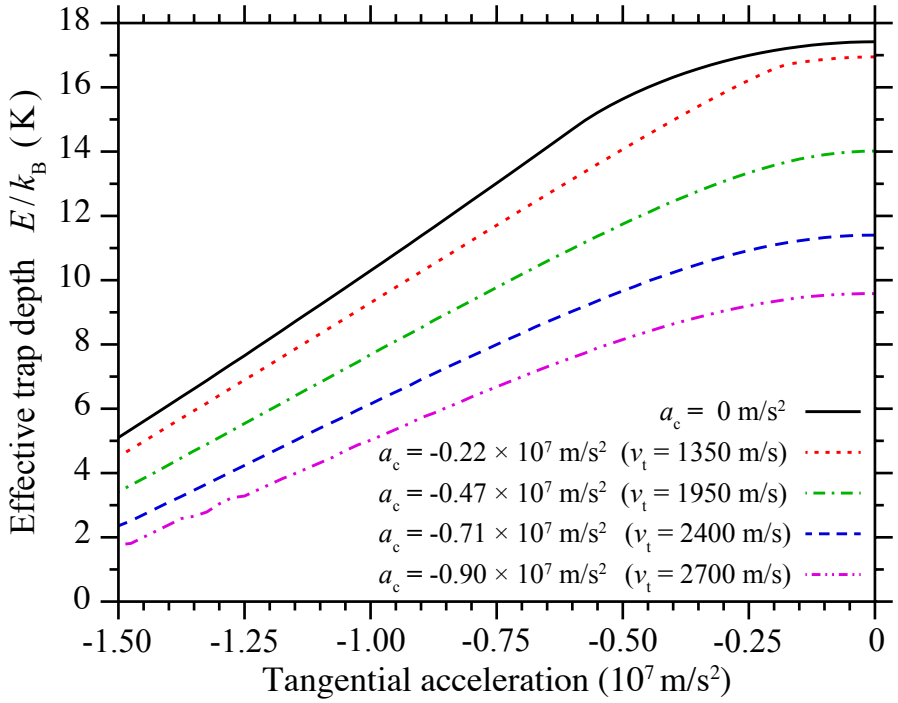

Figure 6.4: Effective depth of the moving decelerator traps for helium atoms in the $|n,k\rangle = |52,35\rangle$ Rydberg-Stark state, when $V_0 = +120$ V. Data for four different centripetal accelerations, $a_c = 0$ m/s^2 ($v_t = 0$ m/s – continuous black curve), $a_c = -0.22 \times 10^7$ m/s^2 ($v_t = 1350$ m/s – dotted red curve), $a_c = -0.47 \times 10^7$ m/s^2 ($v_t = 1950$ m/s – dash-dotted green curve), $a_c = -0.71 \times 10^7$ m/s^2 ($v_t = 2400$ m/s – dashed blue curve), and $a_c = -0.90 \times 10^7$ m/s^2 ($v_t = 2700$ m/s – dash–double-dotted magenta curve), are displayed.

the depth of the moving traps, for a range of tangential velocities and accelerations relevant to the experiments described, is presented in Figure 6.4. In this figure each effective trap depth was calculated using the complete three-dimensional potential energy distribution surrounding one electric field minimum within the decelerator.

6.3 Experimental apparatus

A schematic overview of the apparatus used in the experiments reported here is presented in Figure 6.5. The generation of metastable helium atoms and the Rydberg state photoexcitation scheme are identical to those described in Chapters 4 and 5. The photoexcitation region in the apparatus was

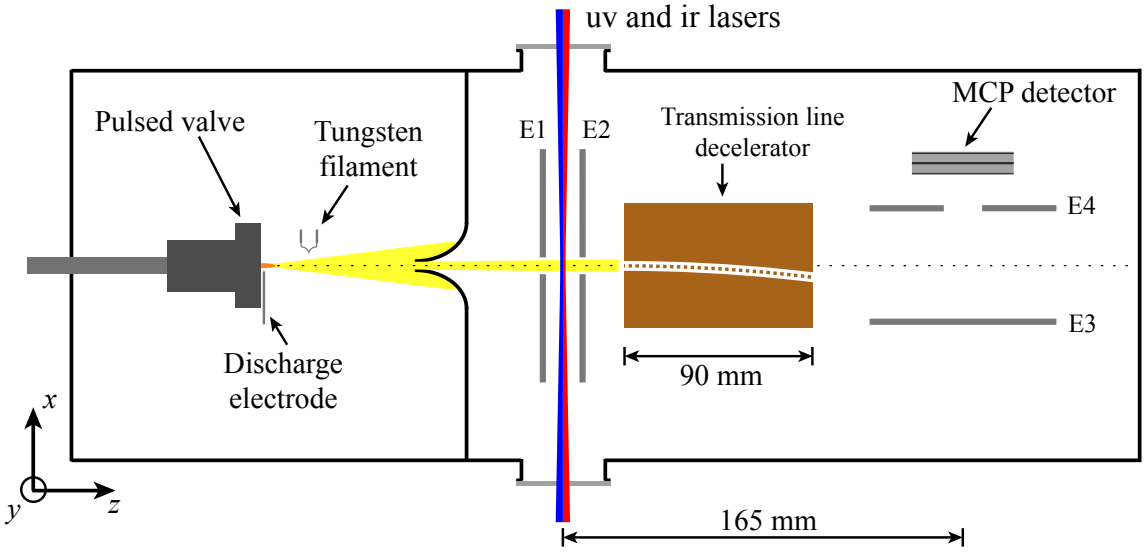

Figure 6.5: Schematic diagram of the experimental apparatus (not to scale). Photoexcitation of the metastable He atoms to selected Rydberg-Stark states is carried out between the electrodes labelled E1 and E2. After traveling through the decelerator the Rydberg atoms are detected by pulsed electric field ionisation upon the application of a potential of +3.5 kV to the electrode labelled E3. The resulting He^+ ions are then accelerated through the aperture in the grounded electrode labelled E4 to an MCP detector.

located between two parallel metallic plates labelled E1 and E2 in Figure 6.5. As the experiments reported here required the excitation of only a small subensemble of the complete atomic beam in a precisely defined time window to selected Rydberg-Stark states, a dc offset potential of +0.30 V was initially applied to E1, while E2 was set to 0 V. This gave rise to a background electric field of ~ 0.23 V/cm at the position where the laser beams crossed the atomic beam. The frequency of the infrared laser was then set to lie resonant with the transition to the low-field-seeking $|n,k\rangle = |52,35\rangle$ Rydberg-Stark state in a larger field of 0.61 V/cm, so that atoms could be excited for selected periods of time by rapidly switching the potential on E1 from +0.30 V to +0.80 V, switching the electric field in the excitation region from its offset value to 0.61 V/cm. In all of the experiments described here excitation was performed for a period of 5 μs in each experimental cycle. The time associated with the middle of this excitation pulse is defined as the photoexcitation time, $t_{\rm ex}$. In the photoexcitation process the linear polarisation of the two laser beams was chosen to permit the predominant excitation of hydrogenic Rydberg-Stark states with azimuthal quantum number $|m_\ell| = 2$.

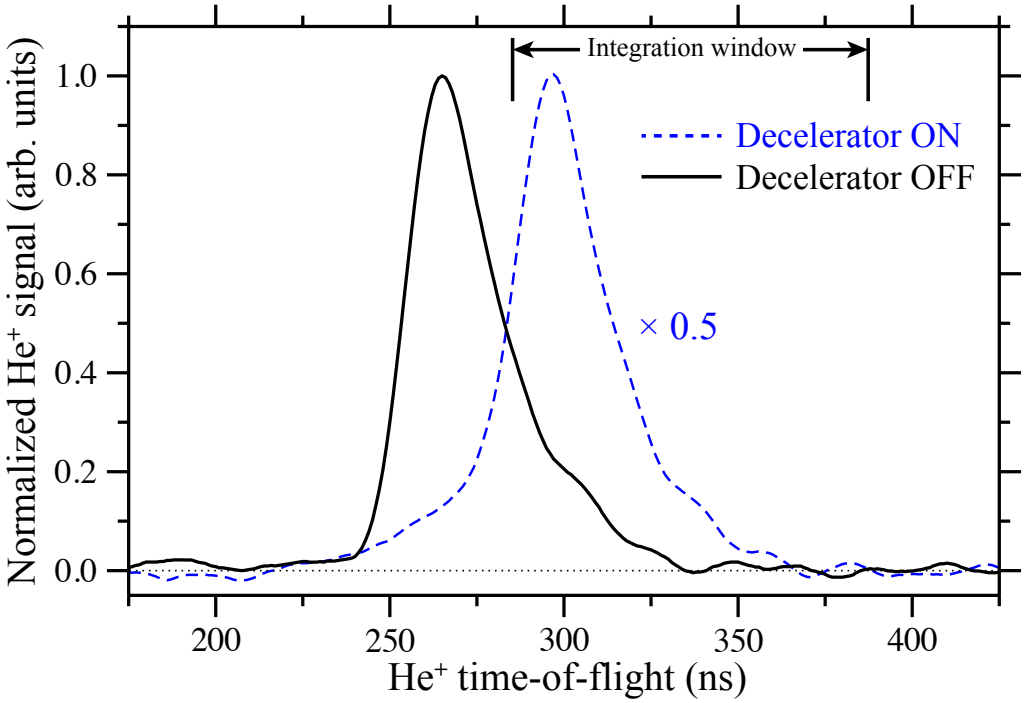

Figure 6.6: He^+ time-of-flight distributions recorded following pulsed electric field ionisation of the helium Rydberg atoms. When the decelerator is operated to guide atoms at a constant speed of 1950 m/s, the maximum of the time-of-flight distribution (dashed blue curve) arrives $\sim$ 25 ns later than that recorded with the decelerator off (continuous black curve). The time-of-flight distribution recorded with the decelerator active has been scaled by a factor of 0.5 (see text for details).

After photoexcitation, the excited Rydberg atoms passed through a small aperture in electrode E2 and entered the transmission-line decelerator within which they were accelerated, decelerated or guided. In the final section of the apparatus, beyond the decelerator, the atoms were detected by pulsed electric field ionisation upon the application of a pulsed potential of +3.5 kV to E3. The He^+ ions produced following ionisation of the excited atoms in the resulting electric field of $\sim$ 550 V/cm were then accelerated toward the MCP detector. The detection geometry employed is similar to that described in Chapter 5 and permitted the position of the Rydberg atoms in the x-dimension, at the time of pulsed electric-field ionisation, to be mapped onto the flight-time of the He^+ ions to the MCP detector.

An example of the mapping of ionisation position onto He^+ flight-time to the MCP in these experiments is presented in Figure 6.6. When the oscillating decelerator potentials are off, but the

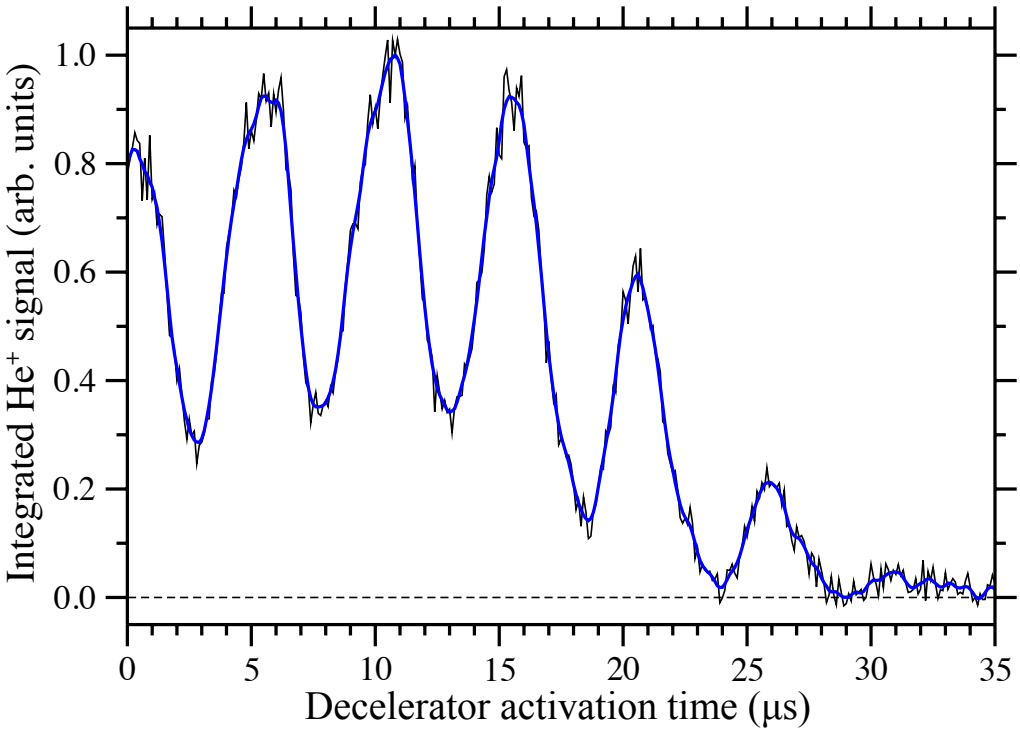

Figure 6.7: Dependence of the integrated He^+ signal on the activation time of the oscillating decelerator potentials, for a helium atom flight-time from the photoexcitation region to the detection region of 82.5 μs, when the decelerator is operated in a guiding mode at a constant speed of 1950 m/s.

non-zero dc potential $V_u = -120/2$ V is applied to the upper plate electrode, the excited Rydberg atoms are ionised at a position in the detection region close to the MCP detector. The resulting He^+ time-of-flight distribution has a maximum at 265 ns. However, if the oscillating decelerator potentials are activated, and set to guide atoms at constant speed over the full length of the decelerator, the curvature of the device leads to a displacement of the Rydberg atoms into the negative x-dimension at the detection position. Because the atoms are then located further from the MCP detector when ionised the He^+ flight-time increases to 290 ns. Accelerated, decelerated and guided atoms can therefore be selectively detected by integrating, and recording, only the delayed component of the time-of-flight distribution encompassed by the vertical bars at the top of Figure 6.6. In the data displayed in this figure the signal recorded with the decelerator active is twice as large as that recorded with the oscillating decelerator potentials off because of the increased blackbody photoionisation, and tunnel ionisation rates in the residual dc electric field of 133 V/cm present in the latter case.

6.4 Results

To demonstrate and characterise the operation of the transmission-line decelerator, experiments have been performed in three modes of operation: (i) guiding at constant speed, (ii) acceleration, and (iii) deceleration. For each type of experiment it was necessary to ensure that the oscillating decelerator potentials were activated at the optimal time to ensure that the 5 μs ($\sim$ 10 mm) long bunches of helium Rydberg atoms prepared in the photoexcitation region were efficiently loaded into a single moving trap. This was achieved by measuring the integrated signal from atoms guided through the curved decelerator at constant speed, as the activation time was varied. This measurement was therefore performed after a fixed Rydberg atom flight-time from the photoexcitation region to the detection region, while recording only the signal in the delayed component of the He^+ time-of-flight distribution (see Figure 6.6), with the results displayed in Figure 6.7. In this figure the decelerator activation time is defined with respect to t_{ex}, the center of the pulsed electric potential applied to E1 for Rydberg state photo-excitation. The oscillating potentials used in recording this data were precalculated to guide atoms close to the center of the unperturbed velocity distribution, traveling at a constant speed of 1950 m/s. The oscillation frequency therefore remained constant throughout the guiding process at $\omega = 2\pi \times 195$ kHz. Since only atoms that were guided away from their initial axis of propagation were detected in this experiment, the signal intensity rose when the atoms were efficiently loaded into one of the moving decelerator traps. As can be seen there are several activation times at which maxima occur in the signal associated with the guided atoms. These maxima correspond to the times at which the bunch of atoms is efficiently loaded into each consecutive moving trap of the decelerator. The temporal periodicity of these maxima corresponds to the time taken for the atoms to travel the 10 mm distance between consecutive traps, i.e., $5d_{cc}/v = 5.1$ μs. When the decelerator is activated at the incorrect time, few atoms are guided and a minimum is observed in the integrated He^+ signal. The minima associated with these out-of-phase activation times do not reach zero intensity at times earlier than 20 μs primarily because a small fraction of the $\sim$ 10 mm long bunch of Rydberg atoms always overlaps with one of the traps at these times when the propagation axis of the atomic beam and the axis of the decelerator coincide. At times greater than 20 μs the atoms have traveled further into the decelerator when it is activated, to positions where the curved center-conductor and atomic beam axes do not overlap. In these cases, the transverse spread of the bunch of atoms is only large enough to result in guiding of a small fraction of atoms near the longi-

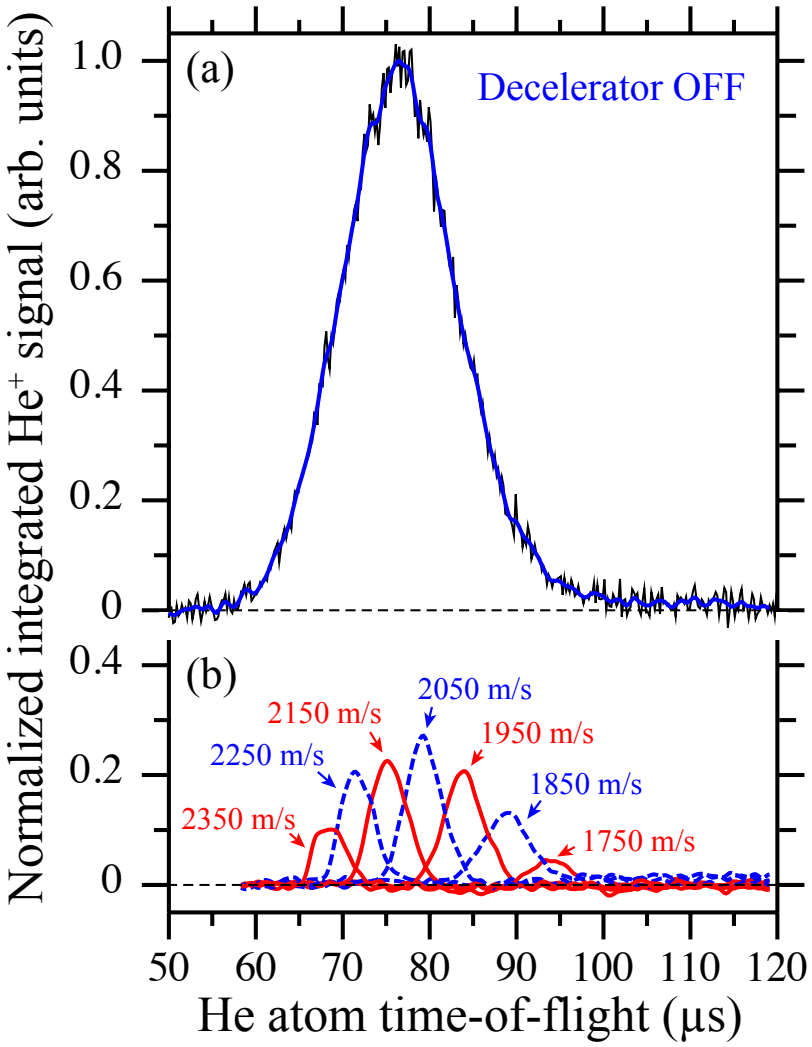

Figure 6.8: (a) Time-of-flight distribution of the unperturbed beam of helium Rydberg atoms recorded with the decelerator off. (b) Helium atom time-of-flight distributions recorded with the decelerator operated to guide atoms at constant speeds ranging from 1750 m/s to 2350 m/s as indicated.

tudinal positions associated with the trap minima. Away from these positions no guiding occurs and the He^+ signal reduces to zero. From the data in Figure 6.7, an activation time of 5.5 μs was chosen for all experiments performed at an initial longitudinal speed $v_0 = 1950$ m/s. This permitted the full length of the decelerator to be used for guiding, acceleration and deceleration.

The ensemble of excited helium Rydberg atoms prepared in the photo-excitation region has a longitudinal velocity distribution with a standard deviation of ~ 140 m/s [see Figure 6.8(a)]. This

corresponds to a translational temperature in the moving frame of reference of $E/k_B \sim 4.7$ K. By adjusting the oscillation frequency of the decelerator potentials, isolated velocity groups within the bunch of excited atoms can therefore be guided through the device. To observe the effects of guiding at a range of speeds, measurements have been made of the time-of-flight of the He Rydberg atoms from the position of photo-excitation to the detection region, a distance of 165 mm. The results of this set of measurements for guiding speeds ranging from 1750 m/s to 2350 m/s, when $V_0 = +120$ V, are displayed in Figure 6.8(b). In recording the data, the appropriate adjustments where made to the decelerator activation time to account for the different flight-time of the atoms from their position of photo-excitation to the first trap of the decelerator at each guiding speed. From these measurements the longitudinal velocity components of the initially prepared beam of helium Rydberg atoms can be clearly identified.

Comparison of the data in Figure 6.8(b) with the time-of-flight distribution of the unperturbed atomic beam, Figure 6.8(a), indicates that when guiding at low speeds (1750 m/s) a large fraction, ~ 0.8, of the excited atoms are efficiently guided through the decelerator. However, close to the maximum of the unperturbed time-of-flight distribution, and for speeds approaching 2350 m/s the efficiency with which the atoms are guided is reduced to ~ 0.3. This change in guiding efficiency can be seen more explicitly in Figure 6.9 where individual data points, representing the ratio of the amplitude of each feature in Figure 6.8(b), to the amplitude of the integrated He^+ ion signal in Figure 6.8(a) at the corresponding time-of-flight, are displayed. The reduction in guiding efficiency with increasing tangential velocity is related in part to the reduction in the effective depth of the traveling electric traps in the decelerator with centripetal acceleration. However, as can be seen from the calculated linear dependence of the effective trap depth on the tangential velocity of the traps, also displayed in Figure 6.9, this effect alone does not completely describe the observed changes in guiding efficiency particularly for tangential velocities in the range from 1950 m/s to 2150 m/s. Because the most significant reduction in guiding efficiency is observed for these speeds close to the intensity maximum of the bunch of excited atoms, and the densities of ground state He atoms and atoms in the metastable $1s2s\,^3S_1$ state are approximately constant across the Rydberg atom cloud, the anomalies in the guiding efficiency that can be seen in Figure 6.8 and Figure 6.9 are thought to arise from interactions between the trapped Rydberg atoms as they travel through the decelerator. These interactions may lead to collision-induced non-adiabatic transitions to untrapped states for pairs of

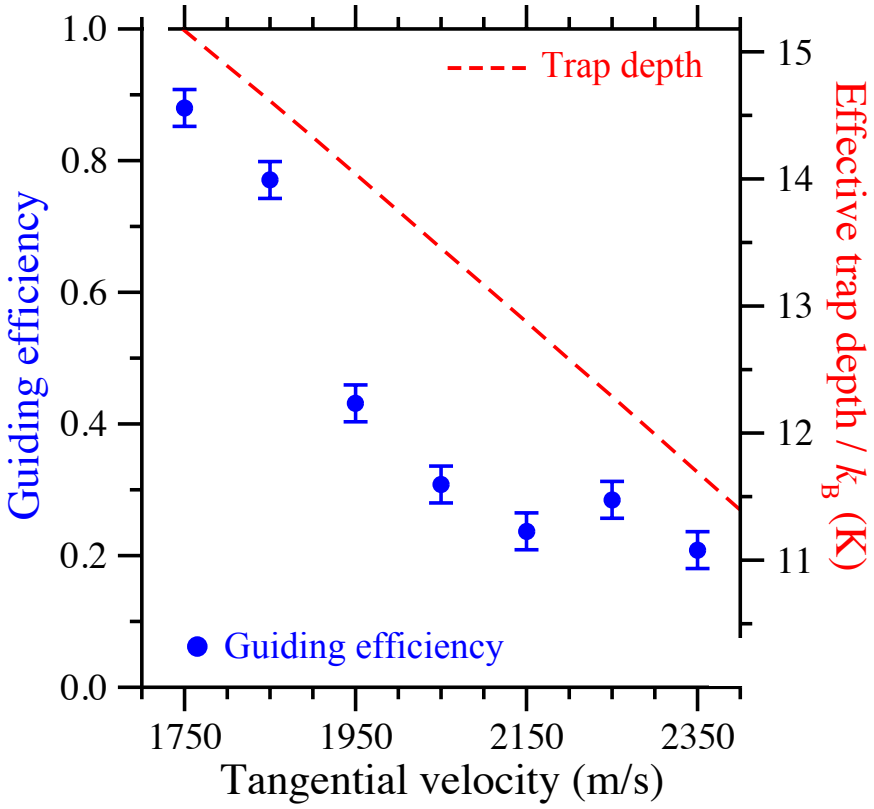

Figure 6.9: Dependence of the experimentally determined efficiency with which atoms were guided at constant speed through the transmission-line decelerator, upon the tangential velocity of the moving traps (blue circles - left vertical axis). The linear dependence of the effective depth of the moving traps upon their tangential velocity (see Section 6.2) is indicated by the dashed red line (right vertical axis).

atoms located close to the electric field minima of the traps, as have been observed previously at lower values of n in three-dimensional electrostatic traps cooled to low temperatures [69], or to state-changing within the highly-degenerate manifold of pair states associated with the hydrogenic Rydberg-Stark states used in the experiments. Detailed investigations of these effects arising during guiding and deceleration of atoms in states with the high values of n employed here, and their disentanglement from possible effects associated with the divergence of the atomic beam in free-flight, will be carried out in a future series of experiments.

To demonstrate acceleration and deceleration of these fast moving beams of helium Rydberg atoms in the transmission-line decelerator, a component of the atomic beam with an initial longitu-

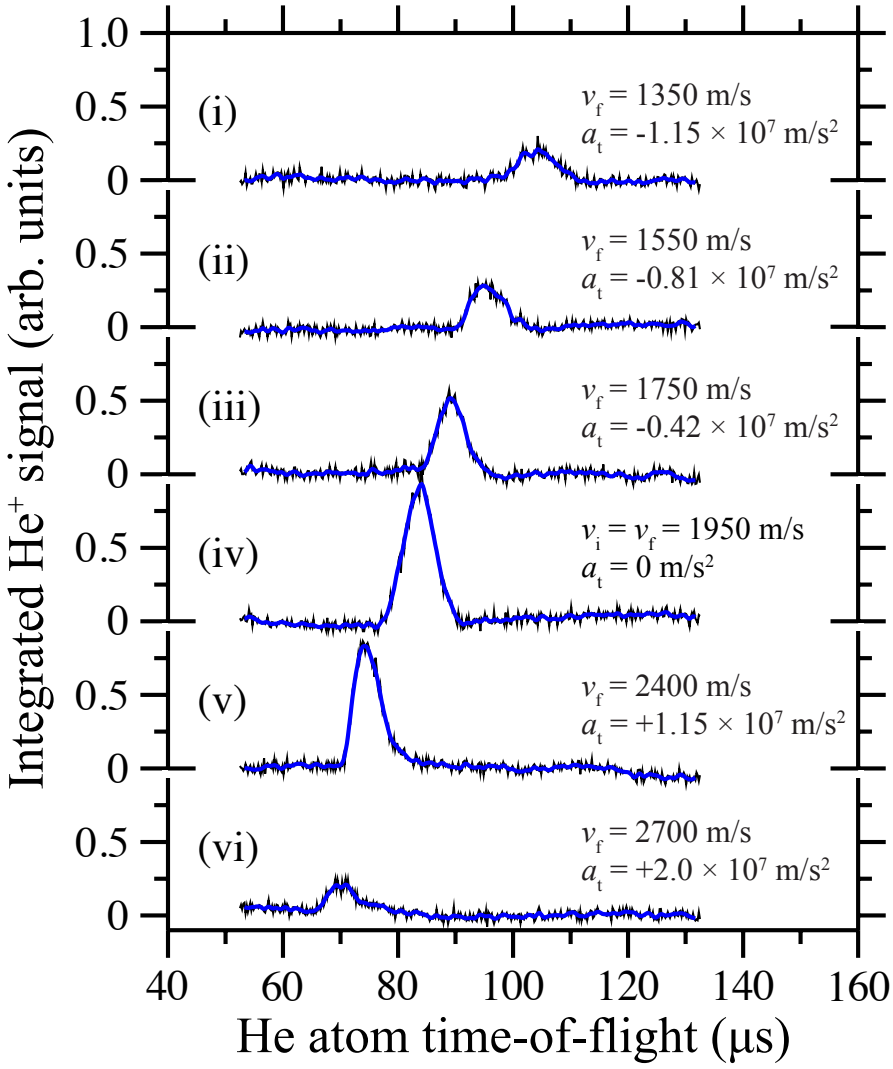

Figure 6.10: Guiding, acceleration and deceleration of helium Rydberg atoms in the transmission-line decelerator. For reference, the time-of-flight distribution of atoms guided at a constant speed of 1950 m/s is included in dataset (iv). Accelerations as high as $a_t = +2.0 \times 10^7$ m/s^2 permit final velocities as high as 2700 m/s to be achieved (vi). While with $a_t = -1.15 \times 10^7$ m/s^2, deceleration to a final velocity of 1350 m/s is demonstrated (i).

dinal speed of 1950 m/s was loaded into a single, moving decelerator trap. The appropriate time dependence [see Equation (6.4)] was then introduced to the frequency of the oscillating decelerator potentials to exert tangential accelerations ranging from $a_t = -1.15 \times 10^7$ m/s^2, to $a_t = +2.0 \times 10^7$ m/s^2 on the trapped atoms. The results of the corresponding set of measurements are presented in Figure 6.10. As with the data recorded for guiding at constant speed, the time-of-flight distributions of

these accelerated and decelerated samples of atoms were recorded by selectively integrating the He^+ signal from the atoms guided away from their initial axis of propagation as they traveled through the decelerator. In these measurements the atoms decelerated to the lowest speeds arrived at the detection region outside the time-of-flight distribution of the undecelerated beam.

For reference, a measurement of the time-of-flight distribution of atoms guided at a constant speed of 1950 m/s is displayed in Figure 6.10(iv). The maximum of this distribution occurs at a flight-time of 84 μs. When a positive frequency chirp is applied to the oscillating decelerator potentials, the atoms confined in the moving traps are accelerated as they travel through the device. Applying an acceleration of $a_t = +1.15 \times 10^7$ m/s^2, for a time of 39 μs, as the trapped atoms travel a distance of 86 mm through the decelerator leads to a final tangential velocity of 2400 m/s [Figure 6.10(v)]. The resulting accelerated beam arrives at the detection region 10 μs earlier than atoms guided at a constant speed of 1950 m/s. Further increasing the acceleration to $a_t = +2.0 \times 10^7$ m/s^2, to accelerate the atoms over the same distance results in a final speed of 2700 m/s, and a further 4 μs reduction in flight-time to the detection region. At these high tangential velocities and accelerations, the effective depth of the moving decelerator traps is less than 0.1 times the depth when guiding at a constant speed of 1950 m/s (see Figure 6.4). Since the bunches of Rydberg atoms fill the moving trap into which they are loaded when the decelerator is activated, the change in the amplitude of the peak of the time-of flight distribution with acceleration is, to a first approximation, expected to scale linearly with trap depth. Therefore the reduction in the amplitude of the accelerated bunch of atoms in Figure 6.10(vi), to ~ 0.2 times that recorded when guiding at constant speed is close to that expected from the calculated data displayed in Figure 6.4.

Applying a negative frequency chirp to the oscillating decelerator potentials leads to deceleration of the trapped atoms and an increase in flight-time from the photoexcitation region to the detection region [Figure 6.10(i-iii)]. Deceleration from an initial speed of 1950 m/s over a distance of 86 mm with $a_t = -0.42 \times 10^7$ m/s^2 ($a_t = -0.81 \times 10^7$ m/s^2), leads to a final tangential velocity of 1750 m/s (1550 m/s) and an arrival time at the detection region 5 μs (12 μs) after the bunch of atoms guided at a constant speed. Further deceleration to a final speed of 1350 m/s over the same distance, with $a_t = -1.15 \times 10^7$ m/s^2, results in an arrival time in the detection region of ~ 104 μs, 20 μs later than atoms guided at 1950 m/s.

When guiding at a constant speed of 1950 m/s the effective trap depth is $E/k_B \simeq 14$ K. How-

ever, when decelerating to 1350 m/s with $a_t = -1.15 \times 10^7$ m/s^2 the mean effective trap depth is $E/k_B \simeq 7$ K. The corresponding experimental data presented in Figure 6.10(iv), and Figure 6.10(i), exhibits a reduction to ~ 0.2 times the intensity of the signal from atoms guided at a constant speed of 1950 m/s, upon deceleration to 1350 m/s. Similar deviations from the efficiencies expected to arise from changes in effective trap depth occur in each of the other sets of data in Figure 6.10. Based upon the data presented in Figure 6.8, the additional loss observed is thought to arise as a result of collisions between the trapped atoms during the deceleration process, and a reduction in the detection efficiency of the decelerated bunches of atoms as they expand during their flight from the exit of the decelerator to the detection region.

6.5 Discussion and Conclusion

The transmission-line decelerator described here is a scalable device which is ideally suited to the high-speed transport, acceleration, deceleration and trapping of gas-phase samples of Rydberg atoms and molecules. Its design gives rise to symmetric electric traps which exhibit approximately equal depths in all three spatial dimensions, distinguishing it from previously developed chip-based decelerators, and permits it to be efficiently coupled to electrostatic transmission-line guides [115]. As has been demonstrated, the array of square, surface-based electrodes that form the segmented center-conductor permit the introduction of curvatures in the plane of the surface without causing excessive distortion to the symmetry of the resulting traps. The presence of the upper plate electrode creates a very well defined electromagnetic environment within the decelerator structure. This is of particular importance for applications, including those in hybrid approaches to quantum information processing, in which inhibition of the absorption of blackbody radiation [109], or spontaneous emission at microwave frequencies [116], is desirable.

The large electric field gradients that can be generated in these transmission-line decelerators permit the controlled removal of significant amounts of kinetic energy from atomic beams over comparatively short distances and timescales. Indeed, the maximal deceleration, from 1950 m/s to 1350 m/s with $a_t = -1.15 \times 10^7$ m/s^2, demonstrated here corresponds to a change in kinetic energy of $\Delta E_{kin}/e = 41$ meV ($\Delta E_{kin}/hc = 330$ cm^{-1}) which, when these experiments were performed constituted the largest removal of kinetic energy from a beam of Rydberg atoms or molecules reported

in the literature.

The possibility of using transmission-line decelerators to remove large amounts of kinetic energy from samples of heavy molecules in high Rydberg states opens up exciting prospects for studies of molecular decay processes of importance in the evolution and chemical reactivity of plasmas in the upper atmosphere of the Earth [117]. As can be seen in the data presented in Figure 6.10, the possibility of generating amplified oscillating electric potentials with frequencies approaching 1 MHz makes these transmission-line decelerators very well suited to the manipulation of atoms and molecules at speeds exceeding 2500 m/s. This will be beneficial for the rapid transport of samples between spatially separated regions of cryogenic experimental apparatus for applications in hybrid quantum information processing, and essential for experiments involving the deceleration and manipulation of beams of light positronium Rydberg atoms [48].

The observed effects of the density of electrically trapped Rydberg atoms on the efficiencies with which they can be manipulated when in states with the high values n employed here, indicate that it will be necessary to carefully consider the role of collisions within ensembles of trapped atoms or molecules in future spectroscopy and scattering experiments where the preparation of guided or decelerated samples in selected internal quantum states is of importance. In hybrid approaches to quantum information processing involving atoms in Rydberg states with values of $n > 50$, and superconducting microwave circuits, these effects may also impose a limit on the particle numbers and densities that can be employed while preserving long Rydberg-state coherence times.

Chapter 7

Rydberg atom trajectories in a curved transmission-line decelerator

To gain further insights into the particle dynamics and phase-space acceptance of the transmission-line decelerator presented in Chapter 6, numerical calculations of Rydberg atom trajectories within the device have been performed. In these calculations, implemented in C++ , initial ensembles of helium Rydberg atoms were generated using Monte Carlo methods. After collimation, these ensembles were then selected for Rydberg excitation as in the experiments. Following this, the trajectories of the atoms in the moving frame of reference associated with a single electric field minimum within the decelerator were calculated, before a transformation back to the laboratory frame of reference was performed to reflect the detection conditions corresponding to those in the experiments. The steps involved in these calculations, and their comparison with the results of the experiments are presented here. An example of the programme codes employed for these calculations is presented in Appendix A.

7.1 Particle generation

The first step in the calculation of Rydberg atom trajectories in the transmission-line decelerator involved the generation of a large number of particles at a position corresponding to that of the pulsed valve in the experiments. To each of the particles generated, an initial position and an initial velocity were assigned. The particle positions in the x-, y- and z-coordinates were selected randomly such

that the particles were uniformly distributed in a 2 mm x 2 mm x 5 mm volume. In addition, to each atom an initial velocity in the x-, y- and z-dimensions was assigned. From the longitudinal velocity distributions of atoms in pulsed supersonic beams (see Chapter 4, Section 3) and the subsequent effects of the skimmer on the transverse velocity distributions, the distribution of relative velocities of the atoms were approximated by Gaussian functions in each dimension. The mean kinetic energies in the moving frame of reference associated with the pulsed supersonic beam were then expressed in terms of a temperature as [79],

$$\langle E_{\mathrm{kin}} \rangle = k_{\mathrm{B}} T. \tag{7.1}$$

The corresponding relative translational temperatures in the x, y and z dimensions were set as input parameters into the calculations. Because of the collimation of the atomic beam by the skimmer, the relative translational temperatures in the x and y-dimension were $\sim$ 100 mK in the experiments. From experimental measurements of the Rydberg atom time-of-flight distributions in the apparatus, the longitudinal velocity distribution of the beams were found to correspond to a relative translational temperature of $\sim$ 5 K. The mean longitudinal speed of the atomic beam, also measured in the experiments, was $\sim$ 1950 m/s.

Following the generation of the atoms in the calculations, they were immediately projected in one computational step to the position of Rydberg photoexcitation. At this position, random sampling weighted by Gaussian and top-hat distributions representing the spatial intensity profiles of the laser beams were implemented. In this process the Gaussian FWHM in the x- and y-dimensions was selected to be 100 μm. While the top-hat distribution in the z-dimension had a length of 6 mm. This length corresponded to the longitudinal extent of the atomic beam which passed through the laser excitation volume within the duration of the electric field pulse applied at photoexcitation. In this process, an representation of the initial phase-space distribution of the excited Rydberg atoms was obtained. Typically, one million excited atoms were generated in each implementation of the calculation to achieve statistically significant results.

7.2 Particle dynamics

Throughout the process of guiding, deceleration and trapping in the decelerator, the ensemble of excited Rydberg atoms are localised close to one single continuously-moving electric-field minimum. Around this electric field minimum, the atoms constantly experience forces arising from the local electric field gradients which influence their trajectories. The dynamics of the bunch of atoms can be most readily determined by choosing a moving frame of reference which coincides with the electric-field minimum of the trap in which to calculate their trajectories. The inhomogeneous electric fields within the transmission-line decelerator were calculated using the software package SIMION [118, 119]. By creating a configuration of electrodes representative of the decelerator described in Chapter 6, and by applying a set of normalised electric potentials to these electrodes, the calculation of the electric fields for a specific instant in time was carried out. The resulting electric field distributions associated with an individual trap of the decelerator are displayed in Figure 7.1.

Figure 7.1(a) contains the electric field distribution in the zy-plane, while Figure 7.1(b) contains the field distribution in the xy-plane when $V_0 = 120$ V. The trap generated in the calculations represents the full three-dimensional electric field distribution as in the experiments. It can be seen in Figure 7.1 that the trap depth differs slightly in each dimension. This is made clearer in the energy profiles in the x, y, and z-dimensions through the electric field minimum displayed in Figure 7.2 for the $|n,k\rangle = |52,35\rangle$ Rydberg-Stark state.

From the potential energy profiles in the z-dimension, it can be seen that the traps exhibit reflection in symmetry through the electric field minimum. For the state considered in calculating the potentials for this figure the lowest saddle point of the trap in this dimension is at $E/k_{\mathrm{B}} \sim 42$ K. In the y-dimension, perpendicular to the surface of the segmented transmission-line the trap exhibits a significant asymmetry at large distances from the electric field minimum. The lowest saddle point in this dimension is adjacent to the upper-plate electrode and lies at ~ 14 K. Although asymmetric at large distances from the electric field minimum, the atoms which are typically localised within 0.5 mm of the minimum do not experience this extreme asymmetry. In this dimension, the high fields, and large trap depths, close to the transmission-line surface arise because of the proximity of 1 mm of the active decelerator electrode, to which a high electrical potential is applied to the ground planes. In the x-dimension, the trap shape is similar to that in the z-dimension. In this dimension, the lowest saddle point of the trap is at $E/k_{\mathrm{B}} \sim 20$ K.

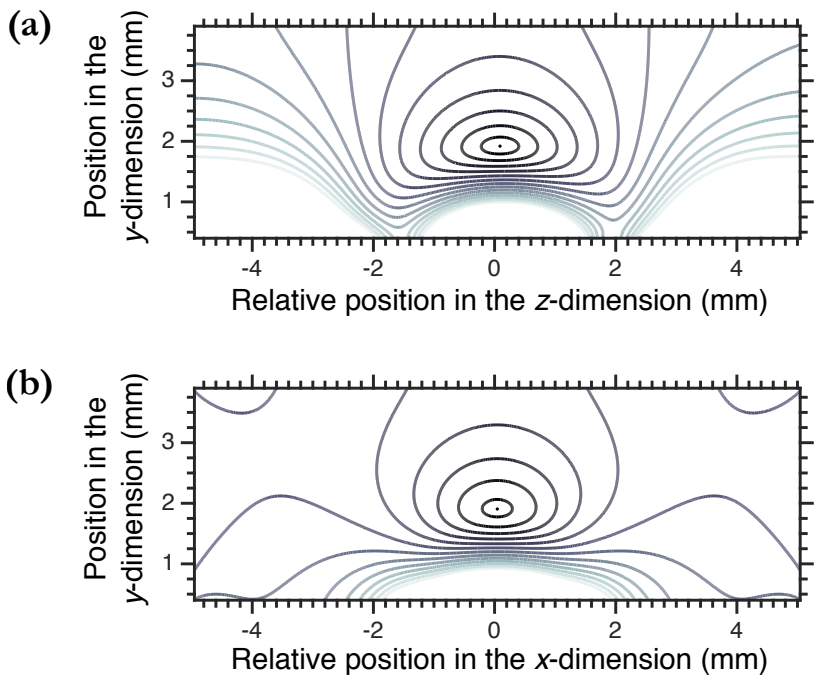

Figure 7.1: Electric field distributions in (a) the *zy*-plane, and (b) the *xy*-plane of a single electric trap in the transmission-line decelerator when $V_0 = 120$ V. The contour lines range from 0 to 300 V/cm in steps of 20 V/cm.

In the moving frame of reference associated with the electric field minimum of a single trap within the decelerator, which is considered in the calculations described here, accelerations and decelerations of the trap applied in the longitudinal direction, or arising from the curvature of the decelerator in the z-dimension are accounted for by introducing the appropriate pseudo-potential,

$$V_{\text{pseudo}} = m\,\vec{a}_{\text{trap}} \cdot \vec{s}, \tag{7.2}$$

where $\vec{s}$ is the displacement from the electric field minimum of the trap, as discussed in Chapter 6. In this reference frame the Rydberg atom trajectories were then calculated numerically by determining the acceleration experienced by each individual atom at discrete time intervals of 20 ns, from the gradients of the combined Stark and pseudo-potentials, i.e.

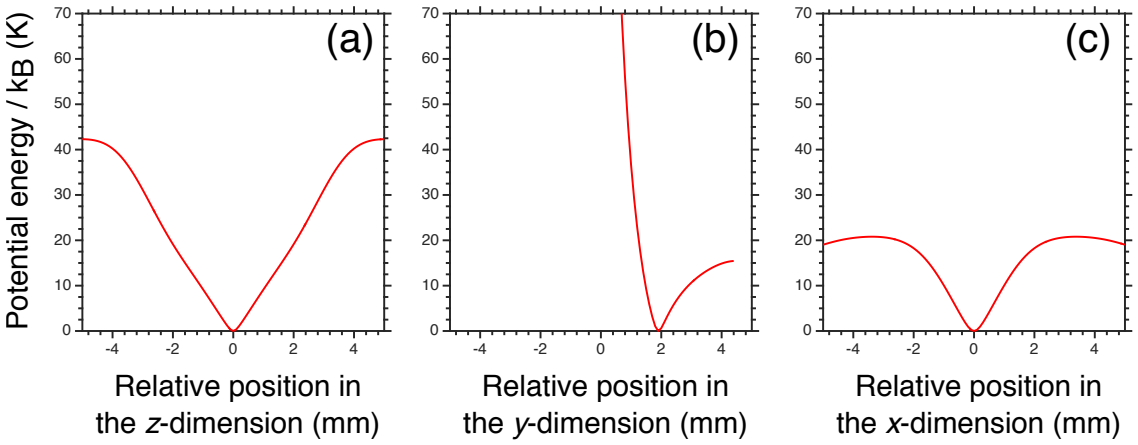

Figure 7.2: Potential energy profiles in the (a) z-, (b) y-, and (c) x-dimensions of a transmission-line decelerator operated with $V_0 = 120$ V for helium atoms in the hydrogenic Rydberg-Stark state $|n,k\rangle = |52,35\rangle$.

$$\vec{a}_{\text{atom}} = \frac{1}{m} \cdot \nabla (V_{\text{Stark}} + V_{\text{pseudo}}). \tag{7.3}$$

The behaviour of the atoms while confined within the moving trap were then determined by solving Newton equations of motion using the leap-frog method [120].

In calculating the individual Rydberg atom trajectories in the electric fields of the traps of the decelerator, data files containing the x, y and z components of the electric field distributions were first imported. Each field distribution imported had a spatial resolution in each dimension of 100 μm. This represented a good compromise between the accuracy of the calculating fields and the computational limits of the SIMION package. As the particle trajectories were calculated, linear interpolation was performed to maximise the accuracy of the calculations. This interpolation was necessary because during their time in the traps the atoms move at velocities up to 200 m/s and therefore can travel distances up to the grid spacing in times on the order of 100 ns. The three-dimensional data structure of the array of electric fields required linear interpolation in each dimension. Thus the field at the position of an atom, F_i is,

$$F_i = F_- + \frac{F_+ - F_-}{d} \Big[q_i - q(F_-) \Big], \tag{7.4}$$

where F_i is the interpolated field at a position q_i of the atom labelled with the index i, and F_- and F_+ are the fields at the beginning and end of a grid unit with spacing $d = 100$ μm, respectively. The linear interpolation function used in this way is continuous, but not differentiable. That is, the first derivative is discontinuous. This implies that there will be inaccuracies in the calculation of the fields in between the grid points and indeed inaccuracies in the calculated electric fields were observed for resolutions below 100 μm. To address this, linear interpolation of the first derivative was also performed to accurately determine the local acceleration of the atom. In this case,

$$G_i = G_- + \frac{G_+ - G_-}{d}\left[q_i - q(F_-)\right], \tag{7.5}$$

where G_i is the interpolated first derivative field at a position q_i, and G_- and G_+ are the electric field gradients between successive grid segments, respectively.

7.3 Boundary conditions and particle detection

When an ensemble of atoms is loaded into one of the travelling traps of the decelerator, in the calculations that determined their trajectories, they are continually monitored to ensure that they remain within the boundaries of the device. These boundaries are defined by the surfaces of the two-dimensional electrode array, and the upper plate electrode in the y-dimension, and distances beyond 5 mm from the electrode field minimum of the trap in the x- and z-dimensions. In addition the strength of the electric field experienced by the atoms at each instant in time is also calculated, and if this field exceeds the ionisation field of the state initially selected at the start of the calculations, the atom is removed from the array of accepted particles. This combination of boundary conditions reflects those experienced by the atoms in the experiments.

Two approaches were employed to model the detection of the atoms in the experiments. The first, corresponding to the detection scheme employed in the work described in Chapter 6, involved first transforming the positions and velocities of each atom from the frame of reference associated with the electric field minimum of the moving decelerator trap to the laboratory-fixed frame of reference. In this new reference frame the atoms were then permitted to exit the decelerator and travel

over the distance from its end to the position of pulsed electric field ionisation. At this location, the boundaries representing the volume from which atoms could be detected after ionisation imposed by the geometry of the ion extraction aperture in front of the MCP detector were used to determine if detection was successful. The resulting set of detected particles and the distributions of their arrival times at the detection position were used to construct calculated time-of-flight distributions.

The second approach to detection of atoms in the calculations was used to model in-situ detection of decelerated or trapped atoms directly from within the decelerator as in the experiments described in Chapter 8. In this case the geometrical boundaries of the detection region, resulting from a circular ion extraction aperture in the upper plate electrode, were set in the moving frame of reference associated with the electric field minimum of the moving trap. In this way, atoms with positions within the range that could be detected at any particular instant in time were counted with the results used to generate the corresponding time-of-flight distribution.

7.4 Phase-space acceptances

To characterise the effects of acceleration and deceleration of atoms trapped in the transmission-line decelerator, the phase-space acceptances of the decelerator were calculated for a range of parameters accessible in the experiments described in Chapter 6 and Chapter 8. These acceptances were determined by randomly generating extended initial phase-space distributions of atoms in the volume from -5 mm to +5 mm of the electric field minimum of a single trap of the decelerator in the z-dimension, from -5 mm to +5 mm of the minimum in the x-dimension and in the full space between the 2D electrode array of the transmission-line and the upper plate electrode in the y-dimension. In each dimension the atoms were assigned random x, y and z velocities ranging from -300 m/s to +300 m/s. From these initial conditions the trajectories of the atoms were calculated. The initial phase-space coordinates of individual atoms were then considered to lie within the acceptance of the decelerator if after a time of 1 ms they remained within the spatial boundaries of the trap, i.e., they remained within ± 5 mm of the electric field minimum in the z-dimension and x-dimension, without being ionised by the electric fields of the device. The results of such calculations for a set of different tangential accelerations are displayed in Figure 7.3.

In Figure 7.3(a) the potential energy profiles of the trap in the direction of propagation of the beam of helium atoms (z-dimension) is displayed for a range of tangential accelerations. In calcu-

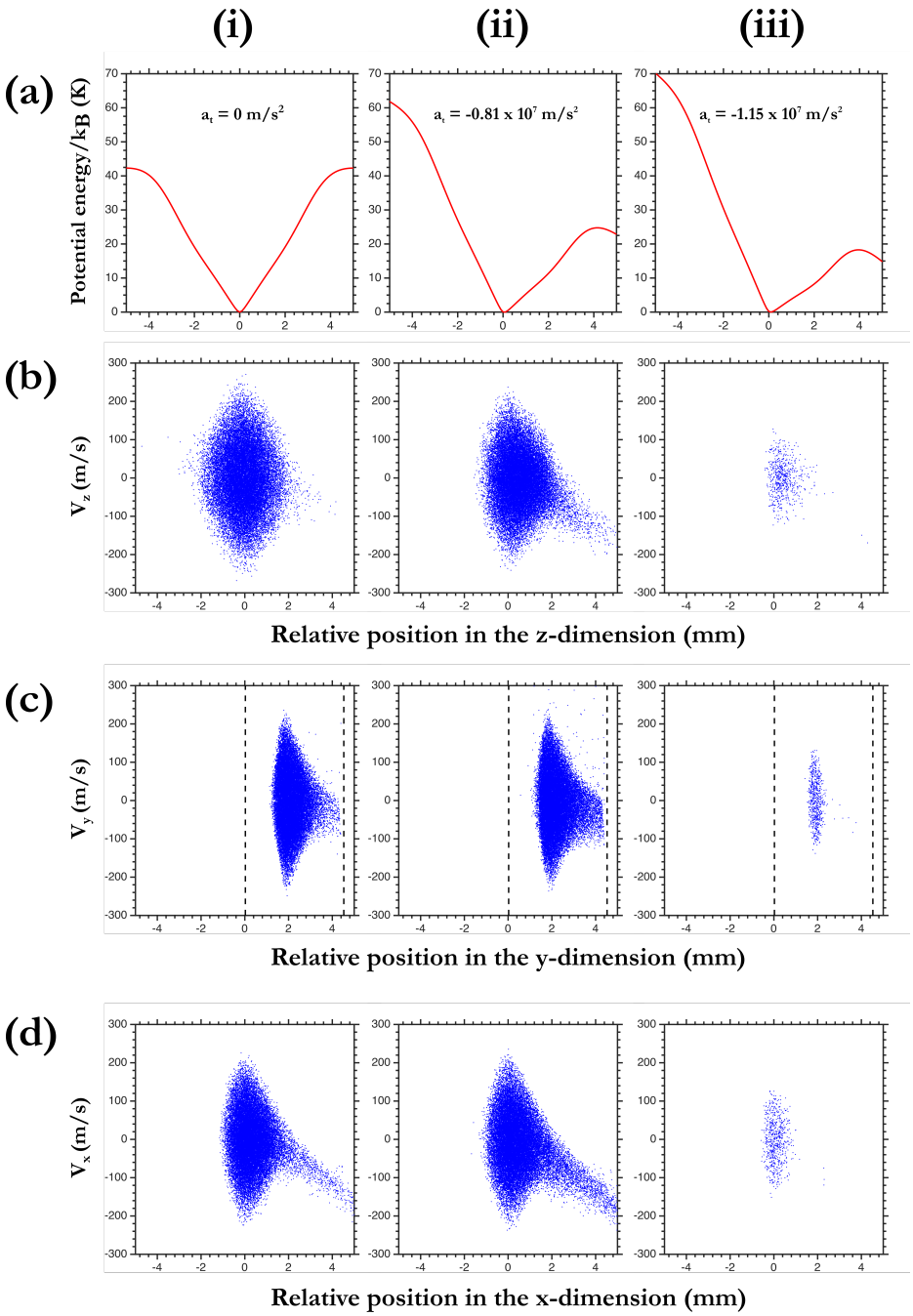

Figure 7.3: (a) Potential energy profiles for selected tangential accelerations, (a-i) $a_t = 0$ m/s^2, (a-ii) $a_t = -0.81$ x 10^7 m/s^2, and (a-iii) $a_t = -1.15$ x 10^7 m/s^2, for helium atoms in Rydberg-Stark states with $|n,k\rangle = |52,35\rangle$. The corresponding phase-space acceptances in (b) the z-dimension, (c) the y-dimension, and (d) the x-dimension are also displayed. The dashed lines in (c) represent the positions of the 2D electrode array ($y = 0$ mm) and the upper plate electrode ($y = 4.5$ mm) of the decelerator.

lating these potentials, atoms in Rydberg-Stark state with $|n,k\rangle = |52,35\rangle$ were considered. When $a_t = 0$ m/s^2, the trap is symmetric in this dimension with its lowest saddle point at $E/k_B \cong 42$ K. In panel (a-ii) the potential energy profile is modified to include a tangential acceleration of $a_t = -0.81$ x 10^7 m/s^2. This is achieved through the introduction of a pseudo potential (see Chapter 6). Under these conditions the lowest saddle point of the trap in this dimension reduces to $E/k_B \cong 25$ K. This distortion of the trap affects the behaviour of the atoms inside it. When the trap decelerates, the centre of mass of the bunch of trapped atoms moves forward into the positive z direction and the atoms are compressed spatially. If the trap is initially filled completely, the lowering of the energy of the saddle point in the positive z direction leads to a loss of trapped atoms. If the acceleration is further increased to $a_t = -1.15$ x 10^7 m/s^2 [Figure 7.3(a-iii)] as expected a further reduction in the trap depth to $E/k_B \cong 20$ K occurs. Under these conditions the trap becomes completely open for $a_t = -2.2$ x 10^7 m/s^2.

In Figure 7.3(b), (c) and (d), the phase-space acceptance of the decelerator in the z, y and x dimensions for each of these accelerations is displayed. When operated to guide atoms at constant speed [Figure 7.3(b-i)], the acceptance of the trap is symmetric with a span of $\sim$4 mm and velocity acceptance from approximately -200 m/s to +200 m/s. The acceptance in this case is consistent with the symmetry of the trap in this dimension. In the y-dimension, the accepted velocities cover a range similar to those in the z-dimension, but the spatial acceptance is asymmetric [see Figure 7.3(c-i)]. This asymmetric phase-space acceptance can be understood by observing the corresponding potential energy distribution in Figure 7.2(b). Because the lowest saddle point of the trap in the y-dimension is lower than in the other dimensions, for lower accelerations atoms will escape from the trap predominantly in the positive y-dimension. The phase-space acceptance in the x-dimension is displayed in Figure 7.3(d). With no tangential acceleration this already indicates that atoms may escape in the positive x-dimension. This is a consequence of the centripetal acceleration resulting from the curvature of the decelerator, and leading to a speed dependent pseudo potential contribution in the x-dimension. This centripetal acceleration is constant when the atoms are guided at constant speed [see Figure 7.3(i)]. However under these conditions the trap is no longer symmetric in the x-dimension and atoms with sufficiently high speeds will escape.

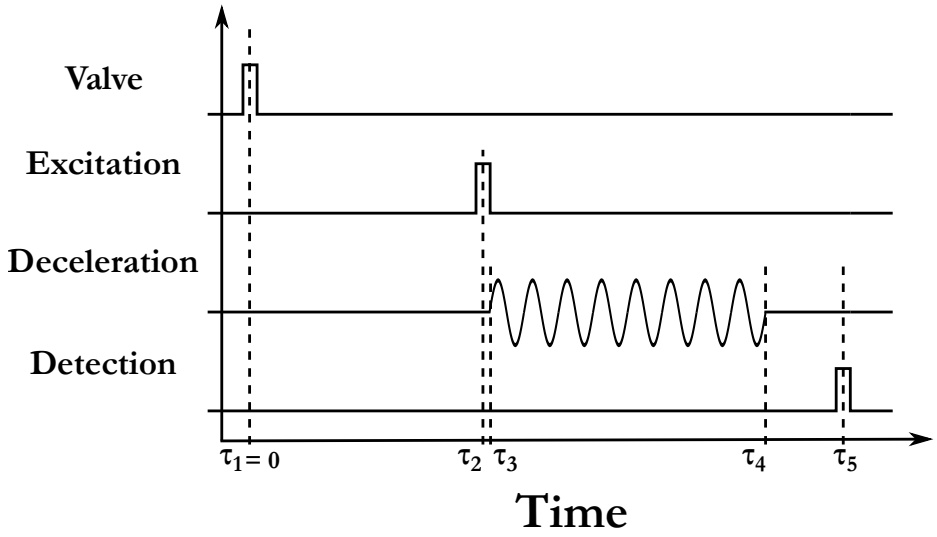

Figure 7.4: Timeline of the particle trajectory calculation. At time τ_1 the initial distribution of the atoms is generated. At the time $\tau_2 = 100$ μs, photo-excitation to Rydberg-Stark states takes place. The transmission-line decelerator is activated at time $\tau_3 = 102.3$ μs and it is subsequently deactivated at time τ_4. At time τ_5, the atoms are analysed for detection by pulsed electric field ionisation.

7.5 Time-of-flight distributions

The phase-acceptances presented in Figure 7.3 show that if the traps of the transmission-line decelerators are accelerated or decelerated, then loss of atoms occurs. This loss is proportional to the acceleration and can be understood in terms of the reduced trap depth. To further investigate how these losses affect the measured time-of-flight distributions of atoms in the experiments presented in Chapter 6, calculations of the time-of-flight distributions were performed including all of the relevant experimental parameters. A timeline displaying the various stages of this calculation is displayed in Figure 7.4.

In the calculation, approximately 10^7 atoms were generated at the valve at time τ_1 in Figure 7.4. This time was set to be time-zero as it marks the beginning of the calculation. The atoms then travelled through the skimmer toward the photo-excitation region where they were randomly sampled in the photoexcitation process. This photoexcitation event took place at time $\tau_2 = 100$ μs, which corresponds to the time required for the centre-of-mass of the ensemble of atoms to reach the photoexcitation region. When 10^6 excited atoms were selected for excitation in this way, the position and velocities of the ensemble were transformed to the frame of reference associated with the electric field minimum of one decelerator trap. The trajectories of the atoms in the trap were then

calculated. After a further time $\tau_4 - \tau_3$ which depended on the acceleration and the final velocity of the trap, the electrical potentials of the decelerator were switched off and the positions and velocities of the atoms were transformed back to the laboratory-fixed frame-of-reference to calculate the final parts of their trajectories between the end of the decelerator and the detection region. In the calculation, detection was carried out when the atoms reached the detection positions, i.e., at the time τ_5 which corresponded to the time of pulsed electric field ionisation. This time depended on their final velocity, after the trap was deactivated.

The total time-of-flight of each atom through the decelerator to the detection position was then used to construct the time-of-flight distribution of the bunch, from excitation to detection. Using this procedure, calculations were performed for a range of accelerations from $a_t = +2.0$ x 10^7 m/s^2 to $a_t = -1.15$ x 10^7 m/s^2 and the results were compared with the time-of-flight distributions recorded in the experiments. This comparison can be seen in Figure 7.5. The relative amplitude of the experimental and calculated time-of-flight distributions were set to be equal when guiding the trapped atoms at constant speed [third panel from bottom of Figure 7.5]. By comparing the results of the calculations with the experimental data, it can be seen that as higher accelerations and decelerations are applied, the amplitude of the time-of-flight signal decreases as expected. This is consistent with the corresponding reduction in the trap depths and the increase in the number of atoms lost during deceleration. However, in general, when $a_t \neq 0$, the results of the calculations show a greater number of detected atoms than the experiments. In order to determine the effects of the acceleration on the capacity of the transmission-line decelerator to trap and transport atoms, and to explain the differences between the experimental results and the calculated time-of-flight distributions, the deceleration efficiency has been extracted and displayed in Figure 7.6.

While the general dependence of the experimental relative deceleration efficiency, and the results of the calculations are consistent, it can be seen from Figure 7.6 that as larger decelerations are applied, the results of the calculations increasingly deviate from the experimental data. Interestingly, in the cases where accelerations were applied the results of the calculations are in good agreement with the experimental data. These discrepancies can be explained in part by considering the effects of collisions on the Rydberg atoms trapped in the moving traps.

In the experiments, although the decelerator is curved to reduce effects of collisions with the trailing components of the atomic beam, there is still some distance (~ 30 mm) over which the traps

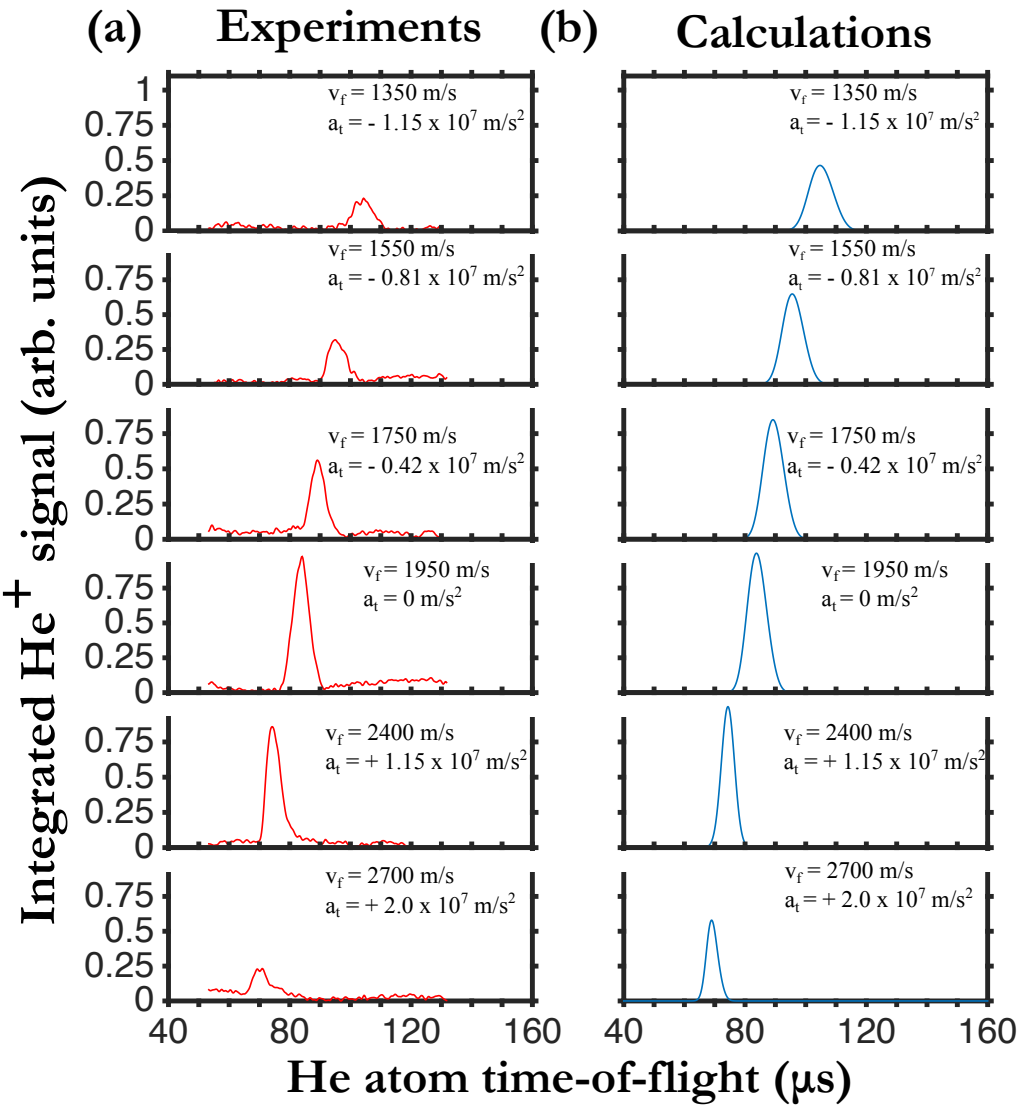

Figure 7.5: (a) Experimental and (b) calculated time-of-flight distributions for the acceleration/deceleration of helium atoms moving with an initial speed of 1950 m/s. The tangential accelerations and final velocities of each case are included in the corresponding panel.

are decelerated and collisions can occur before the decelerated and undecelerated components are transversally separated. In this region collisions between a Rydberg atom and a ground state or metastable helium atom can cause state changing and loss from the trap [121, 69].

At the atom densities of $\sim 10^7$ atoms per cm^{-3} generated in the experiments, the large "classical" electric dipole moment of the atoms can give rise to strong dipole-dipole interactions [108, 122]. Such dipole-dipole collisions can also lead to state changing and loss of atoms from the trap, partic-

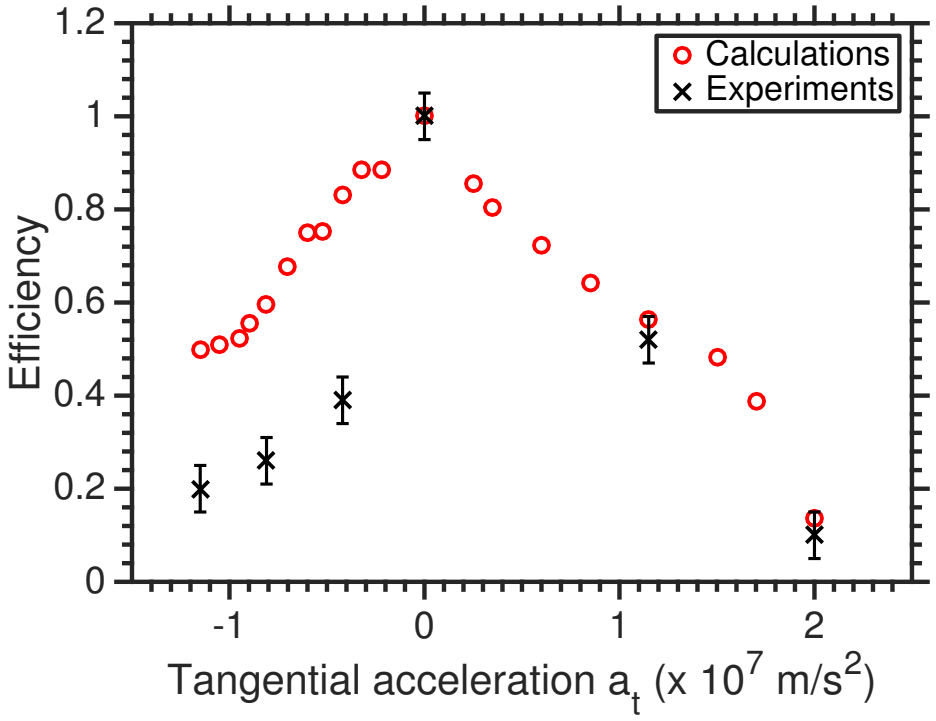

Figure 7.6: Comparison of experimentally recorded and calculated efficiencies with which atoms are accelerated/decelerated as a function of the acceleration applied for helium atoms in $|n,k\rangle = |52,35\rangle$ Stark-states. The red circles represent the results of the calculations, while the black crosses represent the experimental data.

ularly near the electric field minimum. As effects of the density of Rydberg atoms on the efficiency with which ensembles can be guided at constant speeds have been seen [123] (see Chapter 6), it will be important in future work to characterise in greater detail these collisional losses.

Beyond this contribution to the difference in deceleration efficiency observed in the calculations and the experimental work, losses of atoms from the moving trap of the decelerator can also arise from transitions and ionisation driven by blackbody radiation. However, as discussed previously, only direct blackbody photoionisation of the Rydberg atoms gives rise to immediate trap loss. As discussed in Chapter 6, more refined experiments will need to be performed to more clearly identify the origins of these discrepancies between the results of the experiments and the results of the calculations. These will require cooling of the decelerator.

Chapter 8

Stopping and trapping Rydberg atom beams in a transmission-line decelerator

8.1 Introduction

From the experimental results presented in Chapter 6, and the results of the calculations presented in Chapter 7, the maximal acceleration that can be applied in the transmission-line decelerator described could be identified to be ~ 2 x 10^7 m/s^2. Using this information a second generation device was constructed that permitted deceleration to zero velocity in the laboratory-fixed frame of reference and *in-situ* detection of atoms directly from within the device. This decelerator, depicted schematically in Figure 8.1 was designed with a storage ring included at its end which could be used in future experiments.

The possibility to directly detect atoms from traps within the decelerator circumvents limits imposed on the detection efficiency as they travel from the end of the decelerator to the detection region. In previous experiments in which Rydberg atoms have been trapped in stationary traps in surface-electrode Rydberg-Stark decelerators, it was necessary to re-accelerate the atoms off the decelerator before detection [121, 77]. This introduces complications in analysing the decay of the trapped atoms which is avoided if in-situ detection is implemented.

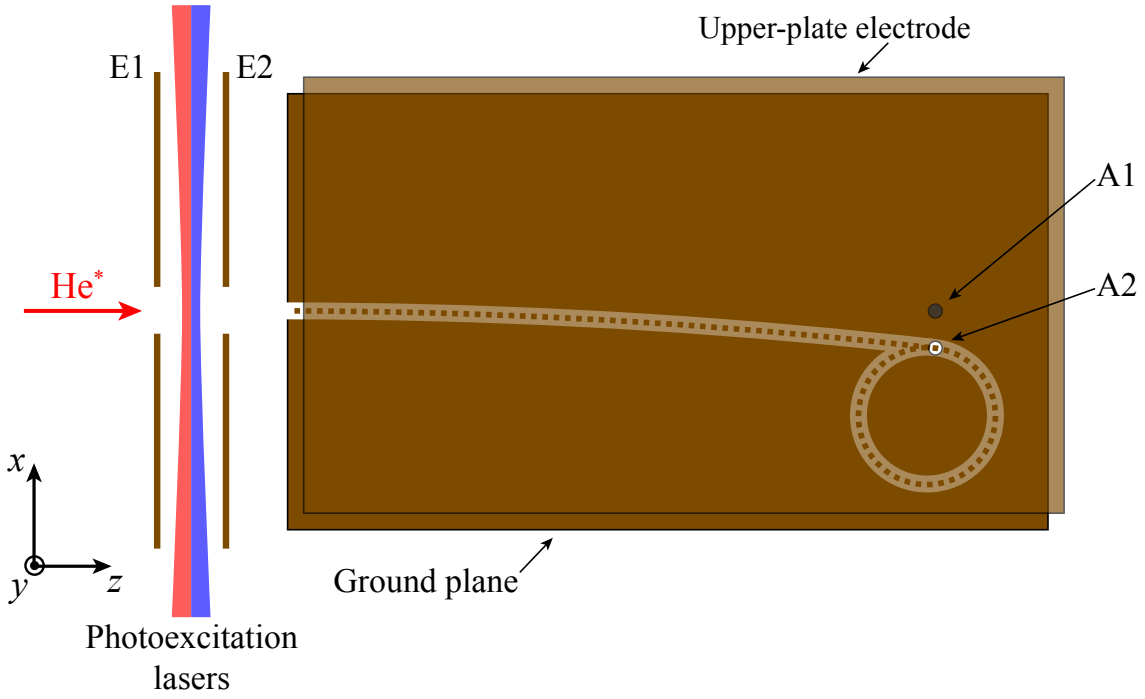

Figure 8.1: Schematic representation of the second generation transmission-line decelerator with storage ring. The apertures in the upper plate (2.5 mm diameter each) allowed direct, *in-situ* He^+ ions detection after pulsed electric field ionisation, when the decelerator is set off (A1) and on (A2), respectively.

8.2 Decelerator design

The general design of the decelerator used in the experiments described here is the same as that described in Chapters 6 and 7 [124]. However, the length of the device was chosen to permit deceleration of beams of helium atoms with initial longitudinal speeds of up to $\sim$ 2000 m/s, to zero-velocity in the laboratory-fixed frame of reference. This can be achieved with an acceleration of ~ -1.3 x 10^7 m/s^2 over a decelerating distance of 156 mm. As in Chapter 6 a curved decelerator was employed. The curvature used was described by the arc of a circle with a radius of 0.81 m. The resulting decelerator was composed of 70 center conductor segments. With future experiments in mind, a circular storage ring with a radius of curvature of 14.3 mm was also included at the end of the decelerator (see Figure 8.1). The junction between the decelerator and the storage ring was formed by two enlarged center conductor segments with a dimension of $(\Delta x, \Delta z) = (3\text{ mm}, 1\text{ mm})$ and $(\Delta x, \Delta z) = (2.5\text{ mm}, 1\text{ mm})$, respectively.

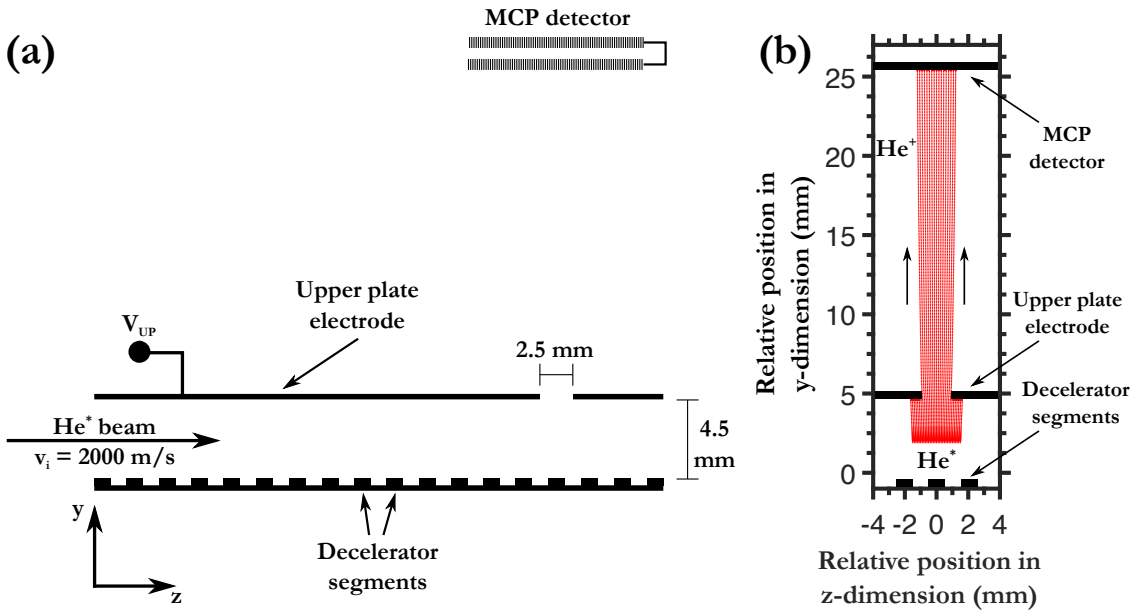

Figure 8.2: (a) Schematic diagram of the in-situ detection region in the transmission-line decelerator. (b) He^+ trajectories for the in-situ detection region to the MCP detector after pulsed electric field ionisation, when $V_{ion} = +350$ V, $V_{UP} = V_C = 0$ V and $V_{MCP} = -1$ kV.

8.3 In-situ Rydberg atom detection

To optimise the detection of guided, decelerated or trapped atoms, the second-generation transmission-line decelerator described here is designed to allow in-situ detection. This permits direct detection of guided, accelerated or decelerated atoms from within the device, and the detection of atoms confined in stationary traps by pulsed electric field ionisation. To achieve this, at a fixed position directly above one of the segments of the decelerator center conductor (segment no. 74), a circular aperture with a diameter of 2.5 mm was prepared in the upper plate electrode (aperture A2 in Figure 8.1). The position of this aperture can be seen in Figure 8.2(a).

At the longitudinal position of this aperture in the upper plate, atoms within the decelerator are detected by pulsed electric field ionisation after applying pulsed potentials $V_{ion} = +350$ V to the ground planes of the device. The resulting fields of ~ 780 V/cm, caused the atoms inside the trap to be ionised. If these atoms are located below the aperture in the upper plate they will then be extracted from the device and accelerated toward the MCP detector located above these plates. Typical He^+ trajectories from the position of the moving decelerating traps to the MCP following this process can be seen in Figure 8.2(b).

To determine the acceptance of the in-situ detection, the trajectories of He^+ ions from the position of the decelerator traps to the MCP detector were calculated. In this calculation, helium ions, generated by pulsed field ionisation of the helium Rydberg atoms, were initially located at a distance of 1.9 mm above the decelerator segments in the y-dimension. Ensembles of ions were prepared covering a range of 3 mm in the z-dimension, centered on the mid-point of the aperture in the upper plate electrode. These ions were then accelerated in the electric field present at ionisation when $V_{\rm ion} = +350$ V is applied to the ground planes, and $V_{\rm UP} = 0$ V is also applied to all other electrodes. This reflects the detection condition in the experiments where all deceleration potentials were switched off 500 ns before the ionisation pulse was applied. As can be seen in Figure 8.2(b), atoms located within ± 0.5 mm of the centre of the aperture in the upper plate in the y and z dimensions are efficiently detected. Therefore the in-situ detection volume is 1 mm x 1 mm x 1 mm.

In the experiments described here, this in-situ detection scheme was employed to detect guided and decelerated atoms as they travelled through the decelerator past the detection zone. In was also used to detect atoms confined in stationary traps located at this detection position. In this latter case the effect of the aperture in the upper plate electrode on the electric fields of the trap must be considered. The effect of this aperture can be seen in the calculated potential energy distributions experienced by the atoms at the position of the aperture. Such distribution for atoms in Rydberg-Stark states for which $|n,k\rangle = |48,35\rangle$ are displayed in Figure 8.3. As can be seen by comparing Figure 8.3(a) and Figure 8.3(b), the presence of the aperture in the upper plate electrode does not significantly alter the depth of the trap in the z-dimension or close to the transmission-line surface in the y-dimension. However, it causes a slight reduction in the trap depth close to the upper plate electrode. This effect can be seen clearly in Figure 8.3(c), in which the potential energy profiles in the y-dimension at $z = 0$ are displayed. For the conditions considered, the depth of the trap changes by a factor of ~ 0.75 with the aperture present. From ~ 21 K to ~ 16 K. Although this would be expected to lead to a small amount of loss from the trap when brought to the detection region of the decelerator, it should not significantly alter the dynamics of atoms close to the trap minimum.

8.4 Experimental setup

To use this second generation transmission-line decelerator with in-situ detection to guide, decelerate and trap fast beams of helium atoms, it was inserted into a similar experimental apparatus to that

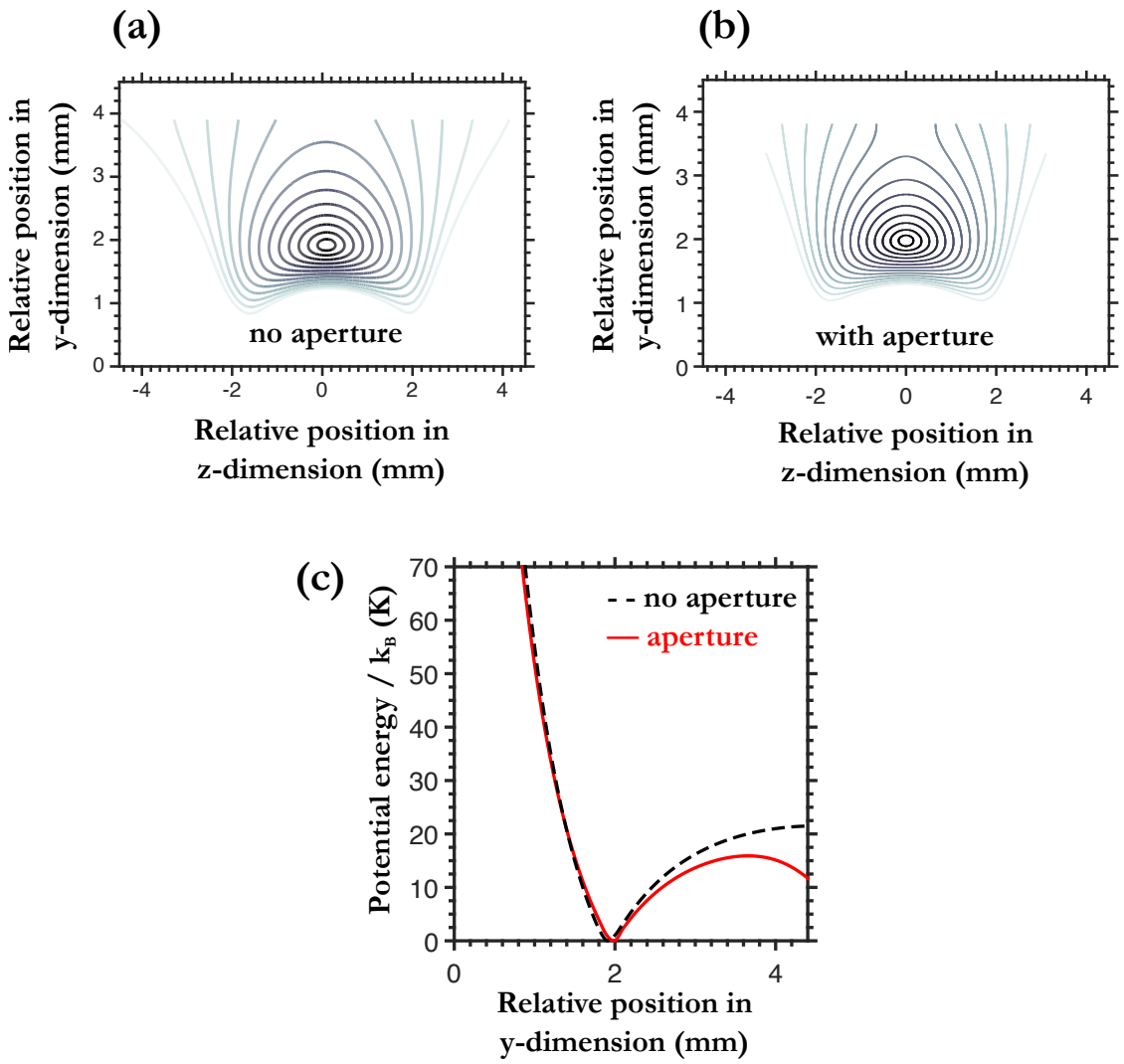

Figure 8.3: Potential energy distributions experienced by helium atoms in Rydberg-Stark states with $|n,k\rangle = |48,35\rangle$ in a trap of the transmission-line decelerator with $V_0 = 150$ V and (a) no aperture in the upper plate, and (b) a 2.5 mm diameter aperture in the upper plate at $z = 0$. The contour lines are displayed in steps of 2 K from 0 K to 28 K. (c) Potential energy profiles in the y-dimension at $z = 0$.

constructed for the work described in Chapter 6. In this case, Rydberg-Stark states for which $n = 48$ were prepared by photo-excitation. These slightly lower values of n used in the experiments reduced effects of electric field ionisation during deceleration with the largest values of $|a_t|$. A short, ~ 3 μs long pulse of excited atoms was generated by modulating the ir laser intensity using an electrooptical modulator, synchronously with a pulsed excitation electric field. Because the MCP detector was located above the upper plate electrode, and a curved decelerator was employed to reduce col-

lisional losses of decelerated and trapped atoms [69, 72], it was necessary to introduce a second aperture in the upper plate electrode on the axis of the atomic beam to detect the atoms when the decelerator was off (aperture A1 in Figure 8.1). This aperture was located at the same position in the z-dimension as the aperture used for in-situ detection of decelerated/trapped atoms but 10 mm away from it in the x-dimension. The geometric restrictions imposed by the electrodes surrounding the excitation region ensured that undecelerated atoms could not reach the off-axis in-situ detection position. While with the decelerator active, atoms that were not loaded into a moving trap were ionised in the decelerator fields and therefore could not reach the on-axis aperture.

8.5 Results

The second generation transmission-line decelerators with in-situ detection described above have been employed to guide, decelerate, stop and trap beams of helium atoms initially moving at ~ 2000 m/s in low-field-seeking Rydberg-Stark states. In these experiments, time-of-flight distributions were recorded from the position at which photoexcitation was performed to the detection positions beneath the apertures in the upper plate electrode, a distance of ~ 160 mm. First a reference measurement was made with the decelerator off to record the time-of-flight distribution of the undecelerated beam of Rydberg atoms. The results of this measurement are displayed in Figure 8.4(a-i). In this situation, the Rydberg atoms were detected at the position of the on-axis ionisation aperture (A1). From the mean flight-time of this bunch of atoms their mean longitudinal speed of $\sim$2000 m/s was determined.

To ensure that the central component of the atomic beam was efficiently loaded into a single moving trap of the decelerator and transported to the off-axis detection position, a sequence of time-dependent electrical potentials were applied to the decelerator electrodes to guide the atoms at a constant speed of $\sim$2000 m/s. In these experiments the decelerator was operated with $V_0 = +150$ V. The optimal time at which to activate the decelerator potentials was determined as in Chapter 6 by detecting guided atoms arriving at the detection position of a fixed time-of-flight of 80.5 μs as the activation time of the decelerator potentials was adjusted with respect to the excitation time. The results of these activation time measurements are displayed in Figure 8.5. As can be seen in this figure, intensity maxima appear in the He^+ ion signal when the decelerator is activated at the time when the excited atoms are located at the positions of the consecutive moving traps of the decelerator

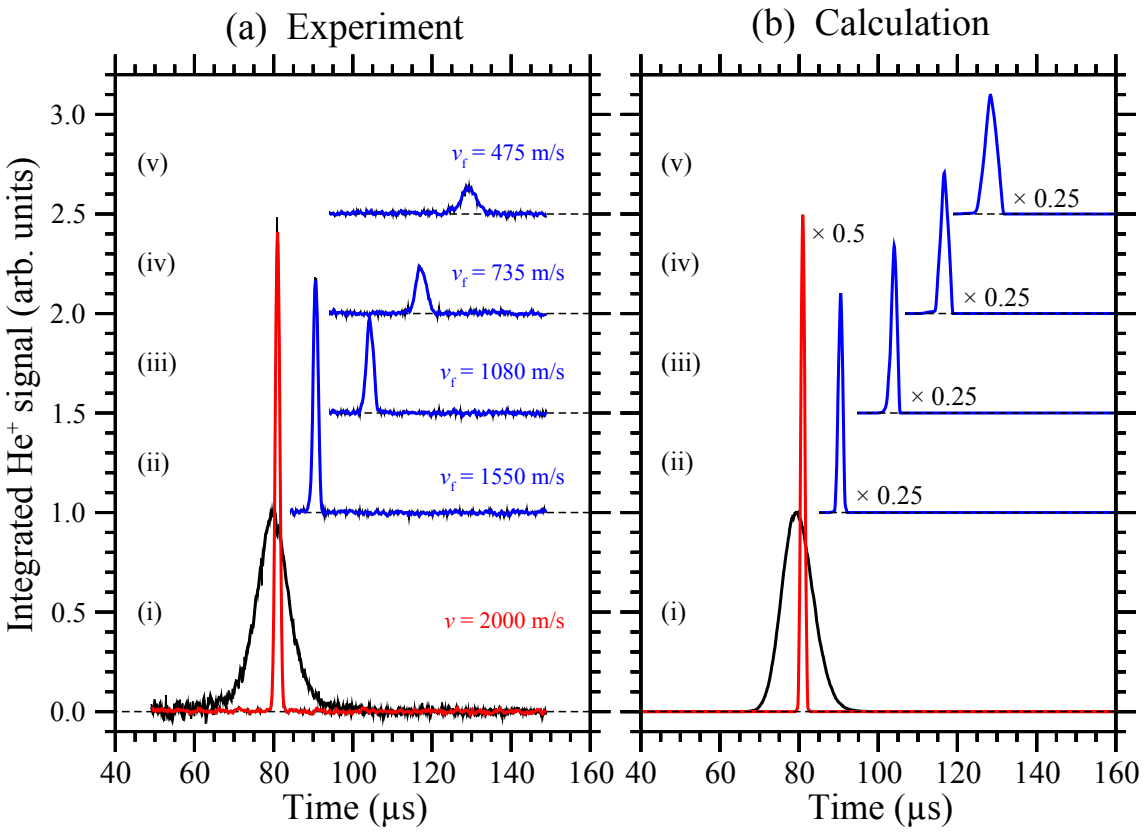

Figure 8.4: (a) Experimentally recorded and (b) calculated time-of-flight distributions with the decelerator off [black curve in (i)], after guiding atoms at constant speed of 2000 m/s [red curve in (i)], and for deceleration with (ii) $a_t = -0.5$ x 10^7 m/s^2, (iii) $a_t = -0.9$ x 10^7 m/s^2, (iv) $a_t = -1.1$ x 10^7 and (v) $a_t = -1.2$ x 10^7 m/s^2.

when it is activated. Because the consecutive traps of the decelerator are spatially separated by 10 mm, the time intervals between these intensity maxima are 5 μs. From this measurement an optimal activation time of 2.3 μs after photoexcitation was selected for all subsequent measurements.

With this activation time set, the helium atom time-of-flight distribution was again recorded but on this occasion with the decelerator activated to guide atoms a constant speed of 2000 m/s. For these measurements, the oscillation frequency of the decelerator was $\omega = 2\pi$ x 200 kHz. The corresponding data is displayed as the red curve in the bottom panel of Figure 8.4(a). This time-of-flight distribution has a much sharper profile than that recorded with the decelerator off. This is because with the decelerator on, the excited atoms remain tightly bunched as they are transported through the decelerator to the detection position and do not disperse.

As described in Chapter 6, applying a frequency chirp to the oscillating potentials permits accel-

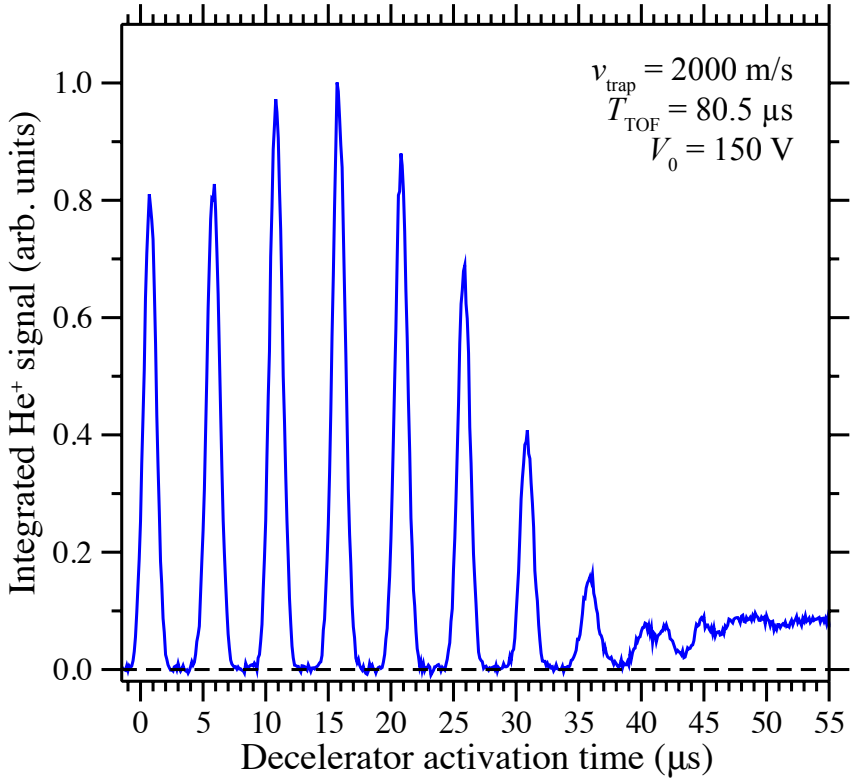

Figure 8.5: Dependence of the integrated He^+ signal recorded at the position of in-situ detection on the activation time of the oscillating decelerator potentials, for a helium atom flight-time from the photoexcitation region to the detection region of 80.5 μs, when the decelerator is operated to guide atoms at a constant speed of 2000 m/s.

eration or deceleration of the moving traps. To decelerate atoms over the length of this decelerator from 2000 m/s to 1550 m/s, 1080 m/s, 735 m/s and 475 m/s requires accelerations of -0.5 x 10^7 m/s^2, -0.9 x 10^7 m/s^2, -1.1 x 10^7 and -1.2 x 10^7 m/s^2, respectively. The time-of-flight distributions recorded for these parameters are displayed in the upper panels in Figure 8.4(a). From these measurements it can be seen that the intensity of the He^+ time-of-flight signal decreases as higher accelerations are applied. This is a consequence of the reduced effective depth of the decelerator traps with increasing acceleration, as discussed in Chapter 6 and Chapter 7.

To characterise the changes in peak intensity in the measured time-of-flight data, a comparison was made with the results of numerical calculations of particle trajectories through the device. These calculations were performed by solving the classical equations of motion of the Rydberg atoms in the moving frame of reference associated with one single trap of the decelerator. The effects of acceleration in this reference frame were included through the introduction of pseudo potentials which

were dependent upon the displacement from the electric field minimum of the trap. Throughout the entire guiding and deceleration processes the instantaneous centripetal acceleration, arising as a result of the curvature of the decelerator, and the applied tangential acceleration, a_t, were accounted for.

Because the in situ detection regions in the decelerator have very well defined spatial dimensions, the longitudinal temperature of the excited ensemble of Rydberg atoms could be accurately determined from the time-of-flight distribution recorded with the decelerator off. Using this data the bunch of atoms was found to have a relative translational temperature in the z dimension of $T_z = \langle E_{\rm kin} \rangle / k_{\rm B} = 3$ K, where $\langle E_{\rm kin} \rangle$ is the mean relative kinetic energy of the atoms. Taking into account the 6 mm longitudinal extent of the excited bunch of atoms, this temperature matches that reported in other experiments with pulsed supersonic beams of metastable helium generated with similar discharge sources [76]. The transverse temperatures of the atoms were determined, from the geometric constraints imposed by the skimmer and focussed narrow-bandwidth laser beams in the experiments, to be $T_x = T_y = 10$ mK. By randomly generating ensembles of Rydberg atoms with these initial parameters, trajectories in the moving traps of the decelerator were calculated numerically until the traps reached the detection aperture A2. The corresponding arrival times of the atoms in this detection region were then used to generate the calculated time-of-flight distributions presented in Figure 8.4(b).

In Figure 8.4(b-i), the calculated intensity of the signal associated with the Rydberg atom beam when the decelerator was off, was normalised in the same way as that recorded experimentally [Figure 8.4(a-i),]. The results of the particle trajectory calculations performed for atoms guided at a constant speed of 2000 m/s exhibit an intense, narrow maximum in the time of flight distribution at a flight time of 80.5 μs. This time-of-flight distribution is in agreement with that observed in the experimental data if it is scaled by a factor of 0.5. This scaling accounts for the differences in the He^+ ion extraction efficiency from the in situ detection region beneath aperture A1, and that in the region beneath aperture A2 in the experiment. It also accounts for effects of collisions between the trapped Rydberg atoms on the efficiency with which they are transported through the decelerator [124]. Neither of these effects are treated in the calculations.

From these calculations, time-of-flight distributions could be obtained as displayed in Figure 8.4(b) (see Chapter 7 for details). The precisely defined geometry of the in-situ detection region

and the absence of a dependence of the detection efficiency on the phase-space properties of the decelerated beams make for a very reliable comparison between the results of the experiments and those of the calculations. In general the calculated time-of-flight distributions are in good agreement with those recorded experimentally. However, in each case the amplitude of the intensity maxima [scaled by a factor of 0.25 with respect to the undecelerated distribution as indicated in Figure 8.4(b)] is greater in the calculated data than in the experimental data. These differences are consistent with the previously recorded time-of-flight distributions with a shorter decelerator shown in Figure 7.5. The differences in the signal intensity indicate a loss of atoms from the travelling traps of the decelerator in the experiments which is not solely a result of their translational motion. This decay of atoms from the moving traps of the decelerator results from a combination of spontaneous emission, effects of blackbody radiation, collisions between the Rydberg atoms within the traps, and collisions between the trapped Rydberg atoms and the background gas in the vacuum chamber.

In the first generation transmission-line decelerator employed in the work described in Chapter 6, the sensitivity of the detection efficiency to the final speed of the decelerated beams of atoms represented an effect that could not be completely characterised. The in-situ detection approach used in the work described here avoids this problem. In this device, when an acceleration of $a_{\mathrm{t}} = -1.20$ x 10^7 m/s^2 was applied, the trapped sample of atoms had a final velocity of 475 m/s, with a time of flight of 130 μs and a time difference at detection between guiding and decelerating of 50 μs. The considerable longer times during which the atoms were trapped in the electric traps of the decelerator are therefore expected to have several consequences on the measurements. First, the trapped atoms have a longer period of time to interact with each other in the trap. As a result collisional trap loss can be enhanced. The additional trapping time also leads to a greater likelihood for blackbody transitions to cause a redistribution of the Rydberg population. Multiple transitions of this kind could lead to sufficiently significant changes in electric dipole moment that atoms could be lost from the decelerator trap.

The information extracted from the changes in deceleration efficiency cannot be directly compared with that discussed in Chapter 6 because of the different finals speeds of the decelerated atoms and these increased trapping times. However, the increased loss with trapping time is not unexpected. In future experiments it will be particularly interesting to control the blackbody temperature of the environment within the decelerator and the Rydberg atom number densities to gain

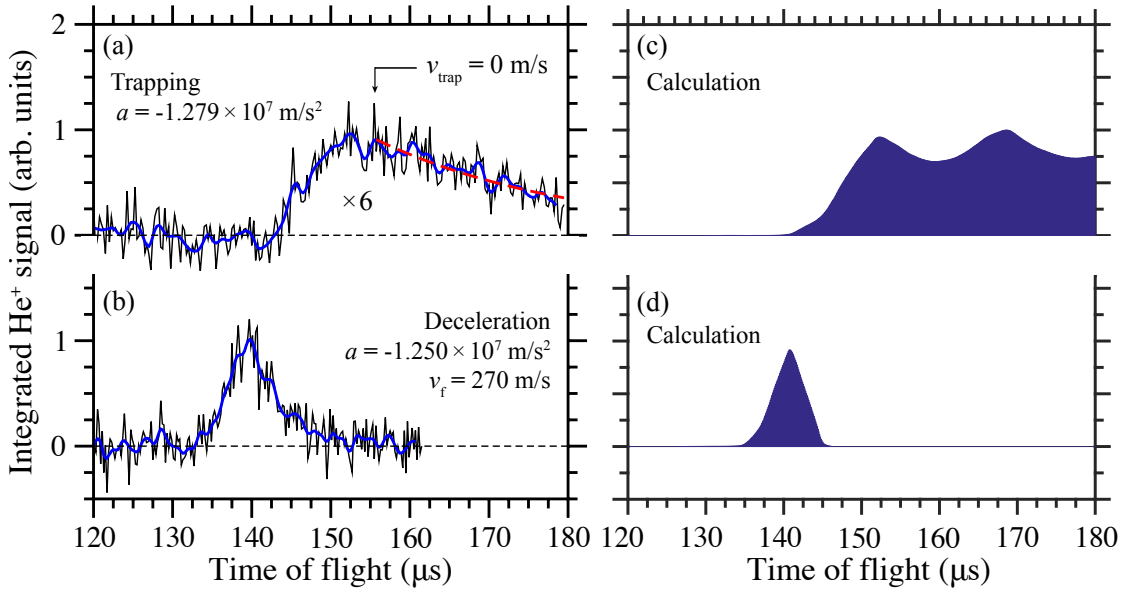

Figure 8.6: Decelerating and storing trapped helium Rydberg atoms. (a) The time-of-flight distribution of a sample of helium Rydberg atoms stored after deceleration to zero-velocity. (b) The time-of-flight signal from a sample of helium Rydberg atoms decelerated to a final velocity of 270 m/s. (c-d) Calculated time-of-flight distributions of decelerated Rydberg atoms for comparison with the experimental data in (a) and (b), respectively.

further insights into the origins of these changes in deceleration efficiency.

A final set of experiments conducted with this second generation transmission-line decelerator involved deceleration to zero-velocity in the laboratory-fixed frame of reference. Following this, the decelerated atoms were stored in stationary traps at the detection position. In these experiments, higher accelerations were applied to achieve the desired final speeds of the Rydberg atoms. By trapping the stationary cloud of atoms beneath the detection aperture the He^+ signal from the trap appears directly in the measured time-of-flight data at longer time delays. Time-of-flight distributions recorded in these experiments are presented in Figure 8.6(a) and (b).

For reference, in Figure 8.6(b) the time of flight distribution associated with a bunch of atoms originally travelling at 2000 m/s, and decelerated to 270 m/s by applying an acceleration $a_t = -1.250$ x 10^7 m/s^2 is displayed. In this dataset, the peak of the time-of-flight distribution occurs after a flight-time of 140 μs and is broadened when compared to the distributions displayed in Figure 8.4(a). This broadening in time is a result of the longer time it takes this slow bunch of atoms to travel through

the detection region below the detection aperture in the upper plate electrode. Numerical calculations of the trajectories of 10^5 atoms have been performed for comparison with the experimental results. The result of this calculation is displayed in Figure 8.6(d) and can be quantitively compared with the experimental data. The position of the maxima in the experiment and calculation are in excellent agreement, and the FWHM of each distribution ($\sim 5\ \mu$s) is the same.

By further decelerating this bunch of trapped atoms with an acceleration of $a_t = -1.279$ x 10^7 m/s^2, the trap can be brought to a standstill in the laboratory-fixed frame of reference at the detection position. As can be seen from Figure 8.6(a), when this is achieved the observed time-of-flight signal persists after the trap is stopped and it displays a long tail with a time constant of $\sim$25 μs. The persistence of this time-of-flight signal demonstrates that the decelerated atoms remain confined in the stationary electric trap. Again this can be compared to the results of the numerical particle trajectory simulation displayed in Figure 8.6(c). In these calculations, the time-of-flight maxima oscillate slightly after the trap comes to a standstill. These oscillations arise from the motion of the atoms in the trap when the contribution from the pseudo potential become zero. Similar effects have been seen in multistage Stark-decelerators composed of ring electrodes in which ground state polar molecules were decelerated in continuously moving electric traps [125]. These oscillations are not seen in the experimental data, because they are washed out as a result of the blackbody transitions, slightly changing the dipole moments of the atoms during deceleration. In the calculation, after detection, because the center of mass of the ensemble of atoms has a velocity of ~ 0 m/s, the atoms remain trapped without significant losses. This can be seen when the calculation is carried out for longer times, as displayed in Figure 8.7. For these longer trapping times, the oscillations caused by the initial phase jump between the moving electric trap and the stationary trap are reduced and the time-of-flight signal remains constant in time. By comparing the experimental data with the results of the numerical calculations, it can be seen however that the experimental data decay as a function of time. The reduction in the signal over 20-30 μs is a consequence of the decay of atoms from the trap. This decay has contributions from fluorescence, as the atoms return to their ground state, collisional state changing, and blackbody transitions and photoionisation. Because the experiments were carried out in a room temperature environment, blackbody transitions are expected to play the dominant role in the trap loss. These transitions cause the Rydberg-Stark population to be redistributed over time. However, the very high values of n of the atoms trapped here are significantly

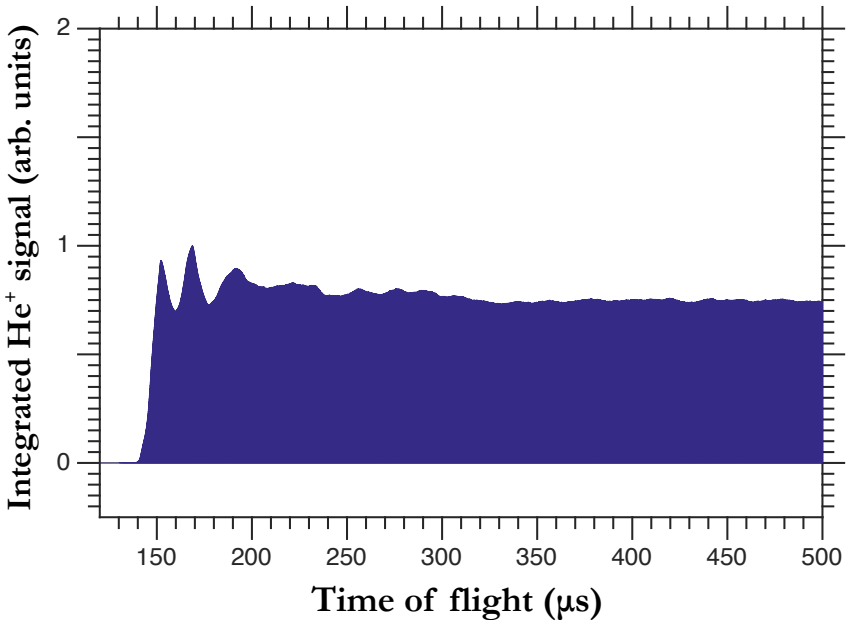

Figure 8.7: Calculated time-of-flight distribution of a sample of helium Rydberg atoms initially traveling at a speed of 2000 m/s and stopped at zero-velocity in the laboratory-fixed frame of reference.

greater than those prepared in traps previously. Because of the large electric dipole moments of the states ∼10000 D they are uniquely sensitive to collisions with each other [72]. In these experiments, because of the electric fields of the trap, the lifetimes of the Stark states are longer than those of the field-free low-ℓ states by a factor of $\sim n$ [28]. The lifetime that results for Rydberg states of helium with principal quantum number $n = 48$ is ∼2 ms. It is therefore expected that fluorescence only represents a minor contribution to the trap decay.

It is worth noting that the decay constant associated with the loss of these $n = 48$ triplet helium Rydberg atoms from the trap in these experiments is ~ 25 μs. This is very similar to the decay-time constant observed previously in experiments with hydrogen atoms in states with $n = 30$ ($\tau \sim 30$ μs) [28], and helium atoms in singlet Rydberg state with $n = 30$ trapped in similar devices ($\tau \sim 22.7$ μs) [76]. The similarity of these trap decay rates in decelerators/traps constructed using similar electrical circuit board materials (copper coated epoxy resin impregnated glass fibre - FR4) may suggest that electric field noise emanating from the surfaces, or collisions following degassing of the material could contribute to the decay of the trapped atoms. It would therefore also be of value in the future to test the construction of these decelerators with different materials, e.g., sapphire substrates, using methods other than chemical etching.

Because the segmented electrical transmission line of the decelerator used here can be considered to be composed of a series of coplanar electrical resonators, the results presented in Figure 8.6 represent a demonstration of electrostatic trapping gas-phase Rydberg atoms above such a circuit element. The decelerator can therefore act as an electrical transmission line in its present form, but only for particular (resonant) microwave frequencies.

Chapter 9

Conclusion and outlook

The work presented in this thesis covers the development and experimental implementation of a new type of chip-based devices which enabled the position and velocity of beams of Rydberg atoms initially travelling in pulsed supersonic beams to be controlled. Using homogeneous electric fields at the position of Rydberg state photoexcitation, atoms in low-field-seeking Rydberg-Stark states with principal quantum numbers ranging from 48 to 52 were prepared by narrow bandwidth cw laser photoexcitation. The choice of principal quantum number was motivated by the desire to prepare states with large electric dipole moments for effective deceleration and trapping, via transitions with sufficient spectral intensity for efficient excitation from low-lying intermediate states. Rydberg states with these high numbers of n are also well suited to integrating with microwave apparatus operating at frequencies of $10-50$ GHz.

The Rydberg-Stark decelerators developed are expected to play a role in the future preparation of beams of atoms and molecules in high Rydberg states with a wide range of velocities, but with narrow velocity distributions. Such samples are of interest in high resolution microwave or millimeter-wave spectroscopy, in which they offer increased interaction times during the measurements leading to a reduction of the transit-time broadening [18].

Measurements of these kind are of importance in the determination of ionisation and dissociation energies of atoms and molecules [16], because the resolution of the recorded spectra is correlated to the precision of these measurements [126]. The surface-based devices described here for decelerating, stopping and trapping Rydberg atoms open up opportunities to confine atoms or molecules on a chip, and increase the interaction times required for these precise spectroscopic measurements. The

samples of cold atoms prepared in this thesis displayed velocity spreads of ± 45 m/s, which would lead them to remain within a 1 mm interaction volume for ~ 10 μs after the traps are decelerated. Under these conditions, the achievable spectral resolution is expected to be ~ 100 kHz. If such experiments were performed with hydrogen molecules this would approach the limit for theoretical values of ~ 10 kHz imposed by the current uncertainty of the proton-to-electron mass ratio [16].

The surface-based guides described in Chapter 5 permitted two-dimensional confinement and transport of samples of Rydberg atoms away from their initial axis of propagation. This was possible by utilising a transmission-line geometry, in which the center conductor was curved with respect to the propagation axis. This allowed the separation of guided atoms away from the unguided components of the beam and is of importance for experiments in which it is desirable to precisely locate atoms above a surface. For example, studies carried out previously on the interaction of helium Rydberg atoms with microwave fields in the vicinity of a solid-state coplanar waveguide [47] highlighted the role the motion of the atomic cloud played in decoherence and dephasing during population transfer and studies of Rabi oscillations. The guides developed here offer the opportunity to precisely control atom-surface distances and thus reduce decoherence. In this way, the limit of the single-atom-single-photon coupling regime may be approached, opening up further scientific opportunities. These include the study of strong light-matter interactions and coupling using Rydberg atoms in circuit cavity quantum electrodynamics settings and exploiting Rydberg atoms in hybrid quantum information processing [127].

The manipulation of the translational motion of beams of atoms in high Rydberg states is also of interest in gravitational free-fall measurements involving antihydrogen and positronium [128]. The experiments with positronium require the preparation of sufficiently long-lived Rydberg states to prevent self-annihilation before the measurements are concluded. In a type of free–fall measurements proposed by Mills and Leventhal [129], positronium atoms would be prepared in high Rydberg states. The beams of positronium Rydberg atoms would then be collimated and possibly decelerated using inhomogeneous electric fields. The surface-based devices presented here would allow for such manipulation, using the large electric dipole moments of the Rydberg states. The transmission-line decelerators presented in this thesis allowed for efficient removal of kinetic energy to completely stop fast beams of helium atoms. In the experiments, the kinetic energy removed from atoms travelling with an initial speed of 2000 m/s was ~ 83 meV. Since typical pulsed beams

of positronium travel at speeds of $\sim 10^5$ m/s, and therefore have kinetic energies of ~ 55 meV, complete deceleration of Ps beams could be foreseen with this device. Other Rydberg atom optical elements are also therefore well suited for focusing and deceleration of positronium. In the context of measurements of gravitational acceleration, Rydberg-Stark decelerators with continuously moving traps such as those presented here also have application in the manipulation of antihydrogen atoms, which are prepared in high Rydberg states. Indeed it is planned to exploit such devices in the AEgIS antihydrogen experiment currently under construction at CERN [130].

The transmission-line decelerators presented in this thesis also open up opportunities for the preparation of cold samples of molecules in excited Rydberg states. Again the large amount of kinetic energy that can be removed using these transmission-line decelerators, together with their scalable nature, makes them well suited to transport heavier atoms or molecules between various regions in an experimental apparatus. The fact that the decelerating particles are also subjected to weak electric fields near the trap minima is a further benefit in the deceleration of molecules with complex and dense energy level structures. For heavier species such as CaF, which have been successfully cooled by using counter-propagating laser beams from an initial speed of 600 m/s to 583 ± 2 m/s [131], to bring such a supersonic beam to a complete stop would require the removal of ~ 110 meV of kinetic energy per molecules. As this is on the same order of magnitude as the energy removed in the experiments described here, it would suggest that Rydberg-Stark decelerators could also be suitable for the deceleration of such samples. By extending the decelerator length and keeping the deceleration applied close to $\sim 10^7$ m/s^2, a wide range of molecular species that can be prepared in long-lived Rydberg-Stark states could be accelerated, decelerated and trapped. If these samples were subsequently de-excited back to their ground states, translationally cold ground state molecules could be prepared.

Appendix A

C++ programme for calculating Rydberg atom trajectories

```
1  //  Programme for calculating Rydberg atom trajectories in three-dimensions in↩
       a transmission-line decelerator.
2
3  //  Created by Patrick Lancuba on 16.09.14
4  //  Last update: 02.12.2015
5
6  // Packages declaration
7  #include <iostream>
8  #include <fstream>
9  #include <string.h>
10 #include <algorithm>
11 #include <vector>
12 #include <cstring>
13 #include <stdio.h>
14 #include <sstream>
15 #include <cmath>
16 #include <stdlib.h>
17 #include <limits>
18 #include <boost/random.hpp>
19 #include <boost/random/normal_distribution.hpp>
20 #include <boost/math/distributions/uniform.hpp>
21 #include<boost/math/distributions.hpp>
22 #include <time.h>
23
24 using namespace std;
25 using namespace boost;
26
27 const int elec = 15; // Number of electrodes
28 const int npla = 51; // Number of planes
29 const int ipla = 15; // Initial plane
30
```

```
31 double E[npla][elec][3][101][46]; // Read-in electric field matrix
32
33 double Vp [] = {0,0,0,0,0,0,0,0,0,0,0,0,0,0,0};
34 double VE = 150;
35 double VT = -0.5*VE;
36 double VGP = -0*VE;
37
38 const double nval = 48;
39 const double kval = 35;
40
41 // Constants. Source: NIST 10.2014
42
43 const double e = 1.602176565e-19;
44 const double a0 = 0.52917721092e-10;
45 const double kb = 1.3806488e-23;
46 const double mhe = 4.002602 * 1.660538921e-27;
47 const double pi = 3.14159265358979323846;
48
49 // Ionisation limit in V/m
50
51 const double Fion = 215*100;
52
53 // Generation of a spatial, uniform distribution at the exit of the valve
54
55 double minx = 6.0e-3;
56 double maxx = 7.0e-3;
57
58 double miny = 1.4e-3;
59 double maxy = 2.4e-3;
60
61 double minz = -10e-3;
62 double maxz = 20e-3;
63
64 // Gaussian velocity distribution at the exit of the valve
65
66 double meanvx = 0.0;
67 double sdvx = sqrt(kb * 0.1 / (log(2) * mhe)); //sigma=sqrt(kb*T/(log(2)*mhe))
68
69 double meanvy = 0.0;
70 double sdvy = sqrt(kb * 0.1 / (log(2) * mhe)); //sigma=sqrt(kb*T/(log(2)*mhe))
71
72 double meanvz = 0.0;
73 double sdvz = sqrt(kb * 4 / (log(2) * mhe)); //sigma=sqrt(kb*T/(log(2)*mhe))
74
75 // Spatial, normal (x-, and y-dimensions) distributions at the photoexcitation↩
       region.
76
77 double pmeanx = 6.5e-3;
78 double psdx = 100e-6/2.3548; // FWHM/(2*sqrt(2*log(2)));
```

```
79
80 double pmeany = 1.9e-3;
81 double psdy = 100e-6/2.3548; // FWHM/(2*sqrt(2*log(2)));
82
83 // Spatial, uniform (z-dimension) distribution at the photoexcitation region
84
85 double pminz = 2.0e-3;
86 double pmaxz = 8.0e-3;
87
88 // Creation of the string for reading the input files
89
90     string make_output_filename(int plane, int number, char* crd) {
91            stringstream ss;
92            ss.setf(ios_base::fixed);
93            ss.precision(1);
94            ss << "Trad_X" << plane << "EW" << number << crd << ".dat";
95            return ss.str();
96            }
97
98 int main(){
99
100        // Generation of normal distributions with the Boost package
101           mt19937 generator; // Mersenne Twister Generator
102            generator.seed(int(time(0))); // A different seed at each turn
103
104        // Random generation of a number between 0 and 1
105            uniform_real<> dis(0,1);
106            variate_generator<mt19937&,uniform_real<> > rnd(generator, dis);
107
108        // Spatial, uniform distribution at the exit of the valve
109            uniform_real<> udx(minx, maxx);
110            uniform_real<> udy(miny, maxy);
111            uniform_real<> udz(minz, maxz);
112            variate_generator<mt19937&,uniform_real<> > ud_x(generator, udx);
113            variate_generator<mt19937&,uniform_real<> > ud_y(generator, udy);
114            variate_generator<mt19937&,uniform_real<> > ud_z(generator, udz);
115
116        // Gaussian velocity distribution at the exit of the valve
117            normal_distribution<> ndvx(meanvx,sdvx);
118            normal_distribution<> ndvy(meanvy,sdvy);
119            normal_distribution<> ndvz(meanvz,sdvz);
120            variate_generator<mt19937&,normal_distribution<> > nd_vx(generator↩
                   , ndvx);
121            variate_generator<mt19937&,normal_distribution<> > nd_vy(generator↩
                   , ndvy);
122            variate_generator<mt19937&,normal_distribution<> > nd_vz(generator↩
                   , ndvz);
123
124 //-------------------------------------------------------------------------//
```

```
125
126         // Pointers declaration
127         double *x0, *y0, *z0, *Ndet, *end1, *end2, *end3, *end4, *end5, *end6,↩
                *end7;
128         char crd [2]; // Coordinates X, Y and Z
129         int index = 0; int idxpla = ipla;
130
131         // For loop for the number of planes
132         for(size_t p=0;p < npla; p++){
133
134              // For loop for the number of electrodes
135              for (size_t num=0; num < elec; num++)  {
136                 int number = int(num)+1;
137                 index = 0;
138
139                 // For loop for the spatial coordinates
140                 for (size_t r=0; r < 3; r++)     {
141                     if(index==0){
142                       strncpy(crd, "X", sizeof(crd));}
143                     if(index==1){
144                        strncpy(crd, "Y", sizeof(crd));}
145                     else if(index==2){
146                        strncpy(crd, "Z", sizeof(crd));}
147
148                     // This converts the string to a char
149                     char *buffer = new char[make_output_filename(idxpla, ↩
                          number, crd).length() + 1];
150                     strcpy(buffer, make_output_filename(idxpla, number, crd).↩
                          c_str());
151
152                     // File input reading
153                     ifstream file;
154                     file.open(buffer); // Opens file
155                     file.seekg(ios::beg); // Set position in input sequence
156                     vector<double> data; // Sequence container representing an↩
                           array that can change in size
157                     double i = 0; // This is needed to iterate between file ↩
                          and vector/array
158
159                     while(file >> i){
160                         data.push_back(i); // Adds number at the end of the ↩
                              array}
161
162                     file.close(); // To close the file
163
164                     // Storage of the values in a matrix E
165                     for (size_t j2=0;j2<46;j2++){
166                         for (size_t j1=0;j1<101;j1++){
167                             cout.precision(16);
```

```
168                             E[p][num][r][j1][j2] = data[j1+j2*101];}
169                     }
170                     index++;
171                     vector<double>().swap(data); // Swap frees data from the ↩
                            vector, but keeps its original size
172
173                 } // End coordinates
174             } // End electrodes
175
176         cout << "Reading plane Nr. " << idxpla << " completed!\n";
177         idxpla++;
178
179         } // End number of planes
180
181         cout << "File reading and creation of matrix E finished!!" << "\n";
182
183         //-------------------------------------------------------------------//
184
185         ofstream filesave;
186         filesave.open("TOF_270_sr.dat",fstream::out);
187
188         // Experimental conditions - time, time interval, number of particles,↩
               accelerations,...
189         double atstart = -1.25e7; // Acceleration
190         double vstart = 2000; // Initial velocity
191         double ac = 0; // Initialized value - dynamic centripetal acceleration↩
               set later
192         double tex = 2.3 * 1e-6; // Flight time between photoexcitation and ↩
              trap loading
193         double lengthpcb = 157.4e-3;
194         //double vfinal = 0;//sqrt(vstart * vstart + 2*at*lengthpcb);
195         //double lengthrem = lengthpcb - (vfinal*vfinal - vstart*vstart)/(2*at↩
              );
196         double tdecel = 500e-6;//-(vstart - vfinal)/at;//lengthpcb/vfinal;
197         double trise = 0.5 * 1e-6;
198         double tfall = 0.5 * 1e-6;
199         double maxtime = tdecel + trise + tfall;
200         double length = 0; //  Length initialized. Value set later in program
201         double radius = 0; //  Radius initialized. Value set later in program
202         double dt0 = 20 * 1e-9;
203         double d = 0.1 * 1e-3; // This is the spacing of the grid
204         int timesteps = static_cast<int> (maxtime/dt0);
205         int nparticles = 100000;
206
207         //-------------------------------------------------------------------//
208
209         // Memory allocation section
210         x0 = (double *) malloc(timesteps * sizeof(double));
211         y0 = (double *) malloc(timesteps * sizeof(double));
```

```
212         z0 = (double *) malloc(timesteps * sizeof(double));
213         Ndet = (double *) malloc(timesteps * sizeof(double));
214         end1 = (double *) malloc(nparticles * sizeof(double));
215         end2 = (double *) malloc(nparticles * sizeof(double));
216         end3 = (double *) malloc(nparticles * sizeof(double));
217         end4 = (double *) malloc(nparticles * sizeof(double));
218         end5 = (double *) malloc(nparticles * sizeof(double));
219         end6 = (double *) malloc(nparticles * sizeof(double));
220         end7 = (double *) malloc(nparticles * sizeof(double));
221
222         cout << "Memory allocated!!" << "\n";
223
224          //-------------------------------------------------------------------------//
225         // Variables declaration
226         double time = 0; double time_temp = 0; double tdet = 0; double xdet = ↩
                0; double ydet = 0; double zdet = 0; double vx0 = 0; double ↩
                vx_temp = 0; double vx = 0; double vy0 = 0; double vy_temp = 0; ↩
                double vy = 0; double vz0 = 0; double vz_temp = 0; double vz = 0; ↩
                double Ex = 0; double Ey = 0; double Ez = 0; double Exd = 0; ↩
                double Eyd = 0; double Ezd = 0; double Ex_temp = 0; double Ey_temp↩
                 = 0; double Ez_temp = 0; double Exd_temp = 0; double Eyd_temp = ↩
                0; double Ezd_temp = 0; double Exp = 0; double Eyp = 0; double Ezp↩
                 = 0; double Exdp = 0; double Eydp = 0; double Ezdp = 0; double ↩
                Exp_temp = 0; double Eyp_temp = 0; double Ezp_temp = 0; double ↩
                Exdp_temp = 0; double Eydp_temp = 0; double Ezdp_temp = 0; double ↩
                Ex2 = 0; double Ey2 = 0; double Ez2 = 0; double Exd2 = 0; double ↩
                Eyd2 = 0; double Ezd2 = 0; double Ex2_temp = 0; double Ey2_temp = ↩
                0; double Ez2_temp = 0; double Exd2_temp = 0; double Eyd2_temp = ↩
                0; double Ezd2_temp = 0; double Exp2 = 0; double Eyp2 = 0; double ↩
                Ezp2 = 0; double Exdp2 = 0; double Eydp2 = 0; double Ezdp2 = 0; ↩
                double Exp2_temp = 0; double Eyp2_temp = 0; double Ezp2_temp = 0; ↩
                double Exdp2_temp = 0; double Eydp2_temp = 0; double Ezdp2_temp = ↩
                0; double Ex3 = 0; double Ey3 = 0; double Ez3 = 0; double Exd3 = ↩
                0; double Eyd3 = 0; double Ezd3 = 0; double Ex3_temp = 0; double ↩
                Ey3_temp = 0; double Ez3_temp = 0; double Exd3_temp = 0; double ↩
                Eyd3_temp = 0; double Ezd3_temp = 0; double Exp3 = 0; double Eyp3 ↩
                = 0; double Ezp3 = 0; double Exdp3 = 0; double Eydp3 = 0; double ↩
                Ezdp3 = 0; double Exp3_temp = 0; double Eyp3_temp = 0; double ↩
                Ezp3_temp = 0; double Exdp3_temp = 0; double Eydp3_temp = 0; ↩
                double Ezdp3_temp = 0; double Exp4 = 0; double Eyp4 = 0; double ↩
                Ezp4 = 0; double Exdp4 = 0; double Eydp4 = 0; double Ezdp4 = 0; ↩
                double Exp4_temp = 0; double Eyp4_temp = 0; double Ezp4_temp = 0;
227
228         double Exdp4_temp = 0; double Eydp4_temp = 0; double Ezdp4_temp = 0; ↩
                double Exp5 = 0; double Eyp5 = 0; double Ezp5 = 0; double Exdp5 = ↩
                0; double Eydp5 = 0; double Ezdp5 = 0; double Exp5_temp = 0; ↩
                double Eyp5_temp = 0; double Ezp5_temp = 0; double Exdp5_temp = 0;↩
                 double Eydp5_temp = 0; double Ezdp5_temp = 0; double Exdd = 0; ↩
                double Eydd = 0; double Ezdd = 0; double Exdd_temp = 0; double ↩
```

```
            Eydd_temp = 0; double Ezdd_temp = 0; double Exdpd = 0; double ↩
            Eydpd = 0; double Ezdpd = 0; double Exdpd_temp = 0; double ↩
            Eydpd_temp = 0; double Ezdpd_temp = 0; double Exd2d = 0; double ↩
            Eyd2d = 0; double Ezd2d = 0; double Exd2d_temp = 0; double ↩
            Eyd2d_temp = 0; double Ezd2d_temp = 0; double Exdp2d = 0; double ↩
            Eydp2d = 0; double Ezdp2d = 0; double Exdp2d_temp = 0; double ↩
            Eydp2d_temp = 0; double Ezdp2d_temp = 0; double Etot = 0; double ↩
            Etotp = 0; double Etot2 = 0; double Etotp2 = 0; double Etotd = 0; ↩
            double Etotdp = 0; double Etotd2 = 0; double Etotdp2 = 0; double ↩
            Etot3 = 0; double Etotp3 = 0; double Etotp4 = 0; double Etotp5 = ↩
            0; double Etotd3 = 0; double Etotdp3 = 0; double Etotdp4 = 0; ↩
            double Etotdp5 = 0; double Etotdd = 0; double Etotdpd = 0; double ↩
            Etotd2d = 0; double Etotdp2d = 0; double EF1 = 0; double EF2 = 0; ↩
            double EF3 = 0; double EF4 = 0; double EF5 = 0; double EF6 = 0; ↩
            double EF7 = 0; double EF8 = 0; double EF9 = 0; double EF10 = 0; ↩
            double EF11 = 0; double EFd1 = 0; double EFd2 = 0; double EFd3 = ↩
            0; double EFd6 = 0; double EFd8 = 0; double EFd10 = 0; double EFsp↩
             = 0; double EFsdp = 0; double EFs = 0; double EFd1d = 0; double ↩
            EFd2d = 0; double EF3dd = 0; double Vpseudo1 = 0; double Vpseudo1p↩
             = 0; double Vpseudo1pp = 0; double Vzero4 = 0; double Vzero6 = 0;↩
              double Vzero7 = 0; double Vzero5 = 0; double Vtot3 = 0; double ↩
            Vtot4 = 0; double Vtot5 = 0; double Vtot6 = 0; double Vpseudo2 = ↩
            0; double Vpseudo2p = 0; double Vpseudo2pp = 0; double Vzero1 = 0;↩
             double Vzero2 = 0; double Vzero3 = 0; double Vtot1 = 0; double ↩
            Vtot2 = 0; double Vzerod3 = 0; double Vzerod3d = 0; double Vtotalx↩
             = 0; double Vtotaly = 0; double Vtotalz = 0;
229
230         double accelx = 0; // Initial acceleration in the y-dim in m/s2
231         double accely = 0; // Initial acceleration in the y-dim in m/s2
232         double accelz = 0; // Initial acceleration in the z-dim in m/s2
233
234         // Indices, arrays, fields, gradient, potentials declaration
235         int idx_z = 0;int idx_y = 0; int idx_x = 0; int idx_zp = 0;int idx_yp ↩
                = 0; int idx_xp = 0;int idx_zp2 = 0;int idx_yp2 = 0;int idx_xp2 = ↩
                0;int idx_z2 = 0;int idx_y2 = 0;int idx_x2 = 0; int idx_zd = 0;int↩
                 idx_yd = 0;int idx_xd = 0;int idx_zdp = 0;int idx_ydp = 0;int ↩
                idx_xdp = 0;int idx_zdp2 = 0;int idx_ydp2 = 0;int idx_xdp2 = 0;int↩
                 idx_zd2 = 0;int idx_yd2 = 0;int idx_xd2 = 0;int idx_z3 = 0; int ↩
                idx_y3 = 0; int idx_x3 = 0; int idx_zp3 = 0; int idx_yp3 = 0; int ↩
                idx_xp3 = 0;int idx_zd3 = 0; int idx_yd3 = 0; int idx_xd3 = 0; int↩
                 idx_zdp3 = 0; int idx_ydp3 = 0; int idx_xdp3 = 0;int idx_zp4 = 0;↩
                 int idx_yp4 = 0; int idx_xp4 = 0; int idx_zp5 = 0; int idx_yp5 = ↩
                0; int idx_xp5 = 0;int idx_zdp4 = 0; int idx_ydp4 = 0; int ↩
                idx_xdp4 = 0; int idx_zdp5 = 0; int idx_ydp5 = 0; int idx_xdp5 = ↩
                0;int idx_zdd = 0;int idx_ydd = 0;int idx_xdd = 0; int idx_zdpd = ↩
                0;int idx_ydpd = 0;int idx_xdpd = 0;int idx_zdp2d = 0; int ↩
                idx_ydp2d = 0;int idx_xdp2d = 0;int idx_zd2d = 0;int idx_yd2d = 0;↩
                 int idx_xd2d = 0;
236
```

```
237         // First and second derivatives of the fields
238         double slope1 = 0; double slope2 = 0; double slope3 = 0; double slope4 ↩
                = 0; double slope5 = 0; double slope6 = 0; double slope7 = 0; ↩
               double slope8 = 0; double slope9 = 0; double slope10 = 0; double ↩
               slope11 = 0; double slope12 = 0; double slope13 = 0; double slope14↩
                = 0; double slope15 = 0; double slope16 = 0; double slope17 = 0; ↩
               double slope18 = 0; double vslopez = 0; double vslopex = 0; double ↩
               vslopey = 0; double vslopex2 = 0; double vslopey2 = 0; double ↩
               vslopez2 = 0; double sloped1 = 0; double sloped2 = 0; double ↩
               sloped3 = 0; double sloped6 = 0; double sloped8 = 0; double slopex ↩
               = 0; double slopey = 0; double slopez = 0; double slopex2 = 0; ↩
               double slopey2 = 0; double slopez2 = 0; double grad1 = 0; double ↩
               grad2 = 0; double grad3 = 0; double gradx = 0; double grady = 0; ↩
               double gradz = 0; double intslopex = 0; double intslopey = 0; ↩
               double intslopez = 0; double intvslopex = 0; double intvslopey = 0;↩
                double intvslopez = 0; double V1 = 0; double V2 = 0; double V3 = ↩
               0; double V4 = 0; double V5 = 0; double SB1 = 0; double SB2 = 0; ↩
               double sign = 0; double factor = 0; double factor2 = 0;
239
240         // Positions and velocities declaration before trap loading
241         double xex = 0; double xex0 = 0; double vxex0 = 0; double yex = 0; ↩
                double zex = 0;
242         double yex0 = 0; double zex0 = 0; double vyex0 = 0; double vzex0 = 0;
243
244         // Arrays initialisation for inserting zero values in the arrays
245         for(size_t pcount=1;pcount<nparticles;pcount++){
246             end1[pcount] = 0; end2[pcount] = 0; end3[pcount] = 0; end4[pcount]↩
                     = 0; end5[pcount] = 0; end6[pcount] = 0; end7[pcount] = 0;
247         }
248         for(size_t pcount2=1;pcount2<timesteps;pcount2++){
249             Ndet[pcount2] = 0;
250         }
251
252         // Photoexcitation section
253         int partcount = 0; double random = 0; double xphoto = 0; double yphoto↩
                = 0; double zphoto = 0; double vxphoto = 0; double vyphoto = 0; ↩
               double vzphoto = 0; double timevalve2photo = 18e-2/vstart; double ↩
               gaussx = 0; double gaussy = 0;
254
255         while (partcount < nparticles){
256             gaussx = 0; gaussy = 0; xphoto = 0; yphoto = 0; zphoto = 0; ↩
                    vxphoto = 0; vyphoto = 0; vzphoto = 0; random = 0;
257
258             vxphoto = nd_vx(); vyphoto = nd_vy(); vzphoto = nd_vz();
259             xphoto = ud_x() + (vxphoto)*timevalve2photo;
260             yphoto = ud_y() + (vyphoto)*timevalve2photo;
261             zphoto = ud_z() + (vzphoto)*timevalve2photo;
262
263             gaussx = exp(-((xphoto-pmeanx)*(xphoto-pmeanx))/(2*psdx*psdx));
```

```
264             gaussy = exp(-((yphoto-pmeany)*(yphoto-pmeany))/(2*psdy*psdy));
265
266             random = rnd();
267             if (random <= gaussx) {
268                 if(random <= gaussy) {
269                     if (zphoto >= pminz) {
270                         if (zphoto <= pmaxz) {
271
272                         end1[partcount] = xphoto; end2[partcount] = yphoto; ↩
                            end3[partcount] = zphoto; end4[partcount] = ↩
                            vxphoto; end5[partcount] = vyphoto; end6[partcount↩
                            ] = vzphoto;
273
274                         partcount++;
275             }}}}
276
277         } // End while loop partcount
278
279         cout << "Photoexcitation section finished!!" << "\n";
280
281         // Beginning of the particles loop
282         cout << "Particle loop started!!" << "\n";
283         nparticles++;
284         for (size_t sdx=1;sdx<nparticles;sdx++){ // Particles loop
285
286            // Output particle count
287            cout << sdx << "\n";
288
289            // Variables in nparticles-loop set to zero
290            sign = 0; xex = 0; xex0 = 0; vxex0 = 0; yex = 0; zex = 0; yex0 = 0;↩
                    zex0 = 0; vyex0 = 0; vzex0 = 0; vx_temp = 0; vy_temp = 0; ↩
                vz_temp = 0; det = 0; ydet = 0; zdet = 0; tdet = 0; vx = 0; vy ↩
                = 0; vz = 0;
291
292            // Particle position calculation before the fields are activated
293            xex0 = end1[sdx]; yex0 = end2[sdx]; zex0 = end3[sdx];
294            vxex0 = end4[sdx]; vyex0 = end5[sdx]; vzex0 = end6[sdx];
295
296            xex = xex0 + vxex0 * tex;
297            yex = yex0 + vyex0 * tex;
298            zex = zex0 + vzex0 * tex;
299
300            // Initialize the arrays with zero values
301            for(size_t count=0;count<timesteps;count++){
302               x0[count] = 0; y0[count] = 0; z0[count] = 0;
303            }
304
305            // Re-initialisation of the arrays.
```

```
306          end1[sdx] = 0; end2[sdx] = 0; end3[sdx] = 0; end4[sdx] = 0; end5[↩
                 sdx] = 0; end6[sdx] = 0;
307
308         // Particle position
309         x0[0] = xex; // Initial x position in m
310         y0[0] = yex; // Initial y position in m
311         z0[0] = zex; // Initial z position in m
312
313         // Trap position in the z-dimension
314         double ztrap = vstart*tex;
315         double ztrap_temp = 0; double Ndet_temp = 0; double vztrap = vstart;↩
                double vztrap_temp = 0; double at = atstart;
316
317         vx0 = vxex0; // Initial velocity in the y-dim in m/s
318         vy0 = vyex0; // Initial velocity in the y-dim in m/s
319         vz0 = vzex0; // Initial velocity in the z-dim in m/s
320         vx_temp = vx0; vy_temp = vy0; vz_temp = vz0;
321         // Initial time (set to zero)
322         time = 0; time_temp = 0;
323
324         // If-condition in case the particles are out of the boundaries ↩
                after in-coupling time
325         if(xex < double(ipla)/1e4 || xex > double(ipla + 2*(npla-1))/1e4 || ↩
                yex <= 0e-3 || yex >= 4.5e-3 || zex <= 0.0e-3 || zex >= 10.0e-3)↩
                {
326             sign = 1;
327             break;
328         }
329
330         // Each particle is loaded in a trap and let evolve for a time ↩
                length corresponding to the guiding, acceleration or ↩
                deceleration time. This calculation is carried out in the moving↩
                frame of reference of the trap.
331
332         for (size_t tidx=1;tidx<timesteps;tidx++){
333
334            // Variables reset to zero
335            Etot = 0; Etot2 = 0; Etotp = 0; Etotp2 = 0; Vpseudo1 = 0; ↩
                   Vpseudo1p = 0; Vpseudo1pp = 0; Vzero6 = 0; Vtot6 = 0; ↩
                   Vzerod3d = 0; Etot3 = 0; Etotp3 = 0; Etotd3 = 0; Etotdp3 = 0;↩
                    Etotp4 = 0; Etotp5 = 0; Etotdp4 = 0; Etotdp5 = 0; Etotdd = ↩
                   0; Etotdpd = 0; Etotd2d = 0; Etotdp2d = 0; EF1 = 0; EF2 = 0; ↩
                   EF3 = 0; EF4 = 0; EF5 = 0; EF6 = 0; EF7 = 0; EF8 = 0; EF9 = ↩
                   0; EFd1 = 0; EFd2 = 0; EFd3 = 0; EFd6 = 0; EFd8 = 0; EFsp = ↩
                   0; EFsdp = 0; EFs = 0; EFd1d = 0; EFd2d = 0; EF3dd = 0; ↩
                   Vzero4 = 0; Vzero5 = 0; Vzero7 = 0; slope1 = 0; slope2 = 0; ↩
                   slope3 = 0; slope4 = 0; slope5 = 0; slope6 = 0; slope7 = 0; ↩
                   slope8 = 0; slope9 = 0; slope10 = 0; slope11 = 0; slope12 = ↩
                   0; slope13 = 0; slope14 = 0; slope15 = 0; slope16 = 0; ↩
```

```
                slope17 = 0; slope18 = 0; sloped1 = 0; sloped2 = 0; sloped3 =↩
                 0; sloped6 = 0; sloped8 = 0; slopex = 0; slopey = 0; slopez ↩
                = 0; slopex2 = 0; slopey2 = 0; slopez2 = 0; vslopex = 0; ↩
                vslopey = 0; vslopez = 0; vslopex2 = 0; vslopey2 = 0; ↩
                vslopez2 = 0; grad1 = 0; grad2 = 0; grad3 = 0; gradx = 0; ↩
                grady = 0; gradz = 0; intslopex = 0; intslopey = 0; intslopez↩
                 = 0; intvslopex = 0; intvslopey = 0; intvslopez = 0; ↩
                Vpseudo2 = 0; Vpseudo2p = 0; Vpseudo2pp = 0; Vtot4 = 0; Vtot5↩
                 = 0; Vzero1 = 0; Vzero2 = 0; Vtot1 = 0; Vtot2 = 0; Vtot3 = ↩
                0; Vzero3 = 0; Vzerod3 = 0;  factor = 0; factor2 = 0; Vtotalx↩
                 = 0; Vtotaly = 0; Vtotalz = 0;
336
337             ac = 0; // Re-initialized centripetal acceleration
338             length = 0; // Re-initialized length flight path
339             radius = 0; // Re-initialized radius
340
341             // Indices cleared at each tidx loop to avoid overwriting
342             idx_zd = 0;idx_yd = 0;idx_xd = 0; idx_zdp = 0; idx_ydp = 0; ↩
                    idx_xdp = 0; idx_zdp2 = 0; idx_ydp2 = 0; idx_xdp2 = 0; ↩
                    idx_zd2 = 0; idx_yd2 = 0; idx_xd2 = 0; idx_z = 0; idx_y = 0;↩
                     idx_x = 0; idx_zp = 0; idx_yp = 0; idx_xp = 0; idx_zp2 = 0;↩
                     idx_yp2 = 0; idx_xp2 = 0; idx_z2 = 0; idx_y2 = 0; idx_x2 = ↩
                    0; idx_z3 = 0; idx_y3 = 0; idx_x3 = 0; idx_zp3 = 0; idx_yp3 ↩
                    = 0; idx_xp3 = 0; idx_zd3 = 0; idx_yd3 = 0; idx_xd3 = 0; ↩
                    idx_zdp3 = 0; idx_ydp3 = 0; idx_xdp3 = 0; idx_zp4 = 0; ↩
                    idx_yp4 = 0; idx_xp4 = 0; idx_zp5 = 0; idx_yp5 = 0; idx_xp5 ↩
                    = 0; idx_zdp4 = 0; idx_ydp4 = 0; idx_xdp4 = 0; idx_zdp5 = 0;↩
                     idx_ydp5 = 0; idx_xdp5 = 0; idx_zdd = 0;idx_ydd = 0;idx_xdd↩
                     = 0; idx_zdpd = 0; idx_ydpd = 0; idx_xdpd = 0; idx_zdp2d = ↩
                    0; idx_ydp2d = 0; idx_xdp2d = 0; idx_zd2d = 0; idx_yd2d = 0;↩
                     idx_xd2d = 0;
343
344             // Determination of time, positions and velocities for each tidx↩
                    loop
345             time = time_temp + dt0;
346             vx = vx_temp + dt0*accelx;
347             vy = vy_temp + dt0*accely;
348             vz = vz_temp + dt0*accelz;
349             x0[tidx] = x0[tidx-1] + dt0*vx; // Symplectic Euler integration
350             y0[tidx] = y0[tidx-1] + dt0*vy; // Symplectic Euler integration
351             z0[tidx] = z0[tidx-1] + dt0*vz; // Symplectic Euler integration
352
353             vx_temp = vx; vy_temp = vy; vz_temp = vz; time_temp = time; ↩
                    vztrap_temp = vztrap; ztrap_temp = ztrap;
354             ztrap = ztrap_temp + vztrap * dt0 + 0.5 * at * dt0 * dt0;
355             vztrap = vztrap_temp + at * dt0;
356             if (vztrap < 0){
357                 at = 0;
358                 vztrap = 0;
```

```
359             }
360
361           // Determination of the centripetal acceleration for each time-step in the loop (negative sign because of the direction of the curvature)
362           length = vstart * time + 0.5 * at * time * time;
363           radius = 0.81; // Radius for the decelerator section
364            ac = -(vstart*vstart + at*at*time*time + 2*vstart*at*time)/radius;
365
366           // Accelerations caused by the field gradients calculated in the previous time-step are re-initialized
367           accelx = 0; accely = 0; accelz = 0;
368
369           // Boundaries during guiding, acceleration or deceleration
370           if(x0[tidx] < double(ipla)/1e4 || x0[tidx] > double(ipla + 2*(npla-1))/1e4 || y0[tidx] <= 0e-3 || y0[tidx] >= 4.5e-3 || z0[tidx] <= 0.0e-3 || z0[tidx] >= 10.0e-3) {
371               sign = 1;
372               break;
373           }
374
375           // Determination of the indices to access the field Matrix E
376           idx_x = int(floor(x0[tidx]*1e4)) - ipla;
377           idx_y = int(floor(y0[tidx]*1e4));
378           idx_z = int(floor(z0[tidx]*1e4));
379
380           idx_xp = idx_x + 0; idx_yp = idx_y + 0; idx_zp = idx_z + 1; idx_x2 = idx_x + 0; idx_y2 = idx_y + 1; idx_z2 = idx_z + 0; idx_xp2 = idx_x + 0; idx_yp2 = idx_y + 1; idx_zp2 = idx_z + 1; idx_xd = idx_x + 1; idx_yd = idx_y + 0; idx_zd = idx_z + 0; idx_xdp = idx_x + 1; idx_ydp = idx_y + 0; idx_zdp = idx_z + 1;  idx_xd2 = idx_x + 1; idx_yd2 = idx_y + 1; idx_zd2 = idx_z + 0; idx_xdp2 = idx_x + 1; idx_ydp2 = idx_y + 1; idx_zdp2 = idx_z + 1; idx_x3 = idx_x + 0; idx_y3 = idx_y + 2; idx_z3 = idx_z + 0; idx_xp3 = idx_x + 0;  idx_yp3 = idx_y + 2; idx_zp3 = idx_z + 1; idx_xd3 = idx_x + 1; idx_yd3 = idx_y + 2; idx_zd3 = idx_z + 0;  idx_xdp3 = idx_x + 1; idx_ydp3 = idx_y + 2; idx_zdp3 = idx_z + 1; idx_xp4 = idx_x + 0; idx_yp4 = idx_y + 0; idx_zp4 = idx_z + 2; idx_xp5 = idx_x + 0; idx_yp5 = idx_y + 1; idx_zp5 = idx_z + 2; idx_xdp4 = idx_x + 1; idx_ydp4 = idx_y + 0; idx_zdp4 = idx_z + 2; idx_xdp5 = idx_x + 1; idx_ydp5 = idx_y + 1; idx_zdp5 = idx_z + 2; idx_xdd = idx_x + 2; idx_ydd = idx_y + 0; idx_zdd = idx_z + 0; idx_xdpd = idx_x + 2; idx_ydpd = idx_y + 0; idx_zdpd = idx_z + 1; idx_xd2d = idx_x + 2; idx_yd2d = idx_y + 1; idx_zd2d = idx_z + 0;  idx_xdp2d = idx_x + 2; idx_ydp2d = idx_y + 1;idx_zdp2d = idx_z + 1;
381
```

```
382             // This section calculates the potentials for each segment of the ↩
                    decelerator
383             if (tidx <= int(trise/dt0) && trise > 0){
384                 factor = double(tidx-1)/double(int(trise/dt0));
385                 V1 = VE*cos(0*pi/5-pi) * factor; V2 = VE*cos(2*pi/5-pi) * ↩
                        factor; V3 = VE*cos(4*pi/5-pi) * factor;
386                 V4 = VE*cos(6*pi/5-pi) * factor; V5 = VE*cos(8*pi/5-pi) * ↩
                        factor;
387                 SB1 = VGP*cos(0*pi/5-pi*5) * factor; SB2 = SB1;
388             }
389
390             else if (tidx > int(trise/dt0) && tidx <= int((maxtime-tfall)/dt0)↩
                    ){
391                 V1 = VE*cos(0*pi/5-pi); V2 = VE*cos(2*pi/5-pi); V3 = VE*cos(4*↩
                        pi/5-pi);
392                 V4 = VE*cos(6*pi/5-pi); V5 = VE*cos(8*pi/5-pi); SB1 = VGP*cos↩
                        (0*pi/5-pi*5); SB2 = SB1;
393             }
394
395             else if (tidx > int((maxtime-tfall)/dt0) && tfall > 0){
396                 factor2 = 1 - (double(tidx) - double(int((maxtime-tfall)/dt0))↩
                        )/(double(int(maxtime/dt0))
397                                 - double(int((maxtime-tfall)/dt0)));
398                 V1 = VE*cos(0*pi/5-pi) * factor2; V2 = VE*cos(2*pi/5-pi) * ↩
                        factor2; V3 = VE*cos(4*pi/5-pi) * factor2;
399                 V4 = VE*cos(6*pi/5-pi) * factor2; V5 = VE*cos(8*pi/5-pi) * ↩
                        factor2;
400                 SB1 = VGP*cos(0*pi/5-pi*5) * factor2; SB2 = SB1;
401             }
402
403             // The potential vector elements are assigned individually
404             Vp [0] = SB1; Vp [1] = SB2; Vp [2] = V1; Vp [3] = V2; Vp [4] = V3;↩
                     Vp [5] = V4; Vp [6] = V5; Vp [7] = V1; Vp [8] = V2; Vp [9] = ↩
                    V3; Vp [10] = V4; Vp [11] = V5; Vp [12] = V1; Vp [13] = V2; Vp↩
                     [14] = VT;
405
406             // Fields calculation for each electrode of the decelerator
407             for (size_t num2=0; num2 < elec; num2++)  {
408                //----------------------idx_x category----------------------//
409                if (idx_x < npla - 1){
410                  Ex = Ex_temp + Vp[num2]*E[idx_x][num2][0][idx_z][idx_y];
411                  Ey = Ey_temp + Vp[num2]*E[idx_x][num2][1][idx_z][idx_y];
412                  Ez = Ez_temp + Vp[num2]*E[idx_x][num2][2][idx_z][idx_y];
413                  Exp = Exp_temp + Vp[num2]*E[idx_x][num2][0][idx_zp][idx_yp];
414                  Eyp = Eyp_temp + Vp[num2]*E[idx_x][num2][1][idx_zp][idx_yp];
415                  Ezp = Ezp_temp + Vp[num2]*E[idx_x][num2][2][idx_zp][idx_yp];
416                  Ex2 = Ex2_temp + Vp[num2]*E[idx_x][num2][0][idx_z2][idx_y2];
417                  Ey2 = Ey2_temp + Vp[num2]*E[idx_x][num2][1][idx_z2][idx_y2];
418                  Ez2 = Ez2_temp + Vp[num2]*E[idx_x][num2][2][idx_z2][idx_y2];
```

```
419                 Exp2 = Exp2_temp + Vp[num2]*E[idx_x][num2][0][idx_zp2][↩
                        idx_yp2];
420                 Eyp2 = Eyp2_temp + Vp[num2]*E[idx_x][num2][1][idx_zp2][↩
                        idx_yp2];
421                 Ezp2 = Ezp2_temp + Vp[num2]*E[idx_x][num2][2][idx_zp2][↩
                        idx_yp2];
422                 Ex3 = Ex3_temp + Vp[num2]*E[idx_x3][num2][0][idx_z3][idx_y3];
423                 Ey3 = Ey3_temp + Vp[num2]*E[idx_x3][num2][1][idx_z3][idx_y3];
424                 Ez3 = Ez3_temp + Vp[num2]*E[idx_x3][num2][2][idx_z3][idx_y3];
425                 Exp3 = Exp3_temp + Vp[num2]*E[idx_xp3][num2][0][idx_zp3][↩
                        idx_yp3];
426                 Eyp3 = Eyp3_temp + Vp[num2]*E[idx_xp3][num2][1][idx_zp3][↩
                        idx_yp3];
427                 Ezp3 = Ezp3_temp + Vp[num2]*E[idx_xp3][num2][2][idx_zp3][↩
                        idx_yp3];
428                 Exp4 = Exp4_temp + Vp[num2]*E[idx_xp4][num2][0][idx_zp4][↩
                        idx_yp4];
429                 Eyp4 = Eyp4_temp + Vp[num2]*E[idx_xp4][num2][1][idx_zp4][↩
                        idx_yp4];
430                 Ezp4 = Ezp4_temp + Vp[num2]*E[idx_xp4][num2][2][idx_zp4][↩
                        idx_yp4];
431                 Exp5 = Exp5_temp + Vp[num2]*E[idx_xp5][num2][0][idx_zp5][↩
                        idx_yp5];
432                 Eyp5 = Eyp5_temp + Vp[num2]*E[idx_xp5][num2][1][idx_zp5][↩
                        idx_yp5];
433                 Ezp5 = Ezp5_temp + Vp[num2]*E[idx_xp5][num2][2][idx_zp5][↩
                        idx_yp5];
434               }
435               else if (idx_x >= npla - 1){
436                 Ex = Ex_temp - Vp[num2]*E[2*(npla-1)-idx_x][num2][0][idx_z][↩
                        idx_y];
437                 Ey = Ey_temp - Vp[num2]*E[2*(npla-1)-idx_x][num2][1][idx_z][↩
                        idx_y];
438                 Ez = Ez_temp - Vp[num2]*E[2*(npla-1)-idx_x][num2][2][idx_z][↩
                        idx_y];
439                 Exp = Exp_temp - Vp[num2]*E[2*(npla-1)-idx_x][num2][0][idx_zp↩
                        ][idx_yp];
440                 Eyp = Eyp_temp - Vp[num2]*E[2*(npla-1)-idx_x][num2][1][idx_zp↩
                        ][idx_yp];
441                 Ezp = Ezp_temp - Vp[num2]*E[2*(npla-1)-idx_x][num2][2][idx_zp↩
                        ][idx_yp];
442                 Ex2 = Ex2_temp - Vp[num2]*E[2*(npla-1)-idx_x][num2][0][idx_z2↩
                        ][idx_y2];
443                 Ey2 = Ey2_temp - Vp[num2]*E[2*(npla-1)-idx_x][num2][1][idx_z2↩
                        ][idx_y2];
444                 Ez2 = Ez2_temp - Vp[num2]*E[2*(npla-1)-idx_x][num2][2][idx_z2↩
                        ][idx_y2];
445                 Exp2 = Exp2_temp - Vp[num2]*E[2*(npla-1)-idx_x][num2][0][↩
                        idx_zp2][idx_yp2];
```

```
446                 Eyp2 = Eyp2_temp - Vp[num2]*E[2*(npla-1)-idx_x][num2][1][↩
                        idx_zp2][idx_yp2];
447                 Ezp2 = Ezp2_temp - Vp[num2]*E[2*(npla-1)-idx_x][num2][2][↩
                        idx_zp2][idx_yp2];
448                 Ex3 = Ex3_temp - Vp[num2]*E[2*(npla-1)-idx_x3][num2][0][↩
                        idx_z3][idx_y3];
449                 Ey3 = Ey3_temp - Vp[num2]*E[2*(npla-1)-idx_x3][num2][1][↩
                        idx_z3][idx_y3];
450                 Ez3 = Ez3_temp - Vp[num2]*E[2*(npla-1)-idx_x3][num2][2][↩
                        idx_z3][idx_y3];
451                 Exp3 = Exp3_temp - Vp[num2]*E[2*(npla-1)-idx_xp3][num2][0][↩
                        idx_zp3][idx_yp3];
452                 Eyp3 = Eyp3_temp - Vp[num2]*E[2*(npla-1)-idx_xp3][num2][1][↩
                        idx_zp3][idx_yp3];
453                 Ezp3 = Ezp3_temp - Vp[num2]*E[2*(npla-1)-idx_xp3][num2][2][↩
                        idx_zp3][idx_yp3];
454                 Exp4 = Exp4_temp - Vp[num2]*E[2*(npla-1)-idx_xp4][num2][0][↩
                        idx_zp4][idx_yp4];
455                 Eyp4 = Eyp4_temp - Vp[num2]*E[2*(npla-1)-idx_xp4][num2][1][↩
                        idx_zp4][idx_yp4];
456                 Ezp4 = Ezp4_temp - Vp[num2]*E[2*(npla-1)-idx_xp4][num2][2][↩
                        idx_zp4][idx_yp4];
457                 Exp5 = Exp5_temp - Vp[num2]*E[2*(npla-1)-idx_xp5][num2][0][↩
                        idx_zp5][idx_yp5];
458                 Eyp5 = Eyp5_temp - Vp[num2]*E[2*(npla-1)-idx_xp5][num2][1][↩
                        idx_zp5][idx_yp5];
459                 Ezp5 = Ezp5_temp - Vp[num2]*E[2*(npla-1)-idx_xp5][num2][2][↩
                        idx_zp5][idx_yp5];
460               }
461               //--------------------idx_xd category--------------------//
462               if (idx_xd < npla - 1){
463                 Exd = Exd_temp + Vp[num2]*E[idx_xd][num2][0][idx_zd][idx_yd];
464                 Eyd = Eyd_temp + Vp[num2]*E[idx_xd][num2][1][idx_zd][idx_yd];
465                 Ezd = Ezd_temp + Vp[num2]*E[idx_xd][num2][2][idx_zd][idx_yd];
466                 Exdp = Exdp_temp + Vp[num2]*E[idx_xd][num2][0][idx_zdp][↩
                        idx_ydp];
467                 Eydp = Eydp_temp + Vp[num2]*E[idx_xd][num2][1][idx_zdp][↩
                        idx_ydp];
468                 Ezdp = Ezdp_temp + Vp[num2]*E[idx_xd][num2][2][idx_zdp][↩
                        idx_ydp];
469                 Exd2 = Exd2_temp + Vp[num2]*E[idx_xd][num2][0][idx_zd2][↩
                        idx_yd2];
470                 Eyd2 = Eyd2_temp + Vp[num2]*E[idx_xd][num2][1][idx_zd2][↩
                        idx_yd2];
471                 Ezd2 = Ezd2_temp + Vp[num2]*E[idx_xd][num2][2][idx_zd2][↩
                        idx_yd2];
472                 Exdp2 = Exdp2_temp + Vp[num2]*E[idx_xd][num2][0][idx_zdp2][↩
                        idx_ydp2];
```

```
473                 Eydp2 = Eydp2_temp + Vp[num2]*E[idx_xd][num2][1][idx_zdp2][↩
                        idx_ydp2];
474                 Ezdp2 = Ezdp2_temp + Vp[num2]*E[idx_xd][num2][2][idx_zdp2][↩
                        idx_ydp2];
475                 Exd3 = Exd3_temp + Vp[num2]*E[idx_xd3][num2][0][idx_zd3][↩
                        idx_yd3];
476                 Eyd3 = Eyd3_temp + Vp[num2]*E[idx_xd3][num2][1][idx_zd3][↩
                        idx_yd3];
477                 Ezd3 = Ezd3_temp + Vp[num2]*E[idx_xd3][num2][2][idx_zd3][↩
                        idx_yd3];
478                 Exdp3 = Exdp3_temp + Vp[num2]*E[idx_xdp3][num2][0][idx_zdp3][↩
                        idx_ydp3];
479                 Eydp3 = Eydp3_temp + Vp[num2]*E[idx_xdp3][num2][1][idx_zdp3][↩
                        idx_ydp3];
480                 Ezdp3 = Ezdp3_temp + Vp[num2]*E[idx_xdp3][num2][2][idx_zdp3][↩
                        idx_ydp3];
481                 Exdp4 = Exdp4_temp + Vp[num2]*E[idx_xdp4][num2][0][idx_zdp4][↩
                        idx_ydp4];
482                 Eydp4 = Eydp4_temp + Vp[num2]*E[idx_xdp4][num2][1][idx_zdp4][↩
                        idx_ydp4];
483                 Ezdp4 = Ezdp4_temp + Vp[num2]*E[idx_xdp4][num2][2][idx_zdp4][↩
                        idx_ydp4];
484                 Exdp5 = Exdp5_temp + Vp[num2]*E[idx_xdp5][num2][0][idx_zdp5][↩
                        idx_ydp5];
485                 Eydp5 = Eydp5_temp + Vp[num2]*E[idx_xdp5][num2][1][idx_zdp5][↩
                        idx_ydp5];
486                 Ezdp5 = Ezdp5_temp + Vp[num2]*E[idx_xdp5][num2][2][idx_zdp5][↩
                        idx_ydp5];
487               }
488               else if (idx_xd >= npla - 1){
489                 Exd = Exd_temp - Vp[num2]*E[2*(npla-1)-idx_xd][num2][0][↩
                        idx_zd][idx_yd];
490                 Eyd = Eyd_temp - Vp[num2]*E[2*(npla-1)-idx_xd][num2][1][↩
                        idx_zd][idx_yd];
491                 Ezd = Ezd_temp - Vp[num2]*E[2*(npla-1)-idx_xd][num2][2][↩
                        idx_zd][idx_yd];
492                 Exdp = Exdp_temp - Vp[num2]*E[2*(npla-1)-idx_xd][num2][0][↩
                        idx_zdp][idx_ydp];
493                 Eydp = Eydp_temp - Vp[num2]*E[2*(npla-1)-idx_xd][num2][1][↩
                        idx_zdp][idx_ydp];
494                 Ezdp = Ezdp_temp - Vp[num2]*E[2*(npla-1)-idx_xd][num2][2][↩
                        idx_zdp][idx_ydp];
495                 Exd2 = Exd2_temp - Vp[num2]*E[2*(npla-1)-idx_xd][num2][0][↩
                        idx_zd2][idx_yd2];
496                 Eyd2 = Eyd2_temp - Vp[num2]*E[2*(npla-1)-idx_xd][num2][1][↩
                        idx_zd2][idx_yd2];
497                 Ezd2 = Ezd2_temp - Vp[num2]*E[2*(npla-1)-idx_xd][num2][2][↩
                        idx_zd2][idx_yd2];
```

```
498                 Exdp2 = Exdp2_temp - Vp[num2]*E[2*(npla-1)-idx_xd][num2][0][↩
                        idx_zdp2][idx_ydp2];
499                 Eydp2 = Eydp2_temp - Vp[num2]*E[2*(npla-1)-idx_xd][num2][1][↩
                        idx_zdp2][idx_ydp2];
500                 Ezdp2 = Ezdp2_temp - Vp[num2]*E[2*(npla-1)-idx_xd][num2][2][↩
                        idx_zdp2][idx_ydp2];
501                 Exd3 = Exd3_temp - Vp[num2]*E[2*(npla-1)-idx_xd3][num2][0][↩
                        idx_zd3][idx_yd3];
502                 Eyd3 = Eyd3_temp - Vp[num2]*E[2*(npla-1)-idx_xd3][num2][1][↩
                        idx_zd3][idx_yd3];
503                 Ezd3 = Ezd3_temp - Vp[num2]*E[2*(npla-1)-idx_xd3][num2][2][↩
                        idx_zd3][idx_yd3];
504                 Exdp3 = Exdp3_temp - Vp[num2]*E[2*(npla-1)-idx_xdp3][num2↩
                        ][0][idx_zdp3][idx_ydp3];
505                 Eydp3 = Eydp3_temp - Vp[num2]*E[2*(npla-1)-idx_xdp3][num2↩
                        ][1][idx_zdp3][idx_ydp3];
506                 Ezdp3 = Ezdp3_temp - Vp[num2]*E[2*(npla-1)-idx_xdp3][num2↩
                        ][2][idx_zdp3][idx_ydp3];
507                 Exdp4 = Exdp4_temp - Vp[num2]*E[2*(npla-1)-idx_xdp4][num2↩
                        ][0][idx_zdp4][idx_ydp4];
508                 Eydp4 = Eydp4_temp - Vp[num2]*E[2*(npla-1)-idx_xdp4][num2↩
                        ][1][idx_zdp4][idx_ydp4];
509                 Ezdp4 = Ezdp4_temp - Vp[num2]*E[2*(npla-1)-idx_xdp4][num2↩
                        ][2][idx_zdp4][idx_ydp4];
510                 Exdp5 = Exdp5_temp - Vp[num2]*E[2*(npla-1)-idx_xdp5][num2↩
                        ][0][idx_zdp5][idx_ydp5];
511                 Eydp5 = Eydp5_temp - Vp[num2]*E[2*(npla-1)-idx_xdp5][num2↩
                        ][1][idx_zdp5][idx_ydp5];
512                 Ezdp5 = Ezdp5_temp - Vp[num2]*E[2*(npla-1)-idx_xdp5][num2↩
                        ][2][idx_zdp5][idx_ydp5];
513               }
514               //--------------------idx_xdd category--------------------//
515               if (idx_xdd < npla - 1){
516                 Exdd = Exdd_temp + Vp[num2]*E[idx_xdd][num2][0][idx_zdd][↩
                        idx_ydd];
517                 Eydd = Eydd_temp + Vp[num2]*E[idx_xdd][num2][1][idx_zdd][↩
                        idx_ydd];
518                 Ezdd = Ezdd_temp + Vp[num2]*E[idx_xdd][num2][2][idx_zdd][↩
                        idx_ydd];
519                 Exdpd = Exdpd_temp + Vp[num2]*E[idx_xdpd][num2][0][idx_zdpd][↩
                        idx_ydpd];
520                 Eydpd = Eydpd_temp + Vp[num2]*E[idx_xdpd][num2][1][idx_zdpd][↩
                        idx_ydpd];
521                 Ezdpd = Ezdpd_temp + Vp[num2]*E[idx_xdpd][num2][2][idx_zdpd][↩
                        idx_ydpd];
522                 Exd2d = Exd2d_temp + Vp[num2]*E[idx_xd2d][num2][0][idx_zd2d][↩
                        idx_yd2d];
523                 Eyd2d = Eyd2d_temp + Vp[num2]*E[idx_xd2d][num2][1][idx_zd2d][↩
                        idx_yd2d];
```

```
524                 Ezd2d = Ezd2d_temp + Vp[num2]*E[idx_xd2d][num2][2][idx_zd2d][↩
                        idx_yd2d];
525                 Exdp2d = Exdp2d_temp + Vp[num2]*E[idx_xdp2d][num2][0][↩
                        idx_zdp2d][idx_ydp2d];
526                 Eydp2d = Eydp2d_temp + Vp[num2]*E[idx_xdp2d][num2][1][↩
                        idx_zdp2d][idx_ydp2d];
527                 Ezdp2d = Ezdp2d_temp + Vp[num2]*E[idx_xdp2d][num2][2][↩
                        idx_zdp2d][idx_ydp2d];
528               }
529               else if (idx_xdd >= npla - 1){
530                 if (2*(npla-1)-idx_xdd >= 0) {
531                    Exdd = Exdd_temp - Vp[num2]*E[2*(npla-1)-idx_xdd][num2↩
                           ][0][idx_zdd][idx_ydd];
532                    Eydd = Eydd_temp - Vp[num2]*E[2*(npla-1)-idx_xdd][num2↩
                           ][1][idx_zdd][idx_ydd];
533                    Ezdd = Ezdd_temp - Vp[num2]*E[2*(npla-1)-idx_xdd][num2↩
                           ][2][idx_zdd][idx_ydd];
534                    Exdpd = Exdpd_temp - Vp[num2]*E[2*(npla-1)-idx_xdpd][num2↩
                           ][0][idx_zdpd][idx_ydpd];
535                    Eydpd = Eydpd_temp - Vp[num2]*E[2*(npla-1)-idx_xdpd][num2↩
                           ][1][idx_zdpd][idx_ydpd];
536                    Ezdpd = Ezdpd_temp - Vp[num2]*E[2*(npla-1)-idx_xdpd][num2↩
                           ][2][idx_zdpd][idx_ydpd];
537                    Exd2d = Exd2d_temp - Vp[num2]*E[2*(npla-1)-idx_xd2d][num2↩
                           ][0][idx_zd2d][idx_yd2d];
538                    Eyd2d = Eyd2d_temp - Vp[num2]*E[2*(npla-1)-idx_xd2d][num2↩
                           ][1][idx_zd2d][idx_yd2d];
539                    Ezd2d = Ezd2d_temp - Vp[num2]*E[2*(npla-1)-idx_xd2d][num2↩
                           ][2][idx_zd2d][idx_yd2d];
540                    Exdp2d = Exdp2d_temp - Vp[num2]*E[2*(npla-1)-idx_xdp2d][↩
                           num2][0][idx_zdp2d][idx_ydp2d];
541                    Eydp2d = Eydp2d_temp - Vp[num2]*E[2*(npla-1)-idx_xdp2d][↩
                           num2][1][idx_zdp2d][idx_ydp2d];
542                    Ezdp2d = Ezdp2d_temp - Vp[num2]*E[2*(npla-1)-idx_xdp2d][↩
                           num2][2][idx_zdp2d][idx_ydp2d];
543
544                 }
545                 else if (2*(npla-1)-idx_xdd < 0) {
546                    Exdd = Exdd_temp - Vp[num2]*E[2*(npla-1)-idx_xdd+1][num2↩
                           ][0][idx_zdd][idx_ydd];
547                    Eydd = Eydd_temp - Vp[num2]*E[2*(npla-1)-idx_xdd+1][num2↩
                           ][1][idx_zdd][idx_ydd];
548                    Ezdd = Ezdd_temp - Vp[num2]*E[2*(npla-1)-idx_xdd+1][num2↩
                           ][2][idx_zdd][idx_ydd];
549                    Exdpd = Exdpd_temp - Vp[num2]*E[2*(npla-1)-idx_xdpd+1][↩
                           num2][0][idx_zdpd][idx_ydpd];
550                    Eydpd = Eydpd_temp - Vp[num2]*E[2*(npla-1)-idx_xdpd+1][↩
                           num2][1][idx_zdpd][idx_ydpd];
```

```
551                 Ezdpd = Ezdpd_temp - Vp[num2]*E[2*(npla-1)-idx_xdpd+1][↩
                        num2][2][idx_zdpd][idx_ydpd];
552                 Exd2d = Exd2d_temp - Vp[num2]*E[2*(npla-1)-idx_xd2d+1][↩
                        num2][0][idx_zd2d][idx_yd2d];
553                 Eyd2d = Eyd2d_temp - Vp[num2]*E[2*(npla-1)-idx_xd2d+1][↩
                        num2][1][idx_zd2d][idx_yd2d];
554                 Ezd2d = Ezd2d_temp - Vp[num2]*E[2*(npla-1)-idx_xd2d+1][↩
                        num2][2][idx_zd2d][idx_yd2d];
555                 Exdp2d = Exdp2d_temp - Vp[num2]*E[2*(npla-1)-idx_xdp2d+1][↩
                        num2][0][idx_zdp2d][idx_ydp2d];
556                 Eydp2d = Eydp2d_temp - Vp[num2]*E[2*(npla-1)-idx_xdp2d+1][↩
                        num2][1][idx_zdp2d][idx_ydp2d];
557                 Ezdp2d = Ezdp2d_temp - Vp[num2]*E[2*(npla-1)-idx_xdp2d+1][↩
                        num2][2][idx_zdp2d][idx_ydp2d];
558               }
559             }
560             //-----------------------------------------------------------------//
561             Ex_temp = Ex; Ey_temp = Ey; Ez_temp = Ez; Exp_temp = Exp; ↩
                    Eyp_temp = Eyp; Ezp_temp = Ezp; Ex2_temp = Ex2; Ey2_temp = ↩
                    Ey2; Ez2_temp = Ez2; Exp2_temp = Exp2; Eyp2_temp = Eyp2; ↩
                    Ezp2_temp = Ezp2; Exd_temp = Exd; Eyd_temp = Eyd; Ezd_temp ↩
                    = Ezd; Exdp_temp = Exdp; Eydp_temp = Eydp; Ezdp_temp = Ezdp↩
                    ; Exd2_temp = Exd2; Eyd2_temp = Eyd2; Ezd2_temp = Ezd2; ↩
                    Exdp2_temp = Exdp2; Eydp2_temp = Eydp2; Ezdp2_temp = Ezdp2;↩
                     Ex3_temp = Ex3; Ey3_temp = Ey3; Ez3_temp = Ez3; Exp3_temp ↩
                    = Exp3; Eyp3_temp = Eyp3; Ezp3_temp = Ezp3; Exd3_temp = ↩
                    Exd3; Eyd3_temp = Eyd3; Ezd3_temp = Ezd3; Exdp3_temp = ↩
                    Exdp3; Eydp3_temp = Eydp3; Ezdp3_temp = Ezdp3; Exp4_temp = ↩
                    Exp4; Eyp4_temp = Eyp4; Ezp4_temp = Ezp4; Exp5_temp = Exp5;↩
                     Eyp5_temp = Eyp5; Ezp5_temp = Ezp5; Exdp4_temp = Exdp4; ↩
                    Eydp4_temp = Eydp4; Ezdp4_temp = Ezdp4; Exdp5_temp = Exdp5;↩
                     Eydp5_temp = Eydp5; Ezdp5_temp = Ezdp5; Exdd_temp = Exdd; ↩
                    Eydd_temp = Eydd; Ezdd_temp = Ezdd; Exdpd_temp = Exdpd; ↩
                    Eydpd_temp = Eydpd; Ezdpd_temp = Ezdpd; Exd2d_temp = Exd2d;↩
                     Eyd2d_temp = Eyd2d; Ezd2d_temp = Ezd2d; Exdp2d_temp = ↩
                    Exdp2d; Eydp2d_temp = Eydp2d; Ezdp2d_temp = Ezdp2d;
562
563           } // End fields extraction
564           // The total fields are calculated here below for the specific ↩
                  position determined by the indices.
565           Etot = sqrt(Ex*Ex+Ey*Ey+Ez*Ez);
566           Ex = 0; Ey = 0; Ez = 0; Ex_temp = 0; Ey_temp = 0; Ez_temp = 0;
567           Etotp = sqrt(Exp*Exp+Eyp*Eyp+Ezp*Ezp);
568           Exp = 0; Eyp = 0; Ezp = 0; Exp_temp = 0; Eyp_temp = 0; Ezp_temp = ↩
                  0;
569           Etot2 = sqrt(Ex2*Ex2+Ey2*Ey2+Ez2*Ez2);
570           Ex2 = 0; Ey2 = 0; Ez2 = 0; Ex2_temp = 0; Ey2_temp = 0; Ez2_temp = ↩
                  0;
571           Etotp2 = sqrt(Exp2*Exp2+Eyp2*Eyp2+Ezp2*Ezp2);
```

```
572             Exp2 = 0; Eyp2 = 0; Ezp2 = 0; Exp2_temp = 0; Eyp2_temp = 0; ↩
                    Ezp2_temp = 0;
573             Etotd = sqrt(Exd*Exd+Eyd*Eyd+Ezd*Ezd);
574             Exd = 0; Eyd = 0; Ezd = 0; Exd_temp = 0; Eyd_temp = 0; Ezd_temp = ↩
                    0;
575             Etotdp = sqrt(Exdp*Exdp+Eydp*Eydp+Ezdp*Ezdp);
576             Exdp = 0; Eydp = 0; Ezdp = 0; Exdp_temp = 0; Eydp_temp = 0; ↩
                    Ezdp_temp = 0;
577             Etotd2 = sqrt(Exd2*Exd2+Eyd2*Eyd2+Ezd2*Ezd2);
578             Exd2 = 0; Eyd2 = 0; Ezd2 = 0; Exd2_temp = 0; Eyd2_temp = 0; ↩
                    Ezd2_temp = 0;
579             Etotdp2 = sqrt(Exdp2*Exdp2+Eydp2*Eydp2+Ezdp2*Ezdp2);
580             Exdp2 = 0; Eydp2 = 0; Ezdp2 = 0; Exdp2_temp = 0; Eydp2_temp = 0; ↩
                    Ezdp2_temp = 0;
581             Etot3 = sqrt(Ex3*Ex3+Ey3*Ey3+Ez3*Ez3);
582             Ex3 = 0; Ey3 = 0; Ez3 = 0; Ex3_temp = 0; Ey3_temp = 0; Ez3_temp = ↩
                    0;
583             Etotp3 = sqrt(Exp3*Exp3+Eyp3*Eyp3+Ezp3*Ezp3);
584             Exp3 = 0; Eyp3 = 0; Ezp3 = 0; Exp3_temp = 0; Eyp3_temp = 0; ↩
                    Ezp3_temp = 0;
585             Etotd3 = sqrt(Exd3*Exd3+Eyd3*Eyd3+Ezd3*Ezd3);
586             Exd3 = 0; Eyd3 = 0; Ezd3 = 0; Exd3_temp = 0; Eyd3_temp = 0; ↩
                    Ezd3_temp = 0;
587             Etotdp3 = sqrt(Exdp3*Exdp3+Eydp3*Eydp3+Ezdp3*Ezdp3);
588             Exdp3 = 0; Eydp3 = 0; Ezdp3 = 0; Exdp3_temp = 0; Eydp3_temp = 0; ↩
                    Ezdp3_temp = 0;
589             Etotp4 = sqrt(Exp4*Exp4+Eyp4*Eyp4+Ezp4*Ezp4);
590             Exp4 = 0; Eyp4 = 0; Ezp4 = 0; Exp4_temp = 0; Eyp4_temp = 0; ↩
                    Ezp4_temp = 0;
591             Etotp5 = sqrt(Exp5*Exp5+Eyp5*Eyp5+Ezp5*Ezp5);
592             Exp5 = 0; Eyp5 = 0; Ezp5 = 0; Exp5_temp = 0; Eyp5_temp = 0; ↩
                    Ezp5_temp = 0;
593             Etotdp4 = sqrt(Exdp4*Exdp4+Eydp4*Eydp4+Ezdp4*Ezdp4);
594             Exdp4 = 0; Eydp4 = 0; Ezdp4 = 0; Exdp4_temp = 0; Eydp4_temp = 0; ↩
                    Ezdp4_temp = 0;
595             Etotdp5 = sqrt(Exdp5*Exdp5+Eydp5*Eydp5+Ezdp5*Ezdp5);
596             Exdp5 = 0; Eydp5 = 0; Ezdp5 = 0; Exdp5_temp = 0; Eydp5_temp = 0; ↩
                    Ezdp5_temp = 0;
597             Etotdd = sqrt(Exdd*Exdd+Eydd*Eydd+Ezdd*Ezdd);
598             Exdd = 0; Eydd = 0; Ezdd = 0; Exdd_temp = 0; Eydd_temp = 0; ↩
                    Ezdd_temp = 0;
599             Etotdpd = sqrt(Exdpd*Exdpd+Eydpd*Eydpd+Ezdpd*Ezdpd);
600             Exdpd = 0; Eydpd = 0; Ezdpd = 0; Exdpd_temp = 0; Eydpd_temp = 0; ↩
                    Ezdpd_temp = 0;
601             Etotd2d = sqrt(Exd2d*Exd2d+Eyd2d*Eyd2d+Ezd2d*Ezd2d);
602             Exd2d = 0; Eyd2d = 0; Ezd2d = 0; Exd2d_temp = 0; Eyd2d_temp = 0; ↩
                    Ezd2d_temp = 0;
603             Etotdp2d = sqrt(Exdp2d*Exdp2d+Eydp2d*Eydp2d+Ezdp2d*Ezdp2d);
```

```
604             Exdp2d = 0; Eydp2d = 0; Ezdp2d = 0; Exdp2d_temp = 0; Eydp2d_temp =↩
                    0; Ezdp2d_temp = 0;
605
606             // Linear interpolation section.
607
608                 // Group 1
609                 slope1 = (Etotp - Etot)/d;
610                 EF1 = Etot + slope1*(z0[tidx] - (floor(z0[tidx]*1e4)/1e4));
611                 slope2 = (Etotp2 - Etot2)/d;
612                 EF2 = Etot2 + slope2*(z0[tidx] - (floor(z0[tidx]*1e4)/1e4));
613                 slope3 = (EF2 - EF1)/d;
614                 EF3 = EF1 + slope3*(y0[tidx] - (floor(y0[tidx]*1e4)/1e4));
615
616                 // Group 2
617                 sloped1 = (Etotdp - Etotd)/d;
618                 EFd1 = Etotd + sloped1*(z0[tidx] - (floor(z0[tidx]*1e4)/1e4));
619                 sloped2 = (Etotdp2 - Etotd2)/d;
620                 EFd2 = Etotd2 + sloped2*(z0[tidx] - (floor(z0[tidx]*1e4)/1e4));
621                 sloped3 = (EFd2 - EFd1)/d;
622                 EFd3 = EFd1 + sloped3*(y0[tidx] - (floor(y0[tidx]*1e4)/1e4));
623
624                 // Group 2-II
625                 slope16 = (Etotdpd - Etotdd)/d;
626                 EFd1d = Etotdd + slope16*(z0[tidx] - (floor(z0[tidx]*1e4)/1e4))↩
                        ;
627                 slope17 = (Etotdp2d - Etotd2d)/d;
628                 EFd2d = Etotd2d + slope17*(z0[tidx] - (floor(z0[tidx]*1e4)/1e4)↩
                        );
629                 slope18 = (EFd2d - EFd1d)/d;
630                 EF3dd = EFd1d + slope18*(y0[tidx] - (floor(y0[tidx]*1e4)/1e4));
631
632                 //  Slope x
633                 slopex = (EFd3 - EF3)/d;
634                 slopex2 = (EF3dd - EFd3)/d;
635
636                 // Gradient between slopes x and interpolated slopex
637                 grad3 = (slopex2 - slopex)/d;
638                 intslopex = slopex + grad3*(x0[tidx] - (floor(x0[tidx]*1e4)/1e4↩
                        ));
639
640                 // Group 3
641                 slope4 = (EFd1 - EF1)/d;
642                 EF4 = EF1 + slope4*(x0[tidx] - (floor(x0[tidx]*1e4)/1e4));
643                 slope5 = (EFd2 - EF2)/d;
644                 EF5 = EF2 + slope5*(x0[tidx] - (floor(x0[tidx]*1e4)/1e4));
645
646                 // Group 3-II
647                 slope10 = (Etotp3 - Etot3)/d;
648                 EFsp = Etot3 + slope10*(z0[tidx] - (floor(z0[tidx]*1e4)/1e4));
```

```
649             slope11 = (Etotdp3 - Etotd3)/d;
650             EFsdp = Etotd3 + slope11*(z0[tidx] - (floor(z0[tidx]*1e4)/1e4))↩
                    ;
651             slope12 = (EFsdp - EFsp)/d;
652             EFs = EFsp + slope12*(x0[tidx] - (floor(x0[tidx]*1e4)/1e4));
653
654             // Slope y
655             slopey = (EF5 - EF4)/d;
656             slopey2 = (EFs - EF5)/d;
657
658             // Gradient between slopes y and interpolated slopey
659             grad1 = (slopey2 - slopey)/d;
660             intslopey = slopey + grad1*(y0[tidx] - (floor(y0[tidx]*1e4)/1e4↩
                    ));
661
662             // Group 4
663             slope6 = (Etot2 - Etot)/d;
664             EF6 = Etot + slope6*(y0[tidx] - (floor(y0[tidx]*1e4)/1e4));
665             sloped6 = (Etotd2 - Etotd)/d;
666             EFd6 = Etotd + sloped6*(y0[tidx] - (floor(y0[tidx]*1e4)/1e4));
667             slope7 = (EFd6 - EF6)/d;
668             EF7 = EF6 + slope7*(x0[tidx] - (floor(x0[tidx]*1e4)/1e4));
669
670             // Group 5
671             slope8 = (Etotp2 - Etotp)/d;
672             EF8 = Etotp + slope8*(y0[tidx] - (floor(y0[tidx]*1e4)/1e4));
673             sloped8 = (Etotdp2 - Etotdp)/d;
674             EFd8 = Etotdp + sloped8*(y0[tidx] - (floor(y0[tidx]*1e4)/1e4));
675             slope9 = (EFd8 - EF8)/d;
676             EF9 = EF8 + slope9*(x0[tidx] - (floor(x0[tidx]*1e4)/1e4));
677
678             // Group 5-II
679             slope13 = (Etotp5 - Etotp4)/d;
680             EF10 = Etotp4 + slope13*(y0[tidx] - (floor(y0[tidx]*1e4)/1e4));
681             slope14 = (Etotdp5 - Etotdp4)/d;
682             EFd10 = Etotdp4 + slope14*(y0[tidx] - (floor(y0[tidx]*1e4)/1e4)↩
                    );
683             slope15 = (EFd10 - EF10)/d;
684             EF11 = EF10 + slope15*(x0[tidx] - (floor(x0[tidx]*1e4)/1e4));
685
686             // Slope z
687             slopez = (EF9 - EF7)/d;
688             slopez2 = (EF11 - EF9)/d;
689
690             // Gradient between slopes z and interpolated slopez
691             grad2 = (slopez2 - slopez)/d;
692             intslopez = slopez + grad2*(z0[tidx] - (floor(z0[tidx]*1e4)/1e4↩
                    ));
693
```

```
694             // Potentials calculation - tangential acceleration
695             Vpseudo1 = mhe*at*(floor(z0[tidx]*1e4)/1e4 - 5.0e-3);
696             Vpseudo1p = mhe*at*(floor((z0[tidx] + d)*1e4)/1e4 - 5.0e-3);
697             Vpseudo1pp = mhe*at*(floor((z0[tidx] + 2*d)*1e4)/1e4 - 5.0e-3);
698             Vzero4 = EF7*1.5*nval*kval*e*a0;
699             Vzero5 = EF9*1.5*nval*kval*e*a0;
700             Vzero6 = EF11*1.5*nval*kval*e*a0;
701             Vtot4 = Vzero4 + Vpseudo1;
702             Vtot5 = Vzero5 + Vpseudo1p;
703             Vtot6 = Vzero6 + Vpseudo1pp;
704             vslopez = (Vtot5 - Vtot4)/d;
705             vslopez2 = (Vtot6 - Vtot5)/d;
706             gradz = (vslopez2 - vslopez)/d;
707             intvslopez = vslopez + gradz*(z0[tidx] - (floor(z0[tidx]*1e4)/1↩
                    e4));
708
709             // For calculating the fields, vslopez is more accurate
710             Vtotalz = Vtot4 + vslopez*(z0[tidx] - (floor(z0[tidx]*1e4)/1e4)↩
                    );
711
712             // Potentials calculation - centripetal acceleration
713             Vpseudo2 = mhe*ac*(floor(x0[tidx]*1e4)/1e4 - 6.5e-3);
714             Vpseudo2p = mhe*ac*(floor((x0[tidx] + d)*1e4)/1e4 - 6.5e-3);
715             Vpseudo2pp = mhe*ac*(floor((x0[tidx] + 2*d)*1e4)/1e4 - 6.5e-3);
716             Vzero1 = EF3*1.5*nval*kval*e*a0;
717             Vzero2 = EFd3*1.5*nval*kval*e*a0;
718             Vzero7 = EF3dd*1.5*nval*kval*e*a0;
719             Vtot1 = Vzero1 + Vpseudo2;
720             Vtot2 = Vzero2 + Vpseudo2p;
721             Vtot3 = Vzero7 + Vpseudo2pp;
722             vslopex = (Vtot2 - Vtot1)/d;
723             vslopex2 = (Vtot3 - Vtot2)/d;
724             gradx = (vslopex2 - vslopex)/d;
725             intvslopex = vslopex + gradx*(x0[tidx] - (floor(x0[tidx]*1e4)/1↩
                    e4));
726
727             // For calculating the fields, vslopex is more accurate
728             Vtotalx = Vtot1 + vslopex*(x0[tidx] - (floor(x0[tidx]*1e4)/1e4)↩
                    );
729
730             // Potentials calculation - y-dimension
731             Vzero3 = EF4*1.5*nval*kval*e*a0;
732             Vzerod3 = EF5*1.5*nval*kval*e*a0;
733             Vzerod3d = EFs*1.5*nval*kval*e*a0;
734             vslopey = (Vzerod3 - Vzero3)/d;
735             vslopey2 = (Vzerod3d - Vzerod3)/d;
736             grady = (vslopey2 - vslopey)/d;
737             intvslopey = vslopey + grady*(y0[tidx] - (floor(y0[tidx]*1e4)/1↩
                    e4));
```

```
738
739                 // For calculating the fields, vslopey is more accurate
740                 Vtotaly = Vzero3 + vslopey*(y0[tidx] - (floor(y0[tidx]*1e4)/1e4↩
                        ));
741
742                 // If a particle is ionised, it is excluded from the ↩
                        calculation
743                 if (EF5 >= Fion){
744                     sign = 1;
745                     break;
746                 }
747
748                 // Acceleration exerted on helium atoms during during the next ↩
                        timestep
749                 accelx = -intvslopex/mhe;
750                 accely = -intvslopey/mhe;
751                 accelz = -intvslopez/mhe;
752
753                 // In-situ detection boundaries
754                 if(x0[tidx] >= -0.5e-3 + 6.5e-3 && x0[tidx] <= 0.5e-3 + 6.5e-3 ↩
                        && y0[tidx] > 0.5e-3 && y0[tidx] < 4.0e-3 && z0[tidx] + ↩
                        ztrap - 5e-3 >= -0.5e-3 + lengthpcb + vstart*tex && z0[tidx↩
                        ] + ztrap - 5e-3 <= 0.5e-3 + lengthpcb + vstart*tex && sign↩
                         == 0) {
755                      Ndet_temp = Ndet[tidx];
756                      Ndet[tidx] = Ndet_temp + 1;
757                 }
758
759             } // End tidx
760             // The potential vector elements are set to zero
761             for (size_t i3 = 0;i3 < elec;i3++){
762                     Vp [i3] = 0;
763             }
764
765         } // End nparticles
766         cout << "Particle loop terminated!!" << "\n";
767
768     // Save to a file
769     for(size_t nc2=1;nc2<timesteps;nc2++){
770          filesave << double(nc2-1)*dt0 + tex << "\t" << Ndet[nc2] << "\n";
771     }
772
773     filesave.close();
774     cout << "Dat File saved!!" << endl;
775
776 return 0;
777 }
```

Bibliography

[1] R. Folman, P. Krueger, J. Schmiedmayer. Microscopic atom optics: from wires to an atom chip. *Advances in atomic, molecular and optical physics*, 48:263, 2002.

[2] J. Reichel, W. Haensel and T. W. Haensch. Atomic micromanipulation with magnetic surface traps. *Phys. Rev. Lett.*, 83:3398, 1999.

[3] R. Folman, P. Krueger, D. Cassettari, B. Hessmo, T. Maier and J. Schmiedmayer. Controlling cold atomc using nanofabricated surfaces: atom chips. *Phys. Rev. Lett.*, 84:4749, 2000.

[4] P. Krueger, X. Luo, M. W. Klein, K. Brugger, A. Haase, S. Wildermuth, S. Groth, I. Bar-Joseph, R. Folman and J. Schmiedmayer. Trapping and manipulating neutral atoms with electrostatic fields. *Phys. Rev. Lett.*, 91:233201, 2003.

[5] D. Cassettari, B. Hessmo, R. Folman, T. Maier and J. Schmiedmayer. Beam splitter for guided atoms. *Phys. Rev. Lett.*, 85:5483, 2000.

[6] E. A. Hinds and I. G. Hughes. Magnetic atom optics: mirrors, guides, traps and chips for atoms. *Journal of Physics D: Applied Physics*, 32:R119, 1999.

[7] D. Stick, W. K. Hensinger, S. Olmschenk, M. J. Madsen, K. Schwab and C. Monroe. Ion traps in a semiconductor chip. *Nature*, 2:36, 2006.

[8] O. J. Orient, A. Chutjian, and V. Garkanian. Miniature, high-resolution, quadruple mass spectrometer array. *Rev. Sci. Instr.*, 68:1393, 1997.

[9] S. Knappe, V. Shah, P. D. D. Schwindt, L. Hollberg and J. Kitching. A microfabricated atomic clock. *Applied Physics Letters*, 85:1460, 2004.

[10] J. I. Cirac and P. Zoller. A scalable quantum computer with ions in an array of microtraps. *Nature*, 404:579, 2000.

[11] D. Kielpinski, C. Monroe and D. J. Wineland. Architecture for a large-scale ion-trap quantum computer. *Nature*, 417:709, 2002.

[12] S. A. Schulz, H. L. Bethlem, J. van Veldhoven, J. Kuepper, H. Conrad, and G. Meijer. Microstructured switchable mirror for polar molecules. *Phys. Rev. Lett.*, 93:020406, 2004.

[13] S. A. Meek, H. L. Bethlem, H. Conrad, and G. Meijer. Trapping molecules on a chip in traveling potential wells. *Phys. Rev. Lett.*, 100:153003, 2008.

[14] S. A. Meek, H. Conrad, and G. Meijer. Trapping molecules on a chip. *Science*, 324:1699, 2009.

[15] Jinjun Liu, Edcel J. Salumbides, Urs Hollenstein, Jeroen C. J. Koelemeij, Kjeld S. E. Eikema, Wim Ubachs, and Frédéric Merkt. Determination of the ionization and dissociation energies of the hydrogen molecule. *J. Chem. Phys.*, 130:174306, 2009.

[16] D. Sprecher, Ch. Jungen, W. Ubachs and F. Merkt. Towards measuring the ionisation and dissociation energies of molecular hydrogen with sub-Mhz accuracy. *Faraday discussions*, 150:51, 2011.

[17] Th. A. Paul, J. Liu and F. Merkt. Nuclear-spin effects in the photoionization of krypton. *Phys. Rev. A*, 79:022505, 2009.

[18] A. Osterwalder and F. Merkt. Using Rydberg states as electric field sensors. *Phys. Rev. Lett.*, 82:1831, 1999.

[19] D. Sprecher, J. Liu, C. Jungen, W. Ubachs and F. Merkt. The ionisation and dissociation energies of hd. *J. Chem. Phys.*, 133:111102, 2010.

[20] J. Liu, D. Sprecher, C. Jungen, W. Ubachs and F. Merkt. Determination of the ionization and dissociation energies of the deuterium molecule (D_2). *J. Chem. Phys.*, 132:154301, 2010.

[21] J. Liu, D. Sprecher, F. Merkt, E. J. Salumbides and W. Ubachs. Determination of the ionization and dissociation energies of H_2 and He_2. *AIP Conf. Proc.*, 1504:495, 2012.

[22] G. Herzberg. Dissociation energy and ionization potential of molecular hydrogen. *Phys. Rev. Lett.*, 23:1081, 1969.

[23] A. Balakrishnan, V. Smith, and B. P. Stoicheff. Dissociation energies of the hydrogen and deuterium molecules. *Phys. Rev. A*, 49:2460, 1994.

[24] Y. P. Zhang, C. H. Cheng, J. T. Kim, J. Stanojevic, and E. E. Eyler. Dissociation energies of molecular hydrogen and the hydrogen molecular ion. *Phys. Rev. Lett.*, 92:203003, 2004.

[25] C. H. Cheng, J. T. Kim, E. E. Eyler, and N. Melikechi. Line shapes and decay dynamics of dissociative resonances above the second dissociation limit of molecular hydrogen. *Phys. Rev. A*, 57:949, 1998.

[26] T. A. Miller, V. E. Bondybey. *Molecular Ions: Spectroscopy, Structure and Chemistry*. Elsevier Science Ltd, 1983.

[27] T. A. Paul. *Development and spectroscopic applications of a solid-state vacuum ultraviolet laser system in atomic and molecular physics*. PhD thesis, ETH Zürich, 2008.

[28] S. D. Hogan. *Cold atoms and molecules by Zeeman deceleration and Rydberg-Stark deceleration*. Habilitation, ETH Zürich, 2012.

[29] T. Thiele, S. Filipp, J. A. Agner, J. Deiglmayr, M. Stammmeier, P. Allmendinger, F. Merkt and A. Wallraff. Manipulating Rydberg atoms close to surfaces at cryogenic temperatures. *Phys. Rev. A*, 90:013414, 2014.

[30] T. Thiele, J. Deiglmayr, M. Stammmeier, J. A. Agner, H. Schmutz, F. Merkt and A. Wallraff. Imaging electric fields in the vicinity of cryogenic surfaces using Rydberg atoms. *arXiv: 1509.05450*, 2015.

[31] F. C. Witteborn and W. M. Fairbank. Experimental comparison of the gravitational force on freely falling electrons and metallic electrons. *Phys. Rev. Lett.*, 19:1049, 1967.

[32] M. Amoretti, C. Amsler, G. Bonomi, A. Bouchta, P. Bowe, C. Carraro, C. L. Cesar, M. Charlton, M. J. T. Collier, M. Doser, V. Filippini, K. S. Fine, A. Fontana, M. C. Fujiwara,R. Funakoshi, P. Genova, J. S. Hangst, R. S. Hayano, M. H. Holzscheiter, L. V. Jørgensen, V.

Lagomarsino, R. Landua,D. Lindelo, E. Lodi Rizzini, M. Macrı, N. Madsen, G. Manuzio,M. Marchesotti, P. Montagna, H. Pruys, C. Regenfus, P. Riedler,J. Rochet, A. Rotondiq, G. Rouleau, G. Testera, A. Variola, T. L. Watson and D. P. van der Werf. Production and detection of cold antihydrogen atoms. *Nature*, 419:456, 2002.

[33] E. A. Hinds and V. Sandoghdar. Cavity QED level shifts of simple atoms. *Phys. Rev. A*, 43:398, 1991.

[34] V. Sandoghdar, C. I. Sukenik, S. Haroche and A. Hinds. Spectroscopy of atoms confined to the single node of a standing wave in a parallel cavity. *Phys. Rev. A*, 53:1919, 1996.

[35] D. F. Gray, Z. Zheng, K. A. Smith and F. B. Dunning. Ionisation of K(nd) Rydberg-state atoms at a surface. *Phys. Rev. A*, 38:1601, 1988.

[36] M. T. Bell and T. P. Softley. Ultracold molecules and ultracold chemistry. *Mol. Phys.*, 107:99, 2009.

[37] S. B. Hill, C. B. Haich, Z. Zhou, P. Nordlander, and F. B. Dunning. Ionization of xenon Rydberg atoms at a metal surface. *Phys. Rev. Lett.*, 85(25):5444, 2000.

[38] G. R. Lloyd, S. R. Procter, and T. P. Softley. Ionization of hydrogen Rydberg molecules at a metal surface. *Phys. Rev. Lett.*, 95:133202, 2005.

[39] G. Sashikesh, M. S. Ford, and T. P. Softley. Ionization of Rydberg h_2 molecules at doped silicon surfaces. *J. Chem. Phys.*, 138:114308, 2013.

[40] J. A. Gibbard, M. Dethlefsen, M. Kohlhoff, C. J. Rennick, E. So, M. Ford, T. P. Softley. Resonant charge transfer of hydrogen Rydberg atoms incident at a Cu(100) projected band-gap surface. *Phys. Rev. Lett.*, 115:093201, 2015.

[41] G. Rempe and H. Walther. Observation of quantum collapse and revival in a one-atom maser. *Phys. Rev. Lett.*, 58:353, 1987.

[42] M. Saffman and T. G. Walker. Creating single-atom and single-photon sources from entangled atomic ensembles. *Phys. Rev. A*, 66:065403, 2002.

[43] M. Saffman,T. G. Walker,and K. Mølmer. Quantum information with Rydberg atoms. *Rev. Mod. Phys.*, 82:2313, 2010.

[44] P. Filipovicz, P. Meystre, G. Rempe and H. Walther. Rydberg atoms - a testing ground for quantum electrodynamics. *Optica Acta*, 32:1105, 1985.

[45] P. Rabl, D. DeMille, J. M. Doyle, M. D. Lukin, R. J. Schoelkopf, and P. Zoller. Hybrid quantum processors: Molecular ensembles as quantum memory for solid state circuits. *Phys. Rev. Lett.*, 97:033003, 2006.

[46] A. Blais, R.-S. Huang, A. Wallraff, S. M. Girvin and R. J. Schoelkopf. Cavity quantum electrodynamics for superconducting electrical circuits: an architecture for quantum computation. *Phys. Rev. A*, 69:062320, 2004.

[47] S. D. Hogan, J. A. Agner, F. Merkt, T. Thiele, S. Filipp, and A. Wallraff. Driving Rydberg-Rydberg transitions from a coplanar microwave waveguide. *Phys. Rev. Lett.*, 108:063004, 2012.

[48] D. B. Cassidy and S. D. Hogan. Atom control and gravity measurements using Rydberg positronium. *Int. J. Mod. Phys. Conf. Ser.*, 30:1460259, 2014.

[49] E. A. Hessels, D. M. Homan, and M. J. Cavagnero. Two-stage Rydberg charge exchange: An efficient method for production of antihydrogen. *Phys. Rev. A*, 57:1668, 1998.

[50] W. A. Bertsche, E. Butler, M. Charlton and N. Madsen. Physics with antihydrogen. *J. Phys. B: At. Mol. Opt. Phys.*, 48:232001, 2015.

[51] D. B. Cassidy, T. H. Hisakado, H. W. K. Tom, and A. P. Mills, Jr. Positronium hyperfine interval measured via saturated absorption spectroscopy. *Phys. Rev. Lett.*, 109:073401, 2012.

[52] T. E. Wall, A. M. Alonso, B. S. Cooper, A. Deller, S. D. Hogan and D. B. Cassidy. Selective production of Rydberg-Stark states of positronium. *Phys. Rev. Lett.*, 114:173001, 2015.

[53] L. V. Jorgensen. The AEGIS antihydrogen gravity experiment. *Hyperfine Interactions*, 212:41, 2012.

[54] W. Gerlach and O. Stern. Der experimentelle Nachweis des magnetischen Moments des Silberatoms. *Z. Phys.*, 8:110, 1922.

[55] J. P. Gordon, H. J. Zeiger, and C. H. Townes. Molecular microwave oscillator and new hyperfine structure in the microwave spectrum of NH_3. *Phys. Rev.*, 95:282, 1954.

[56] W. H. Wing. Electrostatic trapping of neutral atomic particles. *Phys. Rev. Lett.*, 45(8):631–634, 1980.

[57] T. Breeden and H. Metcalf. Stark acceleration of Rydberg atoms in inhomogeneous electric fields. *Phys. Rev. Lett.*, 47:1726, 1981.

[58] T. F. Gallagher. *Rydberg atoms*. Cambridge University Press, 1994.

[59] D. Townsend, A. L. Goodgame, S. R. Procter, S. R. Mackenzie, and T. P. Softley. Deflection of krypton Rydberg atoms in the field of an electric dipole. *J. Phys. B: At. Mol. Opt. Phys.*, 34:439, 2001.

[60] S. R. Procter, Y. Yamakita, F. Merkt, and T. P. Softley. Controlling the motion of hydrogen molecules. *Chem. Phys. Lett.*, 374:667, 2003.

[61] Y. Yamakita, S. R. Procter, A. L. Goodgame, T. P. Softley, and F. Merkt. Deflection and deceleration of hydrogen Rydberg molecules in inhomogeneous electric fields. *J. Chem. Phys.*, 121:1419, 2004.

[62] E. Vliegen and F. Merkt. On the electrostatic deceleration of argon atoms in high Rydberg states by time-dependent inhomogeneous electric fields. *J. Phys. B: At. Mol. Opt. Phys.*, 38:1623, 2005.

[63] E. Vliegen, H. J. Worner, T. P. Softley, and F. Merkt. Nonhydrogenic effects in the deceleration of Rydberg atoms in inhomogeneous electric fields. *Phys. Rev. Lett.*, 92:033005, 2004.

[64] E. Vliegen and F. Merkt. Normal-incidence electrostatic Rydberg atom mirror. *Phys. Rev. Lett.*, 97:033002, 2006.

[65] E. Vliegen, P. Limacher and F. Merkt. Measurement of the three-dimensional velocity distribution of Stark-decelerated Rydberg atoms. *Eur. Phys. J. D*, 40:73, 2006.

[66] E. Vliegen, S. D. Hogan, H. Schmutz, and F. Merkt. Stark deceleration and trapping of hydrogen Rydberg atoms. *Phys. Rev. A*, 76:023405, 2007.

[67] S. D. Hogan and F. Merkt. Demonstration of three-dimensional electrostatic trapping of state-selected Rydberg atoms. *Phys. Rev. Lett.*, 100:043001, 2008.

[68] S. D. Hogan, Ch. Seiler, and F. Merkt. Rydberg-state-enabled deceleration and trapping of cold molecules. *Phys. Rev. Lett.*, 103:123001, 2009.

[69] Ch. Seiler, S. D. Hogan, H. Schmutz, J. A. Agner, and F. Merkt. Collisional and radiative processes in adiabatic deceleration, deflection, and off-axis trapping of a Rydberg atom beam. *Phys. Rev. Lett.*, 106:073003, 2011.

[70] Ch. Seiler, S. D. Hogan and F. Merkt. Trapping cold molecular hydrogen. *Phys. Che. Che. Phys.*, 13:19000, 2011.

[71] S. D. Hogan, Ch. Seiler, and F. Merkt. Motional, isotope and quadratic stark effects in Rydberg-Stark deceleration and electric trapping of h and d. *J. Phys. B: At. Mol. Opt. Phys.*, 46:045303, 2013.

[72] Christian Seiler. *Rydberg-Stark deceleration and trapping of atoms and molecules*. PhD thesis, ETH Zürich, 2013.

[73] S. A. Meek, G. Santambrogio, H. Conrad, and G. Meijer. Taming molecular beams; toward a gas-phase molecular laboratory on a chip. *J. Phys.: Conf. Ser.*, 194:012063, 2009.

[74] S. A. Meek, H. Conrad, and G. Meijer. A Stark decelerator on a chip. *New Journal of Physics*, 11:055024, 2009.

[75] S. D. Hogan, P. Allmendinger, H. Sassmammshausen, H. Schmutz, and F. Merkt. Surface-electrode Rydberg-stark decelerator. *Phys. Rev. Lett.*, 108:063008, 2012.

[76] P. Allmendinger, J. A. Agner, H. Schmutz and F. Merkt. Deceleration and trapping of a fast supersonic beam of metastable helium atoms with a 44-electrode chip decelerator. *Phys. Rev. A*, 88(4):043433, 2013.

[77] P. Allmendinger, J. Deiglmayr, J. A. Agner, H. Schmutz, and F. Merkt. Surface-electrode decelerator and deflector for Rydberg atoms and molecules. *Phys. Rev. A*, 90:043403, 2014.

[78] H. A. Bethe and E. E. Salpeter. *Quantum mechanics of one- and two-electron atoms*. Springer, 1957.

[79] I. V. Hertel and C.-P. Schulz. *Atoms, Molecules and Optical Physics 1*. Springer, 2015.

[80] J. R. Rydberg. The new series in the spectrum of hydrogen. *Astrophysical Journal*, 6:233, 1897.

[81] I. Martinson, L. J. Curtis. Janne Rydberg - his life and work. *Nucl. Instr. and Meth. in Phys. Res. B*, 235:17, 2005.

[82] J. R. Rubbmark, M. M. Kash, M. G. Littman, and D. Kleppner. Dynamical effects at avoided level crossings: A study of the Landau-Zener effect using Rydberg atoms. *Phys. Rev. A*, 23(6):3107, 1981.

[83] G. Herzberg. *Atomic Spectra and Atomic Structure*. Dower Publications, 1944.

[84] E. Schrodinger. Quantizierung als Eigenwertproblem. *Ann. Phys. (Leipzig)*, 80:437, 1926.

[85] L. D. Landau and E. M. Lifshitz. *Quantum Mechanics*. Addison-Wesley, 1958.

[86] R. J. Damburg and V. V. Kolosov. A hydrogen atom in a uniform electric field. iii. *J. Phys. B: At. Mol. Phys.*, 12:2637–2643, 1979.

[87] M. L. Zimmerman, M. G. Littman, M. M. Kash, and D. Kleppner. Stark structrure of the Rydberg states of alkali-metal atoms. *Phys. Rev. A*, 20(6):2251, 1979.

[88] W. C. Martin. Improved ^{4}He i 1snl ionization energy, energy levels, and Lamb shifts for 1sns and 1snp terms. *Phys. Rev. A*, 36:3575, 1987.

[89] G. W. F. Drake and R. A. Swainson. Quantum defects and the 1/n dependence of Rydberg energies: second-order polarization effects. *Phys. Rev. A*, 44:5448, 1991.

[90] H. H. Fielding and T. P. Softley. Observation of the Stark effect in autoionising Rydberg states of molecular hydrogen. *Chem. Phys. Lett.*, 185:199, 1991.

[91] L. Mandel. Photon occupation numbers in black body radiation. *J. Opt. Soc. Am.*, 69:1038, 1979.

[92] F. B. Dunning and R. G. Hulet, editor. *Atomic, Molecular, and Optical Physics: Atoms and Molecules: Volume 29B: Atomic, Molecular, And Optical Physics*. Academic Press, 1996.

[93] G. Scoles. *Atomic and Molecular Beam Methods*. Oxford University Press, 1988.

[94] S. Y. T. van de Meerakker, H. L. Bethlem, and G. Meijer. Taming molecular beams. *Nature*, 4:595, 2008.

[95] H. Haberland, U. Buck, and M. Tolle. Velocity distribution of supersonic nozzle beams. *Rev. Sci. Instr.*, 56:1712, 1985.

[96] T. Halfmann, J. Koensgen and K. Bergmann. A source for a high-intensity pulsed beam of metastable helium atoms. *Meas. Sci. Technol.*, 11:1510–1514, 2000.

[97] G. W. F. Drake. Theory of relativistic magnetic dipole transitions: lifetime of the metastable $^2S_5$ state of the heliumlike ions. *Phys. Rev. A*, 3:908, 1971.

[98] J. R. Woodworth and H. W. Moos. Experimental determination of the single-photon transition rate between the 2^3S_1 and 1^1S_0 states of He i. *Phys. Rev. A*, 12:2455, 1975.

[99] S. S. Hodgman, R. G. Dall, L. J. Byron, G. H. Baldwin, S. J. Buckman, and A. G Truscott. Metastable helium: A new determination of the longest atomic excited-state lifetime. *Phys. Rev. Lett.*, 103:053002, 2009.

[100] P. E. Siska. Molecular-beam studies of Penning ionisation. *Rev. Mod. Phys.*, 65:337, 1993.

[101] W. C. Richardson and D. W. Setser. Penning ionization optical spectroscopy: Metastable helium (he $2\,^3$s) atoms with nitrogen, carbon monoxide, oxygen, hydrogen chloride, hydrogen bromide, and chlorine. *J. Chem. Phys.*, 58(5):1809, 1973.

[102] Toptica Photonics AG, Lochhamer Schlag 19, 82166 Graefelfing (Munich), Germany.

[103] M. G. Littman and H. J Metcalf. Spectrally narrow pulsed dye laser without beam expander. *Applied Optics*, 17:2224, 1978.

[104] J. L. Wiza. Microchannel plate detectors. *Nucl. Inst. and Met.*, 162:587, 1979.

[105] W. B. Colson, J. McPherson and F. T. King. High gain imaging electron multiplier. *Rev. Sci. Instr.*, 44:1694, 1973.

[106] E. Vliegen. *Rydberg states in atom and molecule optics*. PhD thesis, ETH Zürich, 2007.

[107] Y. Xia, Y. Yin, H. Chen, L. Deng, J. Yin. Electrostatic surface guiding for cold polar molecules: Experimental demonstration. *Phys. Rev. Lett.*, 100:043003, 2008.

[108] V. Zhelyazkova and S. D. Hogan. Probing interactions between Rydberg atoms with large electric dipole moments in amplitude-modulated electric fields. *Phys. Rev. A*, 92(011402), 2015.

[109] A. G. Vaidyanathan, W. P. Spencer, and D. Kleppner. Inhibited absorption of blackbody radiation. *Phys. Rev. Lett.*, 47:1592, 1981.

[110] Ch. Seiler, S. D. Hogan and F. Merkt. Dynamical processes in Rydberg-Stark deceleration and trapping of atoms and molecules. *Chimia*, 66:208, 2012.

[111] S. Marx, D. Adu Smith, M. J. Abel, T. Zehentbauer, G. Meijer. Imaging cold molecules on a chip. *Phys. Rev. Lett.*, 111:243007, 2013.

[112] A. Osterwalder, S. A. Meek, G. Hammer, H. Haak, and G. Meijer. Deceleration of neutral molecules in macroscopic traveling traps. *Phys. Rev. A*, 81:051401, 2010.

[113] S. Y. T. van de Meerakker, H. L. Bethlem, N. Vanhaecke, and G. Meijer. Manipulation and control of molecular beams. *Chem. Rev.*, 112:4828, 2012.

[114] M. Quintero-Perez, P. Jansen, T. E. Wall, J. E. van den Berg, S. Hoekstra, and H. L. Bethlem. Static trapping of polar molecules in a traveling wave decelerator. *Phys. Rev. Lett.*, 110:133003, 2013.

[115] P. Lancuba and S. D. Hogan. Guiding Rydberg atoms above surface-based transmission lines. *Phys. Rev. A*, 88:043427, 2013.

[116] D. Kleppner. Inhibited spontaneous emission. *Phys. Rev. Lett.*, 47:233, 1981.

[117] T. P. Softley. Applications of molecular Rydberg states in chemical dynamics and spectroscopy. *Int. Rev. Phys. Chem.*, 23:1, 2004.

[118] Scientific Instrument Services, 1027 Old York Road, Ringoes, NJ 08551-1054, USA.

[119] D. A. Dahl. SIMION for the personal computer in reflection. *International Journal of Mass Spectrometry*, 200:3, 2000.

[120] A. B. Kasturiarachi. Leap-frogging Newton's method. *Int. J. Math. Educ. Sci. Technol.*, 33:521, 2002.

[121] S. D. Hogan, M. Motsch and F. Merkt. Deceleration of supersonic beams using inhomogeneous electric and magnetic fields. *Phys. Che. Che. Phys.*, 13:18705–18723, 2011.

[122] N. Vanhacke, D. Comparat and P. Pillet. Rydberg decelerator using a travelling electric-field gradient. *J. Phys. B: At. Mol. Opt. Phys.*, 38:409, 2005.

[123] I. I. Beterov, D. B. Tretyakov, I. I. Ryabstev, V. M. Entin, A. Ekers and N. N. Bezuglov. Ionisation of Rydberg atoms by blackbody radiation. *New. J. Phys.*, 11:013052, 2009.

[124] P. Lancuba and S. D. Hogan. Transmission-line decelerators for atoms in high Rydberg states. *Phys. Rev. A*, 90(053410), 2014.

[125] P. Jansen, M. Quintero-Perez, T. Wall, J. E. van den Berg, S. Hoekstra, and H. Bethlem. Deceleration and trapping of ammonia molecules in a traveling decelerator. *Phys. Rev. A*, 88:043424, 2013.

[126] M. Niering, R. Holzwarth, J. Reichert, P. Pokasov, T. Udem, M. Weitz, T. W. Hänsch, P. Lemonde, G. Santarelli, M. Abgrall, P. Laurent, C. Salomon, and A. Clairon. Measurement of the hydrogen ^{1}s- ^{2}s transition frequency by phase coherent comparison with a microwave cesium fountain clock. *Phys. Rev. Lett.*, 84:5496, 2000.

[127] A. Wallraff, D. I. Schuster, A. Blais, L. Frunzio, R.-S. Huang, J. Majer, S. Kumar, S. M. Girvin and R. J. Schoelkopf. Strong coupling of a single photon to a superconducting qubit using circuit quantum electrodynamics. *Nature (London)*, 431:162, 2004.

[128] G. Dufour, D. B. Cassidy, P. Crivelli, P. Debu, A. Lambrecht, V. V. Nesvizhevsky, S. Reynaud, A. Yu. Voronin and T. E. Wall. Prospects for studies of the free fall and gravitational quantum states of antimatter. *Advances in High Energy Physics*, 2015, 2015.

[129] A. P. Mills Jr. and M. Leventhal. Can we measure the gravitational free fall of cold Rydberg state positronium? *Nucl. Instr. and Meth. in Phys. Res. B*, 192:102, 2002.

[130] A. Kellerbauer, M. Amoretti, A.S. Belov, G. Bonomi, I. Boscolo, R.S. Brusa,M. Buchner, V.M. Byakov, L. Cabaret, C. Canali, C. Carraro, F. Castelli, S. Cialdi,M. de Combarieu, D. Comparat, G. Consolati, N. Djourelov, M. Doser,G. Drobychev, A. Dupasquier, G. Ferrari, P. Forget, L. Formaro, A. Gervasini,M.G. Giammarchi, S.N. Gninenko, G. Gribakin, S.D.

Hogan, M. Jacquey,V. Lagomarsino, G. Manuzio, S. Mariazzi, V.A. Matveev, J.O. Meier,F. Merkt, P. Nedelec, M.K. Oberthaler, P. Pari, M. Prevedelli, F. Quasso, A. Rotondi, D. Sillou, S.V. Stepanov, H.H. Stroke, G. Testera,G.M. Tino, G. Trenec, A. Vairo, J. Vigue, H. Walters, U. Warring,S. Zavatarelli, D.S. Zvezhinskij. Proposed antimatter gravity measurement with an antihydrogen beam. *Nuclear Instruments and Methods in Physics Research B*, 266:351, 2008.

[131] V. Zhelyazkova, A. Cournol, T. E. Wall, A. Matsushima, J. J. Hudson, E. A. Hinds, M. R. Tarbutt, and B. E. Sauer. Laser cooling and slowing of caf molecules. *Phys. Rev. A*, 89:053416, 2014.